Synthesis and Characterization of Cu-based Multinary Metal Oxides for Photoelectrochemical Water Splitting

vorgelegt von

M. Sc.

Angang Song

von der Fakultät II – Mathematik und Naturwissenschaften

der Technischen Universität Berlin

zur Erlangung des akademischen Grades

Doktor der Ingenieurwissenschaften

- Dr. - Ing.

genehmigte Dissertation

Promotionsausschuss:

Vorsitzender: Prof. Dr. Matthias Drieß

Gutachter: Prof. Dr. Roel van de Krol

Gutachterin: Prof. Dr. Anna Fischer

Tag der wissenschaftlichen Aussprache: 16.12.2019

Berlin 2020

Abstract

In the future, the storage of solar energy in the form of chemical bonds is expected to be a key method for solar energy conversion. Photoelectrochemical (PEC) water splitting is one of the most important approaches to convert solar energy into chemical bonds via production of hydrogen. However, there are numerous scientific challenges in developing this PEC water splitting, including the identification of suitable semiconductor materials to use as photoelectrodes with adequate absorption of incident photons, optimization of interfaces between the different layers of the photoelectrodes and the electrolytes, and the development more efficient co-catalysts for both water splitting half-reactions. Among various semiconductor materials that have been considered as photoelectrodes for use in PEC devices, oxide-based photoelectrodes are particularly attractive due to their potential for inexpensive fabrication, environmental friendliness and chemical stability under oxidizing conditions in aqueous solutions compared to other types of semiconductors. This thesis aims to explore new metal oxide semiconductor materials with bandgaps for that allow good visible light absorption and to understand the charge transport properties and interfaces of different layers in the photoelectrodes.

P-type $CuBi_2O_4$ has recently been reported as a promising photocathode material for photoelectrochemical water reduction due to its optimal optical band gap and positive photocurrent onset potential. However, despite these favorable attributes, $CuBi_2O_4$ photocathodes have shown limitations in charge carrier transport within $CuBi_2O_4$ and across its interface with n-type fluorine doped tin oxide (FTO) substrate. To overcome the later limitation, a very thin and transparent p-type Cu doped NiO (Cu:NiO) back contact layer is inserted between the FTO substrate and $CuBi_2O_4$. It was shown that the addition of a Cu:NiO back contact layer improves the photoelectrochemical performance of $CuBi_2O_4$ photocathodes by improving the charge carrier transport across the $CuBi_2O_4$-substrate interface. These results illustrate the importance of suitable band alignment and suggest a potential improvement strategy for other oxide-based photocathode materials deposited on FTO substrates.

Monoclinic copper vanadate (n-type $Cu_2V_2O_7$) has a nearly ideal bandgap energy of ~2.0 eV, which corresponds to a potential solar-to-hydrogen (STH) efficiency of 16%, that makes it a promising candidate as a top absorber in a tandem photoelectrochemical (PEC) device. However, $Cu_2V_2O_7$ photoanodes have not yet demonstrated high photoconversion efficiencies, and the factors that limit the efficiency have not yet been fully identified. In this thesis, the key physical and photoelectrochemical properties of $Cu_2V_2O_7$ photoanodes, such as optical band gap, doping type, flat-band potential, band positions, charge carrier transport, chemical composition, chemical stability, and faradaic efficiency for O_2 evolution are established. The photoelectrochemical performance of $Cu_2V_2O_7$ photoanodes was found to be strongly limited by poor charge carrier separation efficiency. Time-resolved microwave conductivity (TRMC) measurements revealed that the low mobility (~3.5×10^{-3} cm^2 V^{-1} s^{-1}) and short hole diffusion length (~28 nm) are the main reason for its fast recombination. In addition, cobalt phosphate (Co-

P_i) was used as a water oxidation co-catalyst to overcome the slow water oxidation kinetics that partially limit the performance of $Cu_2V_2O_7$.

In the final part, we assess a tandem photoelectrochemical cell consisting of a W:$BiVO_4$ photoanode top absorber and a $CuBi_2O_4$ photocathode bottom absorber for overall solar water splitting. The $CuBi_2O_4$ photocathode shows an exceptionally positive photocurrent onset potential of ~1.1 V vs. RHE; however, it does not produce a detectable amount of H_2 at any electrochemical potential. This is because most of the photocurrent likely goes towards photo-corrosion of $CuBi_2O_4$ rather than H^+ reduction even when Pt or RuO_x is added as a co-catalyst. Protecting the $CuBi_2O_4$ photocathode with a CdS/TiO_2 heterojunction and adding RuO_x on top of that prevents photo-corrosion and allows for photoelectrochemical production of H_2 at potentials ≤ 0.25 V vs. RHE. Thus, a tandem photoelectrochemical cell composed of a W:$BiVO_4$/Co-Pi photoanode and $CuBi_2O_4$/CdS/TiO_2/RuO_x photocathode produces both hydrogen and oxygen that can be detected under illumination under an applied bias of ≥ 0.4 V. This work is the first experimental demonstration of hydrogen and oxygen production from a $CuBi_2O_4$-$BiVO_4$ based tandem device. To enable bias-free operation of the device, further optimization of the protection layer of the $CuBi_2O_4$ photocathode is needed in order to reduce the loss of photovoltage.

Kurzfassung

Die Speicherung von Sonnenenergie in Form von chemischer Bindungen soll in Zukunft eine Schlüsselmethode für die Umwandlung von Sonnenenergie sein. Photoelektrochemische Wasserspaltung (PEC) ist einer der wichtigsten Ansätze, um Sonnenenergie durch Erzeugung von Wasserstoff in chemische Bindungen umzuwandeln. Es gibt jedoch zahlreiche wissenschaftliche Herausforderungen bei der Weiterentwickelung von PEC-Wasserspaltung. Dazu gehören unter anderem die Identifizierung geeigneter Halbleitermaterialien zur Verwendung als Photoelektroden mit ausreichender Absorbtionsfähigkeit einfallender Photonen, die Optimierung der Grenzflächen zwischen den verschiedenen Schichten der Photoelektroden und den Elektrolyten, sowie die Entwicklung weiterer Effizienter Cokatalysatoren für beide wasserspaltenden Halbreaktionen. Unter verschiedenen Halbleitermaterialien, die als Photoelektroden für die Verwendung in PEC in Betracht kommen, sind Photoelektroden auf Oxidbasis aufgrund ihres Potentials für eine kostengünstige Herstellung, Umweltfreundlichkeit und chemische Stabilität unter oxidierenden Bedingungen in Wasser im Vergleich zu anderen Arten von Halbleitern besonders attraktiv. Diese Dissertation zielt darauf ab, neue Metalloxidhalbleitermaterialien mit geringeren Bandlücken für eine erhöhte Photonenabsorption zu untersuchen und die Ladungstransporteigenschaften und Grenzflächen verschiedener Schichten in den Photoelektroden zu verstehen.

$CuBi_2O_4$ vom P-Typ wurde kürzlich aufgrund seiner optimalen optischen Bandlücke und seines positiven Potentials zum Einsetzen des Fotostroms als vielversprechendes Fotokathodenmaterial für die photoelektrochemische Wasserreduktion beschrieben. Trotz dieser günstigen Eigenschaften zeigten $CuBi_2O_4$ Fotokathoden Einschränkungen beim Ladungsträgertransport innerhalb von $CuBi_2O_4$ und über die Grenzfläche mit einem fluordotierten n-Typ-Zinnoxidsubstrat (FTO). Um die spätere Einschränkung zu überwinden, wird eine sehr dünne und transparente p-Typ Cu-dotierte NiO (Cu:NiO) Rückkontaktschicht zwischen dem FTO Substrat und $CuBi_2O_4$ eingefügt. Es stellte sich heraus, dass die Hinzufügung einer Cu:NiO Rückkontaktschicht die photoelektrochemische Leistung von $CuBi_2O_4$-Photokathoden verbessert, indem der Ladungsträgertransport über die $CuBi_2O_4$-Substratgrenzfläche verbessert wird. Diese Ergebnisse veranschaulichen die Bedeutung einer geeigneten Bandausrichtung und legen eine mögliche Verbesserungsstrategie für andere, auf FTO-Substraten abgeschiedene Fotokathodenmaterialien auf Oxidbasis nahe.

Monoklines Kupfervanadat ($Cu_2V_2O_7$ vom n-Typ) weist eine ideale optimale Bandlückenenergie von 2,0 eV auf, was einem potenziellen Solar-Wasserstoff-Wirkungsgrad von 16% entspricht und es zu einem vielversprechenden Kandidaten für den Top-Absorber in einer photoelektrochemischen (PEC) Tandemzelle. $Cu_2V_2O_7$ Photoanoden haben jedoch noch keine hohen Photoumwandlungseffizienzen gezeigt, und die Faktoren, die die Effizienz

begrenzen, wurden noch nicht vollständig identifiziert. In dieser Arbeit werden die wichtigsten physikalischen und photoelektrochemischen Eigenschaften dieser vielversprechenden $Cu_2V_2O_7$ Photoanoden wie zum Beispiel die optische Bandlücke, Dotierungstyp, Flachbandpotential, Bandpositionen, Ladungsträgertransport, chemische Zusammensetzung, chemische Stabilität und O_2-Entwicklungs-Faraday-Effizienz ermittelt. Es zeigte sich, dass die photoelektrochemische Leistung von $Cu_2V_2O_7$-Photoanoden durch eine sehr schlechte Ladungsträgertrennungseffizienz stark eingeschränkt ist. Zeitaufgelöste Mikrowellenleitfähigkeitsmessungen (TRMC) ergaben, dass die geringe Mobilität (~3.5×10^{-3} cm^2 V^{-1} s^{-1}) und die kurze Lochdiffusionslänge (~28 nm) der Hauptgrund für die schnelle Rekombination sind. Zusätzlich wurde Kobaltphosphat (Co-P_i) als Wasseroxidations-Cokatalysator verwendet, um die langsame Wasseroxidationskinetik zu überwinden, die beiträgt an die geringe Leistung von $Cu_2V_2O_7$.

Darüber hinaus untersuchen wir eine photoelektrochemische Tandemzelle, die aus einem W:$BiVO_4$-Photoanoden-Topabsorber und einem $CuBi_2O_4$-Photokathoden-Bottomabsorber besteht, für solare Wasserspaltung. Die $CuBi_2O_4$-Fotokathode zeigt ein außergewöhnlich positives Einschaltpotential des Fotostroms von ~1,1 V gegenüber RHE; Unabhängig vom elektrochemischen Potential wird jedoch keine nachweisbare Menge an H_2 erzeugt, da der größte Teil des Photostroms wahrscheinlich eher zur Photokorrosion von $CuBi_2O_4$ als zur H_+ -Reduktion führt, selbst wenn Pt oder RuOx als Cokatalysator zugesetzt werden. Das Schützen der $CuBi_2O_4$-Fotokathode mit einem CdS/TiO_2-Heteroübergang und das Hinzufügen von RuOx verhindern Fotokorrosion und ermöglichen die photoelektrochemische Erzeugung von H_2 bei Potentialen $\leqslant$ 0,25 V gegenüber RHE. Eine photoelektrochemische Tandemzelle, die aus einer W:$BiVO_4$/Co-Pi-Photoanode und einer $CuBi_2O_4$/CdS/TiO_2/RuOx-Photokathode besteht, erzeugt somit sowohl Wasserstoff als auch Sauerstoff, was bei Belichtung unter einer angelegten Vorspannung von $\geqslant$ 0,4 V nachgewiesen werden kann. Diese Arbeit ist die erste experimentelle Demonstration der Wasserstoff- und Sauerstoffproduktion aus einem $CuBi_2O_4$-$BiVO_4$-basierten Tandemgerät. Um einen vorspannungsfreien Betrieb der Vorrichtung zu ermöglichen, ist eine weitere Optimierung der Schutzschicht der $CuBi_2O_4$-Photokathode erforderlich, um den Verlust an Photospannung zu verringern.

Table of Contents

Chapter 1. Introduction

1.1 The energy challenge and greenhouse effect

In recent decades, the world has experienced an exponential increase in energy demand due to the world's population growth and increasing standards of living. The world population is estimated to growth from ~7.7 billion in 2019 to ~9.8 billion by 2050 according to predictions by the United Nations.[1] As a consequence, global energy demand is expected to increase by as much as an order of magnitude by 2050, while primary energy demands are expected to increase by 1.5 - 3 times. In order to face this growing energy demand we mainly use uranium and fossil fuels such as petroleum, natural gas and coal, which are finite natural resources as illustrated in **Figure 1.1**. However, these energy resources are not renewable, so they are going to run out and become more and more expensive in the future. According to International Energy Outlook 2018 (IEO2018), the world primary energy consumption grew by 2.2% in 2017, up from 1.2% in 2016, and is the highest since 2013. All fuels except coal and hydroelectricity grew at above-average rates, and natural gas grew the most, followed by renewable power and oil.

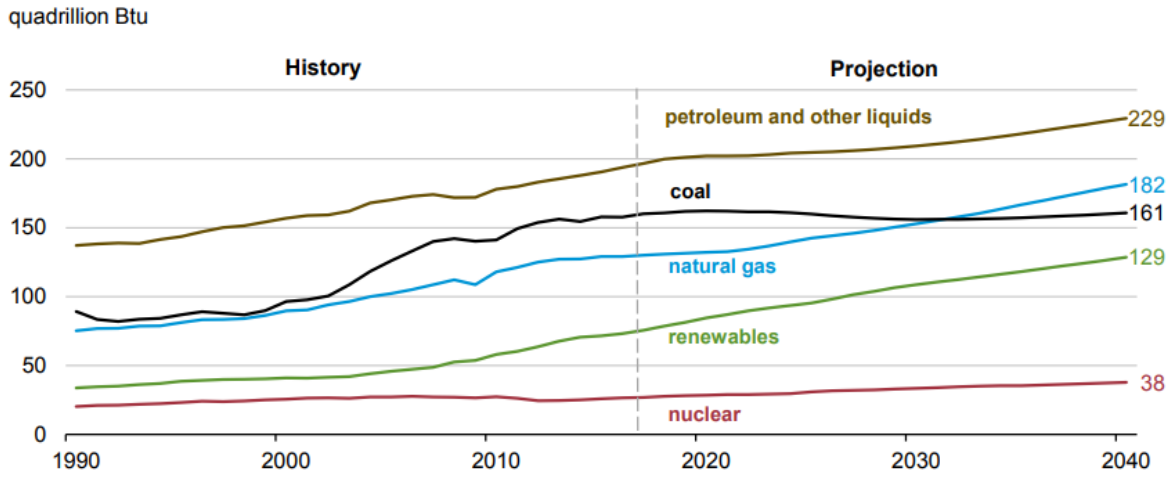

Figure 1.1. Primary energy world consumption in quadrillion Btu per year. This figure was adapted from reference[2].

The overconsumption of fossil fuels also raises serious environmental problems. For example, if the combustion of fossil fuels is complete, the carbon and sulfur are burned to carbon dioxide (CO_2) and sulfur dioxide, which contributes to greenhouse effect and the emission of other pollutants in the atmosphere. According to the Earth System Research Laboratory report from 2019, the CO_2 concentration has increased from 280 ppm in pre-industrial times to 410 ppm, as shown in **Figure 1.2a**.[3] CO_2 emissions produced a global accumulation of 3 ppm in every two years, and this drastic growth in CO_2 emissions in the last few decades is one of the most important parameters that influences global warming and climate change. The annual anomaly of the global average surface

temperature in 2018 was +0.31°C above the 1981-2010 average, and was the 4th warmest since 1891 according to Global Climate Report as shown in **Figure 1.2b**. On a longer time scale, global average surface temperatures have risen at a rate of about 0.73°C per century**,** and as a consequence the sea level is estimated to have risen by perhaps 20 cm. Such changes can have wide-ranging effects on human activities all over the world. Furthermore, many scientists predict that if atmospheric concentrations of greenhouse gases continue to increase, as present trends in fossil fuel consumption suggest will occur, the Earth's temperature may increase by another 2°C and perhaps by up to 4°C in the next century. If this prediction is realized, sea levels could rise between 30 and 60 cm before the end of the 21st century.[4]

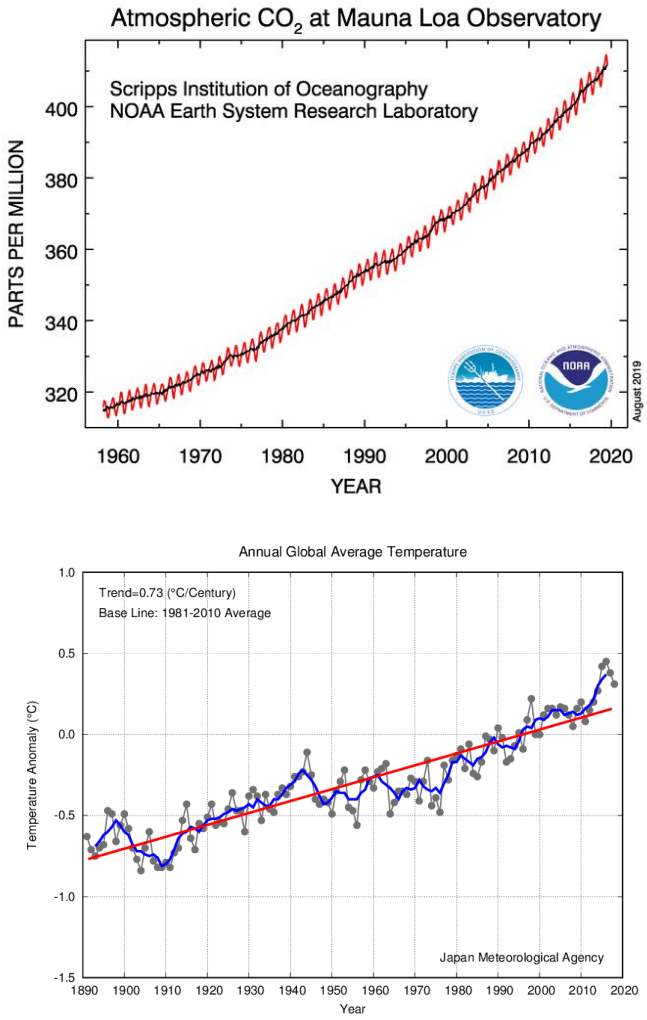

Figure 1.2. (a) Trends in atmosphere CO_2 concentration, reproduced from reference[3]. (b) Annual Anomalies of Global Average Surface Temperature (1891 - 2018).

1.2 Renewable energy resources and sustainable development

To protect the climate and achieve a bright energy future with minimal environmental impacts, the increase in energy demand and environmental problems with fossil fuels must be taken into consideration simultaneously. Saving fossil fuels and developing renewable and non-polluting energy sources has become an urgent matter for all countries. Renewable energies are energy sources that are continually replenished (environmental friendly) by nature and derived directly from the sun (such as thermal, photo-chemical, and photo-electric), indirectly from the sun (such as wind power, hydro power, and bio-power), or from other natural movements and mechanisms of the environment (such as tidal energy, concentrating solar thermal power and geothermal power).[5] **Figure 1.3** shows an overview of renewable energy sources. The main categories are wind energy, marine energy, solar energy, hydro energy, geothermal energy, and bioenergy. Electricity, heat and fuels can be obtained from these natural renewable energy sources. Global electricity generation from renewable energy sources is expected to grow 2.7 times between 2010 and 2035 according to the World Energy Outlook.[6]

However, there are still some significant barriers for most of the renewable energy sources. For example, wind energy requires constant and significant amounts of wind and it can have a significant visual impact on landscapes. Biofuels have low energy densities, collection and transportation can be cost prohibitive, and may actually contribute to global climate change with increased atmospheric CO_2 production. Hydropower plants mainly depend on the available flow of the river and can cause the flooding of surrounding communities and landscapes if a dam is built. The construction for harvesting tidal energy can be costly, and it takes up a lot of space and is difficult for shipping to move around. The start-up/development costs for geothermal energy can be expensive, and the maintenance is also a problem due to corrosion.[5]

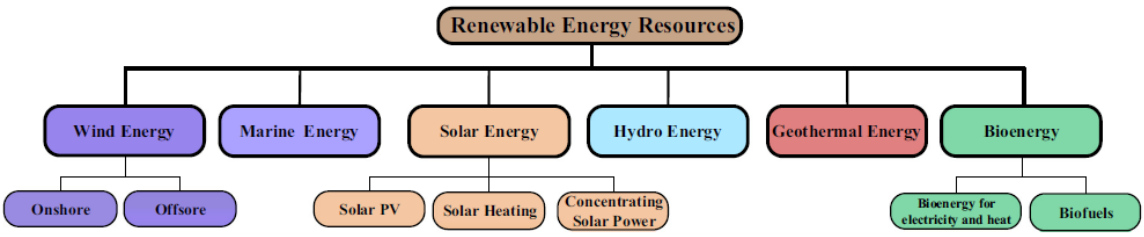

Figure 1.3. Overview of renewable energy sources, this figure was adapted from reference [4].

Among the renewable sources of energy, solar energy would be the best option for future renewable energy demand since it is superior in terms of availability, accessibility, and capacity compared to other renewable energy sources. It also has least negative impacts on the environment, which makes it a promising energy source for managing long term issues in the energy crisis.[7] However, solar energy cannot be employed as such, it must be captured and converted into useful forms of energy. Because solar power is diffuse and intermittent, conversion should involve concentration and storage.[8]

There are several kinds of solar techniques that are currently available such as small-scale photovoltaic (PV) cells, solar concentrated power (CSP) and also large-scale PV systems as shown in **Figure 1.4**.[9] However, each of them is based on quite different concepts and science and each has its unique advantages and drawbacks. Generally speaking, PV has the advantage that it uses not only direct sunlight but also the diffuse component of sunlight, and it produces power even if the sky is not completely clear. This capability allows the effective deployment in many more regions in the world than for CSP. There are also some technical barriers that vary across the type of technology. For example, the main technical barriers for photovoltaic cells include low conversion efficiencies; performance limitations and cost of system components such as batteries and inverters; and inadequate supply of raw materials such as cadmium and tellurium. In addition, safe disposal of batteries becomes difficult in the absence of a structured disposal/recycling process. What's more, storage is another very important concern in the case of stand-alone PV systems, as is the shorter battery life compared to that of the module.[10] One possible solution is to convert solar energy into chemical fuels, such as hydrogen and methanol, a process that would solve both the energy crisis and the environmental emergency.

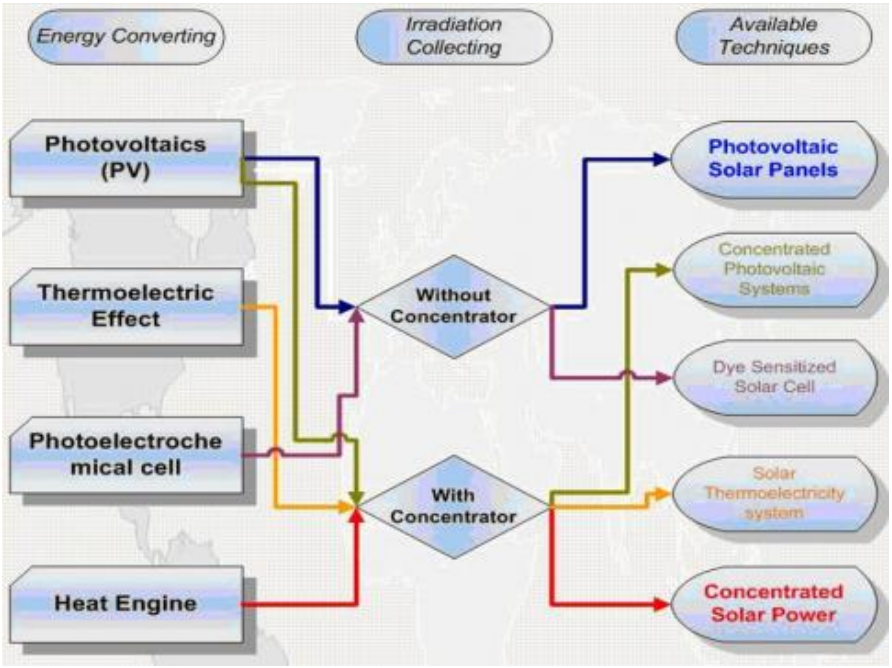

Figure 1.4. Overview of solar technologies, this figure was taken from reference[7].

1.3 Photoelectrochemical water splitting as an elegant method

Hydrogen is an abundant element in the world, and in its molecular form it is the simplest chemical fuel that makes a highly efficient, clean-burning energy carrier without harmful emissions. However, hydrogen is not an energy source, and it does not occur in nature in its elemental or molecular form.[11] Since the most abundant source of

hydrogen is water, photoelectrochemical (PEC) water splitting using sunlight can be used as a direct, efficient and promising route to produce hydrogen without relying on any fossil fuels. After the first demonstration of this concept in 1972 by Akira Fujishima and Kenichi Honda, much attention has been already paid to semiconductor materials which could be used as photoelectrodes for water splitting.[12] Generally, when a semiconductor with the proper properties is immersed in an aqueous electrolyte and illuminated with sunlight, the photon energy will be converted to electrical energy, which is directly used to electrochemically split water into hydrogen and oxygen. In this process, the hydrogen and oxygen are produced at separate electrodes, which helps to avoid serious safety concerns and allows separation of these gases in the following process. Moreover, a photoelectrochemical water splitting device can be constructed entirely from oxide-based semiconductor materials that are low cost and can, in principle, show good stability for hydrogen production in aqueous solutions which can improve commercial viability of a PEC water splitting device.[13]

Chapter 2. Research background

Since photoelectrochemical (PEC) water splitting for the production of hydrogen represents an important and necessary field of research in the face of a growing need for domestic, clean, abundant, environmental friendly and renewable energy, the working principle of a PEC cell is briefly summarized. In this section, we also present an analysis of both the advantage and limitations of recently developed metal oxide semiconductors for solar water splitting to give insight into the potential for viable performance in solar fuel applications.

2.1 Basic principles of PEC water splitting

2.1.1 PEC cell basics

In general, a PEC cell consists of three components: a working electrode, a counter electrode, and an electrolyte. In addition, a reference electrode is often used. A common method is to use light-absorbing materials, such as semiconductors or molecular systems, as working electrode to capture photons and convert the energy of the photons to excited states of charge carriers.[14] The photo-excited charge carriers (electron-hole pairs) can be transported to the interface between the light absorber and the electrolyte, at which reactive sites can facilitate oxidative or reductive electron-transfer half-reactions.[15] In theory, there are three options for the arrangement of photo-electrodes in the assembly of PEC cells as shown in **Figure 2.1**.

(a) photoanode made of n-type semiconductor and cathode made of metal;

(b) photoanode made of n-type semiconductor and photocathode made of p-type semiconductor;

(c) photocathode made of p-type semiconductor and anode made of metal.

The following sections will be limited to the first configuration, although the working principles of PEC cells are the same for all three configurations.

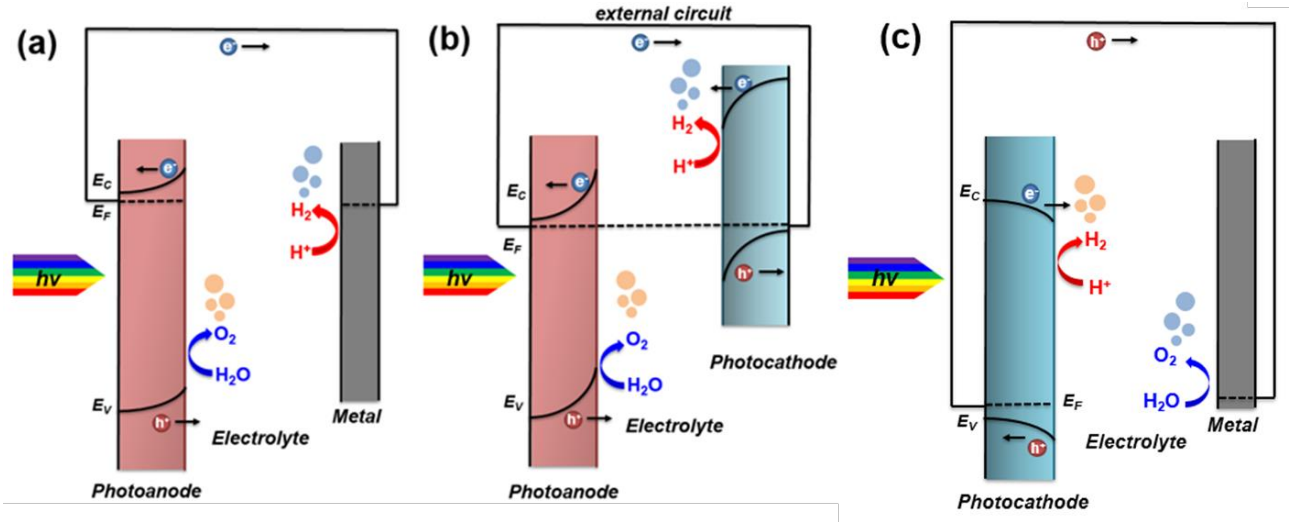

Figure 2.1. (a) Illustration of a PEC cell that consists of a semiconducting photoanode and a metal cathode (b) Illustration of a PEC cell that consists of a semiconducting photocathode and a photoanode (c) Illustration of a PEC cell that consists of a semiconducting photocathode and a metal anode.

2.1.2 Reaction mechanism

Solar water splitting by using a PEC involves several processes within photo-electrodes and at the photo-electrode electrolyte interface. When a photoelectrode (semiconductor) is immersed in the aqueous electrolyte, there will be a charge transfer across the semiconductor/electrolyte junction to maintain the electrostatic equilibrium. Charge carriers will be transferred from the semiconductor to the electrolyte until the Fermi level of the semiconductor reaches the redox potential of the electrolyte. Under illumination, the photogenerated electron-hole pairs will be separated by the space-charge field and the holes travel to the semiconductor- electrolyte interface for oxidation reaction, while the electrons travel to the counter electrode for water reduction reaction as illustrated in **Figure 2.2**.

The equation for the oxygen evolution reaction (OER) is listed below:

$$2H_2O(aq) + 4h^+ \rightarrow 4H^+ + O_2(g) \quad (2.1)$$

This process takes place at the semiconductor-electrolyte interface. The oxygen evolves at the photoanode and the protons migrate to the counter electrode through the internal circuit (aqueous electrolyte). Simultaneously, the electrons, generated as a result of reaction (2.2) at the photoanode, are transferred over the external circuit to the counter electrode, resulting in the reduction of protons to molecular hydrogen as shown below:

$$2H^+(aq) + 2e^- \rightarrow H_2(g) \quad (2.2)$$

Accordingly, the overall reaction of the PEC can be expressed in the form:

$$2\mathrm{H_2O}\,(l) \rightarrow 2\mathrm{H_2(g)} + \mathrm{O_2(g)} \tag{2.3}$$

The change of Gibbs free energy for the splitting of H_2O into H_2 and 1/2 O_2 under standard conditions is

$$\Delta G^{\theta} = +237\,\mathrm{kJ/mol}\,. \tag{2.3a}$$

The standard potential of the electrochemical cell, ΔE^{θ}, can be calculated using the Nernst equation,

$$\Delta G^{\theta} = -nF\Delta E^{\theta} \tag{2.4}$$

where n is the number of moles of electrons transferred and F is the Faraday constant (96485 C/mol). This is corresponds to the standard reversible potential ΔE^{θ} of 1.23 V. Thus, reaction (2.3) only takes place when the energy of the photons absorbed by the photoanode is equal to or larger than the 1.23 eV (λ < 1000 nm) with sunlight.

For overall solar water splitting, four electron-hole pairs must be generated for the production of two hydrogen molecules and one oxygen molecule. In order to drive this reaction, the conduction band position of the semiconductor needs to be more negative than the reduction level of water E (H^+/H_2) while the valence band position needs to be more positive than the oxidation level of water E (O_2/H_2O).

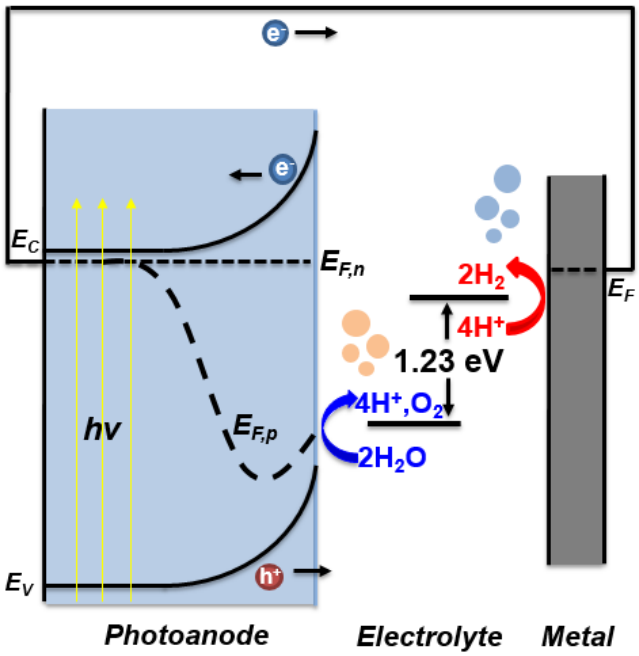

Figure 2.2. The energy diagram of a PEC cell that consists of a semiconducting photoanode and a metal cathode.

2.1.3 Space charge region and quasi-Fermi level

As discussed above, when we immerse the semiconductor into the aqueous electrolyte, a charge transfer between the semiconductor and the electrolyte will take place until an electrochemical equilibrium is achieved. This surface charge is compensated by a charge of the opposite sign, which is induced in the electrolyte within a localized layer, known as the Helmholtz layer. It is ~ 1 nm thick and is formed of oriented water molecule dipoles and electrolyte ions adsorbed at the electrode surface. The height of this potential barrier, known as the Helmholtz barrier, is determined by the nature of the aqueous environment of the electrolyte and the properties of the photo-electrode surface.

When the electronic equilibrium is reached, the Fermi level of the electrons in the semiconductor and redox potential of electrolyte are aligned at the interface of semiconductor/electrolyte junction, which usually lead to an upward band bending in a n-type semiconductor for n-type semiconductor/electrolyte junction and a downward band bending in a p-type semiconductor for p-type semiconductor/electrolyte junction. This region (band bending) is defined as the depletion layer or the space charge layer as illustrated in **Figure 2.3**. The performance characteristics of PEC cells depend, to a large extent, on the height of the potential drop ϕ_{sc}, since the space charge layer is responsible for the separation of the photogenerated electron-hole pairs. The width of the space charge layer (W) can be expressed as:

$$W = \sqrt{\frac{2\,\varepsilon\,\varepsilon_0}{e\,N_D}\left(\varphi_{SC} - \frac{k\,T}{e}\right)} \tag{2.5}$$

where ε is the relative permittivity or dielectric constant, ε_0 is the permittivity of free space, N_D is the ionized donor density, φ_{SC} is the potential drop in the space charge layer, k is the Boltzmann constant, T is the temperature (K), and e is the electronic charge (C). Although this important result was derived for n-type semiconductors, it is also valid for p-type materials if N_D is replaced with the acceptor density, N_A. The donor density (N_D) and the flatband potential (φ_{fb}) can be determined by Mott-Schottky measurements. Mott-Schottky is one of the electrochemical impedance techniques, which tells the flat band potential and carrier density. Mott-Schottky plots are created using the following relationship assuming ideal semiconductor behavior:

$$\frac{1}{C^2} = \frac{2}{e\,\varepsilon\,\varepsilon_0\,N_D}\left(-\varphi_D + \varphi_{fb} - \frac{k\,T}{e}\right) \tag{2.6}$$

where C is the capacitance (F/m^2), ε is the relative permittivity or dielectric constant, ε_0 is the permittivity of free space, N_D is the donor density (m^{-3}), and φ_{fb} is the flat band potential (V vs reference). Meanwhile, the charge carrier diffusion length is also a key parameter in determining the PEC performance of a semiconductor, since the

photons that were absorbed in diffusion region (L_D) also can contribute to the photocurrent. The charge carrier diffusion lengths can be calculated using the following relationship,

$$L_D = \sqrt{\left(\frac{\mu\, k\, T}{e}\right)\tau} \tag{2.7}$$

where μ is mobility ($m^2\ V^{-1}\ s^{-1}$), k is the Boltzmann constant, T is the temperature (K), e is the electronic charge (C), and τ is the charge carrier lifetime (s). Beyond diffusion region, the electrons will recombine with holes in the so-called "recombination region".

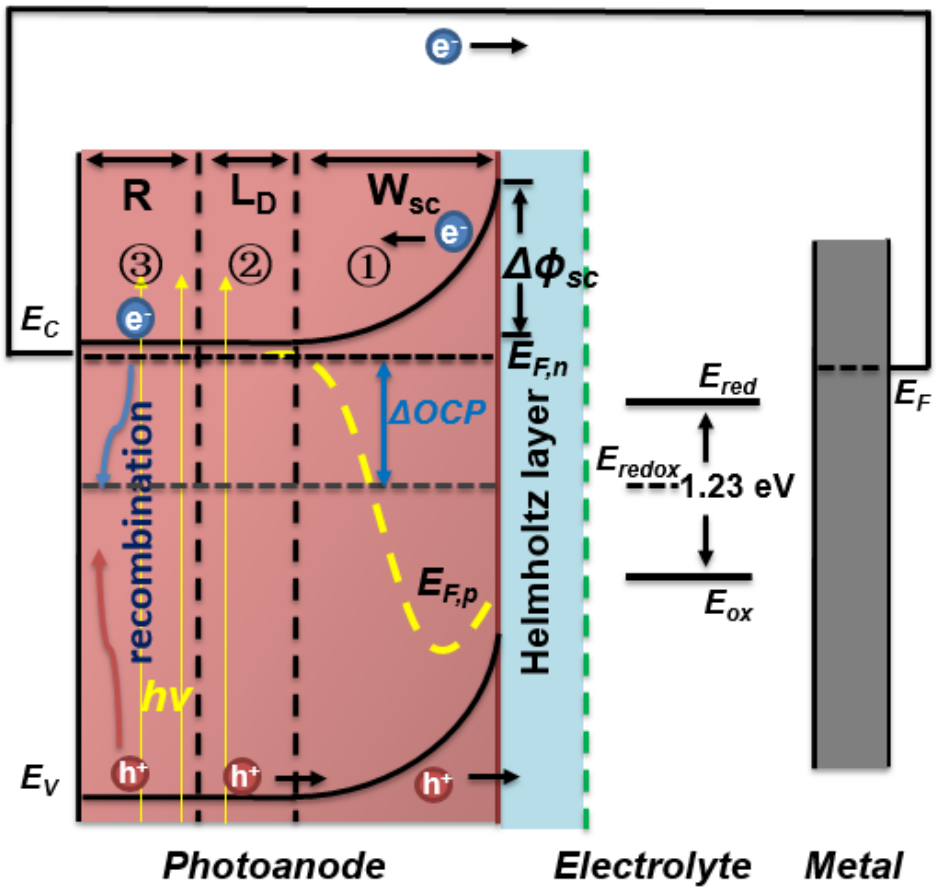

Figure 2.3. The energy diagram of a PEC cell that consists of a semiconducting photoanode and a metal cathode. Principle of operation of PEC cell based on n-type semiconductor.

During the illumination a photovoltage is generated because of the splitting of the initial Fermi level into two separate quasi-Fermi levels for electrons (E_{Fn}) and holes (E_{Fp}). The maximum achievable photovoltage is determined by the amount of Fermi level splitting. Therefore, in order to get a semiconductor/electrolyte junction

with a high photovoltage, the valence band of the n-type semiconductor must be close to formal oxidation potential of electrolyte to enable a large degree of band bending.

The quasi-Fermi levels are associated with the densities of electrons and holes at a certain point in the semiconductor, and are shown below:

$$\mathrm{n} = \mathrm{n_0} + \Delta\mathrm{n} = \mathrm{N_C e^{-(E_C - E^*_{F,n})/kT}} \tag{2.8}$$

$$\mathrm{p} = \mathrm{p_0} + \Delta\mathrm{p} = \mathrm{N_V e^{(E_V - E^*_{F,p})/kT}} \tag{2.9}$$

where n_0 and p_0 are the carrier densities under equilibrium in the dark, Δn and Δp are the increase in carrier densities caused by illumination. For an n-type semiconductor, $p = p_0 + \Delta p \approx \Delta p$ and $n = n_0 + \Delta n \approx n_0$ so that $E_{F,n}$ remains horizontal while $E_{F,p}$ departs from the Fermi level of the bulk in the active region. The position of the quasi-Fermi level is often interpreted as the electrochemical potential of the corresponding species.

2.1.4 Energy and quantum conversion efficiencies

The energy conversion efficiency is also one of the key parameters in a PEC cell.[16] Assuming there is no corrosion reaction at the photoelectrodes and a Faradaic efficiency of unity for both reactions, the solar-to-hydrogen (η_{STH}) efficiency for water splitting devices that require an external bias is usually expressed as the

$$\eta_{STH} = \frac{P^{out}_{electrical} - P^{in}_{electrical}}{P_{light}} = \frac{j_{photo} \times (V_{redox} - V_{bias})}{P_{light}} \tag{2.10}$$

where V_{bias} is the applied voltage measured between the oxygen-evolving photoanode and the hydrogen-evolving photocathode, J_{photo} is the externally measured current density, and P_{light} is the power density of the illumination. V_{redox} is usually taken to be 1.23 V (at room temperature), based on a Gibbs free energy change for water splitting of 237 kJ/mol. In order to obtain a true systems efficiency, these measurements should be done in a two-electrode configuration as opposed to a three-electrode electrochemical cell. In the absence of an applied bias, the efficiency (in %) can be written as $\eta_{STH} = 1.23 \times j_{photo}$, assuming that j_{photo} is given in mA/cm^2 and the incident power of sunlight is 100 mW/cm^2.

For a tandem device the crossing point from two superimposed J-V curve determines operating photocurrent density (J_{op}). The highest efficiency for a p/n- tandem photoelectrochemical cell can be obtained when the two curves intersect closest to their individual maximum power points. By independently characterizing photoanodes and photocathodes, the expected performance of an integrated system with no external electronics can be directly calculated. Overall water splitting efficiencies (STH) for PEC cells can be estimated by overlapping the

individually tested J-V data for each photocathode/anode as illustrated in **Figure 2.4.**[17-19] Note that the sign of the photocurrent of the photocathode has been inverted in this diagram.

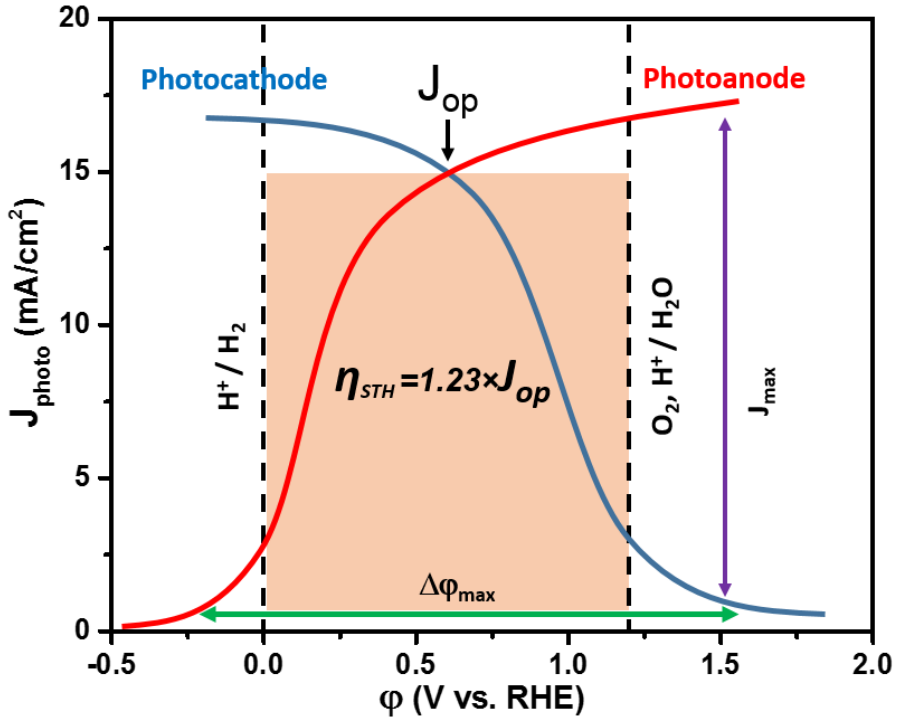

Figure 2.4. Overlaid current density-potential behavior for a p-type photocathode and an n-type photoanode, with overall efficiency projected by the power generated $\eta_{STH} = J_{op}$ (1.23 V) by the cell for splitting water.

The efficiency of a PEC cell may also be expressed as a so-called incident photon-to-current conversion efficiency (IPCE) or external quantum efficiency (EQE) which is defined by the number of electrons generated by light in the external circuit divided by the number of incident photons. The IPCE can be calculated using the following relationship,

$$IPCE = \frac{hc}{e} \times \frac{J_{pho}(\lambda)}{\lambda P(W)} = \frac{J_{pho}(\lambda)}{P(W)} \times \frac{1240}{\lambda(nm)} \quad (2.11)$$

where J_{pho} is the average photocurrent (mA/cm^2), P is the power density of the light incident on the entire photoelectrode (mW/cm^2), λ is the wavelength (nm).

Other efficiency expressions such as absorbed photon-to-current efficiency (APCE) or internal quantum efficiency (IQE) are used to evaluate the performance of a PEC cell as well, which is defined as the fraction of the absorbed photons that are converted to photocurrent measured in the outer circuit:

$$APCE\ \% = \frac{IPCE\ \%}{A} \tag{2.12}$$

where A is the absorptance of the entire photoelectrode. We also can predict the photocurrent density ($J_{AM1.5}$) from the IPCE measurements by multiplying the IPCE values by the AM1.5 solar photon flux and the electronic charge and subsequently integrating this for wavelengths below the absorption edge according to the following relationship,

$$J_{AM1.5} = \int_{250\ nm}^{1000\ nm} (IPCE(\lambda) \times \Phi_{AM1.5}(\lambda) \times q)\ d_{\lambda} \tag{2.13}$$

where $J_{AM1.5}$ is the total solar photocurrent in (A m^{-2}), $\Phi_{AM1.5}(\lambda)$ is the photon flux of AM1.5 sunlight (photons per m^2 per s), and q is the electronic charge (1.602×10^{-19} C).

2.2 Requirements for the ideal semiconductor

To choose a suitable semiconductor for efficient solar water splitting, many requirements should be considered. For example, the semiconductor should possesses the properties of narrow band gap, highly chemical stable, low-cost fabrication, high charge carrier separation efficiency and having suitable positions of conduction and valence bands to straddle the proton reduction and water oxidation redox potentials.

2.2.1 Band gap and band positions

The band gap (E_g) of the photo-electrode has a critical impact on the energy conversion of photons, since only the photons of energy equal to or larger than that of the band gap can be absorbed and used for conversion. Generally, an idea band gap of semiconductor material is about 1.6 – 2.4 eV that can absorb the maximum amount of visible-light and provide the necessary potential to drive water splitting.

Meanwhile, the conduction band of the semiconductor should be more negative than the hydrogen evolution potential and the valence band should be positive to the oxygen evolution level to provide a large photovoltage under illumination for efficient water splitting. In practice, an additional free energy input (overpotential) is needed to drive the kinetics of the electron and hole transfer reactions leading to the generation of hydrogen and oxygen at rates that match the absorbed flux of solar photons.[20] **Figure 2.5** shows the valence and conduction band positions of several binary and ternary oxide semiconductors relative to the reversible hydrogen and oxygen redox energies at pH 7 for solar water splitting. The material that has been used most frequently as a photoelectrode is TiO_2, due to its high stability. However, its band gap is about 3 eV and, as a result, the part of the energy spectrum available for conversion is strongly limited (less than 4 %). Therefore, there is a need to increase the amount of

photons available for conversion from solar spectrum. Several techniques have been explored to improve the light absorption of TiO_2 such as doping and nanostructuring.[21]

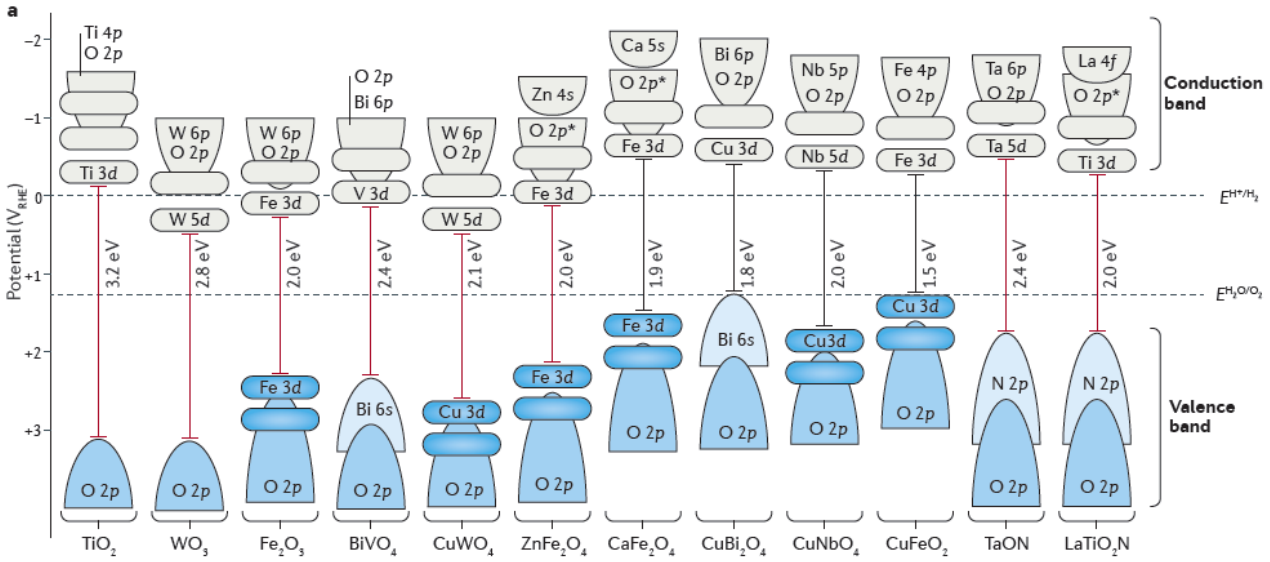

Figure 2.5. Energy band diagram for selected metal oxides semiconductors. This figure is taken from reference [22].

2.2.2 Corrosion resistance

An important requirement for the photo-electrode is resistance to undesired reactions at the semiconductor-electrolyte interface, resulting in degradation of its properties.[23] These reactions include electrochemical corrosion, photo-corrosion and dissolution, and the phenomenon may be due to three distinctly different causes

(1) The deactivation of the photoelectrode due to the loss of photovoltage. It has been shown that the performance of Ta_3N_5 quickly decayed during water oxidation, which was generally attributed to the oxidation of the nitride. A relatively thin amorphous oxide layer was formed at the surface during water oxidation, which not only introduced increased charge transfer resistance, but also shifted the Fermi level positively by 200 mV, leading to significant Fermi-level pinning that greatly limits the measurable photovoltages.[24]

(2) The deactivation of the active sites. For example, the formation and accumulation of peroxo species on WO_3 surfaces during water oxidation can lead to the loss of photoactivities,[25] which is well known for WO_3 at higher pH due to the loosely bound $WO_3(H_2O)_x$ species at the surface.

(3) Big changes to the photoelectrode due to corrosion during the chemical reactions. $BiVO_4$ has been identified as one of the most promising oxide-based photoanodes for use in a photoelectrochemical cell for water splitting. However, it is also known to be prone to photocorrosion during water oxidation process.[26] It was hypothesized

that the photo-induced chemical instability may be a result of the accumulation of holes on the surface and the formation of reactive oxygen species, which could oxidize Bi^{3+} to Bi^{5+} or oxidize O^{2-} to O^{-}.

To date, two different methods are used to prevent photocorrosion of photoelectrodes. First, surface modifications by protection layers are reported to retard the process. Since the oxidation state of one or more of the elements will be changed due to photocorrosion at the semiconductor/electrolyte interface, therefore, if the photoelectrode is coated with an inert layer such as TiO_2 for $BiVO_4$ and is not in direct contact with the electrolyte, the photocorrosion cannot occur even if holes or electrons are available. The second method to suppress photocorrosion is by depositing a co-catalyst layer on top of photoelectrodes. For a semiconductor, catalyst layers not only kinetically suppress photocorrosion and surface recombination, but also improve the rate of interfacial charge transfer.[27, 28]

2.2.3 Low fabrication cost

The cost of materials are very important because the commercial viability of a water splitting PEC is ultimately determined by the cost of hydrogen produced by the PEC, not just the STH efficiency. In addition to the cost of materials, the fabrication process itself could incur significant cost. There are some expensive techniques for high quality thin film preparation such as atomic layer deposition (ALD), pulsed laser deposition (PLD) and molecular beam epitaxy (MBE). Now many less expensive synthesis methods such as magnetron sputtering (MS), physical vapor deposition (PVD), chemical vapor deposition (CVD), spray pyrolysis, electrodeposition, sol–gel and powder pressing have been explored for material fabrication, which has been reviewed elsewhere.[13, 29]

2.3 Semiconducting materials for solar fuels

One of the biggest challenges for PEC water splitting is the identification of suitable semiconductor materials as photoelectrodes. Various semiconductors have been considered as photoelectrodes for use in PECs, however, oxide-based photoelectrodes are particularly attractive because of their high stability in aqueous solutions in addition to inexpensive and easy processing compared to other types of semiconductors.[30-35]

2.3.1 Photocathodes for hydrogen evolution

In general, photocathodes are p-type semiconductors and must supply the required cathodic photocurrent to reduce water to hydrogen and need to be photoelectrochemically stable in aqueous solutions. The optimal photocathode material needs to have the conduction band edge potential to be more negative than that of the hydrogen reduction potential together with a small band gap to utilize a large portion of the incident solar light. **Figure 2.6** shows the band alignment of p-type metal oxide semiconductors employed commonly as

photocathodes for water reduction. The following section will discuss the recent progress on Cu and Fe oxide-based p-type photocathodes for solar water reduction.

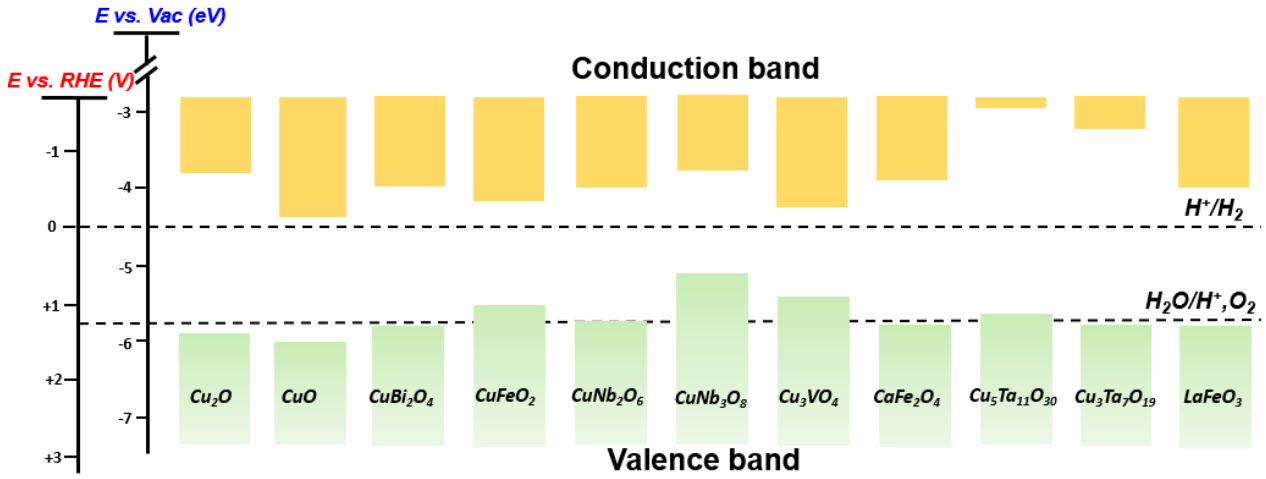

Figure 2.6. Valence and conduction band edges for p-type metal oxide based photocathodes. The dashed lines represent potential levels for water oxidation (1.23 V_{RHE})/reduction (0.0 V_{RHE}). Band levels are obtained from reference[36-48].

2.3.1.1 Copper oxide photocathodes

Cuprous oxide (Cu_2O) photocathodes have been intensively studied because of its relatively low cost, earth-abundance and ideal band-gap energies. However, Cu_2O has been a challenging PEC material to work with since its first demonstration as a photocathode material, because it suffers from a severe photoelectrochemical corrosion when illuminated in aqueous solutions. The Cu_2O is reductively decomposed to Cu with photogenerated electrons because the redox potential for Cu^+ is located within its band gap. Hence, it usually requires protection layers on the surface for stable operation to produce hydrogen gases from water.

A major breakthrough for Cu_2O occurred in 2011, when Paracchino et al. showed that Cu_2O photocathodes could be significantly stabilized with surface modification by Al-doped ZnO (AZO) buffer layer and TiO_2 protection layer as illustrated in **Figure 2.7**. Afterwards, many efforts are paid to address the stability and photoconversion efficiency challenges of Cu_2O by using various nanostructures, buffer layers, protection layers, and electrocatalysts. The best performance of Cu_2O was demonstrated from Cu_2O nanowire arrays in aqueous solution with pH 12, where Ga_2O_3/TiO_2 were used as protective layers resulting in a photocurrent of -10.0 mA/cm^2 at 0 V_{RHE} exceeding 100 hours.[49]

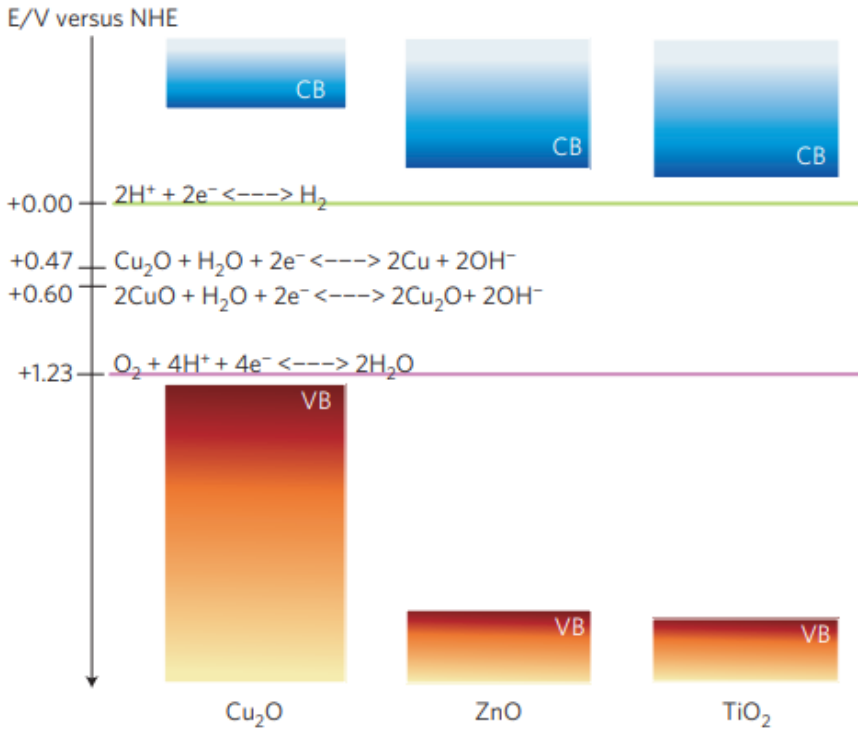

Figure 2.7. Band alignments of the surface-modified Cu_2O photocathode and redox levels of involving electrochemical reactions, this figure is adapted from reference[50].

Cupric oxide (CuO) is another p-type copper oxide with a band gap of 1.4–1.7 eV, where its small band gap allows CuO to harvest higher portion of the solar spectrum than Cu_2O. However, CuO as a photocathode for hydrogen production has received less attention than Cu_2O, due to its conduction band being more positive than that of the Cu_2O, and its tendency toward photocorrosion in the presence of protons, similar to Cu_2O. However, some recent studies by Septina et al. showed that deposition of an n-type CdS buffer layer underneath a protective TiO_2 layer yielded a stable and efficient CuO photoelectrode with the photocurrent of 1.25 mA cm^{-2} at 0 V_{RHE} for 30 minutes.[36]

2.3.1.2 Copper bismuth oxide ($CuBi_2O_4$) photocathode

The p-type metal oxide $CuBi_2O_4$ has a suitable bandgap of ~1.8 eV, which corresponds to a potential solar-to-hydrogen (STH) efficiency of 20%, assuming incident photons with energies above its band gap are absorbed completely. Its positive Fermi level energy (1.26 – 1.43 V_{RHE}) also results in an exceptionally positive photocurrent onset potential (> 1 V vs. RHE), that makes it a promising candidate for the top absorber in a tandem photoelectrochemical (PEC) device.

However, there are some challenges for $CuBi_2O_4$ as a photocathode material. For example, its gradual and incomplete optical absorption cuts the obtainable photocurrent density in half. The biggest limitation is the poor charge carrier transport, primarily for holes, resulting in photogenerated charge recombination and self-reduction from Cu^{2+} to Cu^{+}. This occurs in bulk $CuBi_2O_4$ thin films and the interface between substrates and $CuBi_2O_4$ thin films. In earlier efforts in our group, Berglund et al. found that $CuBi_2O_4$ has a relatively low mobility of 10^{-3} cm^2 V^{-1} s^{-1} and a short carrier diffusion length of 10 − 52 nm. Wang et al. synthesized forward gradient self-doped $CuBi_2O_4$ by varying the concentration of copper vacancies, which produced a record photocurrent of −2.5 mA/cm^2 at 0.6 V vs RHE with H_2O_2 as an electron scavenger as illustrated in **Figure 2.8**. They also proved that $CuBi_2O_4$ photocathodes can be protected with a CdS/TiO_2 heterojunction layer, resulting in a photocurrent density −0.5 mA/cm^2 at 0.0 V_{RHE} for 3 hours and evolved hydrogen with a faradaic efficiency of ~91%.[51]

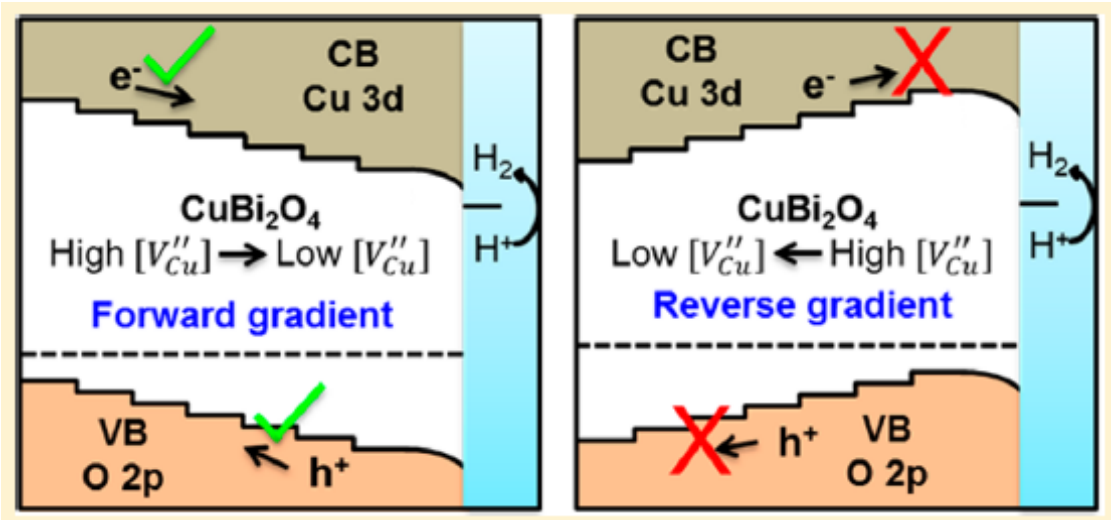

Figure 2.8. Energy diagrams of forward gradient doped $CuBi_2O_4$ film, this figure is adapted from reference[51].

2.3.1.3 Delafossite $CuFeO_2$ photocathode

Delafossite $CuFeO_2$ is a p-type metal oxide semiconductor with a narrow bandgap of 1.5–1.6 eV, which can absorb the entire range of visible light. It is also an earth abundant material with high onset potential, relatively high conductivity and favorable stability in aqueous solutions.[52-54] However, the poor charge transfer, inappropriate surface quality and small photovoltage (~0.35 V) limit its performance for PEC water splitting.[55] That is why $CuFeO_2$ exhibited such low current density. Some researchers show that photocurrent activity of $CuFeO_2$ possess enhancement after modifying with electrocatalyst such as nickel-iron (NiFe) and reduced graphene oxide (RGO) after hybrid microwave annealing.[56] Therefore, the $CuFeO_2$ photocathodes could be a very promising candidate for efficient hydrogen evolution, if its surface is perfectly passivated. As a consequence, more efforts should be paid to explore different HER catalysts, protection layers, and interfacial layers to further improve the

photoconversion efficiency of $CuFeO_2$. Doping, epitaxial growth, and nanostructuring can also be used to overcome the mismatch between carrier transport and optical absorption in the future.

2.3.2 Photoanodes for water oxidation

Photoanode materials are responsible for oxygen evolution in the PEC water splitting process. It must be an n-type semiconductor, with a suitable band gap (< 2.5 eV) to absorb wide range of spectrum, and efficient charge collection and charge carrier motilities. Meanwhile, the materials must be stable in aqueous solution, low cost, and environmentally friendly. **Figure 2.9** shows the band alignment of n-type metal oxide semiconductors employed commonly as photoanodes for water oxidation. This section will focus on selected n-type semiconductors that have been investigated as a photoanode in PEC water splitting. Examples of these materials are ternary oxide-based photoanodes.

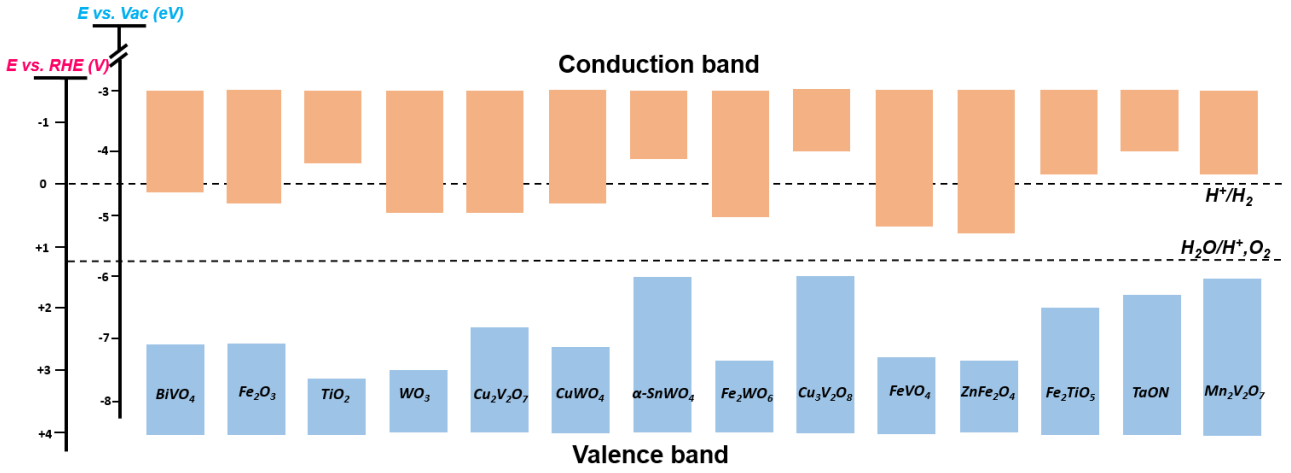

Figure 2.9. Valence and conduction band edges for n-type metal oxide based photoanodes. The dashed lines represent potential levels for water oxidation (1.23 V_{RHE})/reduction (0.0 V_{RHE}). Band levels are obtained from references [57-69].

2.3.2.1 Bismuth vanadate ($BiVO_4$) photoanode

N-type metal oxide semiconductor $BiVO_4$ has attracted a significant amount of interest in the past few years since Kudo et al. first demonstrated that the monoclinic phase of $BiVO_4$ has a high visible light photoactivity.[70] It has a bandgap of ~ 2.4 eV, and can absorb up to 11% of the solar spectrum. In theory, $BiVO_4$ can generate an AM1.5 photocurrent of 7.5 $mAcm^{-2}$, assuming all photons with energies higher than 2.4 eV are absorbed. This corresponds to a STH (solar-to-hydrogen) energy conversion efficiency of 9%. Moreover, its conduction band edge is located close to the reversible hydrogen electrode (RHE) level, which enables water splitting at modest external bias

potentials.[71] However, it has several limitations as a photoanode material. For example, the first identified limitation was slow transfer of photo-generated holes from the surface of the $BiVO_4$ to the electrolyte. The second limitation is the poor charge carrier transport properties as we already know in many other metal oxides. The fundamental limitation of using $BiVO_4$ as a photoanode is the modest optical absorption due to its relatively wide bandgap.

In the past five years, employing various optimization strategies, including gradient doping,[72] surface modification with cocatalysts,[71, 73, 74] the use of host−guest scaffolds[75] and nanostructuring,[76] the onset potentials for PEC water oxidation on $BiVO_4$ as low as 0.2 V vs RHE and photocurrent densities as high as 6.72 mA cm^{-2} at 1.23 V_{RHE} under AM 1.5 illumination have been reported.[77-80] Due to its good PEC performance, most recent PEC devices constructed to perform unassisted solar water splitting employed $BiVO_4$ as the sole photoanode or in conjunction with another photoanode as shown in **Figure 2.10**. STH efficiencies of 7.7% and 7.1% were reported for these novel concepts, respectively.[81-85]

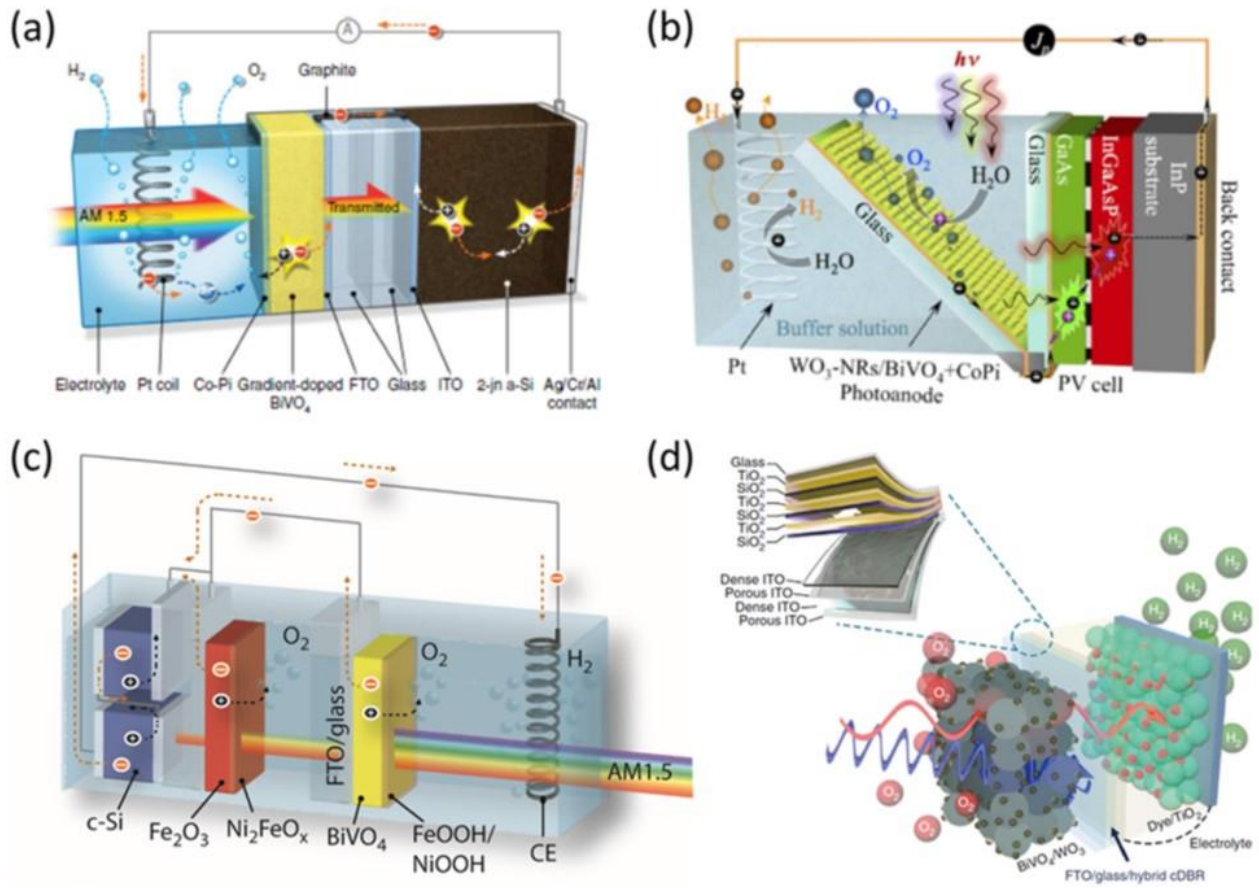

Figure 2.10. Various schematic structures of solar water splitting devices based on $BiVO_4$ photoanode, this figure is taken from reference [30, 81, 86-88].

To further improve the achieved STH efficiency with complex metal oxide photoelectrodes, designing optimum multilayer photoanodes containing $BiVO_4$ should be one focus of future research. Unfortunately, $BiVO_4$ is intrinsically limited by its bandgap of 2.4 eV, we therefore need to find an efficient and stable complex metal oxide with the suitable bandgap range of ≤ 2.0 eV.

2.3.2.2 Other ternary oxide-based photoanodes

In order to achieve a high STH efficiency (>10%), some other alternative complex metal oxides with small bandgap such as metal ferrites ($ZnFe_2O_4$, $MgFe_2O_4$, $CuFe_2O_4$ and $BiFeO_3$), metal tungstates ($CuWO_4$, α-$SnWO_4$ and Fe_2WO_6) and metal vanadates (γ-$Cu_3V_2O_8$, α-CuV_2O_6, β-$Cu_2V_2O_7$, $Cu_{11}V_6O_{26}$, $Cu_5V_2O_{10}$ and $FeVO_4$) should be explored in the future.

2.3.3 Photoanode-photocathode tandem PEC cell for overall unassisted solar water splitting

Eqs. (2.3a) and (2.4) suggest that an energy greater than 1.23 eV should be sufficient to split water. However, due to the different kinetic and thermodynamic non-idealities in the oxidation and reduction reactions, the actual required energy is considerably higher than 1.23 eV. As a consequence, a semiconductor with a large energy bandgap to absorb a maximum portion of the solar spectrum is required for a single semiconductor absorber. To solve this drawback, recent attention has been focused on systems that use eight rather than four photons to accomplish the four-electron splitting of water into molecular oxygen and hydrogen.

Various tandem device configurations have been proposed. One approach is to combine the metal oxide absorber with a conventional photovoltaic cell. This approach has been proposed for $BiVO_4$, WO_3 and Fe_2O_3 photoanodes as illustrated in **Figure 2.10**. These materials have band gaps of 2.4, 2.7 and 2.0 eV respectively, and lower energy photons that are transmitted through the photoanodes are incident on a photovoltaic device with a lower band gap. The PV cell can generate an internal voltage which acts as a bias across the photoelectrochemical cell, thereby enhancing the space charge region in the photoanode and assisting separation of photogenerated electrons/hole pairs. More importantly, it can shift the electrode potential of the metal cathode sufficiently negative of the reversible hydrogen potential so that proton reduction can occur. However, the fabrication of PV-PEC solar cells is complicated and expensive. Without considering the cost factor, PV-PEC systems are very viable hydrogen production method for the practical applications.

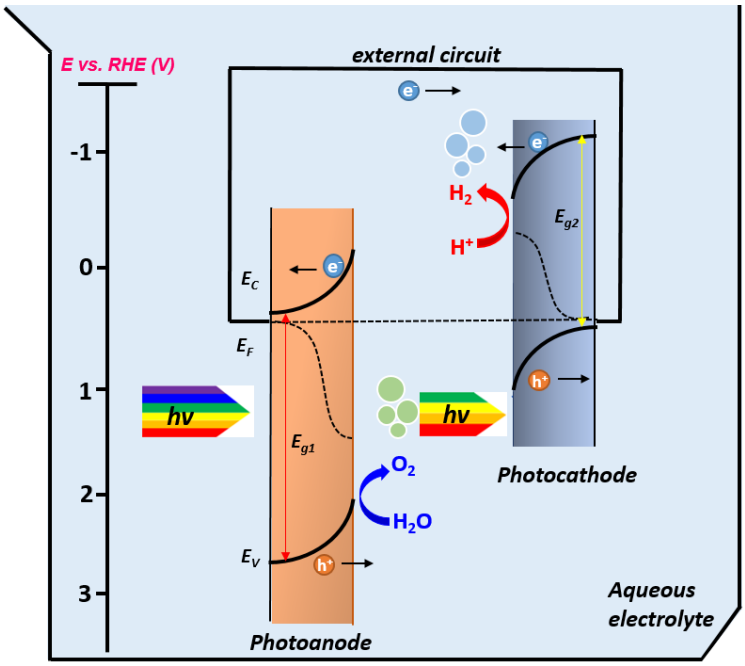

Figure 2.11. Schematic diagram of PEC water splitting approach using a dual-absorber tandem cell.

Another approach is by combining an n-type photoanode in optical series with a p-type photocathode as shown in **Figure 2.11**. In this arrangement, hydrogen is produced by the reduction of protons by electrons photogenerated in the photocathode, and oxygen is formed by the oxidation of water by holes photogenerated in the photoanode. The maximum theoretical efficiency of such as photoanode-photocathode tandem photoelectrochemical cell is around 46% for an appropriate combination of band gaps for the two photoelectrodes, assumping that no overpotentials are needed to drive the water-splitting reactions.[89] However, due to the limitations imposed by interfacial kinetics and energy loss, the experimental efficiencies reported so far have been well below this theoretical maximum.[90] The main source of losses is direct or indirect recombination of electron-hole pairs. Strategies for improving photoanode-photocathode tandem cell efficiency must therefore focus on reducing the rate of recombination, accelerating the rate of interfacial electron transfer and increasing the photovoltage.

2.4 This thesis

Despite the intensive efforts have been carried out to develop photoelectrode materials, however, up to now, no single photoelectrode material meets all the requirements to be used as a top absorber. Therefore, we urgently need to expand our material database and explore more complex metal oxides in order to have a realistic chance of finding novel light absorbers that meet the demanding requirements for practical applications. More than

700000 combinations are possible for multinary metal oxides, which clearly opens up a new realm of possibilities in finding an ideal semiconducting material for solar water splitting.

In Chapter 4, we focus on a new p-type metal oxide material, $CuBi_2O_4$, which has been reported to have a suitable bandgap of 1.5 - 1.8 eV. However, $CuBi_2O_4$ photocathodes have shown limitations in charge carrier transport within $CuBi_2O_4$ and across the interface with n-type fluorine doped tin oxide (FTO). We have clearly shown that the addition of Cu-doped NiO (Cu:NiO) as a back contact layer between FTO and $CuBi_2O_4$ improves the photoelectrochemical performance of FTO/Cu:NiO/$CuBi_2O_4$ photocathodes by improving the charge carrier transport across the $CuBi_2O_4$-substrate interface. We also provided evidence that the band positions of Cu:NiO are favourable to reduce the barrier height at the $CuBi_2O_4$-substrate interface, while simultaneously driving selective extraction of photogenerated holes (blocking of electrons). This work illustrate the importance of suitable band alignment and suggest a potential improvement strategy for other oxide-based photocathode materials deposited on FTO substrates.

In Chapter 5, we focus on another new n-type metal oxide material, $Cu_2V_2O_7$, with a nearly optimal bandgap (1.8 ~ 2.0 eV) and a large absorption coefficient (up to $\alpha \approx 10^5$ cm^{-1}). However, $Cu_2V_2O_7$ photoanodes have not yet demonstrated high photoconversion efficiencies, and the factors that limit the efficiency have not yet been fully identified. In this chapter, many of the key physical and photoelectrochemical properties of $Cu_2V_2O_7$ photoanodes are established including optical band gap, doping type, flat-band potential, band positions, charge carrier transport, chemical composition, chemical stability, and O_2 evolution faradaic efficiency. We found that the photoelectrochemical performance of $Cu_2V_2O_7$ photoanodes is strongly limited by very poor charge carrier separation efficiency. In addition, cobalt phosphate (Co-Pi) was used as a water oxidation co-catalyst for $Cu_2V_2O_7$.

In Chapter 6, we assess a tandem photoelectrochemical cell consisting of a W:$BiVO_4$/Co-Pi photoanode top absorber and a $CuBi_2O_4$/CdS/TiO_2/RuO_x photocathode bottom absorber for overall solar water splitting. This work is the first experimental demonstration of hydrogen and oxygen production from a $CuBi_2O_4$-$BiVO_4$ based tandem device. To enable bias-free operation of the device, further optimization of the protection layer of the $CuBi_2O_4$ photocathode is needed in order to reduce the loss of photovoltage.

Chapter 3. Experimental methodology

3.1 Experimental methods

3.1.1 Cu:NiO thin film deposition

Cu:NiO thin films were deposited on glass (Microscope slides, Gerhard Menyel B.V. & Co. KG)and FTO (TEC 7) substrates by electron beam evaporation using Cu and Ni metal at room temperature. Prior to film deposition, all glass and FTO substrates were cleaned with acetone, isopropanol, ethanol and deionized water in an ultrasonic bath, respectively for 15 minutes at 50 ℃, to remove the organic contamination on the surface of the glass and FTO, and then dried by high purity nitrogen gun. The Cu:NiO thin films had a sandwich structure consisting of Ni (2 nm) / Cu (0.4 nm) / Ni (2 nm) with a total thickness of 4.4 nm. During the deposition process, there was no additional substrate heating. A post deposition annealing treatment was carried on in muffle furnace at 450℃ for 2 hours in air with 5 ℃ /min ramping oxidized the metals to their oxide form. For Mott−Schottky and XRD measurements that require thicker films for a better peak resolution, 22 nm (Ni (10 nm) / Cu (2 nm) / Ni (10 nm)) and 66 nm (Ni (30 nm) / Cu (6 nm) / Ni (30 nm)) thick films of Cu:NiO were prepared by sequential deposition on FTO and amorphous microscope glass followed by annealing at 450 ℃ for 2 hours in air. The as deposited and post anneal thickness values are summarized in **Table 3.1**.

As Deposited Thickness (nm)	Post Anneal Thickness (nm)	Film Sheet Resistance (Ω/□)	Film Resistivity (Ω m)
4.4	7	1.16×10^8	0.82
12	34	9.58×10^7	3.26
66	102	8.33×10^7	8.49

Table 3.1. Sheet resistance of different thickness of Cu:NiO thin films deposited on glass substrates.

3.1.2 Fabrication of $CuBi_2O_4$ photocathodes

$CuBi_2O_4$ thin films were deposited on various substrates using the forward gradient self-doping process described in our previous work.[91] The typical synthesis procedure for a $CuBi_2O_4$ photocathode is as follows. Firstly, 20mM $Cu(NO_3)_2$ precursor was prepared by dissolving $Cu(NO_3)_2 \cdot 3H_2O$ (99−104%, Sigma-

Aldrich) in ethanol (≥99.8%, Sigma-Aldrich). Then 40mM $Bi(NO_3)_3$ precursor was prepared by dissolving $Bi(NO_3)_3 \cdot 5H_2O$ (98%, Alfa Aesar) in a 1/9 mixture of acetic acid (≥99.8%, Sigma-Aldrich)/ethanol (≥99.8%, Sigma-Aldrich). Before deposition was started the substrates were placed on the hot plate and heated to the present temperature of 450 °C. The spray nozzle (Quickmist air atomizing spray) was placed 20 cm above the heating plate and driven by an overpressure of 0.6 bar of nitrogen gas. Pulsed deposition mode was used, with one spray cycle consisting of 5 s spray time followed by a delay of 55 s to allow complete evaporation of the solvent and pyrolysis of any remaining organics. $CuBi_2O_4$ were prepared through a two-step diffusion-assisted spray pyrolysis process, first the $Bi(NO_3)_3$ precursor was sprayed onto the FTO substrate at a deposition temperature of 450 °C, then the $Cu(NO_3)_2$ precursor was sprayed successively on top of the Bi^{3+} based film at 450 °C.[91]

3.1.3 $Cu_2V_2O_7$ photoanode synthesis

$Cu_2V_2O_7$ photoanode thin films were prepared using a low-cost and facile spray pyrolysis process. The typical spray pyrolysis procedure for a $Cu_2V_2O_7$ photoanode is as follows. First, 20mM $Cu(NO_3)_2$ precursor was prepared by dissolving $Cu(NO_3)_2 \cdot 3H_2O$ (99−104%, Sigma-Aldrich) in ethanol (≥99.8%, Sigma-Aldrich). Next, 20 mM $VO(AcAc)_2$ precursor was prepared by dissolving $VO(C_2H_7O_2)_2$ (99%, Alfa Aesar) in absolute ethanol. The Cu solution was then added to the V solution, and the mixture was diluted to the desired concentration with additional ethanol. The substrates (FTO-coated glass, 7 Ω per square, TEC-7, Pilkington) were cleaned by three successive 15 min. ultrasonic treatments in Triton, acetone, and ethanol solutions and placed on a hot plate heated to the preset temperature of 300 °C. For the spray pyrolysis deposition a Quickmist collision atomizer was placed 20 cm above the substrate. The atomizer was controlled with an overpressure of ~2.5 bar of nitrogen gas to achieve a spray rate of 2.0 mL per 5 s spray. The spray cycle used consisted of 5 s spray, followed by a 55 s pause, allowing for the evaporation of solvent and pyrolysis of organic components. The spray cycles were repeated 100 times and a film growth rate of 2 nm per cycle was determined. After deposition, a post annealing treatment of the $Cu_2V_2O_7$ photoanode films was carried out in a muffle furnace at 500 ℃ for 2 hours in air with 5 ℃ /min ramping.

3.1.4 Fabrication of W:$BiVO_4$ photoanode

W:$BiVO_4$ thin films were prepared using spray pyrolysis. The precursor solution was made by dissolving 4 mM $Bi(NO_3)_3 \cdot 5H2O$ (98%, Alfa Aesar) in acetic acid (98%, Sigma-Aldrich) and adding an equimolar amount of vanadium in the form of $VO(AcAc)_2$ (99%, Alfa Aesar) dissolved in absolute ethanol (Sigma-Aldrich). The nozzle-to-substrate distance was kept constant at 20 cm. Each spray cycle consisted of 5 s of spray time and 55 s of delay time to allow for solvent evaporation, and a total of 100 cycles were used to deposit the W:$BiVO_4$ films. More details can be found in previous reports.[74, 86]

3.1.5 Deposition of CdS buffer layer

A CdS buffer layer was deposited on top of the $CuBi_2O_4$ film using chemical bath deposition (CBD). In a typical synthesis procedure, a beaker containing 150 mL of stirred ultrapure water was heated inside a water bath. When the temperature of the solution reached 65 °C, 22 mL of $CdSO_4$ (concentration of 15 mM) solution was added to the bath. Then 22 mL solution of NH_4OH was added to the chemical bath followed by immersion of the $CuBi_2O_4$ films into the solution for 15 min. The CdS-coated $CuBi_2O_4$ films were then rinsed thoroughly with water and dried in an oven under a temperature of 120 °C.

3.1.6 Atomic layer deposition of TiO_2 protection layer

TiO_2 was deposited by atomic layer deposition (ALD). Before deposition, the $CuBi_2O_4$ sample was rinsed thoroughly with deionized water and dried under a stream of N_2 before placing in the ALD reaction chamber. The deposition was carried out at 120 °C using sequential pulses of tetrakis (dimethylamino) titanium (Tprecursor: 85 °C) and H_2O (Tprecursor: 25 °C). The thickness of amorphous TiO_2 thin films is about 20 nm, which was determined from ellipsometric measurements on a piece of silicon witness wafer.

3.2 Characterizations

3.2.1 X-ray Diffraction (XRD)

Samples' crystal structure was checked and confirmed by X-ray diffraction (XRD) measurements by Bruker D8 Advance X-ray diffractometer (for Chapter 4, 5 and 6). X-ray diffraction (XRD) measurements were performed in the 2θ range from 10° to 90° with Cu $K_{\alpha}{}^{1}$ radiation of 0.15406 nm wavelength. The acceleration was operated at a voltage of 40 kV and a current of 40 mA. The step size of the measurements was 0.02° with an integration time of 3.5 seconds per step.

The diffraction satisfies Bragg's law, i.e., $n\lambda = 2d \times \sin\theta$, where n is an integer, λ is the wavelength of the X-rays, d is the interplanar spacing generating the diffraction, and θ is the diffraction angle. For the thin film measurements, it adopts the 2θ configuration. **Figure 3.1** shows the schematic diagram of a diffractometer system. Generally, X-rays are generated in a cathode ray tube. The electrons were accelerated toward a target material by applying a voltage. When electrons have sufficient energy to dislodge inner shell electrons of the target material, characteristic X-ray spectra are produced.[92, 93] EVA software was used to perform crystal structure refinement and composition calculation.

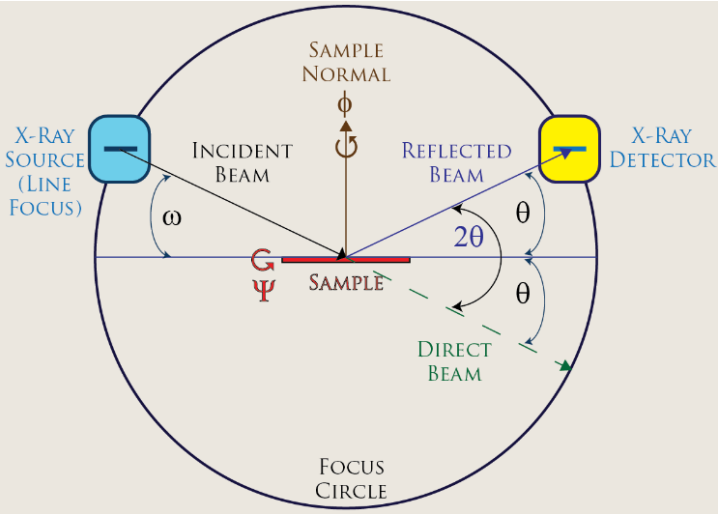

Figure 3.1. Schematic diagram of a diffractometer system[92].

3.2.2 Scanning Electron Microscopy (SEM)

The morphology of photoelectrodes in Chapter 4, 5 and 6 was observed by using a LEO GEMINI 1530 field emission scanning electron microscope (FESEM), operated at an acceleration voltage of 7 kV. The SEM uses electrons to produce magnified images of samples with a resolution of around 1.5 – 3.0 nm. Within the high vacuum column primary electrons are focused and deflected by electronic lenses to produce a narrow scan beam that towards to the target material. Then the secondary electrons are emitted from each spot on the target material. As a result, the angle and velocity of these secondary electrons relates to the surface structure of the target material. A detector catches the secondary electrons and produces an electronic signal, which can be transformed to an image. Energy-dispersive X-ray (EDX) spectroscopy was operated on FESEM to check the elemental dispersion on the sample surface. It was also conducted on the same FESEM using a silicon drift detector (Thermo Fisher Scientific) at an acceleration voltage of 20 kV. Elemental mapping and atom ration can be obtained from EDX measurements to confirm the existence of certain elements.

3.2.3 Transmission Electron Microscopy (TEM)

The cross-section of Cu:NiO back contact in Chapter 4 was observed by transmission electron microscopy. Specimens for transmission electron microscopy were prepared by cutting the respective thin film stack into two pieces, which were then glued face to face. After that, mechanical grinding and Ar ion milling were used for thinning to obtain electron transparent samples. Transmission electron microscopy images were obtained with a Zeiss LIBRA 200 FE operated at 200 kV accelerating voltage. The microscope was equipped with an omega type energy filter that was used to obtain zero loss filtered bright field images.

3.2.4 Atomic Force Microscopy (AFM)

The surface structure was investigated by an atomic force microscope (AFM, Park System, XE-100) operated in tapping mode using an etched Si tip (10 nm tip radius) with force constant of 40 N/m. All scans were performed on a scale of 5 µm × 5 µm with the lateral resolved height information on a square array of 256 × 256 pixels.

AFM images are obtained by measurement of the force on a sharp tip (insulating or not) created by the proximity to the surface of the sample. This force is kept small and at a constant level with a feedback mechanism.[94] When the tip is moved sideways it will follow the surface contours as illustrated in **Figure 3.2**.

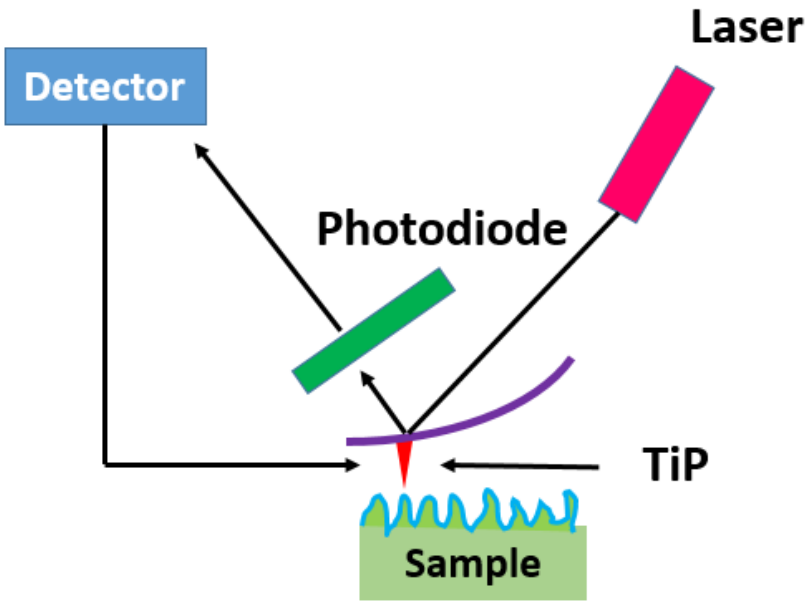

Figure 3.2. Schematic diagram of principle operation of an AFM.

3.2.4 UV-vis Spectroscopy

UV-vis absorption spectra were measured inside an integrating sphere using a PerkinElmer Lambda 950 spectrometer, scanning from 300 nm to 800 nm. UV-Vis spectroscopy is a convenient method to acquire the semiconductor bandgap by measuring the electron transitions from valance band to conduction band. The transflectance of these fims, which is the sum of the transmittance and the reflectance, was measured inside an integrating sphere to determine the true absorptance (absorptance = 1 − transflectance). The absorption coefficient (α) of the films can be calculated by using the following equation:

$$\alpha = \frac{-\ln(1-A)}{d} \tag{3.1}$$

Where A is the absorptance at a single wavelength and *d* is the film thickness. To extract the bandgap of thin films, Tauc plots are calculated based on the absorption coefficient spectrum. In a Tauc plot, $(\alpha h\nu)^m$ is plotted as a function of hν (in eV), with m = 2 for a direct bandgap material, and m = ½ for an indirect bandgap material. The bandgap is then obtained by extrapolation of the curve to the x-axis.

3.2.5 X-ray Photoelectron Spectroscopy (XPS) and Ultraviolet Photoelectron Spectroscopy (UPS)

Surface elemental compositions of the samples were obtained by X-ray photoelectron spectroscopy (XPS). Photoelectrons are generated and emit from sample surface when X-rays irradiate the sample according to photoelectric effect as illustrated in **Figure 3.3**. X-ray Photoemission Spectroscopy (XPS) and Ultraviolet Photoelectron Spectroscopy (UPS) was conducted under ultrahigh vacuum with a base pressure of ~10^{-8} mbar. The films were cleaned in an oxygen plasma prior analysis. XPS was performed with a monochromatic Al Kα X-ray-source (1486.74 eV) with a Specs Focus 500 monochromator. The analyzer was supplied by SPECS (Phoibos 100) and a source-to-analyzer angle of 54° was used. UPS was performed with a He I source (E = 21.21 eV). For every analysis two measurements were conducted, with the ground of the sample holder subjected to 0 and 2 V bias. The work function of the material can be defined as

$$\Phi = h\upsilon - SEC - U \tag{3.2}$$

where *hv* is the photon energy of the UV source, SEC means Secondary Electron Cutoff, and U is the applied bias potential. All spectra were measured using a pass energy and step size of 10 and 0.05 eV, respectively. In a typical measurement, a survey spectrum is first obtained to observe all the elements on the surface of the sample. Then the high-resolution scan of main elements is performed.

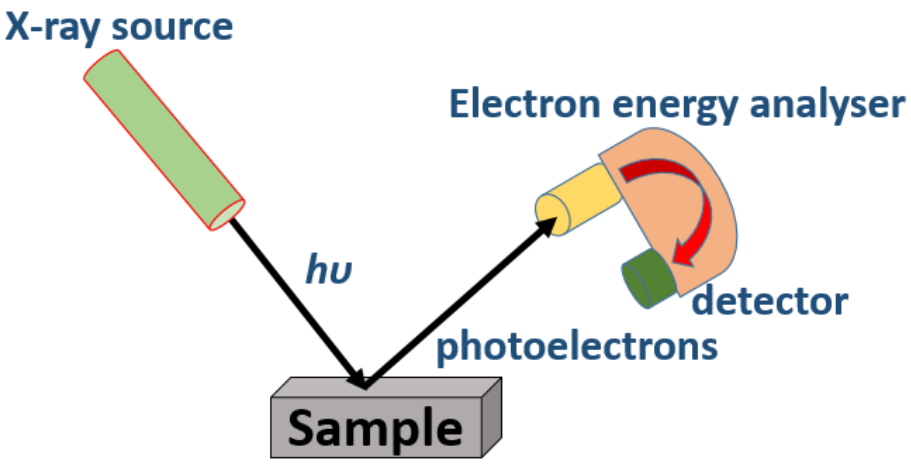

Figure 3.3. Illustration of photoelectric effect in XPS.

For analysis, XPSPEAK41 software were used to fit the data. The 1s peak of adventitious carbon at 284.8 eV was used as a reference for the other peak positions. The films were cleaned in an oxygen plasma atmosphere prior to the measurement. The bias was applied via the sample grounding.

3.2.6 Photoelectrochemical measurements

Photoelectrochemical measurements were performed in three-electrode configuration under the control of a potentiostat (EG&G Princeton Applied Research 273A). Samples were connected as the working electrode while a Pt wire was used as the counter electrode, and an Ag/AgCl electrode (saturated KCl) was used as the reference electrode, as illustrated in **Figure 3.4**.

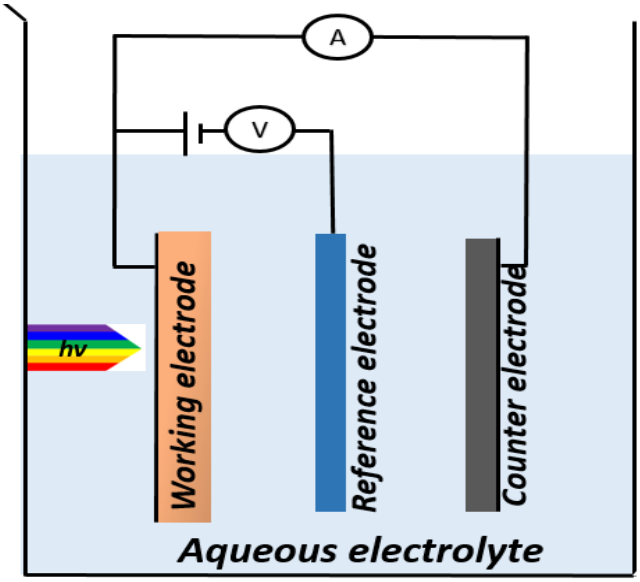

Figure 3.4. Schematic of the three-electrode configuration.

For photocurrent measurements, samples were tested in a 0.3 M K_2SO_4 and 0.2 M phosphate buffer (pH 6.8), in which the pH was checked by a calibrated pH meter (OAKTON). Either H_2O_2 was added to the electrolyte as an electron scavenger, or argon gas was bubbled into the electrolyte to purge dissolved oxygen. A WACOM super solar simulator (Model WXS-50S-5H, class AAA), which was calibrated to closely resemble the AM1.5 global spectrum at 100 mW/cm^2, was used as the illumination source. All of the measured potentials were converted to the reversible hydrogen electrode (RHE) scale using the Nernstian relation:

$$V_{RHE} = V_{Ag/AgCl} + 0.0591(\mathrm{V}) \times pH + 0.197(V) \quad (3.3)$$

3.2.7 Incident Photon to Current Conversion Efficiency (IPCE) measurements

Incident photon-tocurrent conversion efficiency (IPCE) and absorbed photon-to-current efficiency (APCE) measurements were performed with a 300 W xenon lamp (Oriel) connected to a grating monochromator (Acton Spectra Pro 2155). IPCE and APCE values were calculated using the following formulas:

$$IPCE\ \% = \frac{J_{pho}\,(\lambda)}{P(W)} \times \frac{1240}{\lambda(nm)} \times 100 \tag{3.4}$$

$$APCE\ \% = \frac{IPCE\ \%}{A} \tag{3.5}$$

where J_{pho} is the average photocurrent (mA/cm^2), P is power density of the light incident on the entire photocathode (mW/cm^2), λ is the wavelength (nm), and A is the absorptance of the entire photoelectrodes. **Figure 3.5** shows the power spectra of the incident light for the back illumination IPCE measurements.

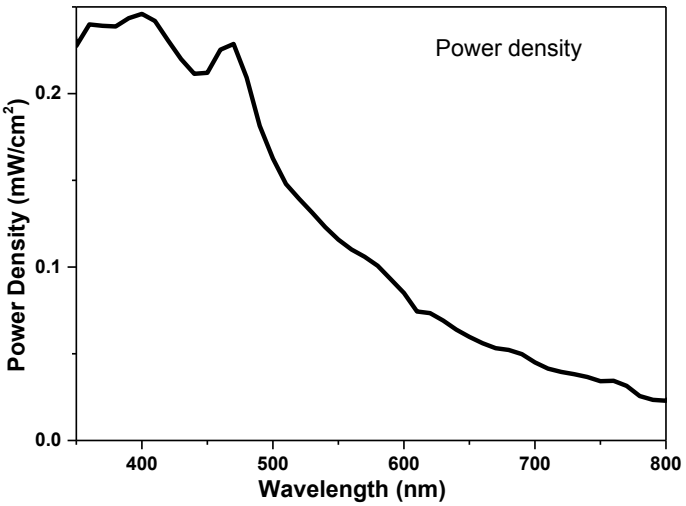

Figure 3.5. Power spectra for back illumination IPCE measurements.

The IPCE measurements were done at a fixed potential with Ar bubbling or with H_2O_2 added as an electron scavenger. The predicted AM1.5 photocurrent density ($J_{AM1.5}$) of the photocathodes was estimated by multiplying the IPCE values with the AM1.5 solar photon flux and the electronic charge and subsequently integrating this for wavelengths below 800 nm according to the following relationship,[95]

$$J_{AM1.5} = \int_{280\ nm}^{800\ nm} (IPCE(\lambda) \times \Phi_{AM1.5}(\lambda) \times q)\ \mathrm{d}\lambda \tag{3.6}$$

where $J_{AM1.5}$ is the total solar photocurrent in (A m^{-2}), λ is the light wavelength (m), $\Phi_{AM1.5}(\lambda)$ is the photon flux of AM1.5 sunlight (photons per m^2 per s), and q is the electronic charge (1.602×10^{-19} C).

3.2.8 Impedance and Mott-Schottky (MS) measurements

Similar to PEC measurements, electrical impedance spectroscopy (EIS) and Mott-Schottky measurements were performed with a VersaSTAT 3 Potentiostat (AMETEK Co., Ltd.) by using a three-electrode configuration. EIS was performed in the dark near the flat band potential of the photoelectrodes. The measurements were performed in 0.3 M K_2SO_4 and 0.2 M phosphate buffer (pH 6.8). Note that above 100 Hz, the real part of the impedance is constant, whereas the imaginary part has a slope of -1. This implies that the system behaves as a resistance in series with a pure capacitance, which is a prerequisite for Mott-Schottky analysis. Mott−Schottky plots were constructed based on the following relationship,

$$\frac{1}{C^2} = \frac{2}{e\,\varepsilon\,\varepsilon_0\,N_D}\left(\varphi - \varphi_{fb} - \frac{k\,T}{e}\right) \quad \text{(for n-type photoanode)} \tag{3.7}$$

$$\frac{1}{C^2} = \frac{2}{e\,\varepsilon\,\varepsilon_0\,N_A}\left(-\varphi + \varphi_{fb} - \frac{k\,T}{e}\right) \quad \text{(for p-type photocathode)} \tag{3.8}$$

where C is the capacitance (F/m^2), ε is the relative permittivity or dielectric constant, ε_0 is the permittivity of free space, N_D is the donor density (m^{-3}), N_A is the acceptor density (m^{-3}), and φ_{fb} is the flat band potential (V vs reference). Relative permittivity values of 500, 100, and 80 were used for $Cu_2V_2O_7$, Cu:NiO, and $CuBi_2O_4$, respectively.[38]

3.2.9 Time-resolved Microwave Conductivity (TRMC) measurements

The charge carrier mobility and lifetime were investigated by time resolved microwave conductivity (TRMC) measurements, which based on the measurement of the change of the microwave power reflected by a sample induced by a pulsed laser as illustrated in **Figure 3.6**. For TRMC measurements, all samples were prepared on quartz substrates. TRMC measurements were conducted using a wavelength tunable optical parametric oscillator (OPO) coupled to a frequency-tripled diode-pumped Q-switched Nd:YAG laser at wavelengths of 405, 450, and 550 nm as the excitation source with a 3 ns pulse (full-width at half maximum) and a X-band (8400−8700 MHz) microwave probe. During TRMC measurements the $Cu_2V_2O_7$ samples were exposed to air. The charge carrier diffusion lengths were calculated using the following relationship,

$$L_D = \sqrt{\left(\frac{\mu\,k\,T}{e}\right)\tau} \tag{3.9}$$

where μ is mobility ($m^2 V^{-1} s^{-1}$), k is the Boltzmann constant, T is the temperature (K), e is the electronic charge (C), and τ is the charge carrier lifetime (s). Further details of the TRMC measurement have been described elsewhere.[55, 96, 97]

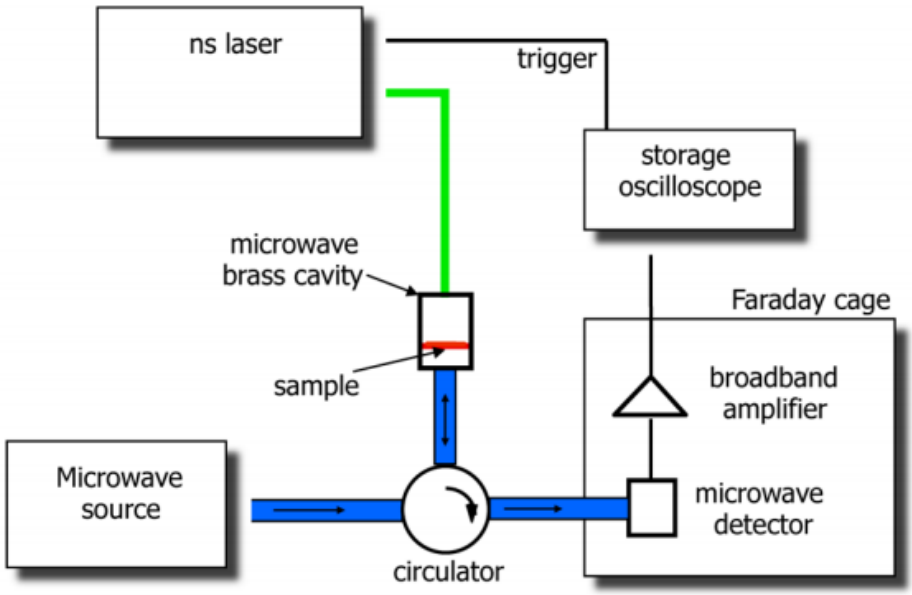

Figure 3.6. Schematic representation of the time-resolved microwave photoconductance setup, this figure is taken from reference[98, 99].

3.2.10 Gas production measurements

For gas detection, electrochemical mass spectrometer measurements were carried out in a PEC cell with different photoelectrodes as the working electrode, a Pt wire as the counter electrode, and an Ag/AgCl as the reference electrode. To calibrate the PEC cell, a Pt sheet was used as the working electrode, and a calibration line was recorded for the gas signal as a function of the current as shown in **Figure 3.7**. The photoelectrodes were illuminated from the backside using a 150 W Xe lamp with an AM 1.5 G filter. The light power was adjusted to approximately 650 mW/cm^2. For a specific current, the Faradaic efficiency for the photoelectrodes could then be calculated using the following equation, under the assumption that the Pt sheet has 100% Faradaic efficiency for the oxygen evolution reaction:

$$\eta_{faradaic} = \frac{gas \text{ signal from photoelecgtrodes}}{\text{gas signal from Pt sheet}} \tag{3.10}$$

After each mass spectrometry measurement the electrolyte was refreshed to avoid undesired shifts in the pH.

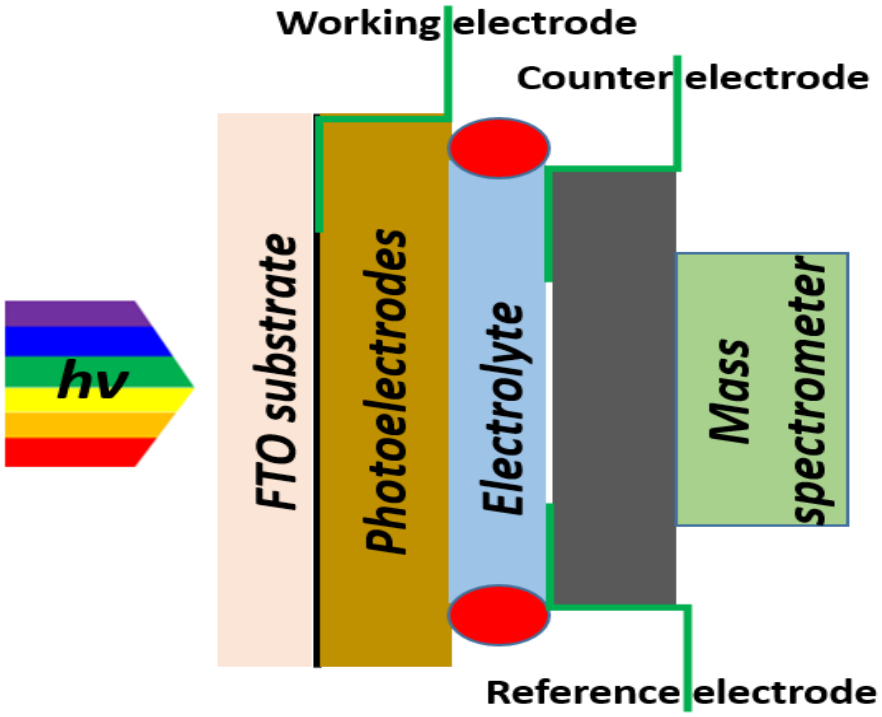

Figure 3.7. Sketch of the PEC cell used for the differential electrochemical mass spectrometry (DEMS) measurements.

Chapter 4. Cu:NiO as a hole-selective back contact to improve the photoelectrochemical performance of $CuBi_2O_4$ thin film photocathodes

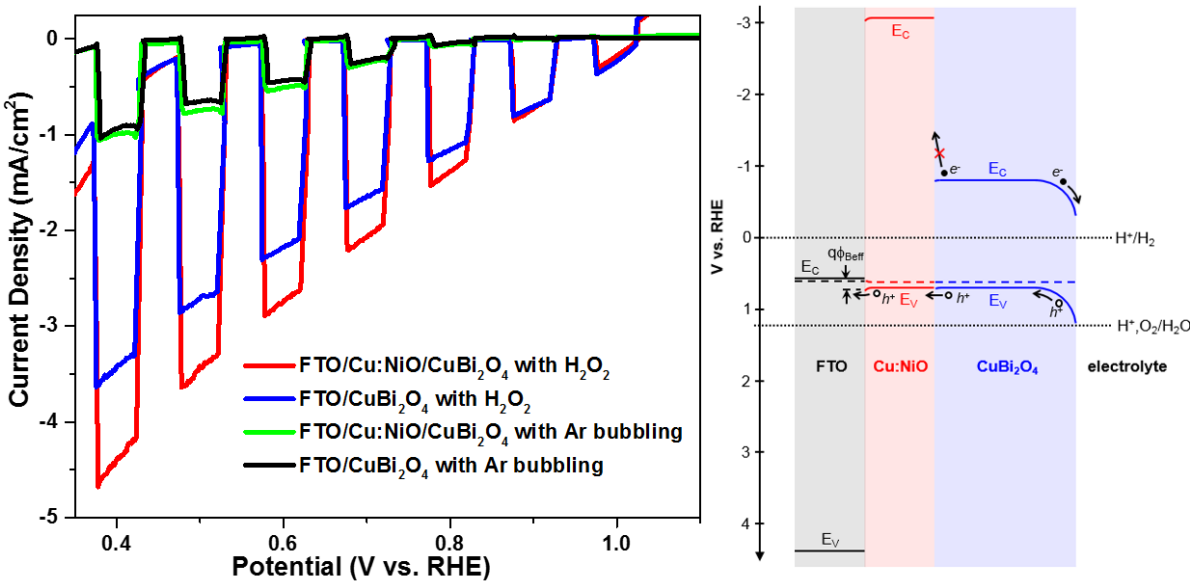

The main part of this Chapter was published: A. Song, P. Plate, A. Chemseddine, F. Wang, F. F. Abdi, M. Wollgarten, R. van de Krol and S. P. Berglund, *Journal of Materials Chemistry A*, 2019, **7**, 9183-9194.

P-type $CuBi_2O_4$ has recently been reported as a promising photocathode material for direct photoelectrochemical solar water reduction due to its optimal optical band gap and positive photocurrent onset potential. However, despite its favorable optical band gap energy and light absorption, this material suffers from poor charge carrier transport within bulk $CuBi_2O_4$ thin films and at $CuBi_2O_4$-substrate interface. This limitation can be addressed by inserting a very thin backing contact layer between FTO and $CuBi_2O_4$. Here we successfully demonstrate this approach for the first time by using p-type transparent Cu:NiO, which is prepared by electron beam evaporation combined with a post deposition annealing process in air as an electron blocker for $CuBi_2O_4$ photocathode. $CuBi_2O_4$ photocathodes with a 7 nm thick Cu:NiO back contact layer produce photocurrent densities up to 2.83 mA/cm^2 at 0.6 V versus RHE under back illumination with H_2O_2 as an electron scavenger, which is 24% higher than photocathodes without the back contact layer. The observed improvement in photocurrent density with Cu:NiO was due to a decreased recombination of photo-generated charge carriers at $CuBi_2O_4$-substrate interface from improved charge separation in addition to improved charge carrier transport through the electron blocker layer compared to the $CuBi_2O_4$ film alone.

4.1 Introduction

P-type semiconductor $CuBi_2O_4$ has recently attracted a lot of attentions as a photocathode material since it possesses several attractive features for photoelectrochemical (PEC) solar water splitting. First, it is reported to have an optimal optical bandgap in the range of 1.5–1.8 eV,[100-104] which is the ideal range for the top absorber layer in a dual absorber photoelectrochemical device with maximum utilization of the AM1.5 solar spectrum.[105, 106] Second, its conduction band is estimated to be at a more negative potential than the thermodynamic potential for water reduction to enable solar H_2 production.[38, 107-109] Third, its Fermi level is located at a more positive potential (>1.0 V vs. RHE) than many other p-type photocathode materials such as Cu_2O, $CuFeO_2$ and p-type Si.[30, 110-114] Positive Fermi level energy results in an exceptionally positive photocurrent onset potential, which is very important for a photocathode when it is combined with an n-type photoanode material to assemble a p-n photoelectrochemical cell for overall water splitting. Therefore, it is currently considered as a promising photocathodes for overall water splitting.

However, there are several limitations in $CuBi_2O_4$ that must be overcome to make it more efficient as a photocathode for water reduction. One of the biggest limitations is the relatively poor charge carrier transport of photogenerated electrons and holes within $CuBi_2O_4$, which is a common problem for metal oxide photoelectrode materials.[30, 38, 110, 115] Previously, we improved the charge carrier transport in $CuBi_2O_4$ thin film photocathodes by using gradient self-doping to create an internal electric field,[91] which improved the charge separation efficiency and overall photoelectrochemical performance significantly.

Another limitation of $CuBi_2O_4$ thin film photocathodes is the relatively poor charge carrier transport of holes across the $CuBi_2O_4$-substrate interface when n-type fluorine doped tin oxide (FTO) is used as the substrate. For p-type photocathode materials, such as $CuBi_2O_4$, the minority carriers (electrons) must be transferred to the redox species at the semiconductor-electrolyte interface to drive the photoelectrochemical reduction reaction while the majority carriers (holes) must be separated and transported across the semiconductor-substrate interface. FTO has a reported work function of ~5.0 eV vs .vacuum (0.5 V vs. RHE),[116-118] which is well matched to the Fermi level of many n-type photocathode materials. However, the Fermi level of p-type $CuBi_2O_4$ is around 5.8 eV vs. vacuum (1.3 V vs. RHE).[38, 91] This mismatch between the work function of degenerately doped FTO and the Fermi level of $CuBi_2O_4$ can result in the formation of a Schottky barrier at the $CuBi_2O_4$-FTO interface impeding hole transport.[119, 120] Additionally, defect states can lead to recombination at the interface, which has been observed for other metal oxide semiconductors deposited directly on conducting substrates.[121-123] In this work, we address this limitation by inserting a very thin p-type Cu doped NiO (Cu:NiO) back contact layer between the FTO substrate and the $CuBi_2O_4$ thin film, which significantly improves charge carrier transport across the $CuBi_2O_4$-substrate interface.

Nickel oxide (NiO) have been widely used in a range of areas as hole-injection buffer layers especially in light emitting diodes (OLEDs), organic photovoltaics (OPVs), and organic–inorganic perovskite solar cells due to its p-type conductivity, high transparency and suitable Fermi level of 5.0–5.6 eV (0.5 – 1.1 V vs. RHE).[124-126] Furthermore, it has been shown that the p-type conductivity of NiO can be improved with Cu doping so that Cu:NiO can act as an effective hole selective back contact with lower resistance to hole transport.[122] For p-type photocathode materials, such as $CuBi_2O_4$, the minority carriers (electrons) must be transferred to the redox species at the semiconductor-electrolyte interface to drive the photoelectrochemical reduction reaction while the majority carriers (holes) must be separated and extracted at the semiconductor-substrate interface.[27, 31] Therefore, Cu:NiO might be a suitable back contact material for $CuBi_2O_4$ thin film photocathodes. In the following section we confirm this by showing that $CuBi_2O_4$ photocathodes with a Cu:NiO back contact layer have lower electrical resistivity, higher charge carrier separation efficiency, and higher photocurrent density.

4.2 Theoretical model (Derivation of Equation for Back-to-Back Schottky Diodes)

The current densities across back-to-back Schottky barriers, J_1 and J_2 (A/cm^2), are governed by the following equations.[127-131]

$$J_1 = J_{s1}\left[\exp\left(\frac{qV_1}{kT}\right) - 1\right] \tag{4.1}$$

$$J_{s1} = A^{**}\, T^2 \exp\left(\frac{-q\phi_{Beff1}}{kT}\right) \tag{4.2}$$

$$J_2 = J_{s2}\, \left[\exp\left(\frac{qV_2}{kT}\right) - 1\right] \tag{4.3}$$

$$J_{s2} = A^{**}\, T^2 \exp\left(\frac{-q\phi_{Beff2}}{kT}\right) \tag{4.4}$$

A** is the reduced effective Richardson constant (A $cm^{-2}\,K^{-2}$), T is the temperature (K), q is the electronic charge (1.602×10^{-19} C), k is the Boltzmann constant ($1.381 \times 10^{-23}\ m^2\,kg\,s^{-2}\,K^{-1}$), ϕ_{Beff1} and ϕ_{Beff2} are the effective barrier heights (eV), V is the overall applied voltage (V), and V_1 and V_2 are resulting voltages at each back-to-back Schottky barrier (V). From continuity and symmetry, the overall current density (J) and applied voltage (V) are related to the individual values as follows:

$$J = J_1 = J_2 \tag{4.5}$$

$$V = V_1 + V_2 \tag{4.6}$$

Substitution of variables can be used to solve for J.

$$V_1 = \frac{kT}{q} \ln\left[1 + \frac{J}{J_{s1}}\right] \tag{4.7}$$

$$V_2 = \frac{-kT}{q} \ln\left[1 - \frac{J}{J_{s2}}\right] \tag{4.8}$$

$$V = \frac{kT}{q} \ln\left[1 + \frac{J}{J_{s1}}\right] - \frac{kT}{q} \ln\left[1 - \frac{J}{J_{s2}}\right] \tag{4.9}$$

$$J = \frac{J_{s1}\, J_{s2} \exp\left(\frac{qV}{2kT}\right) - J_{s1}\, J_{s2} \exp\left(\frac{-qV}{2kT}\right)}{J_{s1} \exp\left(\frac{qV}{2kT}\right) + J_{s2} \exp\left(\frac{-qV}{2kT}\right)} = \frac{J_{s1}\, J_{s2} \sinh\left(\frac{qV}{2kT}\right)}{J_{s1} \exp\left(\frac{qV}{2kT}\right) + J_{s2} \exp\left(\frac{-qV}{2kT}\right)} \tag{4.10}$$

Under the assumption that the barrier height of each Schottky barrier, scales linearly with the applied voltage, the effective barrier heights can be defined in terms of the ideality factors, n_1 and n_2.

$$\phi_{Beff1} = \phi_{B01} + V_1 \left(1 - \frac{1}{n_1}\right) \tag{4.11}$$

$$\phi_{Beff2} = \phi_{B02} - V_2 \left(1 - \frac{1}{n_2}\right) \tag{4.12}$$

ϕ_{B01} and ϕ_{B02} are the barrier heights at zero bias (eV).

$$J = \frac{2\,A^{**}\,T^2 \exp\left(\frac{-q\left[\phi_{B01}+V_1\left(1-\frac{1}{n_1}\right)\right]}{kT}\right) A^{**}\,T^2 \exp\left(\frac{-q\left[\phi_{B02}-V_2\left(1-\frac{1}{n_2}\right)\right]}{kT}\right) \sinh\left(\frac{qV}{2kT}\right)}{A^{**}\,T^2 \exp\left(\frac{-q\left[\phi_{B01}+V_1\left(1-\frac{1}{n_1}\right)\right]}{kT}\right) \exp\left(\frac{qV}{2kT}\right)+A^{**}\,T^2 \exp\left(\frac{-q\left[\phi_{B02}-V_2\left(1-\frac{1}{n_2}\right)\right]}{kT}\right) \exp\left(\frac{-qV}{2kT}\right)} \tag{4.13}$$

By the symmetry of the system the back-to-back Schottky diodes should have similar barrier heights at zero bias and ideality factors.

$$\phi_{B01} = \phi_{B02} = \phi_{B0} \tag{4.14}$$

$$n_1 = n_2 = n \tag{4.15}$$

Furthermore, if the channel resistance is low, then voltages at each Schottky barrier can be assumed to be equal.

$$V_1 = V_2 = \frac{V}{2} \tag{4.16}$$

$$J = \frac{2\,A^{**}\,T^2 \exp\left(\frac{-2q\phi_{B0}}{kT}\right) \exp\left(\frac{-q(V-V)}{2kT}\right) \exp\left(\frac{-q(V-V)}{2nkT}\right) \sinh\left(\frac{qV}{2kT}\right)}{\exp\left(\frac{-q\phi_{B0}}{kT}\right)\left[\exp\left(\frac{-qV}{2kT}\right) \exp\left(\frac{qV}{2nkT}\right) \exp\left(\frac{qV}{2kT}\right)+\exp\left(\frac{-qV}{2kT}\right) \exp\left(\frac{-qV}{2nkT}\right) \exp\left(\frac{qV}{2kT}\right)\right]} \tag{4.17}$$

$$J = \frac{2\,A^{**}\,T^2 \exp\left(\frac{-2q\phi_{B0}}{kT}\right) \sinh\left(\frac{qV}{2kT}\right)}{\exp\left(\frac{qV}{2nkT}\right)+\exp\left(\frac{-qV}{2nkT}\right)} \tag{4.18}$$

$$J = \frac{A^{**}\,T^2 \exp\left(\frac{-2q\phi_{B0}}{kT}\right) \sinh\left(\frac{qV}{2kT}\right)}{\cosh\left(\frac{qV}{2nkT}\right)} \tag{4.19}$$

4.3 Results and discussion

4.3.1 Photoelectrochemical and Optical Properties

For this study $CuBi_2O_4$ thin films were deposited on various substrates using the forward gradient self-doping process described in our previous work.[91] To prepare photocathodes for photoelectrochemical analysis the $CuBi_2O_4$ thin films were deposited directly on fluorine doped tin oxide (FTO) substrates or on top of FTO/Cu:NiO substrates, in which a thin Cu doped NiO layer was first prepared by electron beam evaporation of Ni and Cu followed by post annealing in air. The $CuBi_2O_4$ photocathodes were tested as working electrodes in a photoelectrochemical cell under simulated AM1.5 illumination. **Figure 4.1a** shows representative chopped (dark/light) linear sweep voltammetry (LSV) scans for $CuBi_2O_4$ thin films synthesized on top of FTO and FTO/Cu:NiO substrates. The thickness of the Cu:NiO and $CuBi_2O_4$ thin films were approximately ~7 nm and ~260 nm, respectively. The measurements were performed in 0.3 M K_2SO_4 and 0.2 M phosphate buffer (pH 6.65) either with H_2O_2 added as an electron scavenger to test the $CuBi_2O_4$ photocathodes without limitations in the reaction kinetics and surface recombination,

or with Ar bubbling to remove dissolved O_2 and test for proton reduction. In **Figure 4.1a**, the photocurrent density is clearly higher in magnitude for the FTO/Cu:NiO/$CuBi_2O_4$ photocathode compared to the FTO/$CuBi_2O_4$ photocathode. With an optimal $CuBi_2O_4$ thickness of 260 nm the FTO/Cu:NiO/$CuBi_2O_4$ photocathode produces a photocurrent density of -0.5 mA/cm^2 and -2.83 mA/cm^2 at 0.6 V versus RHE under backside illumination with Ar bubbling and H_2O_2 as an electron scavenger, respectively, which is an improvement of 21.9% and 24.4% compared to the FTO/$CuBi_2O_4$ photocathode. The improvement in photocurrent density was consistent for both frontside and backside illumination (see **Figure S A1**) and held for a range of $CuBi_2O_4$ film thicknesses between 150 and 380 nm as shown in the inset of **Figure 4.1a**. See **Figure S A2a** and **Figure S A2b** for the individual LSV scans for different $CuBi_2O_4$ film thicknesses. To prove that the enhancement was not simply due to the Cu:NiO film producing additive photocurrent, chopped LSV measurements were performed on a FTO/Cu:NiO electrode (7 nm of Cu:NiO without $CuBi_2O_4$). As shown in **Figure S A3,** the photocurrent density of the FTO/Cu:NiO sample was barely distinguishable from the dark current density reaching only -0.0005 mA/cm^2 at 0.4 V versus RHE under backside illumination. In addition, increasing the thickness of the Cu:NiO layer in the FTO/Cu:NiO/$CuBi_2O_4$ photocathode actually decreases the photocurrent density of the device as shown in **Figure S A4**. This is further evidence for enhancement in photocurrent does not come from the Cu:NiO layer itself. Instead the improved performance of the FTO/Cu:NiO/$CuBi_2O_4$ photocathode is due to electronic interactions between the FTO, Cu:NiO, and $CuBi_2O_4$ layers, which will be further explained throughout this article. To gain additional information about the role of the Cu:NiO back contact layer at enhancing the photocurrent, we measured the external incident photon-to-current conversion efficiency (IPCE) and calculated absorbed photon-to-current efficiency (APCE) of the FTO/$CuBi_2O_4$ and FTO/Cu:NiO/$CuBi_2O_4$ photocathodes at 0.6 V vs. RHE with H_2O_2 and with Ar bubbling . These results are shown in **Figure S A5** and **Figure 4.1b**. With H_2O_2 added the IPCE and APCE values are significantly higher for the FTO/Cu:NiO/$CuBi_2O_4$ photocathode for UV light (≤ 400 nm) and visible light (400 - 700 nm). As a fast redox couple, H_2O_2 is expected to reduce surface recombination and limitations in reaction kinetics at the semiconductor-liquid interface. Therefore the APCE values give a representation of the overall charge separation within the solid-state regions of the photocathodes. Since the FTO/Cu:NiO/$CuBi_2O_4$ photocathode has consistently higher APCE values than the FTO/$CuBi_2O_4$ photocathode for all wavelengths, it can be inferred that the Cu:NiO back contact layer improves the overall charge separation in the individual layers and/or at the solid-state interfaces. The IPCE values can also be used to calculate the predicted AM1.5 photocurrent density ($J_{AM1.5}$) according to the equation in the Experimental section. This results in a predicted photocurrent density of 3.07 mA/cm^2 and 2.55 mA/cm^2 at 0.6 V_{RHE} for $CuBi_2O_4$ photocathode based on FTO and Cu:NiO layer respectively, which is very close to the 2.83 mA/cm^2 and 2.25 mA/cm^2 obtained for the chopped LSV measurements under AM1.5 solar simulation.

Lastly, the FTO/$CuBi_2O_4$ and FTO/Cu:NiO/$CuBi_2O_4$ photocathodes were compared in terms of photoelectrochemical stability. **Figure 4.1c** shows dark/light constant potential measurements for the

photocathodes in 0.3 M K_2SO_4 and 0.2 M phosphate buffer (pH 6.65) with Ar bubbling and with H_2O_2 added at 0.6 V vs. RHE. With Ar bubbling both photocathodes show a fast initial decay in photocurrent (~50% within 15 min) due to photo-corrosion of $CuBi_2O_4$, which is a common challenge for metal oxide photocathodes containing copper.[38, 110] To address this challenge, strategies such as conformal protection layers with co-catalysts can be utilised.[36, 91, 113] With H_2O_2 added the FTO/$CuBi_2O_4$ and FTO/Cu:NiO/$CuBi_2O_4$ photocathodes still show a drop in photocurrent but the decay is much slower (~50% in 120 min) and the FTO/Cu:NiO/$CuBi_2O_4$ photocathode shows significantly higher photocurrent for the entire period of time, which further validates the effectiveness of Cu:NiO as a back contact layer for $CuBi_2O_4$.

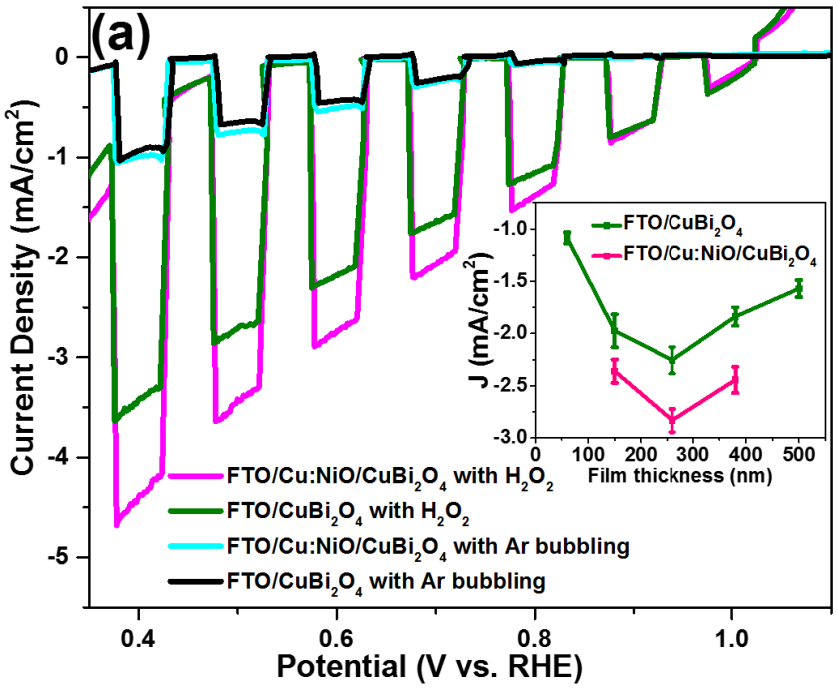

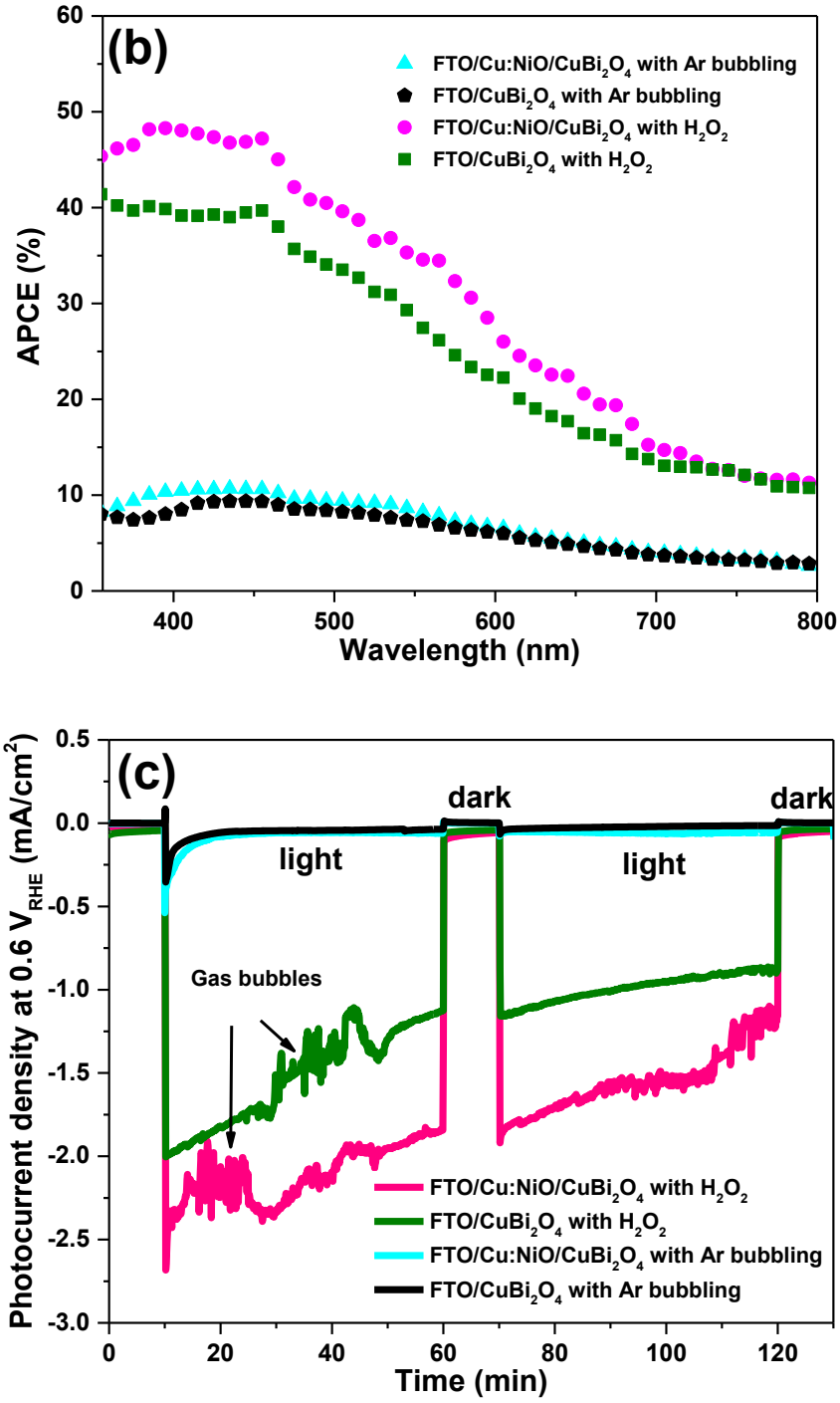

Figure 4.1. (a) Chopped LSV scans for $CuBi_2O_4$ photocathodes synthesized to a thickness of ~260 nm on FTO and on FTO/Cu:NiO substrates. Inset shows the average photocurrent densities at 0.6 V vs RHE extracted from LSV scans for photocathodes with different thicknesses. (b) APCE spectra of $CuBi_2O_4$ on FTO, $CuBi_2O_4$ on FTO/Cu:NiO in 0.3 M K_2SO_4 and 0.2 M phosphate buffer (pH 6.65) with Ar bubbling and with H_2O_2 at a potential of 0.6 V vs.

RHE. (c) Constant potential measurement at 0.6 V vs RHE for 260 nm $CuBi_2O_4$ films based on bare FTO and 7 nm Cu:NiO in the dark and light (AM1.5 irradiation). All measurements were performed under backside illumination.

The APCE values shown in **Figure 4.1b**, which were calculated using optical absorption of the entire photocathodes, provide strong evidence that the improvement in photoactivity of the FTO/Cu:NiO/$CuBi_2O_4$ photocathode is not due to an optical effect of the Cu:NiO layer. In fact the very thin Cu:NiO layer has only a minor influence on the overall optical absorption. **Figure 4.2a** shows the absorptance spectra for a bare glass substrate along with a 7 nm Cu:NiO film, a 260 nm $CuBi_2O_4$ film, and a 260 nm $CuBi_2O_4$ on top of 7 nm Cu:NiO, all deposited on top of a glass substrate. **Figure 4.2b** shows the absorptance spectrum of a bare FTO substrate along with that of FTO/Cu:NiO, FTO/$CuBi_2O_4$ and FTO/Cu:NiO/$CuBi_2O_4$ photocathodes. These spectra show that the absorptance values are only slightly higher for the Cu:NiO/$CuBi_2O_4$ layering compared to $CuBi_2O_4$, regardless of whether the substrate is glass or FTO. If we consider the case of 100% APCE under AM1.5 illumination, the maximum obtainable increase in photocurrent density due to the slightly higher absorption is calculated to be 8.4 % and 2.0 % using the spectra in **Figure 4.2a** and **Figure 4.2b**, respectively. Recall that the measured increase in photocurrent density is much larger at 22-24% (see **Figure 4.1a**). Clearly the increased photocurrent density is due to additional photophysical processes besides slightly higher optical absorption of the Cu:NiO/$CuBi_2O_4$ layering. Moreover, the increased optical absorption likely only occurs in the Cu:NiO layer rather than the $CuBi_2O_4$ layer, especially when backside illumination is used. At longer wavelengths the Cu:NiO layer may undergo free carrier absorption, which commonly occurs in highly doped metal oxide semiconductors used as transparent conducing oxides (TCOs).[132-134] Similar to the FTO coated glass the Cu:NiO coated glass sample shows a low baseline absorptance of 5-10% that extends to energies that are much lower than the reported bandgap of NiO (3.6-4.3 eV or 288-344 nm light).[126, 135] **Figure S A6a** and **S A6b** show the transflectance spectra and direct bandgap tauc plots for Cu:NiO films of different thicknesses of 7, 34 and 102 nm. The Tauc plots of the Cu:NiO films indicate that the bandgap is ~3.75 eV. **Figure S A6c** shows a Tauc plot of bare FTO substrate indicating a bandgap of ~3.7 eV.

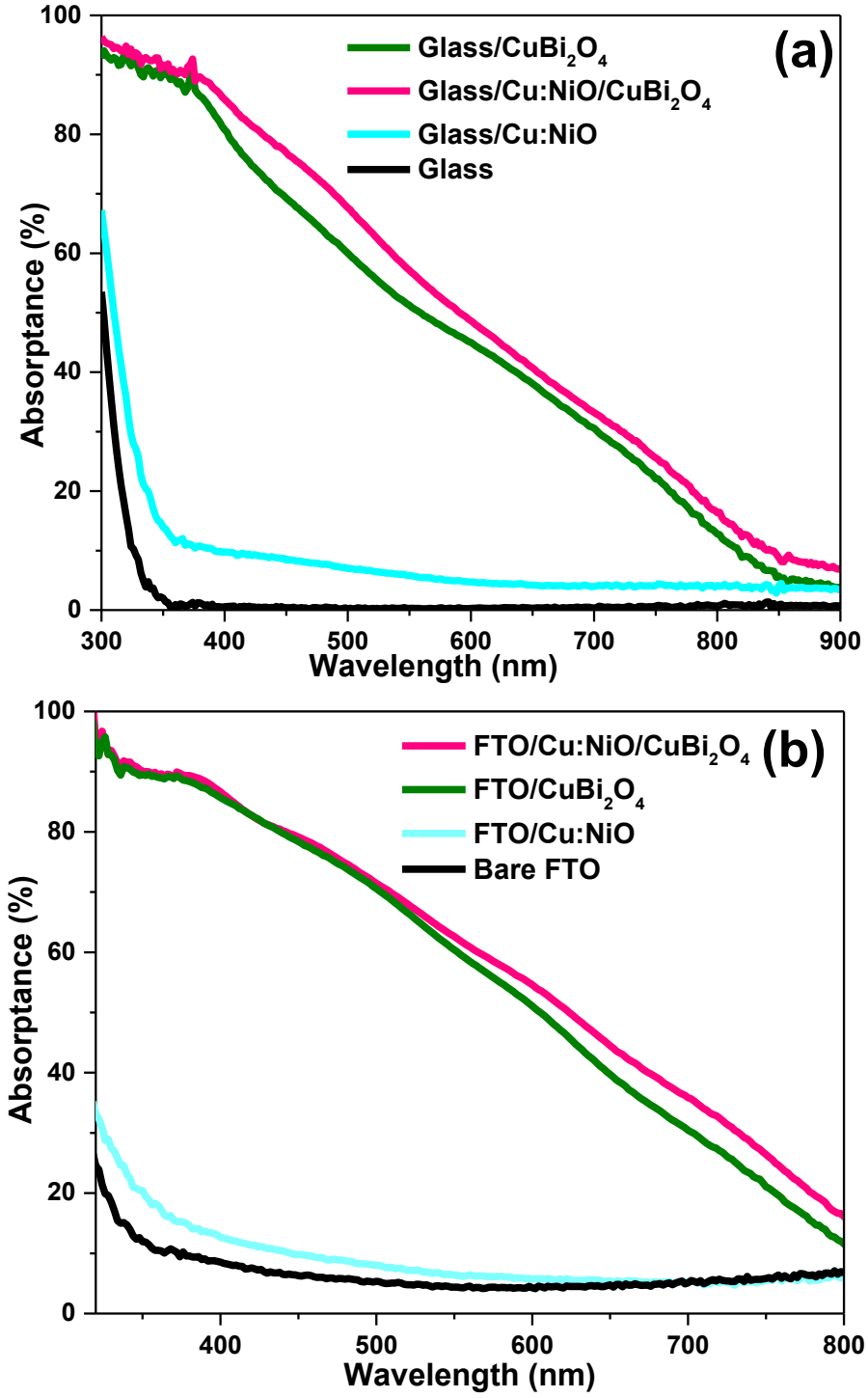

Figure 4.2. (a) UV-vis absorptance spectra for a bare glass substrate (black line) along with a 7 nm Cu:NiO film (indigo line), a 260 nm $CuBi_2O_4$ film (green line) and a 7nm/260 nm Cu:NiO /$CuBi_2O_4$ film stack (pink line), all deposited on top of glass. (b) Absorptance spectra for bare FTO, FTO/ Cu:NiO (7nm) and FTO/$CuBi_2O_4$ and FTO/ Cu:NiO (7nm) /$CuBi_2O_4$.

4.3.2 Crystal Structure and Morphology

The crystal structure and morphology of the $CuBi_2O_4$ thin film photocathodes and the individual FTO, Cu:NiO, and $CuBi_2O_4$ layers were investigated because crystal structure, crystallite orientation, nanostructure, and surface area can have a significant influence on the photoelectrochemical performance. The Cu:NiO intermediate layer can also influence the growth of $CuBi_2O_4$ during synthesis. **Figure 4.3** shows SEM images of a bare FTO substrate, 7 nm Cu:NiO deposited on FTO, 260 nm $CuBi_2O_4$ film deposited on FTO, and a 7nm/260nm Cu:NiO/$CuBi_2O_4$ film stack. It also shows a cross-section TEM image of a Cu:Ni film as deposited on FTO and after annealing to form a Cu:NiO film. **Figure 4.3a** shows that the FTO surface is composed of angular crystal facets on the order of 10-500 nm, which is typical for fluorine doped tetragonal SnO_2. [136] Close examination of **Figure 4.3b** reveals that the Cu:NiO layer is composed of small particles that cover the FTO facets. The $CuBi_2O_4$ films appear similar in **Figure 4.3c** (on FTO) and **Figure 4.3d** (on 7 nm Cu:NiO) so the underlying Cu:NiO does not significantly influence the morphology of the deposited $CuBi_2O_4$ thin film. **Figure 4.3e** shows the cross-section TEM image of a Cu:Ni film as deposited. The TEM image shows that the thickness is very close to the expected value of 4.4 nm (2 nm Ni / 0.4 nm Cu / 2 nm Ni) based on the QCM monitoring during deposition. **Figure 4.3f** shows a TEM cross-section of a Cu:Ni film that was annealed to form Cu:NiO. Annealing increases the thickness due to the incorporation of oxygen to form the NiO crystal structure. The thickness in the TEM image matches the expected value of about 7 nm (estimated using the molar masses and mass densities of Ni and NiO with a starting thickness of 4 nm for the Ni metal).

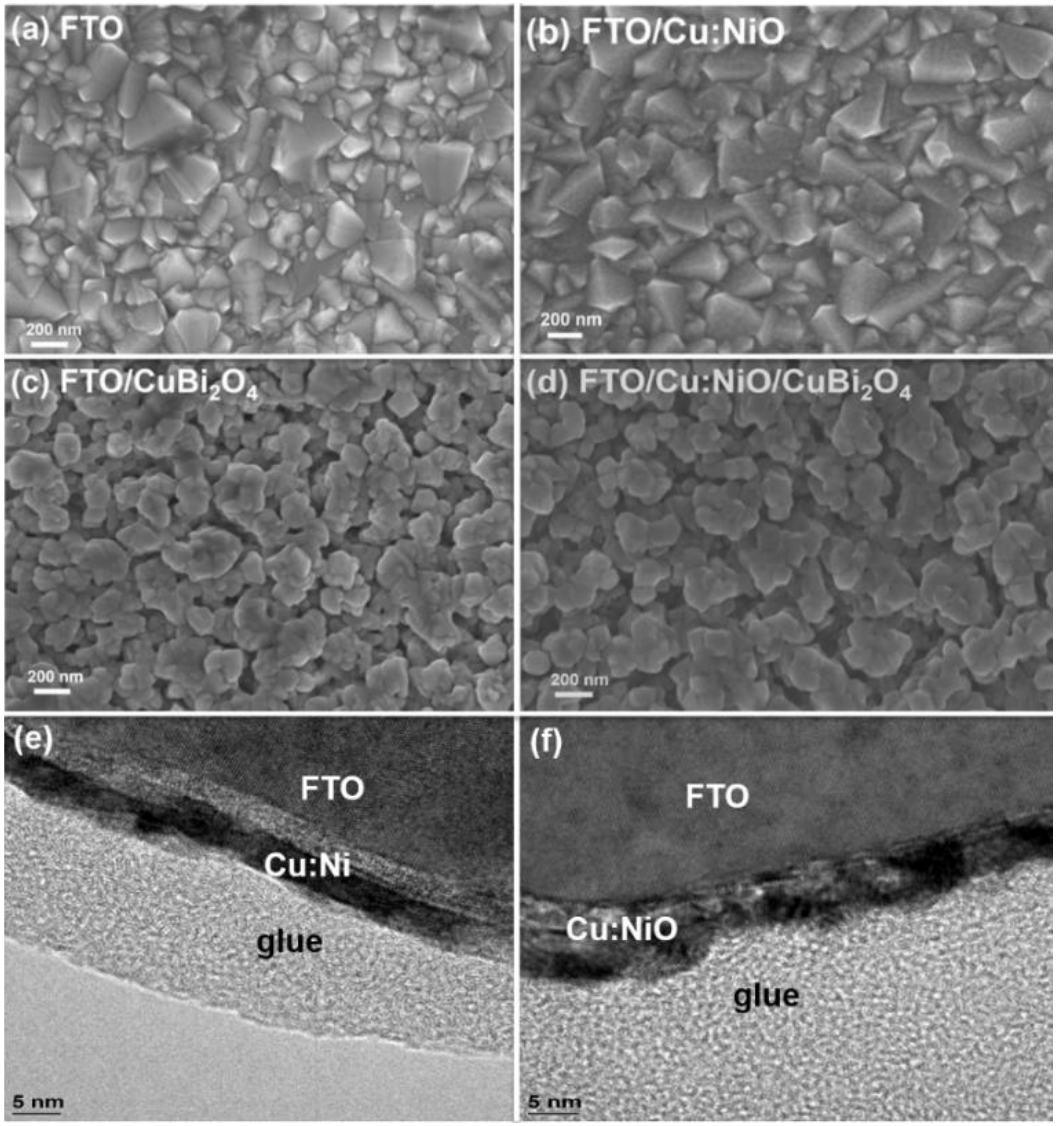

Figure 4.3. SEM images of a (a) bare FTO substrate, (b) 7 nm Cu:NiO deposited on FTO, (c) 260 nm $CuBi_2O_4$ deposited on FTO, (d) 260 nm $CuBi_2O_4$ deposited on 7 nm Cu:NiO on FTO. Cross-section TEM images of (e) 4.4 nm Cu:Ni film as deposited on FTO and (f) after annealing at 450 ◦C in air to form Cu:NiO.

The surfaces of the bare FTO, FTO/Cu:NiO, FTO/$CuBi_2O_4$ and FTO/Cu:NiO/$CuBi_2O_4$ photocathodes were compared using atomic force microscopy (AFM) as shown in **Figure 4.4**. AFM reveals that the root mean squared (RMS) roughness and real surface area of $CuBi_2O_4$ films deposited directly on FTO are 90 nm and 30 μm^2, respectively, , for a scanned area of 25 μm^2. For $CuBi_2O_4$ films deposited on FTO/Cu:NiO the RMS roughness and real surface area are 82 nm and 30 μm^2, respectively, so the FTO/Cu:NiO/$CuBi_2O_4$ photocathode has a slightly lower surface roughness than the FTO/$CuBi_2O_4$. This may be due to the underlying Cu:NiO layer smoothing out the sharp peaks and trenches of the FTO surface as the RMS surface roughness is 60 nm for the FTO/Cu:NiO substrate compared to 92 nm for bare FTO as shown in

see **Figure 4.4a** and **4.4b**. All substrates and deposited films show a similar real surface areas in the range of 28 – 31 μm^2 for a cross-sectional area of 5 µm x 5 µm. Therefore the higher photocurrent density of the FTO/Cu:NiO/$CuBi_2O_4$ photocathode is not due to an increase in roughness or surface area.

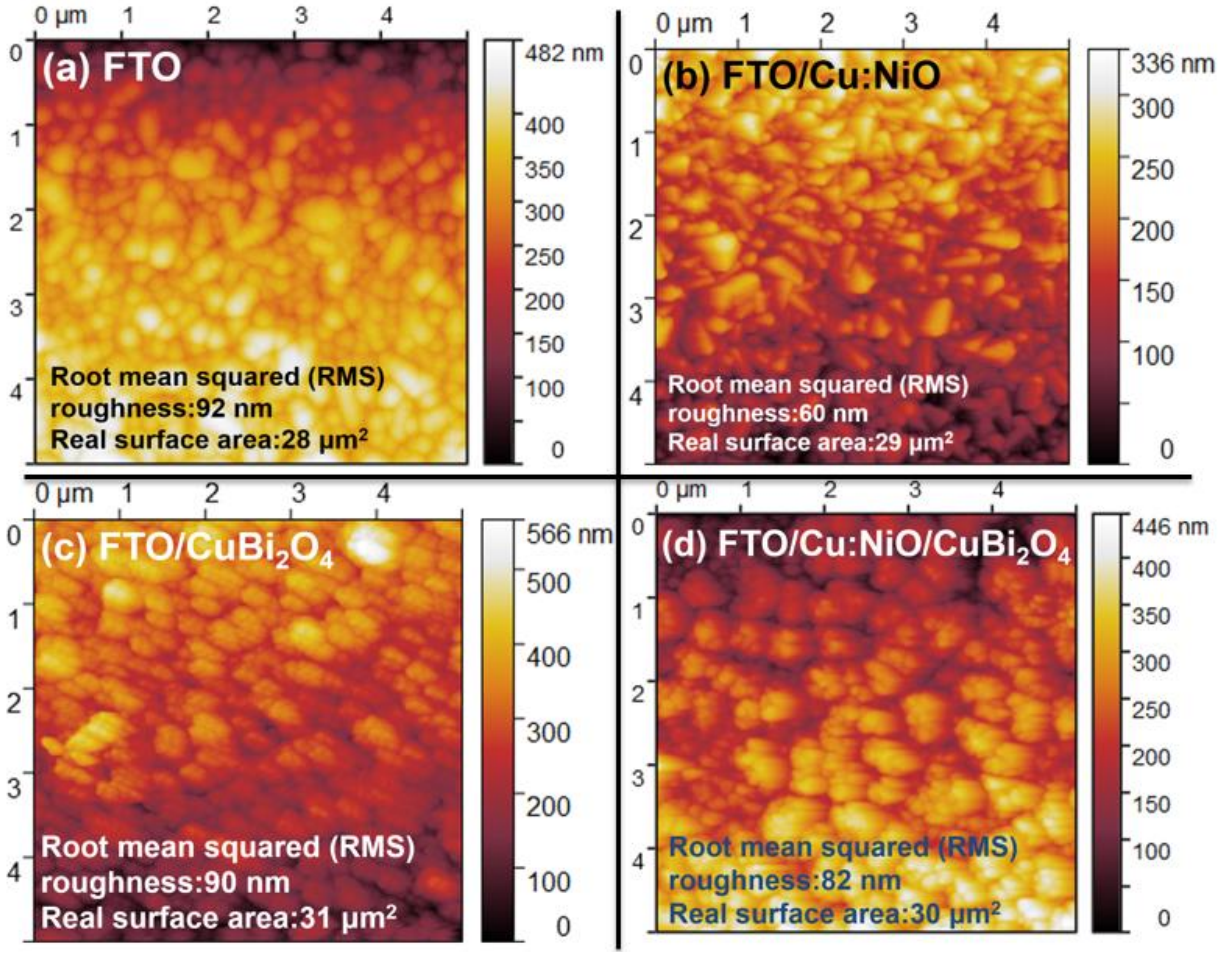

Figure 4.4. AFM images of (a) bare FTO, (b) a 7 nm Cu:NiO layer, (c) $CuBi_2O_4$ thin films deposited on FTO substrate and (d) $CuBi_2O_4$ thin films deposited on a 7 nm Cu:NiO layer on FTO.

The crystallinity and chemical composition of each deposited layer was confirmed using X-ray diffraction (XRD) and energy-dispersive X-ray (EDX) measurements. **Figure 3.8a** shows the X-ray diffractograms of Cu:NiO thin films with thicknesses of 7, 34, and 102 nm deposited on glass substrates along with that for a bare glass substrate. The diffractogram of the 102 nm Cu:NiO thin film mainly exhibits the crystal structure of cubic nickel oxide (NiO, JCPDS47-1049). However, two small peaks are also visible for monoclinic cupric oxide (CuO, JCPDS 48-1548). No metallic Cu or Ni peaks were observed and neither were any Cu_2O peaks, indicating that the deposited film was fully oxidized, which is in agreement with the phase diagram of copper oxide, which shows that CuO is a stable phase at the annealing temperature of 450°C

in air at atmospheric pressure.[137] In the diffractogram for the 34 nm Cu:NiO thin film no peaks are visible for the CuO phase. This may be due to the amount of CuO being too low or it could be due to the Cu more easily diffusing into the 34 nm NiO film compared to the 102 nm film. The 7 nm Cu:NiO thin film was also measured by XRD (magenta line) but no peaks could be discerned from the background signal. **Figure 4.5b** shows the X-ray diffractogram of a FTO/$CuBi_2O_4$ sample (blue line), FTO/Cu:NiO/$CuBi_2O_4$ sample (red line), and bare FTO substrate. Both of these $CuBi_2O_4$ films show strong XRD peaks at 20.95°,28.02°, 33.30° and 46.69°, which can be assigned to the (200), (211), (310), and (411) lattice planes of tetragonal $CuBi_2O_4$, respectively, according to the $CuBi_2O_4$ reference data (JCPDS 42-0334).[138, 139] Since the diffractograms are nearly the same for these samples the underlying Cu:NiO layer has no obvious influence on the crystal structure of the deposited $CuBi_2O_4$ film.

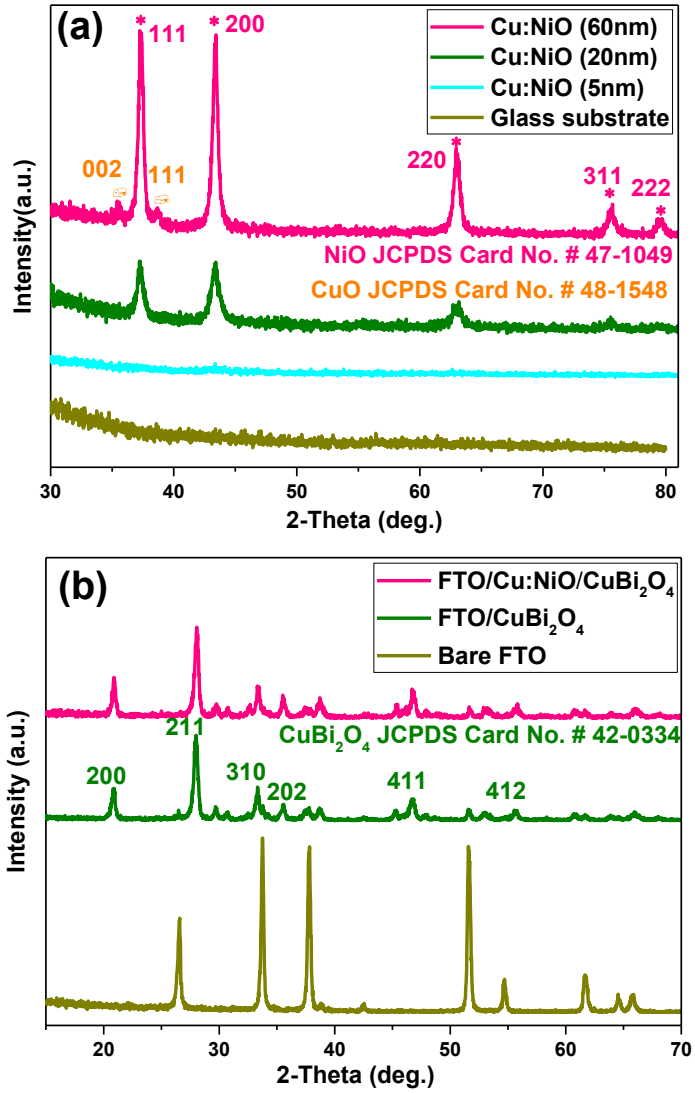

Figure 4.5. XRD diffractograms for (a) a bare glass substrate (olivine line) and Cu:NiO thin films deposited on glass substrates with thicknesses of 7 nm (indigo line), 34 nm (green line), and 102 nm (pink line), and XRD diffractograms for (b) a bare FTO substrate (olivine line) and ~260 nm $CuBi_2O_4$ deposited on a FTO substrate (green line) and a 7 nm Cu:NiO layer on FTO (pink line).

To confirm the chemical composition of the prepared films, energy-dispersive X-ray (EDX) mapping of a representative film area was carried out on a FTO/$CuBi_2O_4$ photocathode. The relevant SEM images with EDX mapping overlaid are shown in **Figure 4.6**, the EDX signals from Cu, O, Bi and Sn appear to be homogeneously distributed over the film area. EDX was also performed on the 7 nm Cu:NiO layer as shown in **Figure S A7**. Clearly Cu, Ni and O are also well mixed and homogenously distributed in the Cu:NiO film. From EDX the atom ratio of Cu to Ni is about 1 to 10 (0.09 at. % Cu and 0.84 at. % Ni), as expected based on the QCM measurements of the Cu and Ni thicknesses during electron beam evaporation.

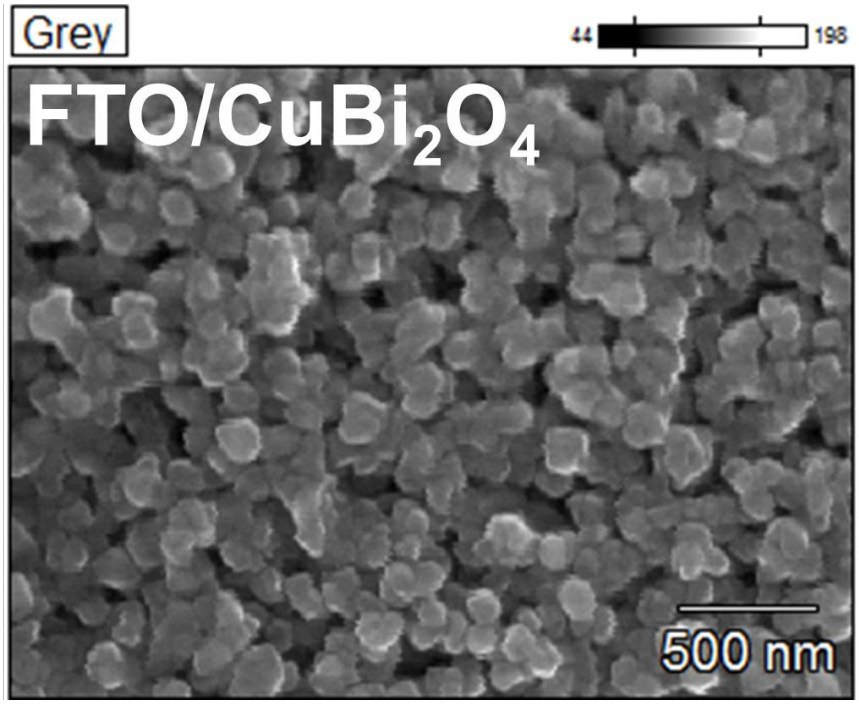

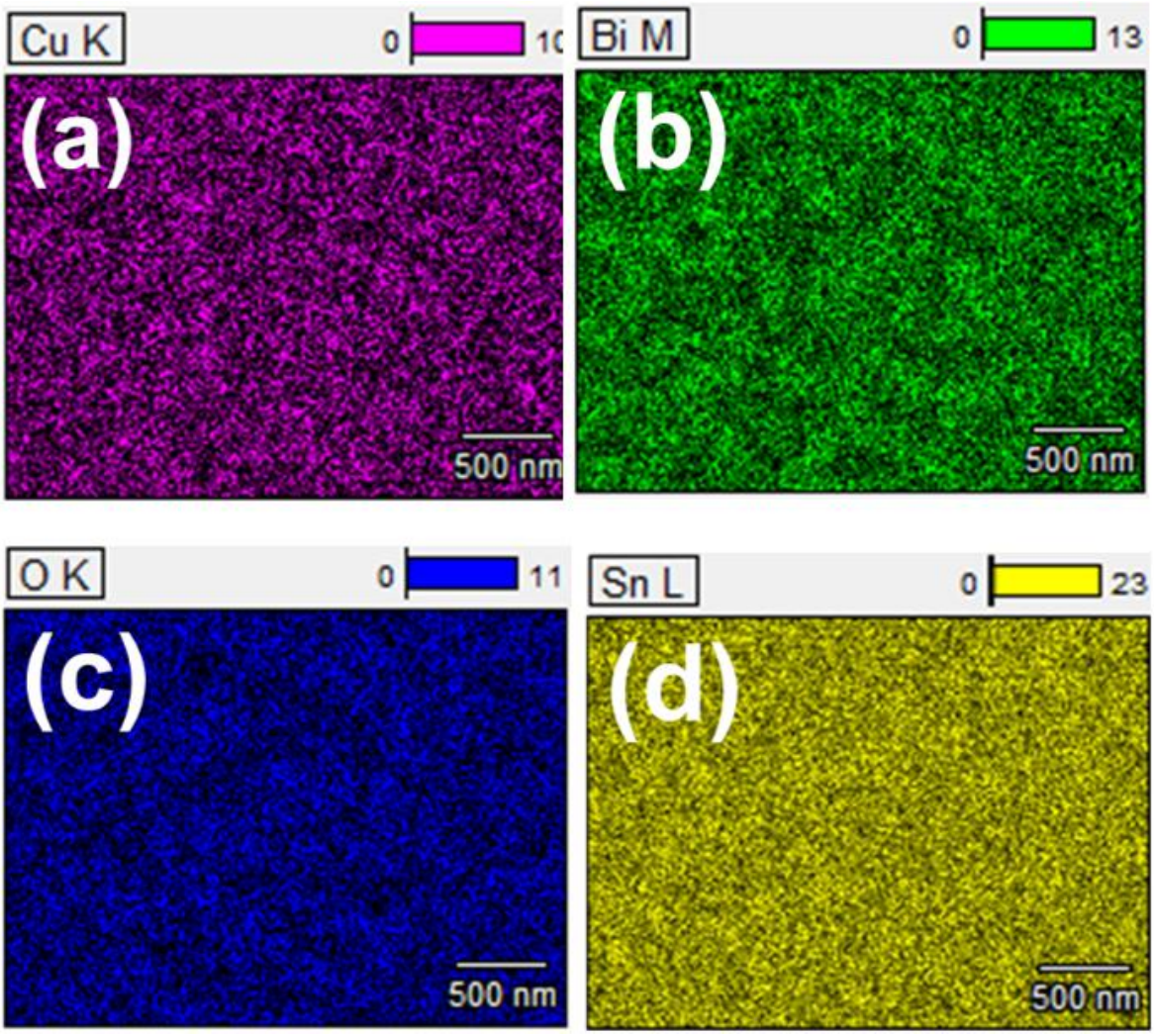

Figure 4.6. Top-view SEM image of 260 nm $CuBi_2O_4$ deposited on FTO and corresponding EDX elemental mapping of (a) Cu (b) Bi, (c) O and (d) Sn.

4.3.3 Electronic and Semiconductor Properties

For the solid-state current vs. voltage (I-V) measurements the surface of the FTO and FTO/Cu:NiO substrates were laser cut in the pattern shown in **Figure 4.7**. The width and length of each cut was approximately 230 µm and 9.75 cm, respectively.

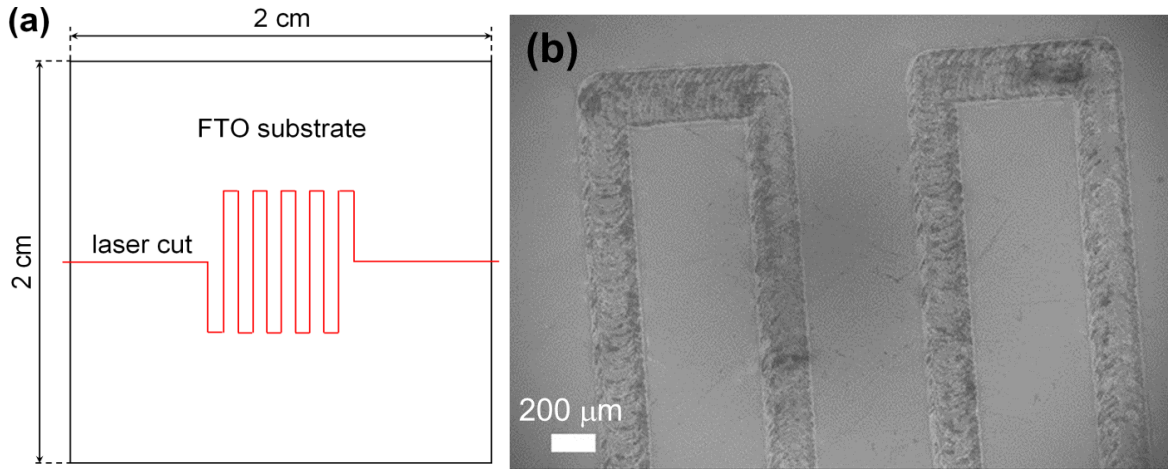

Figure 4.7. (a) Drawing of the laser cut pattern used for solid-state I-V measurements. (b) SEM image of an FTO substrate with a laser cut.

To analyse the electronic interactions between FTO, Cu:NiO, and $CuBi_2O_4$ we performed solid-state current density vs. voltage (J-V) measurements on FTO/$CuBi_2O_4$/FTO, FTO/Cu:NiO/FTO, and FTO/Cu:NiO/$CuBi_2O_4$/Cu:NiO/FTO samples. The samples were prepared by depositing Cu:NiO or $CuBi_2O_4$ layers over the trenches in laser-cut FTO and FTO/Cu:NiO substrates, which were then measured as illustrated in **Figure S A8**. The FTO/$CuBi_2O_4$/FTO and FTO/Cu:NiO/FTO samples were modelled based on thermionic emission theory using the following equation derived for back-to-back Schottky diodes.

$$J = \frac{I}{L\,d} = \frac{A^{**}\,T^2 \exp\left(\frac{-q\phi_{B0}}{kT}\right) \sinh\left(\frac{-qV}{2kT}\right)}{\cosh\left(\frac{qV}{2nkT}\right)} \tag{4.20}$$

Here, J is the current density (A/cm^2), I is the current (A), L is the laser cut length (9.75 cm), d is the deposited film thickness (cm). For these samples it is assumed that FTO behaves more like a metal than a semiconductor since it is degenerately doped. The work function of FTO (4.8-5.0 eV) is much different than the Fermi level of $CuBi_2O_4$ (5.71 – 5.93 eV) so a Schottky barrier should form at each FTO/$CuBi_2O_4$ interface.[38, 91, 116] As a result the FTO/$CuBi_2O_4$/FTO sample should be composed of back-to-back Schottky diodes.[129, 130] Plots of the band bending behaviour of the back-to-back Schottky diodes at zero bias and under bias are depicted in **Figure S A9**. The samples were heated on a hot-plate to perform I-V measurements at different temperatures and the above equation was re-arranged to construct a modified Richardson plot.

$$\ln\left[\frac{J\cosh\left(\frac{qV}{2nkT}\right)}{T^2\sinh\left(\frac{qV}{2kT}\right)}\right] = \ln(A^{**}) - \phi_{B0}\left(\frac{q}{kT}\right) \tag{4.21}$$

The above equations were fit simultaneously to obtain values for A**, ϕ_{B0}, and n. The fitting of J for different temperatures are shown in **Figure 4.8**.

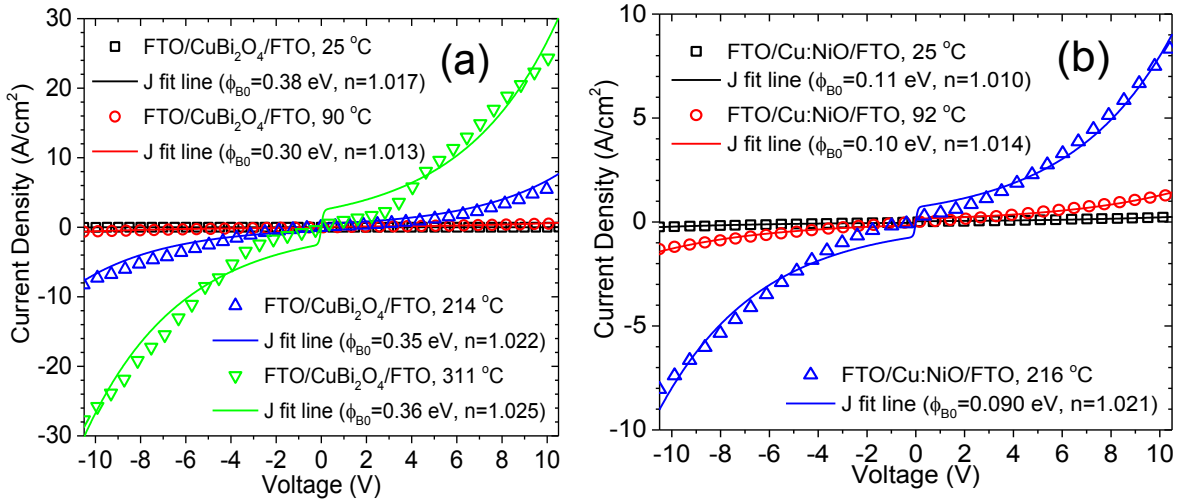

Figure 4.8. Current density vs. voltage (J-V) measurements at different temperatures for (a) $FTO/CuBi_2O_4/FTO$ and (b) FTO/Cu:NiO/FTO samples with J fit lines included.

Figure 4.9a and **b** show the experimental current density vs. voltage (J-V) data for $FTO/CuBi_2O_4/FTO$, $FTO/Cu:NiO/CuBi_2O_4/Cu:NiO/FTO$, and FTO/Cu:NiO/FTO samples along with the fit lines for the $FTO/CuBi_2O_4/FTO$ and FTO/Cu:NiO/FTO samples. **Figure 4.9c** and **d** show the modified Richardson plots for the $FTO/CuBi_2O_4/FTO$ and FTO/Cu:NiO/FTO samples at applied biases of ±1, ±2, and ±4 V with linear fit lines. The modified Richardson plots were constructed by performing the J-V measurements at different temperatures. By simultaneously fitting the experimental data in both the J-V measurements and modified Richardson plots, the barrier height (ϕ_{B0}) at zero bias and ideality factor (n) can be determined for the $FTO/CuBi_2O_4$ and FTO/Cu:NiO interfaces and the reduced effective Richardson constant (A^{**}) can be estimated for the $CuBi_2O$ and Cu:NiO layers. For these measurements, nearly identical values of ϕ_{B0} were obtained two ways: (1) fitting the J-V data with the curved fit line and (2) fitting the modified Richardson plots with a linear fit line (slope = $-\phi_{B0}$). The ϕ_{B0} values were 0.37-0.38 and 0.11-0.12 eV for the $FTO/CuBi_2O_4$ and FTO/Cu:NiO interfaces, respectively. In addition, the FTO/Cu:NiO/FTO sample shows a drastically higher current density that is nearly linear versus voltage so it is ohmic in nature. This may be why the fit line, which was derived for Schottky barriers, strays from the experimental data between -2 and 2 V. These experimental results provides direct evidence that there is a significantly lower barrier for charge carrier transfer across the FTO/Cu:NiO interface compared to the $FTO/CuBi_2O_4$ interface. The $FTO/Cu:NiO/CuBi_2O_4/Cu:NiO/FTO$ sample also shows higher current density than the $FTO/CuBi_2O_4/FTO$ sample, which is consistent with the higher photocurrent density of the $FTO/Cu:NiO/CuBi_2O_4$ photocathode described in the sections above. However, the

combined FTO/Cu:NiO/$CuBi_2O_4$ interface could not be unambiguously modeled because it contained parallel interfaces due to the laser cutting process. Examination of the schematic in **Figure S A8d** shows that there is a FTO/Cu:NiO/$CuBi_2O_4$ interface on top of FTO and a FTO/$CuBi_2O_4$ interface on the sidewall of the FTO trench.

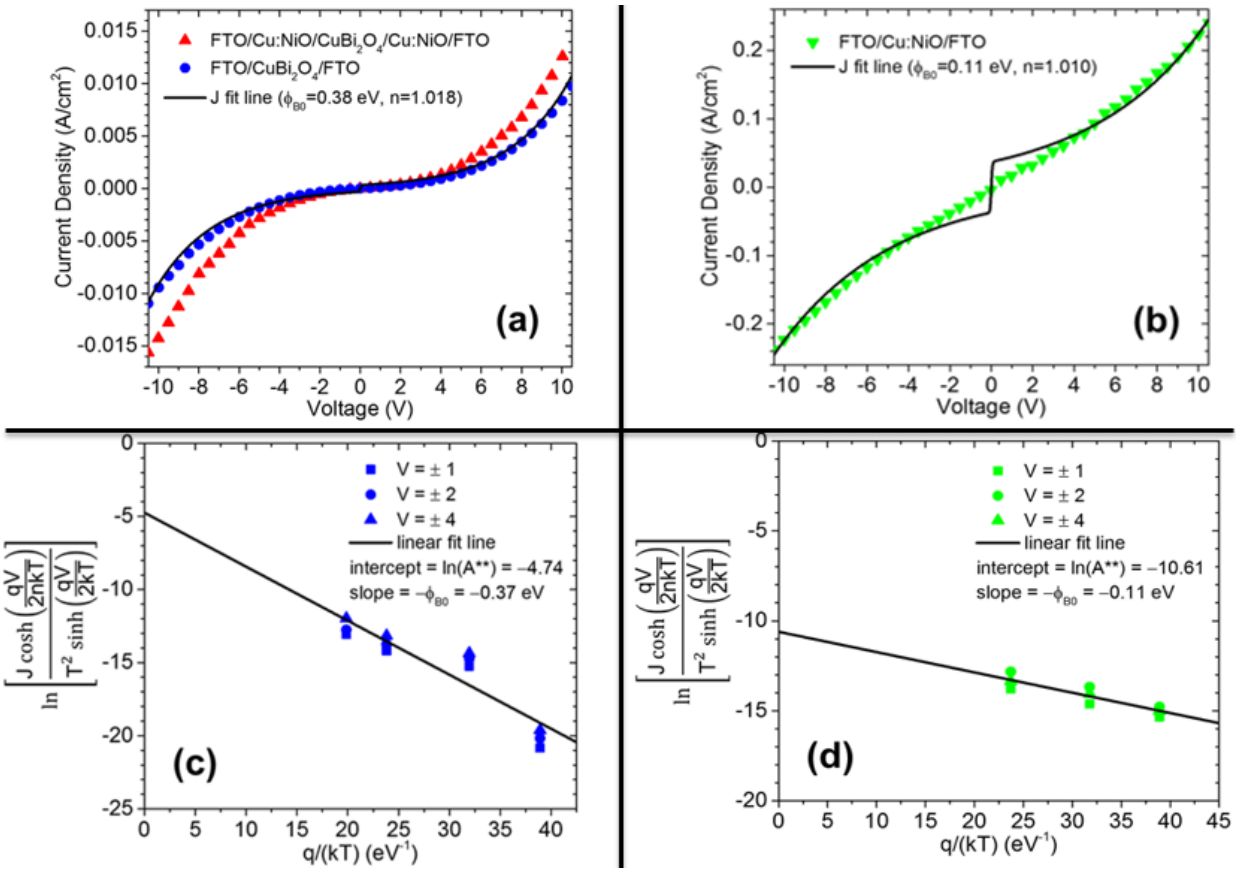

Figure 4.9. J-V curves for (a) FTO/Cu:NiO/$CuBi_2O_4$/Cu:NiO/FTO (red triangles) and FTO/$CuBi_2O_4$ /FTO (blue circles), and (b) FTO/Cu:NiO/FTO samples including J fit lines. Modified Richardson plots for (c) FTO/$CuBi_2O_4$ /FTO and (d) FTO/Cu:NiO/FTO samples with linear fit lines.

The Fermi levels of the FTO, Cu:NiO, and $CuBi_2O_4$ layers were determined using two different analytical methods (1) Mott-Schottky analysis and (2) ultraviolet photoelectron spectroscopy (UPS). **Figure 4.10a** shows the Mott–Schottky plots for a FTO/$CuBi_2O_4$ photocathode measured at three different frequencies. All three curves have similar slopes with an extrapolated x-axis intercept of about 1.12 V vs. RHE, which can be used to estimate the flatband potential (φ_{fb}). This value for φ_{fb} can then be used to estimate the Fermi level (E_F) while taking into account the potential drop across the Helmholtz layer.[140] From the slope of the Mott-Schottky plot the acceptor density (N_A) is estimated to be ~ 3.2×10^{18} cm^{-3}, which places the Fermi level within 0.077 eV of the valence band. Considering the band gap energy of ~ 1.5 eV, this places the conduction band at ~ 0.3 V vs. RHE, which is more negative than the electrochemical potential for

water reduction. As a consequence, the $CuBi_2O_4$ thin films are thermodynamically capable of photoelectrochemical water reduction, which we recently demonstrated for a forward gradient self-doped $CuBi_2O_4$ photocathode with a CdS/TiO_2 overlayer for protection against photocorrosion and Pt as a co-catalyst.[91] The Mott−Schottky plot for $CuBi_2O_4$ photocathode deposited on 7 nm Cu:NiO was also measured, as shown in **Figure S A10a**. The estimated φ_{fb} value is at about 1.17 V vs RHE, which is a little bit higher than $CuBi_2O_4$ photocathode deposited on FTO. **Figure 4.10b** shows the Mott-Schottky plot for the FTO/Cu:NiO sample with 34 nm of Cu:NiO. The x-axis intercept indicates a ϕ_{fb} value of 0.71 V vs RHE and N_A is calculated to be ~ 4.6×10^{18} cm^{-3}, which is reasonable for a degenerately doped semiconductor. **Figure S A10b** shows that the flatband potential of the bare FTO substrate is around 0.31 V vs. RHE, which closely matches the work function of FTO obtained using other analytical methods.[116-118]

Figure 4.10c shows UPS cutoff spectra of $CuBi_2O_4$ film deposited on a FTO substrate. The work function, defined as the difference between the vacuum energy level and Fermi level, can be derived from the low kinetic energy cut-offs in the secondary emission feature. The photon energy of the UV source (He I discharge) is 21.21 eV. Given that the Fermi level at the surface of $CuBi_2O_4$ film is considered independently, the work function is measured as 21.21−15.47=5.72 eV vs vacuum. Using 4.5 eV vs. vacuum as the reference value the electrochemical reduction of water (0.0 V vs. RHE) this places the work function obtained by UPS at 1.22 V vs. RHE, which is very close to the ϕ_{fb} value obtained by Mott-Schottky (**Figure 4.10a**). The photon energy of the UV source (He I discharge) is 21.21 eV. The valence band position with respect to the position of the Fermi level is determined by the linear portion of the low binding energy side of the appropriate valence band peak to the energy axis (E_F−E_V=0.25eV, see **Figure S A10c**), this is slightly larger than the value of estimated from the Mott-Schottky analysis (< 0.1 eV). This discrepancy may arise from the very small information depth (~ 0.5 nm) of UPS measurements. The corresponding value versus the vacuum energy level is 5.72+0.25= 5.97 eV. **Figure 4.10d** shows UPS cutoff spectra of Cu:NiO film deposited on FTO substrate, the work function is measured as 21.21−15.84=5.37 eV, and the valence band position is 5.37+0.36= 5.73 eV versus the vacuum energy level.[100] Mott−Schottky and UPS measurements were also performed for bare FTO substrate (see **Figure S A10d** and see **Figure S A10e**). The Mott-Schottky and UPS results for all samples are summarized in **Table SA1** in the Supporting Information. Averaging the flat band potential and work function for each material results in average E_F values of 4.71, 5.16, and 5.71 eV vs. vacuum for FTO, Cu:NiO, and $CuBi_2O_4$, respectively.

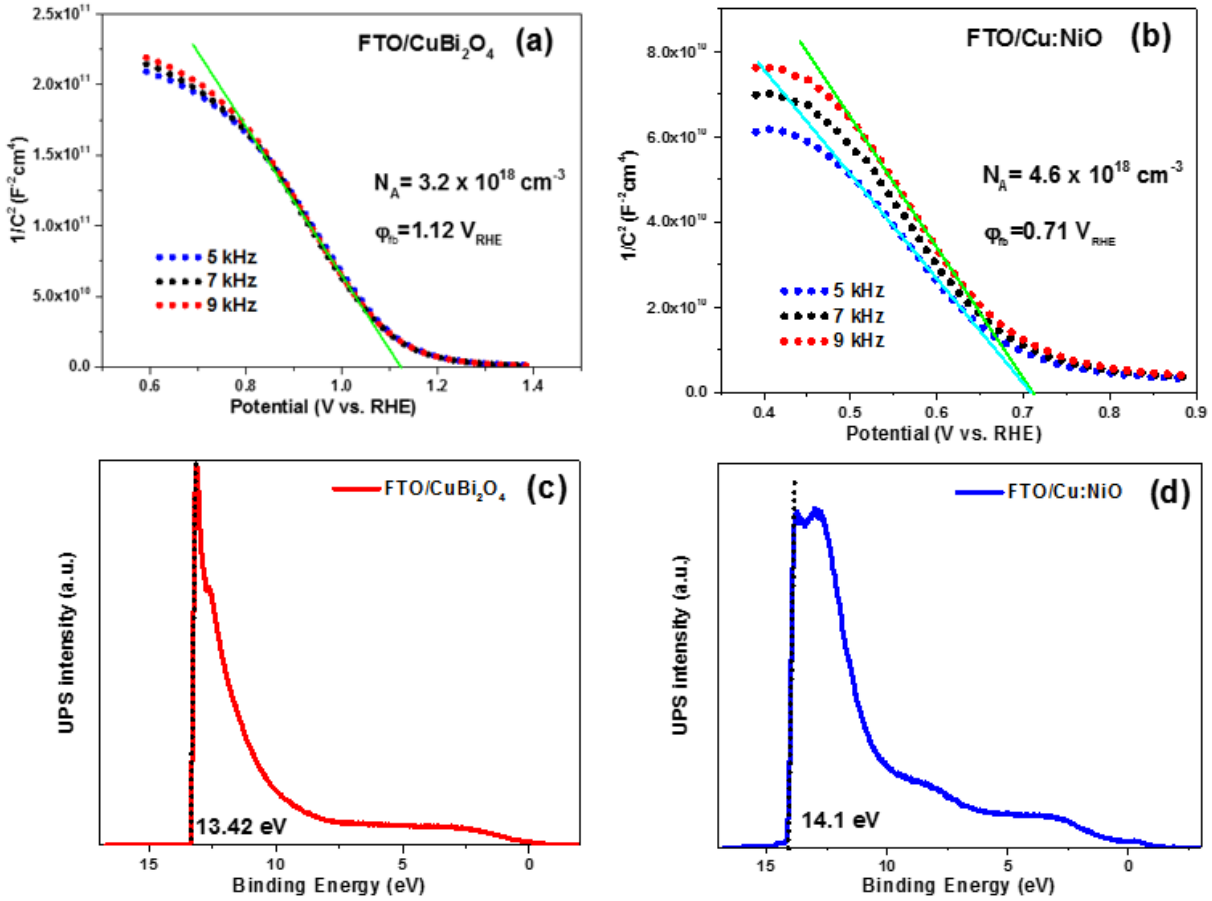

Figure. 4.10. Mott–Schottky plot for (a) ~260 nm $CuBi_2O_4$ on bare FTO, (b) 34 nm Cu:NiO on FTO. UPS cutoff spectra measured with a 2 V bias for (c) ~260 nm $CuBi_2O_4$ film on FTO and (d) 34 nm Cu:NiO film on FTO. Mott–Schottky measurements were performed in 0.3 M K_2SO_4 and 0.2 M phosphate buffer (pH 6.65) at 5 kHz, 7 kHz, and 9 kHz with a voltage modulation of 15mV.

By combining the various parameters that were experimentally determined by UV-vis, Mott-Schottky, UPS, and solid-state J-V measurements we can now construct detailed band diagrams for FTO, Cu:NiO, and $CuBi_2O_4$ as individual thin films and as layers in FTO/$CuBi_2O_4$ and FTO/Cu:NiO/$CuBi_2O_4$ photoelectrodes. **Figure 4.11a** shows the band positions of FTO, Cu:NiO, and $CuBi_2O_4$ as separated materials (without contact) in relation to the electrochemical redox potentials for water reduction (H^+/H_2) and water oxidation ($H^+,O_2/H_2O$) at 0.0 and 1.23 V vs. RHE, respectively. It shows that the $CuBi_2O_4$ conduction band (E_C) is more negative than the H^+/H_2 redox potential so that fully exited carriers are thermodynamically capable of reducing water. It also shows that Fermi levels of Cu:NiO is between that of FTO and $CuBi_2O_4$. **Figure 4.11b** shows the expected band diagram of a FTO/$CuBi_2O_4$ photocathode. Here the large mismatch in Fermi level between FTO and $CuBi_2O_4$ leads to a Schottky barrier at the FTO/$CuBi_2O_4$

interface with an effective barrier height (ϕ_{Beff}) up to 0.37-0.38 eV as confirmed by the solid-state I-V measurements. The conduction band of FTO, which is degenerately doped and n-type, is also much lower than the conduction band of $CuBi_2O_4$. These factors are most certainly increase recombination rate of photogenerated electrons and holes at the FTO/$CuBi_2O_4$ interface, especially if there are defect states in the FTO conduction band or at the surface. **Figure 4.11c** shows the expected band diagram of a FTO/Cu:NiO/$CuBi_2O_4$ photocathode. As confirmed by the solid-state I-V measurements, the FTO/Cu:NiO interface is more ohmic in nature (significantly lower ϕ_{Beff}) than the FTO/$CuBi_2O_4$ interface. As the Fermi level of Cu:NiO is closer to the work function than FTO as indicated in Figure 8a. Lastly, the conduction band of Cu:NiO is significantly higher than conduction band of $CuBi_2O_4$, so the Cu:NiO interfacial layer can in effect block photogenerated electrons from reaching the defect states in the conduction band of FTO. Rather electrons are reflected back into the $CuBi_2O_4$ resulting in a higher photoelectrochemical efficiency and photocurrent density as observed in the photoelectrochemical mesurements above. Similar electron or hole blocking layers have been used in other photoelectrochemical and photovoltaic devices including NiO as an electron blocking layer in polymer bulk-heterojunction and perovskite solar cells, p-AlGaN as an electron blocking layer for InGaN/GaN quantum well light-emitting diodes, and SnO_2 as a hole blocking layer for $BiVO_4$ photoanodes.[123, 141-144]

In summary we have shown that Cu:NiO has suitable band positions to act as a hole selective back contact layer for $CuBi_2O_4$ photocathodes. However, one challenge that remains is the relatively high resistivity of Cu:NiO compared to other commonly used transparent conducting oxide (TCO) materials like FTO. Recall that the photocurrent density of the FTO/Cu:NiO/$CuBi_2O_4$ photocathodes decreased with increasing Cu:NiO thicknesses (see **Figure S A4** in the Supporting Information). This was most likely due to increasing resistance with increasing Cu:NiO thickness. Four -point probe measurements of the FTO substrates (TEC 7) confirmed that the sheet resistance is 7.02 Ω/sq, which corresponds to resistivity of 2.8 E-6 Ωm. In contrast the 7, 34, and 102 nm Cu:NiO thin films have resistivities of 0.82, 3.3, and 8.5 Ω m as shown in **Table 3.1**, so optimization of Cu:NiO to improve its conductivity as a p-type TCO material may be beneficial.

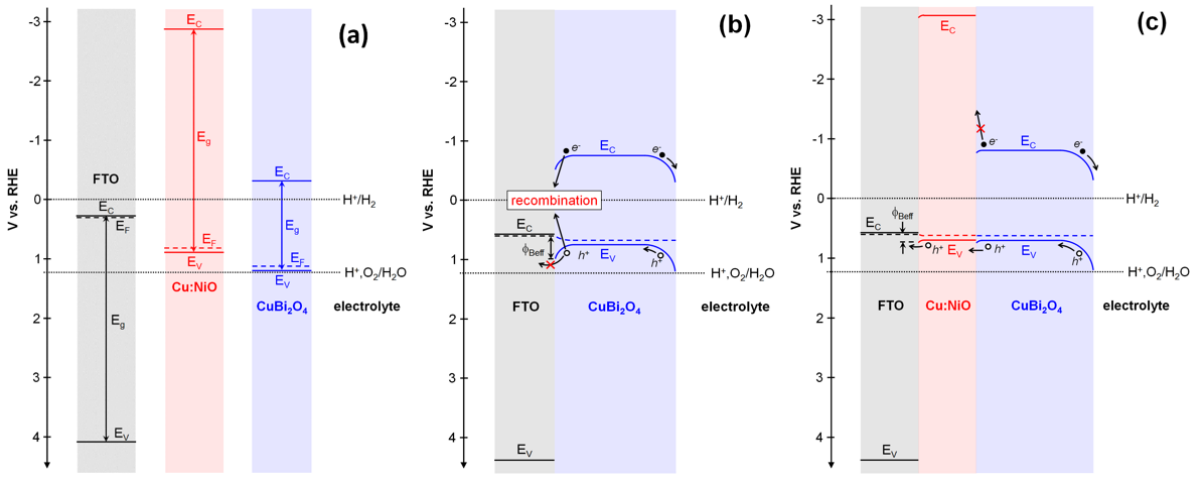

Figure. 4.11. Estimated band diagrams of FTO, Cu:NiO, and $CuBi_2O_4$ (a) as separated materials without contact, (b) in a FTO/$CuBi_2O_4$ photocathode, and (c) in a FTO/Cu:NiO/$CuBi_2O_4$ photocathode in relation to electrochemical redox potentials for water reduction (H^+/H_2) and water oxidation ($H^+,O_2/H_2O$). E_F is the Fermi level, E_C is the conduction band, E_V is the valence band, and ϕ_{Beff} is the effective barrier height

4.4 Conclusions

In this chapter, we have clearly shown that Cu doped NiO (Cu:NiO) as a back contact layer between FTO and $CuBi_2O_4$ improves the photoelectrochemical performance of FTO/Cu:NiO/$CuBi_2O_4$ photocathodes by improving the charge carrier transport across the $CuBi_2O_4$-substrate interface. Through a series of systematic investigations of the optical and semiconductor properties of FTO, Cu:NiO, and $CuBi_2O_4$ as individual thin films and layers in the FTO/Cu:NiO/$CuBi_2O_4$ device, we determined that the band positions in Cu:NiO are appropriate to reduce the barrier height at the $CuBi_2O_4$-Cu:NiO interface compared to the $CuBi_2O_4$-FTO interface while simultaneously selecting for the extraction of electrons rather than holes. As a consequence, the photocurrent density has been enhanced by 24% from 2.25 mA/cm^2 for FTO/$CuBi_2O_4$ photocathodes to 2.83 mA/cm^2 FTO/Cu:NiO/$CuBi_2O_4$ photocathodes at 0.6 V versus RHE under backside illumination with H_2O_2 as an electron scavenger. This is the highest reported photocurrent density to date for a $CuBi_2O_4$ based photocathode.

Chapter 5. Evaluation of β-$Cu_2V_2O_7$ as a photoanode material for photoelectrochemical water oxidation

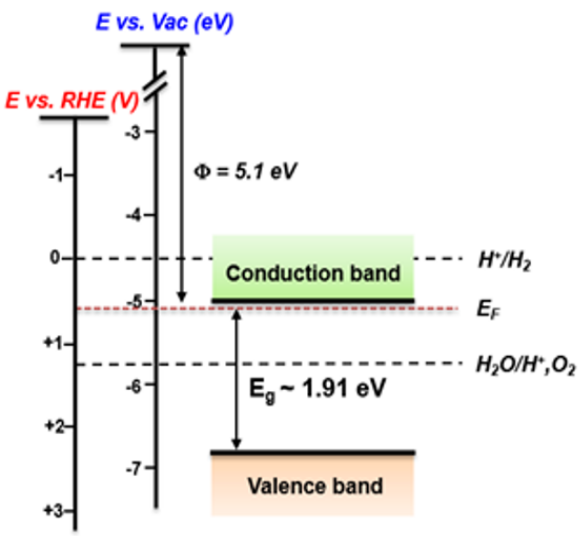

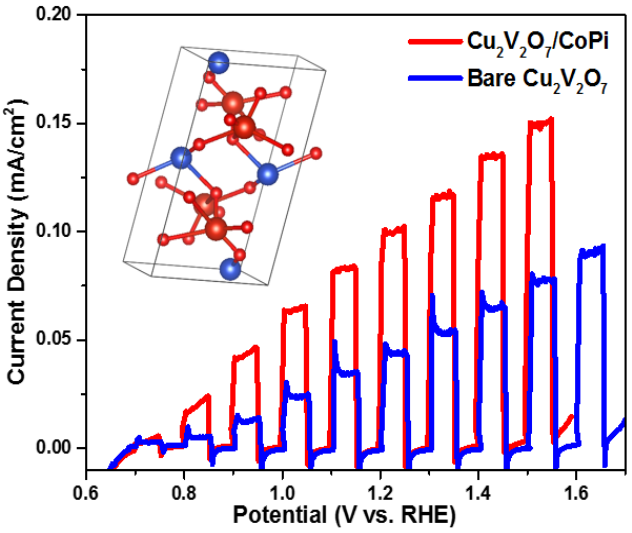

In this chapter, monoclinic copper vanadate (n-type β-$Cu_2V_2O_7$) thin films were prepared for the first time by spray pyrolysis and evaluated as a potential photoanode material for solar water oxidation. The deposition parameters were optimized to obtain phase pure photoanodes of β-$Cu_2V_2O_7$. β-$Cu_2V_2O_7$ has a bandgap energy of ~2.0 eV, which corresponds to a theoretical solar-to-hydrogen (STH) efficiency of 16%, that makes it a promising candidate for the top absorber in a tandem photoelectrochemical (PEC) device. However, β-$Cu_2V_2O_7$ photoanodes have not yet demonstrated high photoconversion efficiencies, and the factors that limit the efficiency have not yet been fully identified. In this work, the key physical and photoelectrochemical properties of this promising material, such as optical band gap, doping type, flat-band potential, band positions, charge carrier dynamics, and chemical stability are established. The photoelectrochemical performance of β-$Cu_2V_2O_7$ photoanodes was found to be strongly limited by poor charge carrier separation efficiency. Time-resolved microwave conductivity (TRMC) measurements revealed that the low mobility (~3.5×10^{-3} cm^2 V^{-1} s^{-1}) and short hole diffusion length (~28 nm) are the main reason for its fast recombination. In addition, cobalt phosphate (Co-P_i) was used as a water oxidation co-catalyst to overcome the slow water oxidation kinetics.

Keywords: solar water splitting; photoelectrochemical; $Cu_2V_2O_7$ photoanode; charge carrier transport; OER catalyst

5.1 Introduction

A number of complex metal oxide phases can exist within the CuO-V_2O_5 system. It is known that by variation of the Cu to V ratio in the $Cu_xV_{1-x}O_z$ system a number of temperature dependent stoichiometric phases and polytypes can exist.[145, 146] Of these, the high temperature orthorhombic α-$Cu_2V_2O_7$ (Blossite) and low temperature monoclinic β-$Cu_2V_2O_7$ (Ziesite) polymorphs have been identified as potential photoanode materials.[147-149] Both polymorphs are n-type metal oxide semiconductors, which have been reported to have suitable indirect and direct optical band gaps in the range of 1.8 – 2.1 eV and large absorption coefficient (up to $\alpha \approx 10^4$ cm^{-1}), allowing for the utilization of a significant portion of the solar spectrum for the generation of photocurrent.[63, 150-153] With a band gap close to 2.0 eV, a maximum theoretical photocurrent density of ~15 mA cm^{-2} is achievable under AM1.5 illumination, assuming all photons with energies higher than the bandgap are absorbed and utilized with 100% efficiency.[64, 154] However, the experimental solar photo current densities reported so far for the α-$Cu_2V_2O_7$ (Blossite) and β-$Cu_2V_2O_7$ (Ziesite) polymorphs have been well below this theoretical limit. Furthermore, an incomplete understanding of limitations for this material system remains.

In this work, a straightforward spray pyrolysis procedure is developed for the deposition of the low temperature β-$Cu_2V_2O_7$ (Ziesite) polymorph. Using this procedure, thin films of β-$Cu_2V_2O_7$ have been deposited on FTO-coated glass (F-doped SnO_2) and quartz substrates. Subsequently, the quintessential properties relevant to PEC water oxidation such as optical absorption, band positions, carrier dynamics and chemical stability are reported. On the

basis of these findings, an initial realistic evaluation of the suitability of $Cu_2V_2O_7$ as a photoanode material for solar water splitting is provided. In addition, these studies are a first step in identifying the features that limit the performance of β-$Cu_2V_2O_7$ as a photoanode.

5.2 Results and discussion

5.2.1 Structural and morphology characterization

XRD, Raman spectroscopy, SEM, and energy-dispersive X-ray (EDX) measurements were used to gain information on the structure, chemical composition, and morphology of deposited films. **Figure 5.1a** shows the XRD pattern for a $Cu_2V_2O_7$ photoanode synthesized by spray pyrolysis on a fluorine-doped tin oxide (FTO) coated glass substrate at 300°C, followed by annealing in air at 500 °C. The X-ray diffractogram for the prepared film matches very well with the reference pattern for the mineral Ziesite, β-$Cu_2V_2O_7$. This phase has been reported to have a monoclinic crystal structure with the space group *C*2/*c*, unit cell parameters *a* = 7.685, *b* = 8.007, *c* = 10.09 Å and β = 110.27°.[155-158] There was no secondary phase detected for films with various thicknesses (from 50 to 400 nm), (see **Figure S B1**). The structure of the β-$Cu_2V_2O_7$ films was also measured with Raman spectroscopy, the data are shown in **Figure 5.1b**. The Raman peaks observed at 392, 846.6, and 914 cm^{-1} can be attributed to the vibrations of the bonds in β-$Cu_2V_2O_7$.[150, 159, 160] The peak centered at 914 cm^{-1} is the characteristic band assigned to the VO_3 stretching mode.[161] No peaks corresponding to the V_2O_5 and CuO phase was detected, which confirms the phase purity of our β-$Cu_2V_2O_7$ films.

The β-$Cu_2V_2O_7$ photoanodes were inspected visually by eye and under magnification using a scanning electron microscope (SEM). A photograph of a thin film β-$Cu_2V_2O_7$ photoelectrode deposited at 300°C on an FTO-coated glass substrate is shown in **Figure B2**. The film has a dark brown color, indicating good visible light absorption. The as-deposited films consist of grains with ill-defined shapes and with some degree of surface roughness as shown in **Figure S B3**. **Figure 5.1c** shows the morphology of the $Cu_2V_2O_7$ film after annealing at 500°C. We can see that the grains exhibit well defined edges, and have a relatively broad size distribution (50 – 400 nm). The cross-sectional SEM images were used to estimate the thickness of the $Cu_2V_2O_7$ films for different spray precursor volume conditions. The thickness of the films prepared using 200 mL precursor solution is found to be ∼ 200 nm as shown in **Figure 5.1d**. We also obtained thickness values of ∼ 100 nm and ∼ 300 nm (**Figure S B4**) from the samples sprayed with 100 mL and 300 mL of the precursor, which indicates a linear relationship between the sprayed precursor volume and the film thickness.

The chemical composition of the annealed films was analysed by energy-dispersive X-ray (EDX) mapping of a representative film area. The relevant SEM images with EDX mapping overlays are shown in **Figure S B5**. The EDX signals from Cu, V, and O appear to be homogeneously distributed over the entire film area. The average atom

ratio of Cu to V is about 1 to 1 (23.5 at. % Cu and 23.6 at. % V), which is expected from the phased-pure β-$Cu_2V_2O_7$ phase indicated by XRD.

The surface roughness of the β-$Cu_2V_2O_7$ photoanodes were also measured using atomic force microscopy (AFM) as shown in **Figure S B6**. AFM reveals that the root mean squared (RMS) roughness and the fractional increase in surface area of β-$Cu_2V_2O_7$ films deposited directly on FTO are 50 nm and 3.2%, respectively.

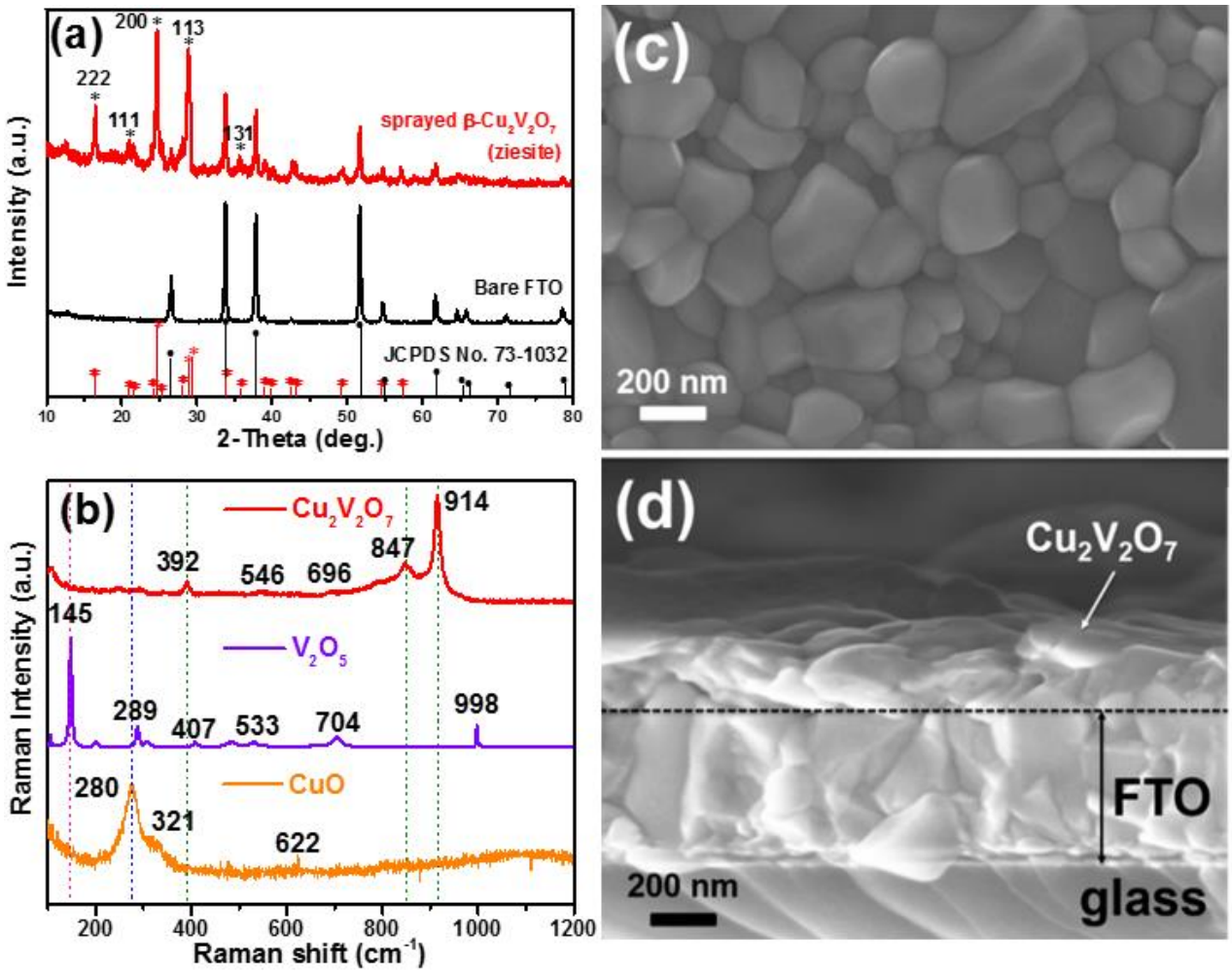

Figure 5.1. (a) XRD diffractograms for a bare FTO substrate and a $Cu_2V_2O_7$ photoanode synthesized by spray pyrolysis onto an FTO substrate. The red lines at the bottom represent the reference pattern for $Cu_2V_2O_7$ (PDF no. 73-1032) and black lines represent the reference pattern for SnO_2 (PDF no. 00-046-1088) with line lengths proportional to the expected peak intensities for randomly-oriented crystallites. (b) Raman spectrum of $Cu_2V_2O_7$ film fabricated by spray pyrolysis. (c) SEM image of the $Cu_2V_2O_7$ film deposited on FTO after annealing at 500°C for 2 hours in air. (d) cross-sectional view.

5.2.2 Optical absorption properties

The optical properties of the $Cu_2V_2O_7$ thin films synthesized by spray pyrolysis were investigated with UV−vis spectroscopy. The transflectance of these fims , which is the sum of the transmittance and the reflectance, was measured inside an integrating sphere to determine the true absorptance (absorptance = 1 − transflectance). **Figure 5.2a** shows the absorptance spectra of 200 nm $Cu_2V_2O_7$ thin film deposited on quartz as a function of wavelength (absorptance spectra for other thicknesses are shown in **Figure S B7**). The absorption edge is located at about 650 nm. The absorption coefficient (α) of the films can be calculated by using the following equation:

$$\alpha = (-\ln(1 - A))/d \tag{5.1}$$

Where A is the absorptance at a single wavelength and *d* is the film thickness. **Figure 5.2b** shows absorption coefficient as a function of photon energy (wavelength), which was calculated from the 200 nm film. At 450 nm the absorption coefficient for the film is 4.06×10^4 cm^{-1}, which corresponds to a light penetration depth of α^{-1} = 246 nm. In other words, a $Cu_2V_2O_7$ film thickness of 566 nm (2.3 α^{-1}) is required to absorb 90% of the incident light having a wavelength of 450 nm.

To extract the bandgap of $Cu_2V_2O_7$, Tauc plots are calculated based on the absorption coefficient spectrum and shown in **Figure 5.2c**. However, neither the direct nor indirect Tauc plot shows a steep, linear section that would allow for extrapolation to a bandgap value. One possible reason for this is the occurrence of localized Cu–Cu transitions between occupied and empty 3d states, which may partially obscure the valence-to-conduction band transitions.[162] Another possible reason is the surface roughness of the films (**Figure S B6**); the optical scattering may reduce the quality of the Tauc plots, even when the absorption spectra are recorded in an integrating sphere. Nevertheless, a rough estimate for the indirect and direct bandgaps for the $Cu_2V_2O_7$ thin film can be made, yielding values of 1.91 and 2.05 eV, respectively. An absorption onset of 650 nm is observed from **Figure 5.2a**, which places the bandgap of $Cu_2V_2O_7$ synthesized by spray pyrolysis in the range of 1.9 – 2.1 eV. This is consistent with previously reported values.[145, 162] However, even at photon energy below 1.9 eV the absorption is ~ 10 % (α = ~5 x 10^3 cm^{-1}) which increases at lower photon energies, indicating a significant band tailing and a large concentration of free charge carriers.

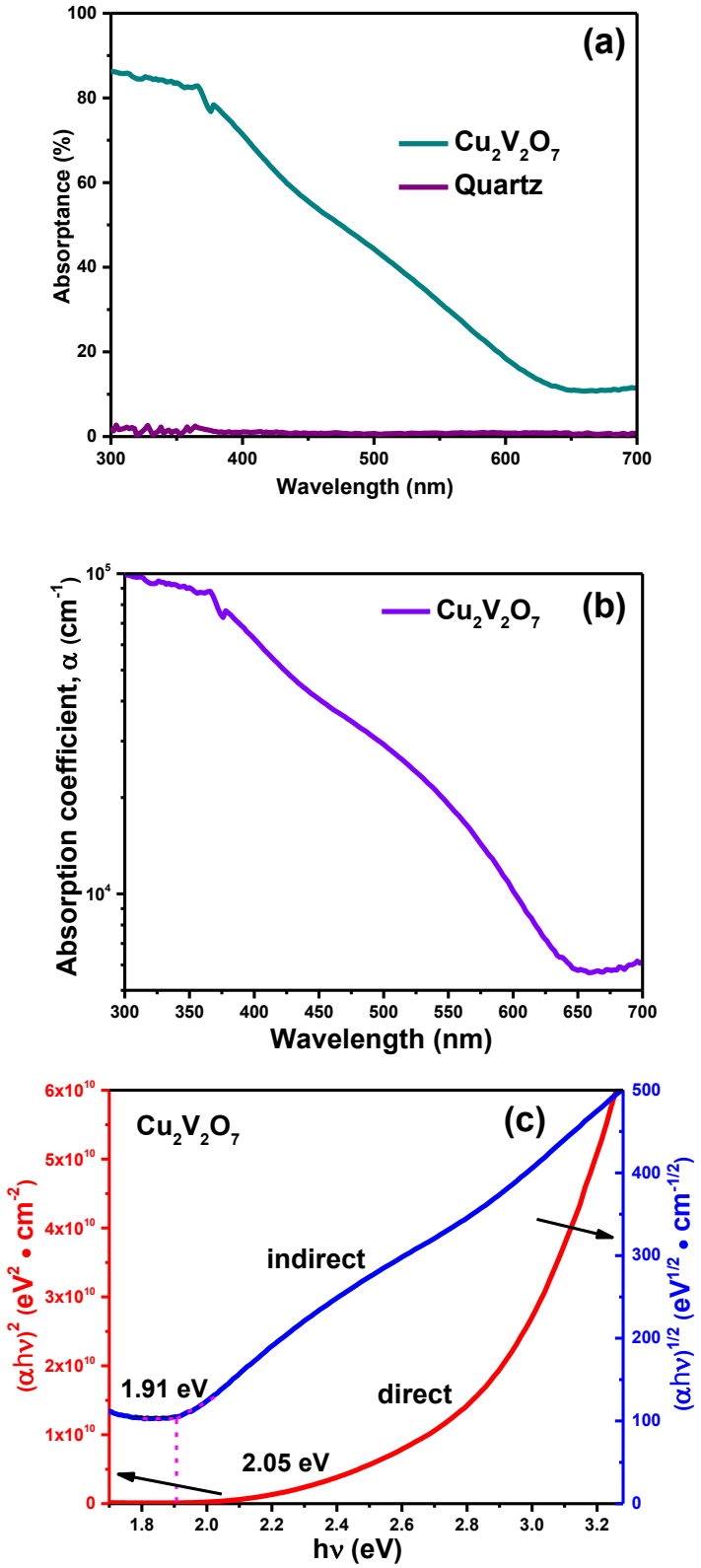

Figure 5.2. (a) Absorptance spectra for $Cu_2V_2O_7$ film deposited on quartz substrate with estimated thicknesses of 200 nm as determined by SEM cross section (b) absorption coefficient for $Cu_2V_2O_7$ film, plotted as a function of

wavelength (c) Tauc plot for bandgap analysis of the $Cu_2V_2O_7$ film. Indirect and direct bandgaps are estimated from the intercept of the $(\alpha h\nu)^{0.5}$ and $(\alpha h\nu)^2$ curves with the x-axis, respectively.

5.2.3 Charge carrier mobility and lifetime

Since the charge carrier transport in the bulk material plays a crucial role in the PEC process, time-resolved microwave conductivity (TRMC) measurements were performed to investigate the charge transport dynamics of $Cu_2V_2O_7$. In TRMC measurements, the combined carrier (electron and hole) mobility of the semiconductor is at least as high as the peak in the measured signal ($(\phi\Sigma\mu)_{max}$), and the carrier lifetime can be extracted from the exponential decay of the signal after the peak.[38, 57, 58, 163] **Figure 5.3a** shows the TRMC signal for a 200 nm $Cu_2V_2O_7$ film that was synthesized by spray pyrolysis on a quartz substrate. The excitation wavelength is 450 nm and the measurements were done for various incident laser pulse intensities. A mobility between 3.4×10^{-3} and 4.1×10^{-3} $cm^2\ V^{-1}\ s^{-1}$ was obtained for laser pulse intensities between 5.4×10^{14} and 9.5×10^{14} photons cm^{-2}. We also performed TRMC measurements on $Cu_2V_2O_7$ films deposited on quartz substrates at other wavelengths (405 nm and 550 nm) under various incident laser pulse intensities as shown in **Figure S B8a** and **Figure S B8b**. The mobility values for the $Cu_2V_2O_7$ film measured at various wavelengths were all of the same order of magnitude, ranging from 3.0×10^{-3} to 4.7×10^{-3} $cm^2\ V^{-1}\ s^{-1}$.

Figure 5.3b shows the maximum TRMC signal $(\phi\Sigma\mu)_{max}$ versus incident laser pulse intensity for $Cu_2V_2O_7$ films deposited on quartz substrates under 3 different laser wavelengths. The mobility $(\phi\Sigma\mu)_{max}$ decreases gradually with increasing the light intensities, which is due to nongeminate higher order electron−hole recombination.[58] The effective lifetime of the charge carriers in the $Cu_2V_2O_7$ film can be defined as the time that it takes for the signal to decrease by 50% of its starting value. Using this definition, an average value of (80 ± 5) ns is found for our $Cu_2V_2O_7$ films. Based on these lifetimes and mobilities, the charge carrier diffusion length can be calculated, which is a key parameter in determining the PEC performance of a semiconductor. A value of (28 ± 0.5) nm is found for our $Cu_2V_2O_7$ films. To the best of our knowledge this is the first report of charge carrier lifetime and diffusion lengths for $Cu_2V_2O_7$ thin films. Like for many other metal oxides, the carrier diffusion length of $Cu_2V_2O_7$ is relatively short, much shorter than the light penetration depth, α^{-1}. This means that most electron−hole pairs in bulk $Cu_2V_2O_7$ films will recombine before reaching the semiconductor/electrolyte interface, resulting in modest charge carrier separation efficiencies. We will discuss strategies to overcome this limitation in the following sections.

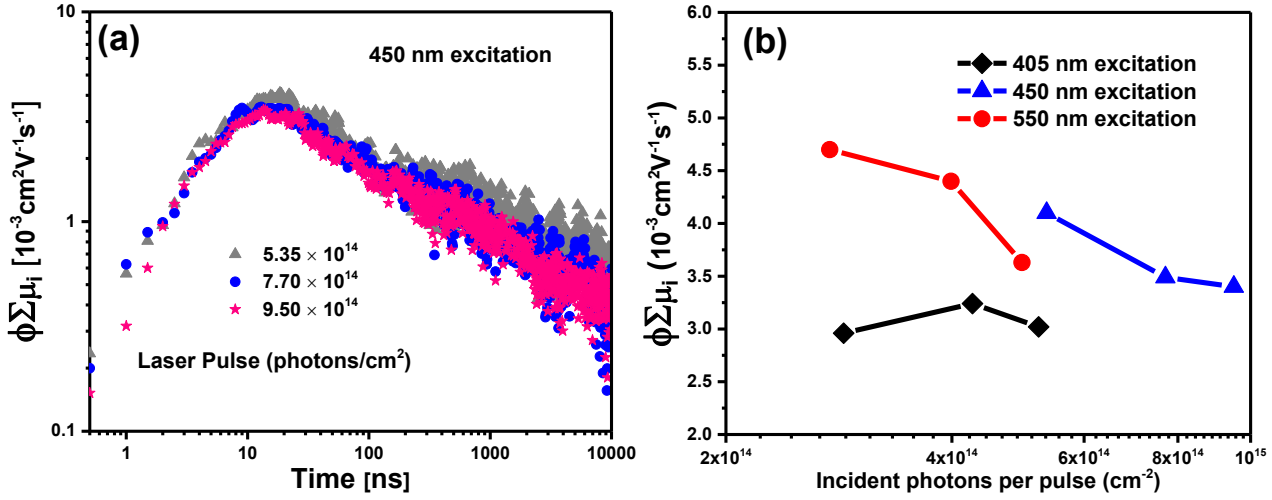

Figure 5.3. (a) TMRC signal under various incident laser pulse intensities for a $Cu_2V_2O_7$ film synthesized by spray pyrolysis on a quartz substrate at 450 nm wavelength. (b) Maximum TRMC signal $(\phi\Sigma\mu)max$ vs incident laser pulse intensity for $Cu_2V_2O_7$ films deposited on quartz substrates under 3 different laser wavelength.

5.2.4 Photoelectrochemical properties

In order to investigate the photoelectrochemical activity of the sprayed $Cu_2V_2O_7$ films, chopped linear sweep voltammetry (LSV) measurements were conducted under simulated AM1.5 illumination (**Figure 5.4a**). For the water oxidation experiments, argon bubbling was used to remove dissolved O_2. The current–voltage (J–V) curves show moderate photocurrents, but a relatively positive onset potential of ~0.65 V vs. RHE. Photoelectrochemical measurements were performed systematically by varying the thicknesses of the thin film (50 – 400 nm) in order to optimize the performance of $Cu_2V_2O_7$ photoanodes as shown in **Figure S B10b**. The optimum photocurrent was ~ 0.05 mA/cm^2 at 1.23 V versus RHE for a 200 nm bare $Cu_2V_2O_7$ photoanode measured with argon bubbling. Furthermore, after depositing a CoP_i catalyst layer on top of the $Cu_2V_2O_7$ photoanodes, we observe higher photocurrent densities than for the bare $Cu_2V_2O_7$ photoanode. The Co-P_i catalyst was electrodeposited (in the dark) on $Cu_2V_2O_7$ photoanodes at 0.9 V versus Ag/AgCl for 30 s (see **Figure S B9a**) in an electrochemical cell using a three-electrode configuration. The electrolyte consisted of 0.5 mM of $Co(NO_3)_2.6H_2O$ in 0.3 M K_2SO_4 and 0.2 M phosphate buffer (pH 6.8). [74, 164] Three linear sweep voltammetry (LSV) cycles were performed in order to activate the CoP_i-modified $Cu_2V_2O_7$ photoanodes as shown in **Figure S B9b**. The photocurrent for 200 nm $Cu_2V_2O_7/CoP_i$ is ~0.1 mA/cm^2 at 1.23 V versus RHE, which is two times higher than that from the electrode without catalyst. This is one of the highest photocurrent densities reported for a pure $Cu_2V_2O_7$ photoelectrode.[63, 150] The improvement due to CoP_i was consistent for both frontside and backside illumination (see **Figure S B10a**) and held for a range of $Cu_2V_2O_7$ film thicknesses between 50 and 400 nm as shown in the inset of **Figure 5.4a** (see **Figure S B10c** for the individual LSV scans for different $Cu_2V_2O_7$ film thicknesses).

The quantum efficiency of $Cu_2V_2O_7$ photoanodes was determined by measuring the incident photon-to-current conversion efficiency (IPCE, also called external quantum efficiency, EQE) and the absorbed photon-to-current efficiency (APCE). **Figure S B11** shows power spectra for front illumination IPCE measurements. **Figure 5.4b** shows IPCE spectra of the $Cu_2V_2O_7$ films measured at 1.23 V versus RHE without and with CoP_i catalyst. Consistent with the J–V curve analysis, the photoanode with CoP_i catalyst possesses a higher IPCE value than the electrode without catalyst for all wavelength. The 650 nm wavelength corresponds to a photon energy of 1.91 eV, which matches the indirect band gap of $Cu_2V_2O_7$ (**Figure 5.4c**). However, the IPCE values are still very low, we achieve only ~2.9% and ~1.2% at 1.23 V vs RHE at a wavelength of 350 nm for the $Cu_2V_2O_7$ photoanodes with and without CoP_i catalyst, respectively. The IPCE values under backside illumination are even lower at 0.9% and 0.4%, respectively (**Figure S B10d**).

The IPCE values can also be used to calculate the predicted AM1.5 photocurrent density ($J_{AM1.5}$) according to equation (3.5) in the Experimental section. For frontside illumination the $J_{AM1.5}$ values are 0.097 mA/cm^2 and 0.041 mA/cm^2 at 1.23 V_{RHE} for the $Cu_2V_2O_7$ photoanodes measured with or without CoP_i catalyst, respectively, which are very close to the values of 0.1 mA/cm^2 and 0.05 mA/cm^2 obtained for the chopped LSV measurements under AM1.5 solar simulation (see **Figure S B10f**).

Figure S B12a and **Figure S B12b** shows the APCE spectra for $Cu_2V_2O_7$ photoanodes measured with Ar bubbling and with CoP_i catalyst at 1.23 V vs RHE under front and back illumination. $Cu_2V_2O_7$ photoanodes with CoP_i catalyst exhibits a significantly higher APCE value than that without catalyst for all wavelengths under both front and back illumination. The APCE values were calculated using the IPCE data in **Figure 5.4b**, **Figure S B10d** and the absorptance spectra shown in **Figure S B7**. We assumed the injection efficiency is 100%, and, therefore, the APCE represents the charge separation efficiency. The APCE values are 3.5% and 1.4% at 350 nm for the $Cu_2V_2O_7$ photoanodes measured with CoP_i catalyst and with Ar bubbling, respectively. Thus, the CoP_i catalyst indeed improves the charge separation efficiency for the $Cu_2V_2O_7$ photoanodes. Nevertheless, the charge separation efficiency are still relatively low due to the poor carrier transport properties (low mobility, short lifetime and diffusion length) as we discussed above.

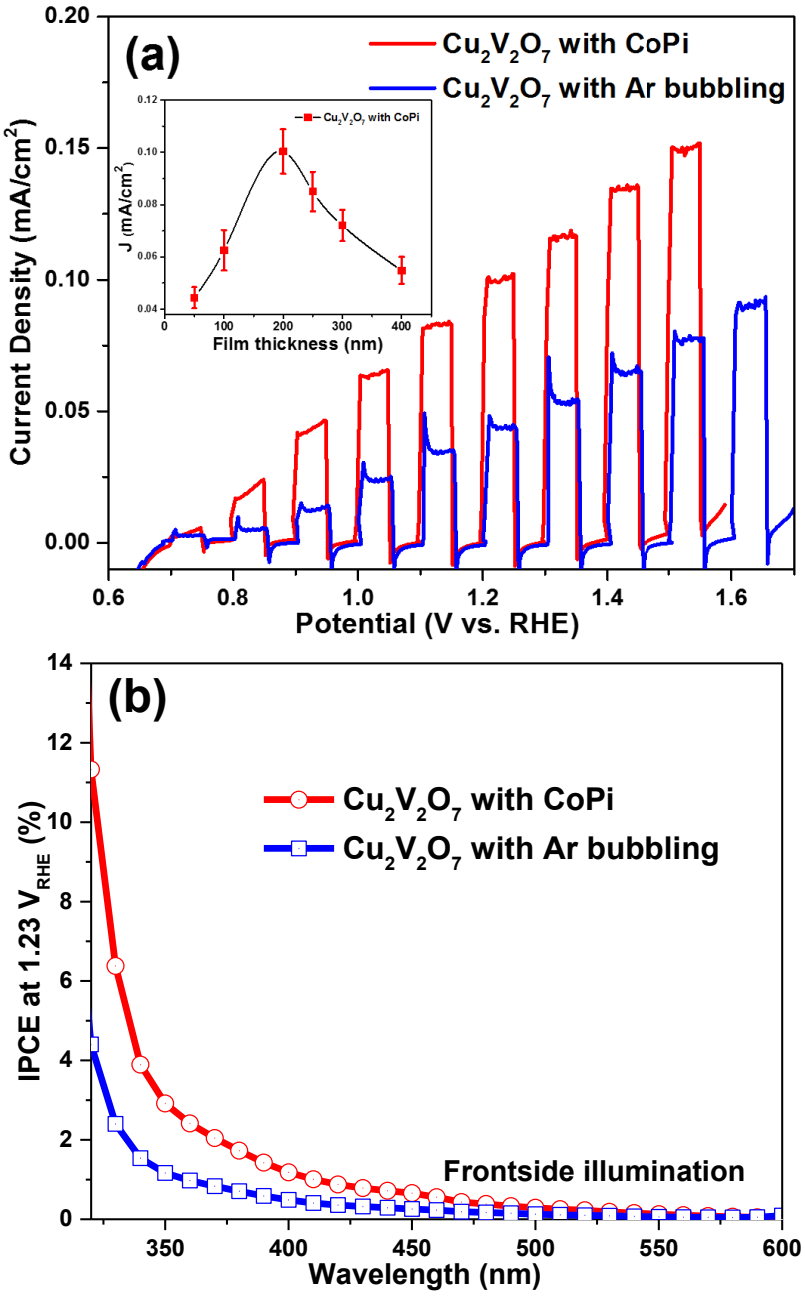

Figure 5.4. (a) Chopped LSV scans for $Cu_2V_2O_7$ photoanodes with Ar bubbling (blue line) and with CoPi catalyst (red line) synthesized to a thickness of ~200 nm on FTO substrate. Inset shows the average photocurrent densities (at least 3 samples) at 1.23 V vs RHE extracted from LSV scans for photoanodes with CoPi catalyst at different thicknesses (see **Figure S B10** for LSV scans). (b) IPCE spectra of $Cu_2V_2O_7$ on FTO with Ar bubbling (blue dot line) and with CoPi catalyst (red dot line) in 0.3 M K_2SO_4 and 0.2 M phosphate buffer (pH 6.8) at a potential of 1.23 V vs. RHE. All measurements were performed under frontside illumination.

Electrical impedance spectroscopy (EIS) was performed in the dark near the flat band potential before Mott–Schottky measurement (see **Figure S B13**). Note that above 100 Hz, the real part of the impedance is constant, whereas the imaginary part has a slope of -1. This implies that the system behaves as a resistance in series with a pure capacitance, which is a prerequisite for Mott-Schottky analysis.

Figure 5.5 shows a Mott–Schottky plot for a 200 nm $Cu_2V_2O_7$ photoanode measured at different frequencies. The extrapolated x-axis intercepts can be used to estimate the flat-band potential (ϕ_{fb}) at about 0.61 ± 0.03 V vs. RHE, which is in excellent agreement with the photocurrent onset potential of the film (~0.68 V vs. RHE). Using the slopes in the Mott–Schottky plot, the donor density (N_D) is estimated to be about 6×10^{18} cm^{-3}, which is reasonable for a metal oxide semiconductor[165]. The space charge width (W) can be estimated to be about 70 nm at 1.23 V vs RHE using Eq. (2.5) in the Experimental Section. An open-circuit potential (OCP) measurement under chopped AM1.5 illumination reveals that the films show n-type conductivity, i.e., the OCP shifts to a more negative value upon illumination due to band flattening, as shown in **Figure S B14**.

One distinct feature of the IPCE is that at lower wavelengths the photon to charge efficiency is much higher and increases sharply, this has been observed in previous reports of β-$Cu_2V_2O_7$ and often the case for copper based metal oxide photo-electrodes with indirect band gaps.[63] For planar films as is the case in this study there is a trade-off between light absorption and charge collection. These issues are often resolved through engineering nano-structured photoelectrodes in order to maximize light trapping. As we can see from the UV-Vis of these $Cu_2V_2O_7$ optical absorption close to the band gap is too low to obtain efficient planar devices. Photons in the wavelength range of 600 to 450 nm with energies corresponding to indirect transitions in $Cu_2V_2O_7$ can only generate charge carriers deep within the films, far away from the space charge region (W_{sc}) at the photo-anode electrolyte interface.

To explain the shape of the IPCE spectra and the differences in the profile of the IPCE measurements for back- and front-side illumination we adopted the assumptions from the Gärtner model, that there is complete charge separation within the space charge region (W_{sc}), which is calculated to be 70 nm at 1.23 V vs RHE. Furthermore, charges generated in the bulk, within a distance L_D (= 28 nm) from the edge of the space charge region are also expected to contribute to the photocurrent. Using the absorption coefficient at different wavelengths it is possible to determine the number of photons absorbed within the space charge region and diffusion length region of the 200 nm thick $Cu_2V_2O_7$ thin films for either back- or front-side illumination (see **Figure S B14a**). The profile does not directly correspond to what is measured in the IPCE which show a much sharper increase at high energy wavelength for back- and front-side illumination of the $Cu_2V_2O_7$ samples.

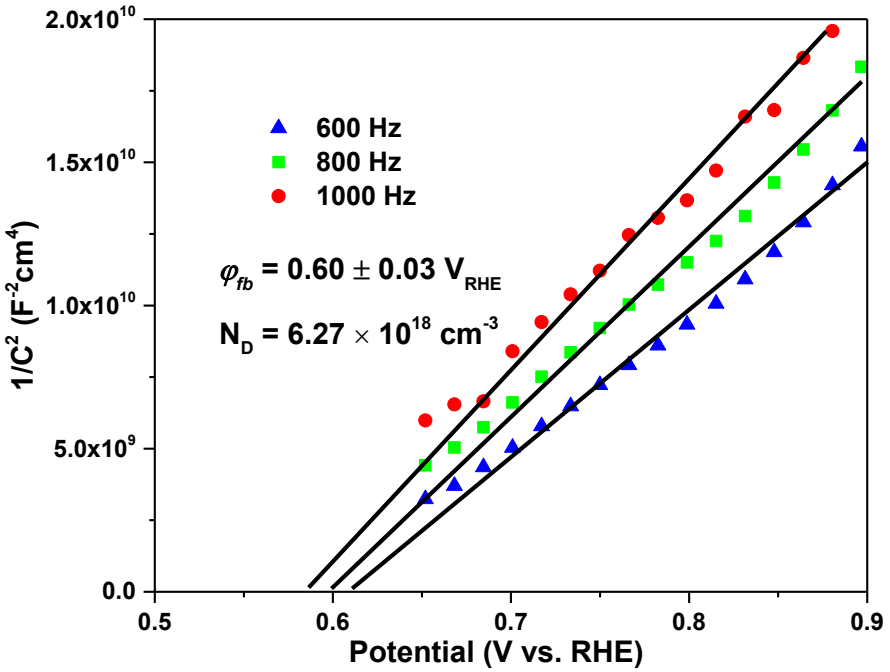

Figure 5.5. Mott–Schottky plot for a 200 nm $Cu_2V_2O_7$ on bare FTO. Mott–Schottky measurements were performed in 0.3 M K_2SO_4 and 0.2 M phosphate buffer (pH 6.8) at different frequency with a voltage modulation of 15mV.

5.2.5 Chemical composition

In order to determine the chemical and electronic structures of the $Cu_2V_2O_7$ films, XPS and UPS were performed for a 200 nm $Cu_2V_2O_7$ film. For data analysis the 1s peak of adventitious carbon at 284.8 eV was used as a reference for the other peak positions (see **Figure S B16**). No other elements or contaminants (except adventitious carbon) were detected in the survey spectrum (see **Figure S B17a**). **Figure 5.6a** shows the Cu $2p_{1/2}$ and Cu $2p_{3/2}$ peaks located at 954.1 and 933.7 eV, respectively, which can be attributed to the Cu^{2+} multiplets, indicating that Cu exhibits a valence state of 2+ in $Cu_2V_2O_7$.[166] The main peak is accompanied by two strong satellites at about 9 eV higher binding energies, which is also consistent with a Cu oxidation state of 2+.[167] The core level spectra of V 2p and O 1s are displayed in **Figure 5.6b**. The peaks for V $2p_{3/2}$ (516.7 eV) and V $2p_{1/2}$ (524.3 eV) can be indexed to V^{5+} and the results match well with those reported in the literature.[163, 168] The main O 1s peak occurs at 530.1 eV and is attributed to lattice oxygen. The minor peak at the highest energy of 531.5 eV corresponds to surface adsorbed hydroxyl species, OH. We also performed XPS on an area of the photocathode that was PEC tested to examine elemental changes during water oxidation. The XPS spectra for the survey spectrum, Cu 2p, O 1s, V 2p, and C 1s regions for PEC tested samples are shown in **Figure S B18a**, **b**, **c** and **d**, respectively. Since there was no big difference in XPS spectra for the pristine and PEC tested samples, the PEC experiments do not seem to lead to any chemical changes at the surface of the material.

Figure 5.6c shows the UPS spectrum of a $Cu_2V_2O_7$ film measured with a 2 V bias. The work function, defined as the difference between the vacuum energy level and Fermi level, can be derived from the low kinetic energy cut-off in the secondary emission feature (Eq. 3.2). The photon energy of the UV source (He I discharge) is 21.21 eV. Given that the Fermi level at the surface of $Cu_2V_2O_7$ film is considered independently, the work function is determined to be 21.21 – 2 – 14.1 = 5.11 eV. Using 4.5 eV vs. vacuum as the reference value for the electrochemical reduction of water (0.0 V vs. RHE) this places the work function obtained by UPS at 0.61 V vs. RHE, which is close to the ϕ_{fb} value of 0.65 V vs. RHE obtained by the Mott-Schottky analysis. The valence band maximum (VBM) position of 1.82 eV below E_F is determined by the linear extrapolation of the UPS spectrum at the low binding energy side to the binding energy axis (see **Figure S B17b**). Our measured band positions are in a good agreement with the values reported previously.[63]

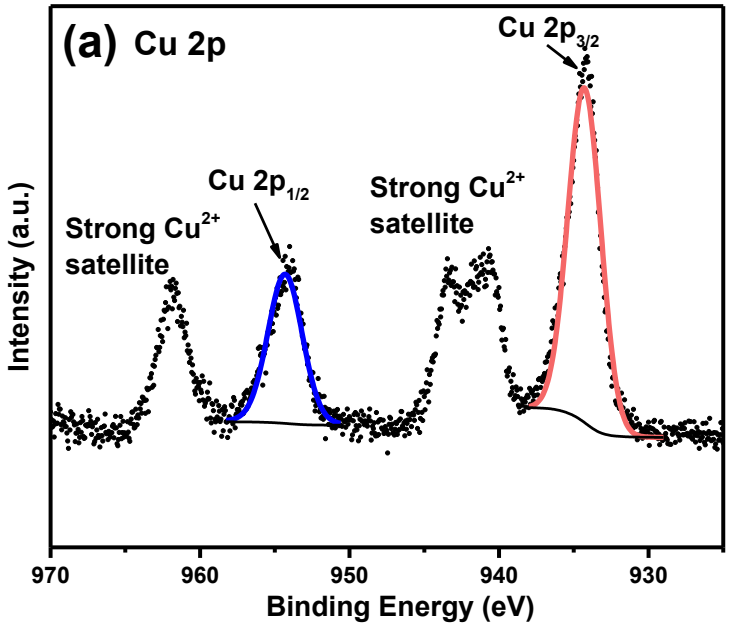

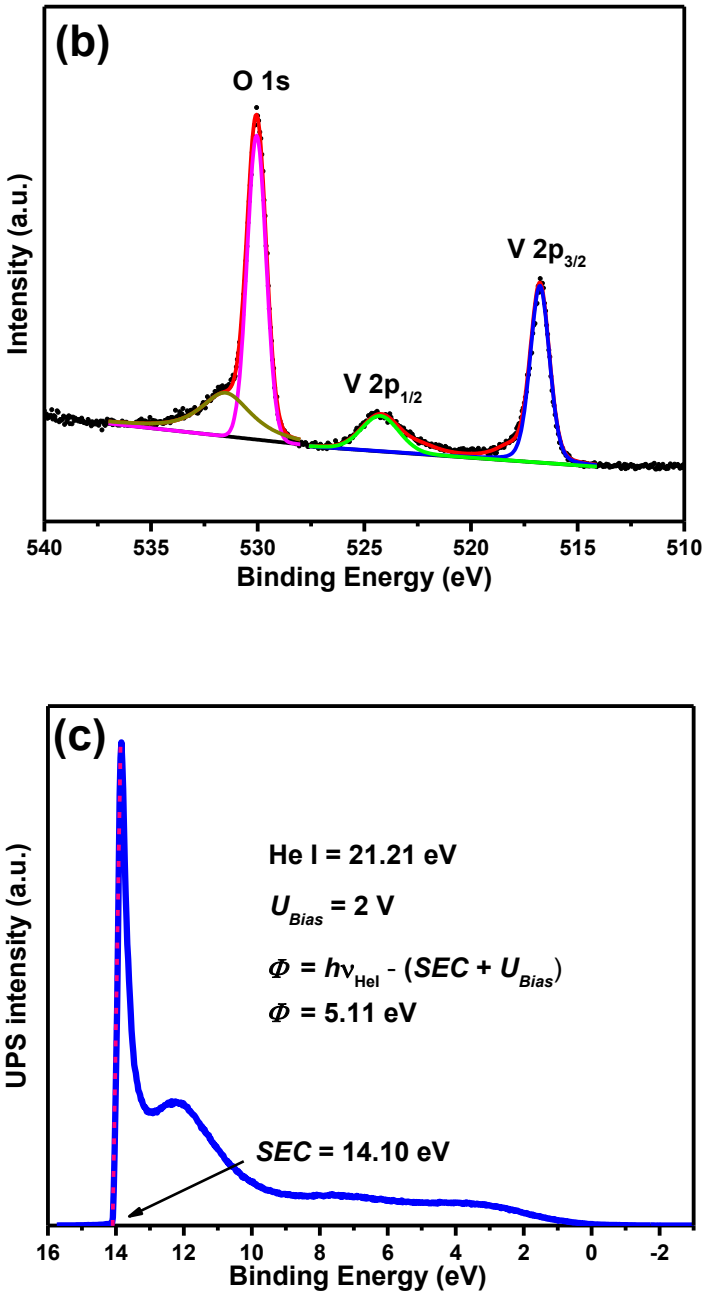

Figure 5.6. XPS spectra of (a) Cu 2p, (b) V 2p and O 1s for $Cu_2V_2O_7$ film. (c) UPS cutoff spectra measured with a 2 V bias for ~200 nm $Cu_2V_2O_7$ film on FTO.

By combining the various parameters that were experimentally determined by UV-vis, Mott-Schottky and UPS measurements we can now construct detailed band diagrams for $Cu_2V_2O_7$ photoelectrode. **Figure 4.12** shows the band diagram of our spray pyrolysis deposited $Cu_2V_2O_7$ film with respect to the electrochemical redox potentials of the water oxidation (H^+,O_2/H_2O) and reduction (H^+/H_2) reactions. It shows that the conduction band (CB) of

$Cu_2V_2O_7$ is about 500 mV more positive than the H^+/H_2 reduction potential so that the photovoltage gained by $Cu_2V_2O_7$ electrodes for solar water oxidation is strongly limited. This will also limit the onset and flatband potential positions for $Cu_2V_2O_7$ electrodes. The maximum overpotential for the OER as defined by the valence band edge is relatively high ($\eta_{OER,max}$ = 1.1 ± 0.1 V).

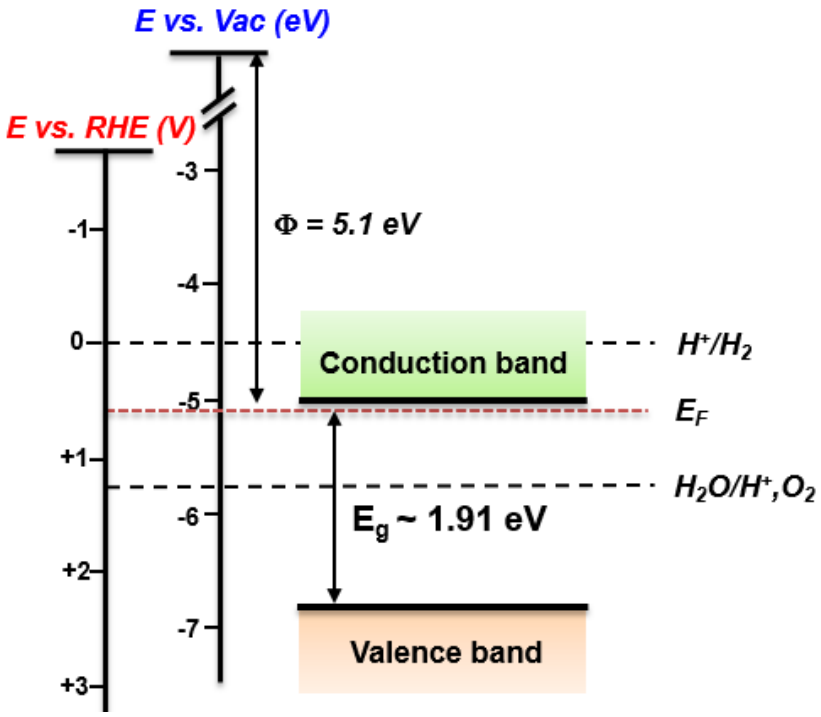

Figure 5.7. Schematic band diagram of $Cu_2V_2O_7$ film constructed from UPS and Mott−Schottky measurements. The positions of the valence band, Fermi level E_F and the conduction band with respect to the vacuum level, the hydrogen electrode (RHE) potential, as well as water oxidation and reduction potentials are depicted.

5.2.6 Photoelectrochemical Stability and O_2 Production

Stability tests of the $Cu_2V_2O_7$ photoelectrodes have been carried out in a 0.3 M K_2SO_4 electrolyte with 0.2 M phosphate buffer (pH 6.8) under Ar bubbling and with a CoPi catalyst. The results are shown in **Figure 5.8a**. The photocurrents show an initial fast decay, which is attributed to surface recombination or poor catalyst activity. The photocurrent density decreases by 58% within the first 3 min. After this decay, the photocurrent remained stable over the entire 120 min measurement time. For $Cu_2V_2O_7$ photoanodes modified with CoP_i, the photocurrent decreases by only 45% within the first 3 min. We did LSV scans for $Cu_2V_2O_7$ and $Cu_2V_2O_7/CoP_i$ photoanodes after 120 min PEC stability measurements (see **Figure S B19**), there was not a significant drop in photocurrent compared to **Figure 5.4a**, indicating that the stability performance of $Cu_2V_2O_7$ photoanodes was good. After the 120 min of photocurrent measurement, the illuminated area of the $Cu_2V_2O_7$ electrode showed no change and was almost

indistinguishable from the non-illuminated area (see **Figure S B20**). This means that no significant dissolution occurred. The total photogenerated charge (377 mC/cm^2 for the red curve of **Figure 5.8a**) exceeded the corresponding molar amount of $Cu_2V_2O_7$ in the film by a factor of 1.3. This turn-over number (TON) indicates the good stability of both $Cu_2V_2O_7$ and $Cu_2V_2O_7$/CoPi photoanodes at (near) neutral pH.

In order to measure O_2 directly and calculate the Faradaic efficiency, differential electrochemical mass spectrometry (DEMS) measurements were performed on the $Cu_2V_2O_7$ photoanode. **Figure 5.8b** shows the DEMS LSV scans for a 200 nm $Cu_2V_2O_7$ photoanode under illumination. The current density and O_2 signal from the DEMS are 0.1 V mismatched with the onset in O_2 production occurring around 1.1 V vs RHE, this because the delay detection from the PEC to the mass spectrometer. The data in **Figure 5.8b** clearly show that the photocurrent leads to oxygen evolution. DEMS LSV scans for a 200 nm $Cu_2V_2O_7$ photoanode without illumination is also performed (see **Figure S B21**). To calculate the faradaic efficiency, the sample was kept at a constant potential of 1.5 V vs RHE while recording the current and the O_2 signal of the mass spectrometer. After 5 min, the light was switched on for 15 min, resulting in a clear increase in photocurrent and O_2 signal (**Figure S B22**). To calibrate the PEC cell, the gas signal was measured vs different current for a Pt sheet as shown in **Figure S B23.** The amount of photogenerated charge was compared to the total molar amount of generated oxygen, from which a Faradaic efficiency ($\eta_{Faradaic}$) of 95.8 % is calculated for the O_2 evolution reaction.

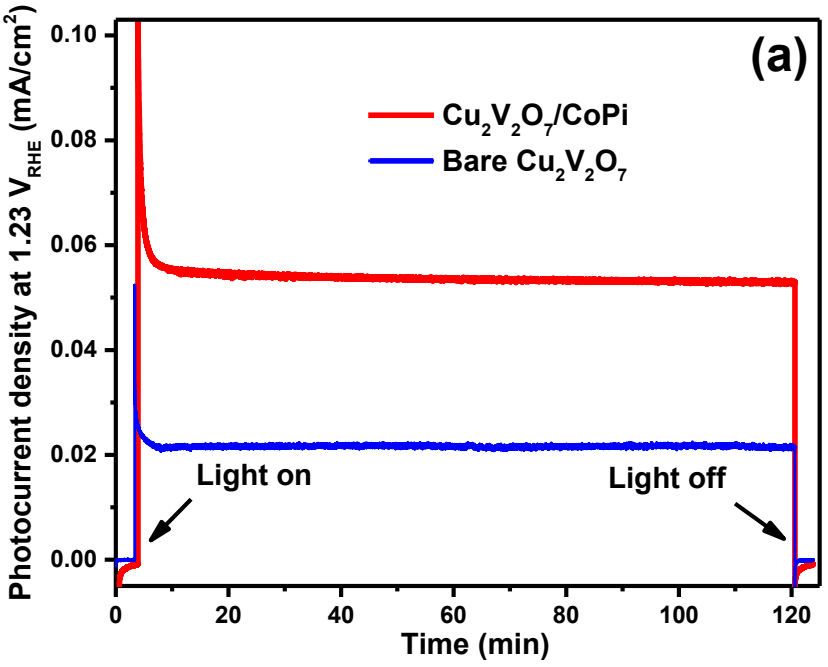

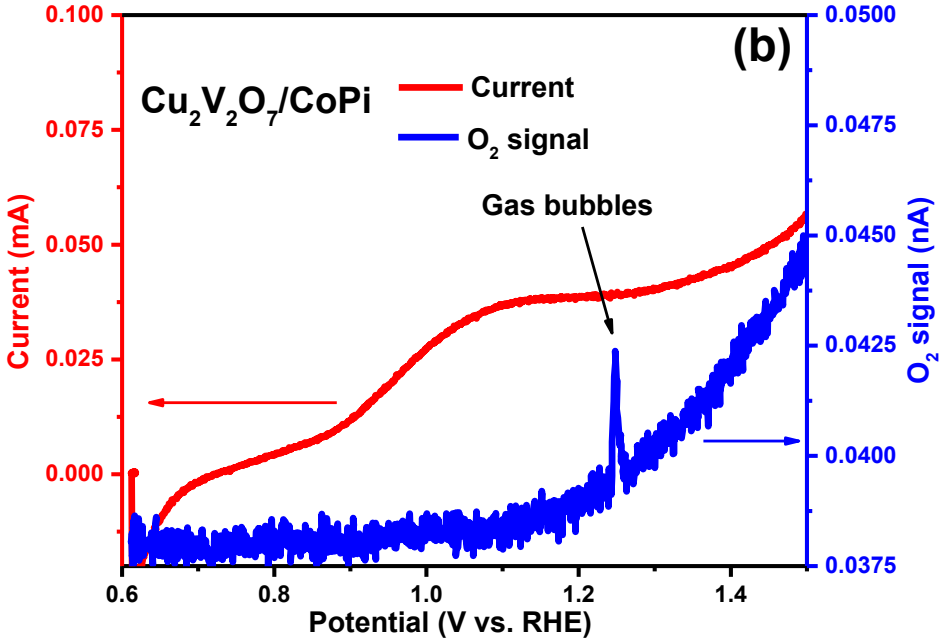

Figure 5.8. (a) Constant potential measurement at 1.23 V vs RHE for 200 nm $Cu_2V_2O_7$ films in the dark and light (AM1.5 irradiation). Measurements were done in 0.3 M K_2SO_4 and 0.2 M phosphate buffer (pH 6.8) with Ar bubbling (blue line) and with CoPi catalyst (red line) under frontside illumination. (b) DEMS LSV scans for a 200 nm $Cu_2V_2O_7$ photoanode, showing current (red) and O_2 signal (blue). Measurements were done in 0.3 M K_2SO_4 and 0.2 M phosphate buffer (pH 6.8) under back illumination with a scan rate of 5 mV/s.

5.3 Conclusions

$Cu_2V_2O_7$ is a promising photoanode material for use as the top absorber layer in a dual absorber PEC device. It has an optimal bandgap (1.8 ~ 2.0 eV) and a large absorption coefficient (up to $\alpha \approx 10^5$ cm^{-1}). In this work we have identified critical optoelectronic and PEC properties of the $Cu_2V_2O_7$ photoanodes synthesized by a facile spray pyrolysis method, including bandgap, absorption coefficient, band positions, carrier mobility, carrier lifetime, carrier diffusion length, flat band potential and O_2 evolution faradaic efficiency (see Table 5.1). Previous reports on $Cu_2V_2O_7$ as a photoanode material have shown relatively low photoconversion efficiencies, but the material limitations were not fully understood. Our study showed that a larger limiting factor is poor charge carrier transport, primarily for electrons, which reduces the obtainable photocurrent density to about 0.1 mA/cm^2 at 1.23 V vs RHE for our optimized $Cu_2V_2O_7$ photoanode even with CoPi as an OER catalyst. Another one of the biggest limitation is the relatively positive conduction band minimum.

With a better understanding of the performance limiting factors for $Cu_2V_2O_7$ photoanodes, strategies can now be explored to improve the photoconversion efficiency. For example, a tandem photoelectrode with relatively large photovoltage is needed or heterojunction solution (like $Cu_2V_2O_7$ on n-Si) may be explored to shift the onset potential cathodically. Different interfacial layers can be used to further improve the photoconversion efficiency.[169] Finally, doping, and nanostructuring can be used to overcome the mismatch between carrier transport and optical absorption. Similar strategies have been highly successful in the development of other metal oxide materials for PEC water splitting, such as $CuBi_2O_4$, Fe_2O_3, $BiVO_4$, and Cu_2O, and are likely to improve the PEC performance of $Cu_2V_2O_7$ as well.[28, 91, 115, 170]

Table 5.1. Summary of Key PEC Parameters of $Cu_2V_2O_7$

Parameter	value
band gap energy, Eg	1.90 ± 0.05 eV (indirect),
	2.05 ± 0.05 eV (direct)
absorption coefficient at 450 nm, α	4.06×10^4 cm^{-1}
carrier mobility, μ	$3.5 \pm 0.7 \times 10^{-3}$ cm^2 V^{-1} s^{-1}
carrier lifetime, τ	80 ± 5 ns
carrier diffusion lengths, L_D	28 ± 0.5nm
flat band potential, ϕ_{fb}	0.61 ± 0.03 V vs. RHE
work function, Φ	5.11 eV vs. Vac
valence band maximum, VBM	2.45 ± 0.03 V vs. RHE
O_2 evolution faradaic efficiency, η	95.8 %

Chapter 6. Assessment of a W:$BiVO_4$–$CuBi_2O_4$ tandem photoelectrochemical cell for overall solar water splitting

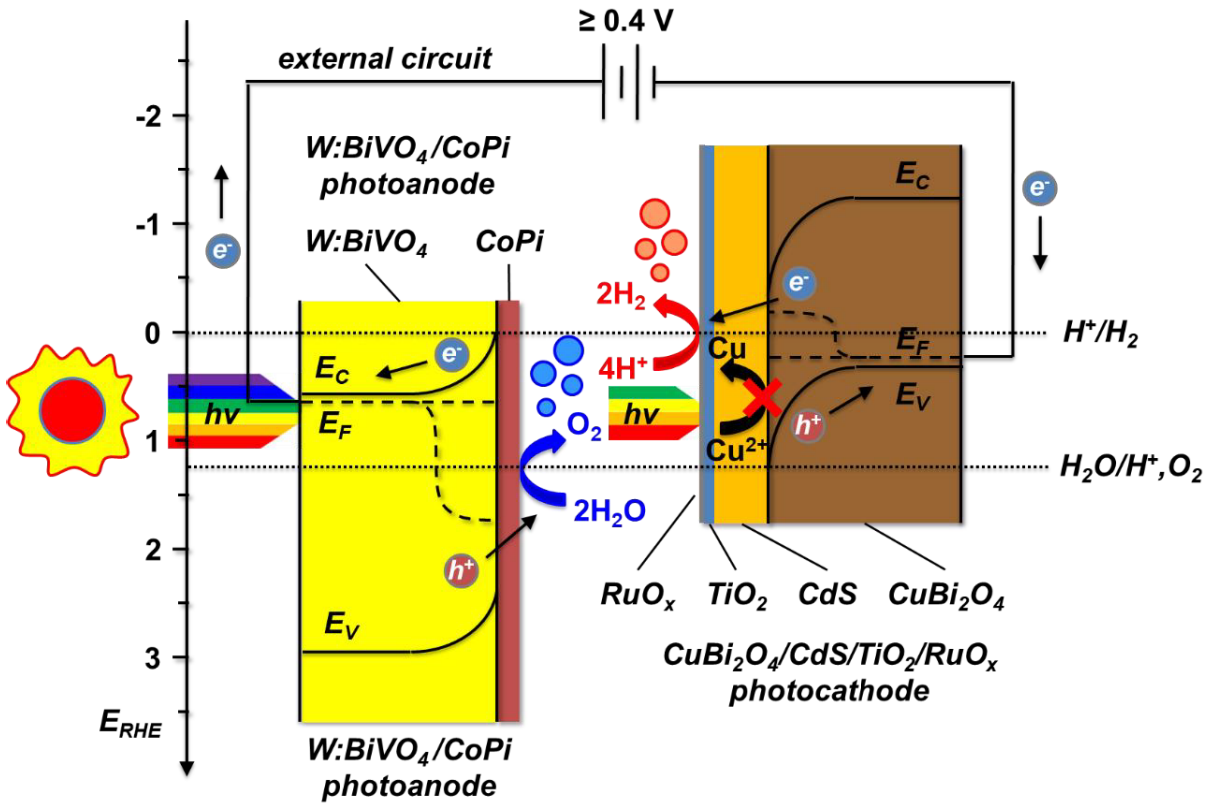

In this chapter, we assess a tandem photoelectrochemical cell consisting of a W:$BiVO_4$ photoanode top absorber and a $CuBi_2O_4$ photocathode bottom absorber for overall solar water splitting. We show that the W:$BiVO_4$ photoanode oxidizes water and produces oxygen at potentials ≥ 0.65 V vs. RHE when Co-Pi is added. The $CuBi_2O_4$ photocathode shows an exceptionally positive photocurrent onset potential of ~1.1 V vs. RHE; however, it does not produce a detectable amount of H_2 no matter the electrochemical potential because most of the photocurrent likely goes towards photo-corrosion of $CuBi_2O_4$ rather than H^+ reduction even when Pt or RuO_x is added as a co-catalyst. Protecting the $CuBi_2O_4$ photocathode with a CdS/TiO_2 heterojunction and adding RuO_x on top of that prevents photo-corrosion and allows for photoelectrochemical production of H_2 at potentials ≤ 0.25 V vs. RHE. A tandem photoelectrochemical cell composed of a W:$BiVO_4$/Co-Pi photoanode and $CuBi_2O_4$/CdS/TiO_2/RuO_x photocathode produces both hydrogen and oxygen that can be detected under illumination under an applied bias of ≥ 0.4 V. This applied bias is required because the CdS/TiO_2 heterojunction significantly decreases the photocurrent onset potential of $CuBi_2O_4$ from ~1.1 V to ~ 0.6 V vs. RHE, which in turn decreases the photocurrent density crossover point between the W:$BiVO_4$/CoPi photoanode and $CuBi_2O_4$/CdS/TiO_2/RuO_x photocathode. We hypothesize that the decreased photocurrent onset potential for the $CuBi_2O_4$/CdS/TiO_2/RuO_x photocathode due to the relatively low quasi-Fermi level splitting i.e. low photovoltage within $CuBi_2O_4$ since the conduction band is adequately positioned to reduce H^+. This work is the first experimental demonstration of hydrogen and oxygen production from a $CuBi_2O_4$-$BiVO_4$ based tandem device and the first identification of this crucial limitation in photovoltage for protected $CuBi_2O_4$ photocathodes that must be overcome to efficiently drive overall water splitting.

Keywords: overall solar water splitting; photoelectrochemical tandem cells; $CuBi_2O_4$; W:$BiVO_4$

6.1 Introduction

Solar photoelectrochemical (PEC) water splitting by employing photoelectrodes in a PEC cell has been demonstrated to be a promising approach to convert abundant solar energy into chemical bonds in the form of hydrogen fuel, which does not emit greenhouse gases.[13, 22, 30, 169] During the past few decades, extensive efforts on photoelectrochemical water splitting have been focused on exploring oxide-based semiconductor photoelectrode materials for use in a typical 3-electrode PEC cell with the semiconductor photoelectrode as the working electrode, a metal such as Pt as the counter electrode, and a reference electrode such as Ag/AgCl.[16, 171, 172] In 3-electrode configuration, an additional bias is usually applied to the counter electrode to drive one of the two half-reactions for water splitting. In order to perform overall water splitting a PEC cell must be used in 2-electrode configuration without the application of an external bias. This can be done using a single photoelectrode with band positions that straddle the redox potentials for both of the water splitting half-reactions or by combining a photoanode and photocathode together in a tandem PEC device.[112, 173-177]

Semiconductors with suitable band gaps (1.6–2.5 eV), good stability in aqueous solutions, and low cost in terms of materials and synthesis are highly desirable for use as photoelectrodes. Among the n-type semiconductors under investigation, bismuth vanadate ($BiVO_4$) with a band gap of 2.4 eV has recently received a lot of attention as a photoanode material and it has been optimized to be one of the highest performing metal oxide photoanode material for water oxidation.[86, 178] For p-type semiconductors, $CuBi_2O_4$ has recently been discovered as a potential candidate as a photocathode material for PEC water splitting due to its optimal optical bandgap in the range of 1.5–1.8 eV, conduction band location that is more negative than the thermodynamic potential for proton reduction, and positive onset potential in the range of 1.1-1.4 V vs. RHE, which is more positive than many other p-type photocathode materials including Cu_2O, $CuFeO_2$, and Si.[38, 91, 165] Therefore, $CuBi_2O_4$ has great potential as a photocathode material for overall solar water splitting, especially in a tandem PEC device. $BiVO_4$ can only absorb photons with wavelengths less than 510 nm due to its bandgap of 2.4 eV.[179, 180] $CuBi_2O_4$ has a smaller bandgap of ~1.7 eV so it can utilize the photons with longer wavelengths up to ~750 nm. Hence, by combining a $BiVO_4$ photoanode as a top-absorber photoanode and a $CuBi_2O_4$ photocathode as a bottom absorber in a tandem PEC device, a larger range of the AM1.5 solar spectrum can be utilized while simultaneously straddling the two half-reactions for water splitting.[181, 182] A theoretical efficiency of approximate 8% is achievable for a $BiVO_4$-$CuBi_2O_4$ tandem cell assuming all photons with energies higher than the bandgaps are absorbed and utilized with 100% efficiency.

In this work, we assess a tandem PEC system based on a W:$BiVO_4$ photoanode and a $CuBi_2O_4$ photocathode for overall water splitting. We reveal the upper limit in stable photocurrent density that can be achieved from the $BiVO_4$-$CuBi_2O_4$ tandem cell by utilizing H_2O_2 as an electron and hole scavenger and we measure the actual performance of the tandem cell for overall water splitting with the addition of cobalt phosphate (Co-Pi) as a co-catalyst on the W:$BiVO_4$ photoanode and Pt or RuO_x on the $CuBi_2O_4$ photocathode. We confirm that W:$BiVO_4$ with Co-Pi (W:$BiVO_4$/Co-Pi) is effective as an photoanode for producing oxygen while $CuBi_2O_4$ must be coated with a conformal protection layer of CdS/TiO_2 along with RuO_x as a co-catalyst ($CuBi_2O_4$ /CdS/TiO_2/RuO_x) in order to function as a stable photocathode and produce hydrogen. Additionally, we demonstrate hydrogen production from a W:$BiVO_4$/Co-Pi-$CuBi_2O_4$/CdS/TiO_2/RuO_x tandem device and we discuss the limitations of $CuBi_2O_4$ as the photocathode material in terms of photo-corrosion and photovoltage.

6.2 Results and Discussion

6.2.1 Photoelectrochemical Performance

Figure 6.1 is a simplified energy diagram of a tandem cell that was developed and analyzed in this study. The tandem cell consists of a W:$BiVO_4$/Co-Pi photoanode and a $CuBi_2O_4$/CdS/TiO_2/RuO_x photocathode submerged in

aqueous electrolyte and "wired" for overall photoelectrochemical water splitting. The energy levels (E_C, E_V, E_F, and quasi-Fermi level splitting) for the photoanode and photocathode are shown along with the electrochemical potentials for water oxidation (H_2O/H^+, O_2) and proton reduction (H^+/H_2) at 1.23 V vs. RHE and 0.0 V vs. RHE, respectively. The diagram depicts absorption of the photons with wavelengths ≥ 510 nm by the W:$BiVO_4$/Co-Pi photoanode to generate electron-hole pairs and the resulting quasi-Fermi level splitting. Internal band bending in the W:$BiVO_4$ thin film drives the photogenerated holes towards photoanode-electrolyte interface where they perform the water oxidation half-reaction producing oxygen ($2H_2O + 4\ h^+ \rightarrow 4H^+ + O_2$). Photons with wavelengths ≤ 510 nm are transmitted through the W:$BiVO_4$/Co-Pi photoanode towards the $CuBi_2O_4$/CdS/TiO_2/RuO_x photocathode. The $CuBi_2O_4$ layer absorbs photons with wavelengths of 510 – 750 nm to produce electron-hole pairs and the internal band bending drives the photogenerated electrons to the photocathode-electrolyte interface where they perform the proton reduction half-reaction producing hydrogen ($2H^+ + 2e^- \rightarrow H_2$). Lastly, **Figure 6.1** shows that an applied bias of ≥ 0.4 V was needed by the W:$BiVO_4$/Co-Pi-$CuBi_2O_4$/CdS/TiO_2/RuO_x tandem device to drive overall water splitting. This is due to the relatively small quasi-Fermi level splitting (i.e. photovoltage) within $CuBi_2O_4$.

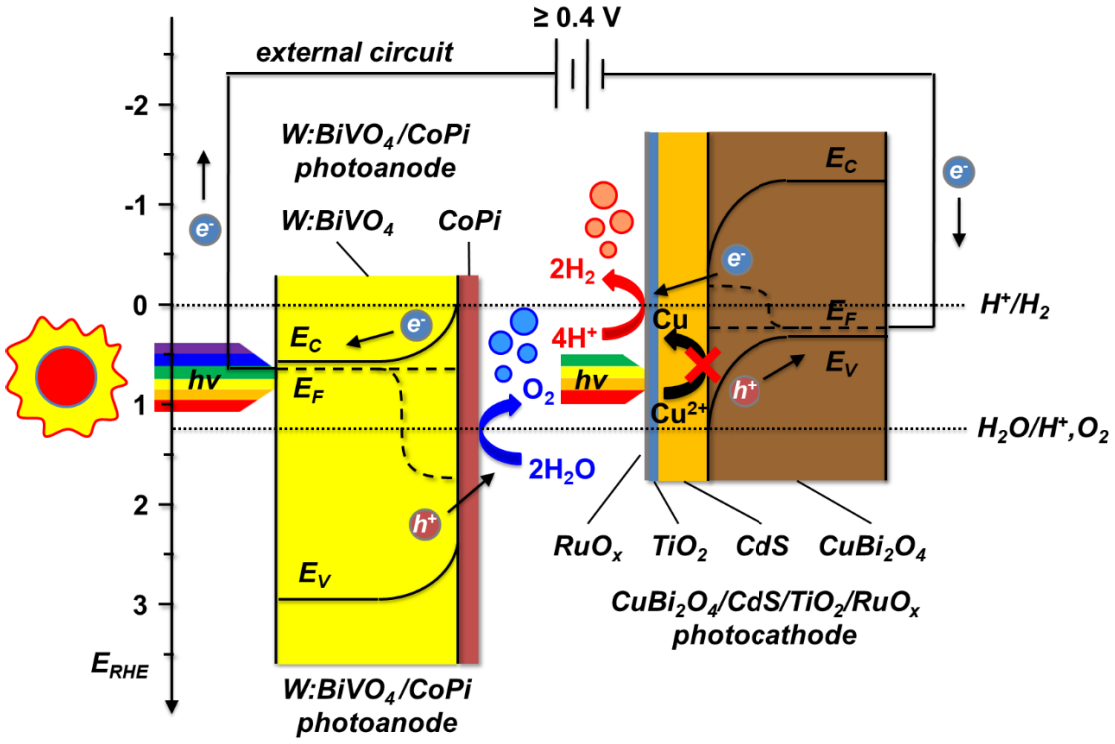

Figure 6.1. Simplified energy diagram of a tandem cell consisting of a W:$BiVO_4$/Co-Pi photoanode and a $CuBi_2O_4$/CdS/TiO_2/RuO_x photocathode submerged in aqueous electrolyte and "wired" for overall photoelectrochemical water splitting. The electrochemical potentials for water oxidation (H_2O/H^+, O_2) and proton

reduction (H^+/H_2) are included. Band-gap energies and energy levels (E_C, E_V, E_F, and quasi-Fermi level splitting) for the photoanode and photocathode are approximated from UV-vis measurements, UPS measurements, Mott−Schottky analysis, and photocurrent onset potentials for H_2 and O_2 evolution. The diagram illustrates that the CdS/TiO_2 heterojunction layer protects $CuBi_2O_4$ from photo-corrosion (i.e. blocks photoelectrochemical reduction of Cu^{2+}) and that the quasi-Fermi level splitting (photovoltage) within $CuBi_2O_4$ is relatively small so that an applied bias of ≥ 0.4 V is required to drive overall water splitting.

In order to predict and assess the overall performance of the tandem device we first discuss the performance of the W:$BiVO_4$ photoanode and $CuBi_2O_4$ photocathode as individual photoelectrodes in three-electrode configuration. **Figure 6.2a** shows linear sweep voltammogram (LSV) results for a 200 nm thick W:$BiVO_4$ photoanode and a 260 nm thick $CuBi_2O_4$ photocathode in three-electrode configuration directly under simulated AM1.5 solar illumination. In addition, the figure shows the response for a $CuBi_2O_4$ photocathode placed behind a W:$BiVO_4$ photoanode to filter the incident illumination and simulate the effect of W:$BiVO_4$ as the top absorber and $CuBi_2O_4$ as the bottom absorber in a tandem device. The measurements were performed with H_2O_2 as both a hole scavenger for W:$BiVO_4$ and an electron scavenger for $CuBi_2O_4$ so that the maximum performance of the tandem device could be predicted without limitations in the reaction kinetics for the water splitting half-reactions. Note that positive current density values are used for anodic current from W:$BiVO_4$ and also for cathodic current from $CuBi_2O_4$. This was done to obtain the crossover point in photocurrent density for the W:$BiVO_4$ photoanode and $CuBi_2O_4$ photocathode i.e. the operating photocurrent density (J_{op}), which is indicated by an arrow in **Figure 6.2a**. The J_{op} value determines the maximum photocurrent density that can be obtained when a photoanode and photcathode are combined in a tandem PEC device.[16] Since the crossover point in photocurrent density determines the J_{op} value it is important to use a photoanode with a relatively negative photocurrent onset potential and a photocathode with a positive photocurrent onset potential.[30] Recall that one motivation for choosing $CuBi_2O_4$ as the photocathode material in a tandem PEC device is that it has a relatively positive photocurrent onset potential (i.e. positive Fermi level) compared to other p-type photoanode materials. **Figure 6.2a** shows that the $CuBi_2O_4$ photocathode, under direct solar illumination, has a photocurrent onset potential of ~1.1 V vs. RHE, and the crossover point with the W:$BiVO_4$ photoanode is ~1.23 mA/cm^2 at 0.79 V vs. RHE. In an actual tandem device the $CuBi_2O_4$ photocathode would be placed behind the W:$BiVO_4$ photoanode so this must be considered in the analysis. As shown in **Figure 6.2a**, placing the $CuBi_2O_4$ photocathode behind a W:$BiVO_4$ photoanode to filter some of the incident illumination has two detrimental effects on the performance of the $CuBi_2O_4$ photocathode: (1) its photocurrent onset potential decreases to from ~1.1 to ~0.96 V vs. RHE and (2) its photocurrent density decreases for all potentials due to the absorption of fewer photons. This reduces the J_{op} value to 0.77 mA/cm^2 at 0.67 V vs. RHE. One strategy to reduce the detrimental effects on the $CuBi_2O_4$ photocathode would be to use a thinner W:$BiVO_4$ photoanode that filters less of the incident illumination. **Figure S C1** in the Supporting Information shows

LSV scans for W:$BiVO_4$ photoanodes of different thicknesses (50, 100, 200 nm) in front of a $CuBi_2O_4$ photocathode. Decreasing the thickness of the W:$BiVO_4$ photoanode does allow more light to be transmitted to the $CuBi_2O_4$ photocathode thereby improving its photocurrent onset potential and its overall photocurrent density. However, it simultaneously decreases the photocurrent density of the W:$BiVO_4$ photoanode so the photocurrent crossover point shifts to the right and the J_{op} value does not change significantly. Therefore, the J_{op} value of 0.77 mA/cm^2 at 0.67 V vs. RHE for a 200 nm W:$BiVO_4$ photoanode and a 260 nm $CuBi_2O_4$ photocathode represents the maximum obtainable photocurrent density of the W:$BiVO_4$-$CuBi_2O_4$ tandem device. Again, this is under the assumption that facile and efficient charge transfer for each half-reaction is possible, since this result is obtained with H_2O_2 added as an electron/hole scavenger.

The incident photon-to-current conversion efficiency (IPCE) of the individual photoelectrodes in the tandem device can provide additional insights about its performance. **Figure 6.2b** shows IPCE values for a W:$BiVO_4$ photoanode at 1.23 V vs. RHE and a $CuBi_2O_4$ photocathode at 0.6 V vs. RHE under direct illumination and behind W:$BiVO_4$. Again, H_2O_2 was added to the electrolyte as an electron/hole scavenger to identify the maximum possible efficiency. Figure 2b also includes the integrated photocurrent density (integrated from smaller to larger wavelengths of light). The W:$BiVO_4$ photoanode exhibits an IPCE onset at a wavelength of ~510 nm followed by a sharp increase of the IPCE values to 60-85% for wavelengths between 350 and 450 nm. The integrated photocurrent density reaches 2.2 mA/cm^2. Under direct illumination, the $CuBi_2O_4$ photocathode shows an IPCE onset near red light (wavelength ~800 nm) that gradually increases to a value of ~40% for 350 nm light and the integrated photocurrent density reaches 2.5 mA/cm^2. The $CuBi_2O_4$ photocathode behind W:$BiVO_4$ shows a similar IPCE onset of ~800 nm; however, the IPCE levels off at ~10% for wavelengths between 600 and 510 nm and then decreases to ~0% for wavelengths below 510 nm. The decrease in IPCE for wavelengths below 510 nm is expected since the W:$BiVO_4$ photoanode will absorb and block most of the below 510 nm. The flattening of IPCE for the $CuBi_2O_4$ photocathode between 510 and 600 nm is likely due to light scattering or diffuse reflectance by the W:$BiVO_4$ photoanode. This is confirmed by the UV-vis measurements on the photoelectrodes. **Figure S C2** in the Supporting Information shows the absorption spectra for a W:$BiVO_4$ photoanode, $CuBi_2O_4$ photocathode, $CuBi_2O_4$ photocathode behind a W:$BiVO_4$ photoanode. For wavelengths between 510 and 600 nm the total absorption of the $CuBi_2O_4$ photocathode behind W:$BiVO_4$ is actually lower than that of the $CuBi_2O_4$ photocathode under direct illuminunation. Therefore the reflectance of W:$BiVO_4$ photoanode as a top absorber layer is another important factor that must be considered in the design of a tandem device. In **Figure 6.2b** the integrated photocurrent density of the $CuBi_2O_4$ photocathode behind W:$BiVO_4$ reaches 1.1 mA/cm^2. All three of the integrated photocurrent densities in **Figure 6.2b** are close to the actual photocurrent densities from the LSV measurements (**Figure 6.2a**) for $CuBi_2O_4$ and W:$BiVO_4$ at 0.6 V and 1.23 V vs. RHE, respectively. Therefore, the IPCE measurements provide accurate representation of the light

harvesting efficiency these photoelectrodes by themselves and under the absorption conductions for a tandem device.

For overall photoelectrochemical water splitting an electron or hole scavenger cannot be used. Instead the photogenerated electrons and holes must go towards the water splitting half reactions, water oxidation and proton reduction. Typically, this requires the deposition of electrocatalysts or co-catalysts onto the surface of the photoelectrodes. Co-Pi is a typical co-catalyst for $BiVO_4$ photoanodes used for water oxidation and Pt is well known as an electrocatalyst for proton reduction.[74, 100, 164] Therefore, we tested W:$BiVO_4$ photoanodes with and without Co-Pi deposited on the surface (W:$BiVO_4$/CoPi and W:$BiVO_4$) and $CuBi_2O_4$ photocathodes with Pt ($CuBi_2O_4$/Pt). The Co-P_i catalyst was electrodeposited (in the dark) on W:$BiVO_4$ photoanodes at 0.9 V versus Ag/AgCl for 30 s (see **Figure S C3a**) in an electrochemical cell consisting of 0.5 mM of $Co(NO_3)_2.6H_2O$ in 0.3 M K_2SO_4 and 0.2 M phosphate buffer (pH 6.8) using a three-electrode configuration.[74, 164] Three LSV cycles were performed in order to activate the CoP_i-modified W:$BiVO_4$ photoanodes (see **Figure S C3b**). Another requirement for overall water splitting is that the photoelectrodes must be stable. We have shown that $CuBi_2O_4$ photocathodes can undergo photocorrosion even with Pt added as a electrocatalyst since the photocurrent density decays over time as exposed Cu^{2+} on the surface of $CuBi_2O_4$ is reduced to Cu^+ and Cu.[38] Later we will show that this photocorrosion can be suppressed by depositing a conformal overlayer of CdS/TiO_2 along with Pt as an electrocatalyst resulting in relatively stable $CuBi_2O_4$/CdS/TiO_2/Pt photocathodes that produce hydrogen with a Faradaic efficiency of ~91%.[91] Others have shown that RuO_x can also be used as an electrocatalyst for photocathodes as an alternative to Pt with improved stability.[183] In an effort to improve stability further we tested $CuBi_2O_4$/CdS/TiO_2/RuO_x photocathodes for our tandem device in this study. Ruthenium oxide catalyst was photoelectrodeposited from an aqueous solution of 1.17 mM $KRuO_4$ in 25 mL deionized water, using a constant current of −0.03 mA cm^{-2} for 10 min with constant illumination from solar simulator. Four times short light chop during the deposition revealed 0.3 V of photovoltage at this small current density (see **Figure S C4**). The photoelectrodeposition was carried out in a three-electrode configuration with a platinum counter electrode and an Ag/AgCl electrode (saturated KCl) as the reference electrode.

Figure 6.2c shows LSV scans for the various photoelectrodes under simulated solar illumination in aqueous buffered electrolyte (pH 6.8) without an electron/hole scavenger. The addition of CoPi to W:$BiOV_4$ results in a clear improvement in performance towards water oxidation in the aqueous electrolyte. At the water oxidation potential of 1.23 V vs. RHE the W:$BiVO_4$ produces a photocurrent density of 0.5 mA/cm^2 while the W:$BiVO_4$/CoPi reaches 2.6 mA/cm^2. In addition, the photocurrent density of the W:$BiVO_4$/CoPi photoanode towards water oxidation shown in **Figure 6.2b** is only slightly lower than that of the W:$BiVO_4$ photoanode with H_2O_2 as a hole scavenger (**Figure 6.2a**) and the photocurrent onset potential of the W:$BiVO_4$/CoPi photoanode is nearly the same as the

W:$BiVO_4$ photoanode with H_2O_2 at ~0.5 V vs. RHE. Therefore the W:$BiVO_4$ photoanode should be an effective top absorber in a tandem device for driving the water oxidation half-reaction.

In contrast, the $CuBi_2O_4$/Pt and $CuBi_2O_4$/CdS/TiO_2/RuO_x photocathodes show much worse performance towards proton reduction in **Figure 6.2c** compared to the $CuBi_2O_4$ photocathode with H_2O_2 as an electron scavenger (**Figure 6.2a**). The photocurrent onset potential of the $CuBi_2O_4$/Pt is reasonable at ~1.07 V vs. RHE, but the onset potential of the $CuBi_2O_4$/CdS/TiO_2/RuO_x is reduced to ~0.73 V vs. RHE. At 0.4 V vs. RHE the $CuBi_2O_4$/Pt and $CuBi_2O_4$/CdS/TiO_2/RuO_x photocathodes produce photocurrent densities of ~1.03 mA/cm^2 and ~0.2 mA/cm^2. Here, the higher photocurrent density of the $CuBi_2O_4$/Pt is likely due to higher photocorrosion rather than proton reduction. In **Figure 6.2b** the J_{op} values (crossover points) are ~0.30 mA/cm^2 at 0.64 V vs. RHE for W:$BiVO_4$/CoPi combined with $CuBi_2O_4$/Pt and ~0.1 mA/cm^2 at 0.57 V vs. RHE for W:$BiVO_4$/CoPi with $CuBi_2O_4$/CdS/TiO_2/RuO_x. These differences between the LSV scans in **Figures 6.2a** and **6.2c** illustrate the tremendous challenge of constructing a tandem PEC cell for overall water splitting with a $CuBi_2O_4$ photocathode. **Figure 6.2a** reveals that $CuBi_2O_4$ has ideal band positions for producing a reasonable amount of photocurrent in a tandem device. Unfortunately the addition of a CdS/TiO_2 protection layer on $CuBi_2O_4$ to suppress photocorrosion and RuO_x to facilitate the proton reduction reaction decreases the J_{op} value from a maximum obtainable value of 0.77 mA/cm^2 (**Figure 6.2a**) to an actual value of 0.1 mA/cm^2 for overall water splitting (**Figure 6.2b**).

Figure 6.2d shows the IPCE values without an electron/hole scavenger for a W:$BiVO_4$ photoanode with Co-Pi at 1.23 V vs. RHE and a $CuBi_2O_4$ photocathode with Pt as at 0.6 V vs. RHE under direct illumination and behind a W:$BiVO_4$ photocathode. The integrated photocurrent densities are included. Similar to the results for W:$BiVO_4$ in **Figure 6.2b**, the W:$BiVO_4$/Co-Pi in **Figure 6.2d** shows an IPCE onset at a wavelength of ~510 nm with a sharp increase in IPCE at lower wavelengths although the IPCE values reach a smaller range of 40-50% for wavelengths between 450 and 350 nm. The integrated photocurrent density is 10% smaller at 2.0 mA/cm^2 which may due to the different light intensities. In **Figure 6.2d**, $CuBi_2O_4$/Pt under direct illumination and $CuBi_2O_4$/Pt behind W:$BiVO_4$ show IPCE onsets at ~800 nm but for all wavelengths IPCE values are significantly smaller than those for $CuBi_2O_4$ with H_2O_2 as an electron/hole scavenger (**Figure 6.2b**). The integrated photocurrent densities for $CuBi_2O_4$/Pt alone and $CuBi_2O_4$/Pt behind W:$BiVO_4$ are also relatively low at 0.7 and 0.4 mA/cm^2, respectively. This result provides additional evidence of the relatively poor efficiency of $CuBi_2O_4$ towards the proton reduction half-reaction even with the addition of Pt. The IPCE values for a $CuBi_2O_4$/CdS/TiO_2/RuO_x photocathode are included in **Figure S C5** in the Supporting Information and the IPCE values are even lower at ~6% for wavelengths between 500 and 350 nm. Therefore, the identification of a protection layer that does not reduce the photocurrent onset efficiency of $CuBi_2O_4$ along with a suitable electrocatalyst are the keys to developing a more efficient $CuBi_2O_4$-based photocathode for a tandem device.

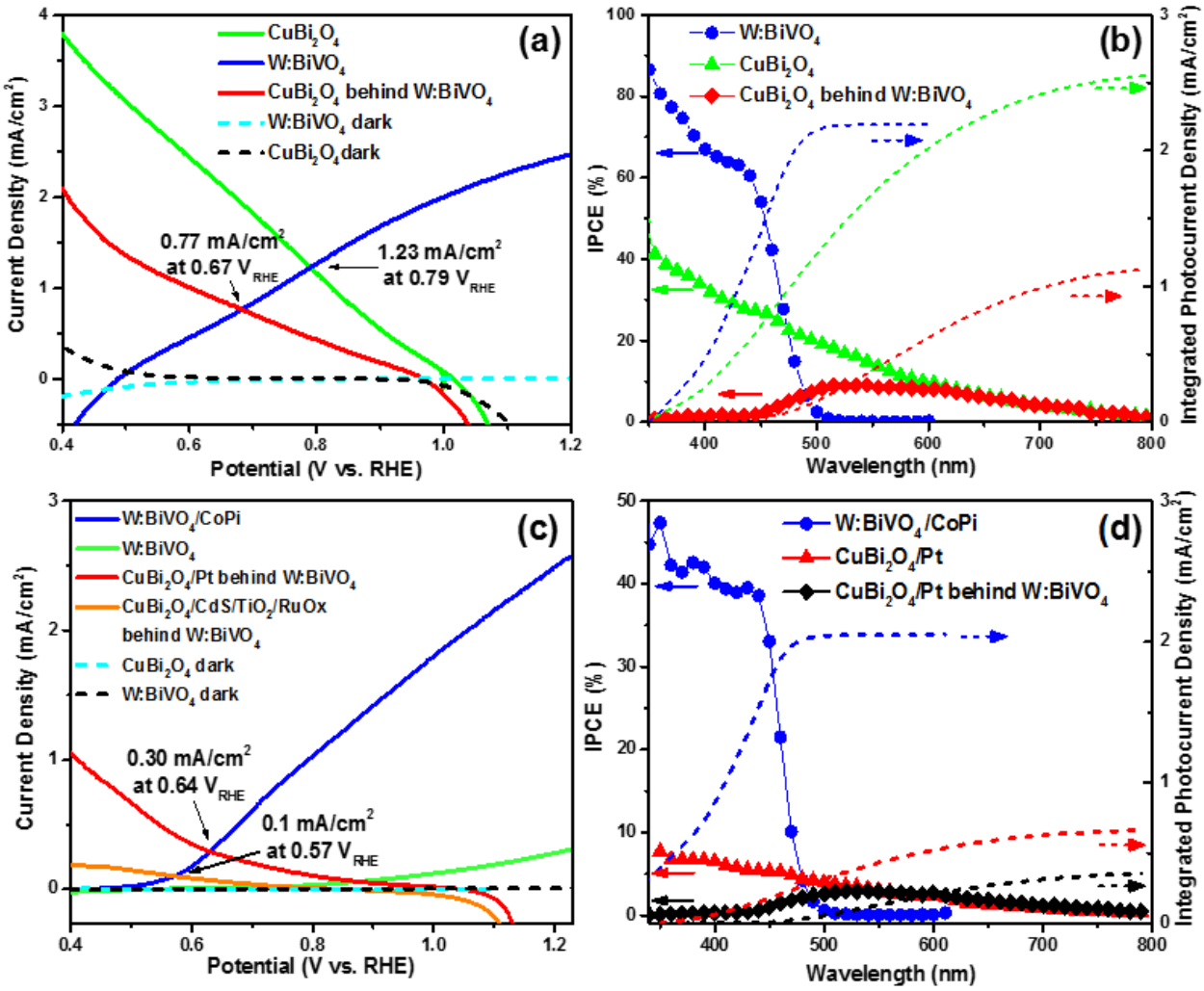

Figure 6.2. (a) LSV scans for a W:$BiVO_4$ photoanode (blue solid line) and $CuBi_2O_4$ photocathode under direct AM1.5 illumination (red green line) and) a $CuBi_2O_4$ photocathode with a W:$BiVO_4$ photoanode filtering the incident AM1.5 illumination (solid red line) all measured with H_2O_2 added as an electron/hole scavenger. (b) IPCE spectra of a W:$BiVO_4$ photoanode (blue circles) and $CuBi_2O_4$ photocathode under direct illumination (green triangles) and a $CuBi_2O_4$ photocathode behind a W:$BiVO_4$ photoanode filtering the incident illumination (red diamonds) measured all with H_2O_2 added as an electron/hole scavenger. (c) LSV scans for a W:$BiVO_4$ photocathode (green solid line), W:$BiVO_4$ photocathode with CoPi catalyst (blue solid line), $CuBi_2O_4$ photocathode with Pt as an electrocatalyst behind a W:$BiVO_4$ photocathode (red solid line), and $CuBi_2O_4$ photocathodes with CdS/TiO_2/RuO_x protection and electrocatalyst layers behind a W:$BiVO_4$ photocathode (orange solid line) measured with Ar bubbling (without an electron/hole scavenger). (d) IPCE spectra of a W:$BiVO_4$ photocathode with CoPi catalyst (blue circles) and $CuBi_2O_4$ photocathode with Pt as an electrocatalyst under direct illumination (red triangles) and a $CuBi_2O_4$ photocathode with Pt behind W:$BiVO_4$ photoanode measured with Ar bubbling (without an electron/hole scavenger). The applied

potential was 0.6 and 1.23 V vs. RHE for $CuBi_2O_4$ and W:$BiVO_4$, respectively. All measurements were performed in three-electrode configuration in 0.3 M K_2SO_4 and 0.2 M phosphate buffer electrolyte (pH 6.8) as the base electrolyte with H_2O_2 or with Ar bubbling as indicated. The film thickness of the $CuBi_2O_4$ and W:$BiVO_4$ photoelectrodes were 260 nm and 200 nm, respectively. For IPCE measurements the applied potentials for the $CuBi_2O_4$ and W:$BiVO_4$ photoelectrodes were 0.6 and 1.23 V vs. RHE, respectively. Note that positive current density values are used for anodic current from W:$BiVO_4$ and also for cathodic current from $CuBi_2O_4$.

To assess the performance of real $BiVO_4$-$CuBi_2O_4$ tandem devices, PEC measurements were performed in two-electrode configuration with the $BiVO_4$-based photoanode and $CuBi_2O_4$-based photocathode "wired" together in a single electrochemical cell. Recall, that several photoelectrode configurations showed positive J_{op} values in **Figure 6.2a** and **6.2c**. Thus, a tandem device of these photoelectrodes in two-electrode configuration should produce photocurrent even without an applied bias. **Figure 6.3** shows these two-electrode current density vs. time measurements at zero applied bias. It includes the results for a W:$BiVO_4$-$CuBi_2O_4$ tandem device with H_2O_2 added as an electron and hole scavenger as well as W:$BiVO_4$-$CuBi_2O_4$, W:$BiVO_4$-$CuBi_2O_4$/Pt, and W:$BiVO_4$/CoPi-$CuBi_2O_4$/CdS/TiO_2/RuO_x tandem devices in aqueous electrolyte with Ar bubbling. At the start of each measurements tandem devices were kept in the dark for the first 60 seconds and then simulated AM1.5 solar illumination (100 mW cm^{-2}) was activated. In all cases the W:$BiVO_4$-$CuBi_2O_4$ tandem cell exhibited a transient spike in current density immediately upon activation of the simulated solar illumination because of capacitive charging effects.[184] The heights of these transient spikes in **Figure 6.3** are similar in magnitude to the J_{op} values shown in **Figure 6.2a** and **6.2c** confirming that the J_{op} provides a reasonable prediction of tandem performance. After the initial transient spike, the W:$BiVO_4$-$CuBi_2O_4$ tandem device measured with H_2O_2 provided a sustained photocurrent density of ~0.6 mA/cm^2 for >60 min. As shown in **Figure S C6** it maintained a relatively stable photocurrent for many hours with the photocurrent finally dropping to ~0.3 mA/cm^2 after 14 hours of continuous operation. In **Figure 6.3**, the $CuBi_2O_4$/Pt-W:$BiVO_4$/CoPi tandem device measured with Ar bubbling showed a photocurrent density of ~0.1 mA/cm^2 after the initial transient spike, but the photocurrent density dropped steadily to ~0.015 mA/cm^2 after 60 min presumably due to photocorrosion of the exposed $CuBi_2O_4$ on the surface. In contrast, the W:$BiVO_4$/CoPi-$CuBi_2O_4$/CdS/TiO_2/RuO_x tandem device measured with Ar bubbling, showed a lower current density after the initial transient spike at ~0.03 mA/cm^2, but it remained relatively stable for at least 60 min without a noticeable decay due to the improved stability provided by the protection layers. Upon light activation, the W:$BiVO_4$-$CuBi_2O_4$ tandem device measured with Ar bubbling showed the largest transient decay in photocurrent density upon activation followed by a negligible amount of photocurrent density for the remainder of the measurement.

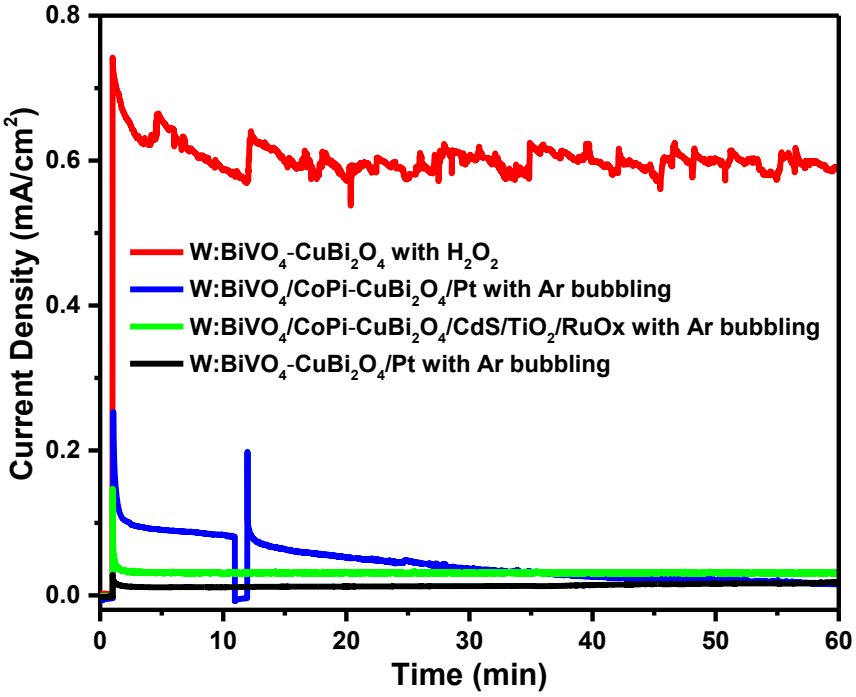

Figure 6.3. Two-electrode current density vs. time measurements for a W:$BiVO_4$-$CuBi_2O_4$ tandem device with H_2O_2 added as an electron/hole scavenger (red line), W:$BiVO_4$-$CuBi_2O_4$/Pt tandem device with Ar bubbling (blue line), W:$BiVO_4$/CoPi-$CuBi_2O_4$/CdS/TiO_2/RuO_x tandem device with Ar bubbling (green line), and W:$BiVO_4$-$CuBi_2O_4$/Pt tandem device with Ar bubbling (black line). The tandem devices were kept in the dark for the first 60 seconds and then simulated AM1.5 solar illumination (100 mW cm^{-2}) was activated. For the W:$BiVO_4$-$CuBi_2O_4$/Pt tandem device the light was also blocked for 60 seconds starting at 11 minutes.

The W:$BiVO_4$/CoPi photoanode and $CuBi_2O_4$/CdS/TiO_2/RuO_x photocathode were further analyzed with additional PEC measurements in two-electrode configuration. **Figure 6.4** shows two-electrode illuminated and dark LSV scans for a tandem device consisting of a W:$BiVO_4$/CoPi photoanode and $CuBi_2O_4$/CdS/TiO_2/RuO_x photocathode (W:$BiVO_4$/CoPi vs. $CuBi_2O_4$/CdS/TiO_2/RuO_x) and a W:$BiVO_4$/CoPi photoanode connected to a Pt wire cathode (W:$BiVO_4$/CoPi vs. Pt) The W:$BiVO_4$/CoPi vs. Pt was performed to confirm the effect of the $CuBi_2O_4$/CdS/TiO_2/RuO_x photocathode. The W:$BiVO_4$/CoPi photoanode was the working electrode (WE) and the $CuBi_2O_4$/CdS/TiO_2/RuO_x photocathode or Pt wire was the counter electrode (CE). The LSV scans for W:$BiVO_4$/CoPi vs. $CuBi_2O_4$/CdS/TiO_2/RuO_x and W:$BiVO_4$/CoPi vs. Pt under illumination are clearly different. The W:$BiVO_4$/CoPi vs. $CuBi_2O_4$/CdS/TiO_2/RuO_x tandem device shows a photocurrent onset with an applied bias of -0.1 V and reaches a photocurrent density of ~0.025 mA/cm^2 at an applied bias of 0 V. This positive photocurrent at 0 V implies that overall unbiased water splitting should occur as long as both hydrogen and oxygen are being produced. As the applied bias is increased the photocurrent density also increases and eventually saturates at ~0.2 mA/cm^2 between

0.3 V and 0.5 V. Beyond 0.5 V the photocurrent density increases further. Concurrently, the W:$BiVO_4$/CoPi vs. Pt device shows no photocurrent density until the applied bias reaches 0.5 V at which point the photocurrent density continuously increases. V. This result implies that when the applied biases is increased beyond 0.5 V the electrochemical potential of the counter electrode, either the $CuBi_2O_4$/CdS/TiO_2/RuO_x photocathode or the Pt wire, is negative enough to drive the reduction reaction. For applied biases between -0.1 V and 0.5 V, the $CuBi_2O_4$/CdS/TiO_2/RuO_x photocathode drives the reduction reaction with photogenerated electrons and the W:$BiVO_4$/CoPi photoanode drives the oxidation reaction with photogenerated holes. In other words, the $CuBi_2O_4$/CdS/TiO_2/RuO_x photocathode contributes a photovoltage of 0.5 V – (-0.1V) = 0.6 V to the tandem device.

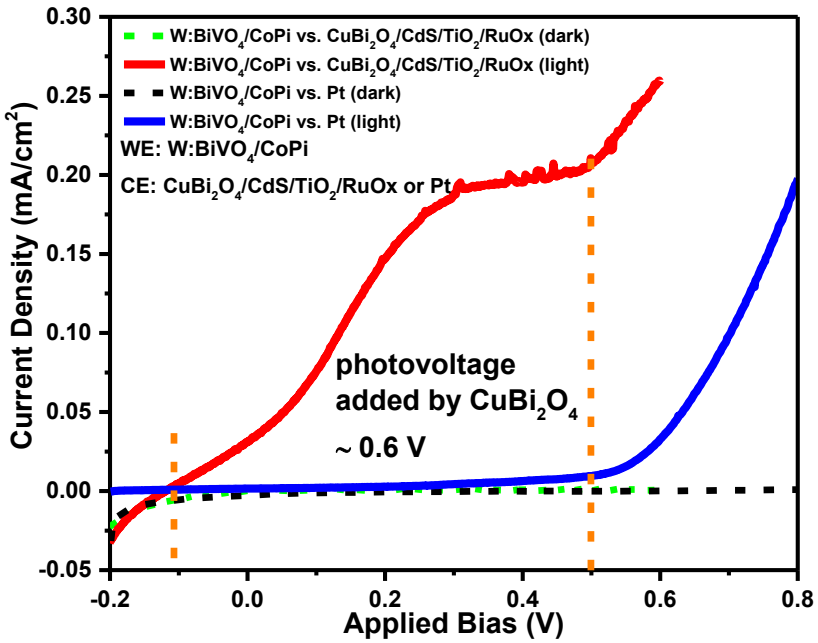

Figure 6.4. Two-electrode LSV scans for a tandem device consisting of a W:$BiVO_4$/CoPi photoanode and $CuBi_2O_4$/CdS/TiO_2/RuO_x photocathode (W:$BiVO_4$/CoPi vs. $CuBi_2O_4$/CdS/TiO_2/RuO_x) under illumination (red solid line) and in the dark (green dash line) and a single photoelectrode device consisting of a W:$BiVO_4$/CoPi photoanode vs. Pt wire measured under illumination (blue solid line) and in the dark (black dash line). The measurements were performed in 0.3 M K_2SO_4 and 0.2 M phosphate buffer (pH 6.8) electrolyte in two-electrode configuration with the W:$BiVO_4$/CoPi photoanode as the working electrode (WE) and the $CuBi_2O_4$/CdS/TiO_2/RuO_x photocathode or Pt wire as the counter electrode (CE). The electrolyte was continuously purged with Ar gas during the measurements.

To confirm the production of H_2 the W:$BiVO_4$/CoPi-$CuBi_2O_4$/CdS/TiO_2/RuO_x tandem device was analyzed using a custom designed electrochemical cell that was connected directly to a mass spectrometer. The current and H_2 gas signal vs. time were simultaneously measured in two-electrode configuration with various applied biases (0, 0.2, 0.3, 0.4, 0.6, and 0.5 V) along with activation of simulated solar illumination. The results are shown in **Figure 6.5**.

Consistent with **Figure 6.4**, the W:$BiVO_4$/CoPi-$CuBi_2O_4$/CdS/TiO_2/RuO_x tandem device produces photocurrent at all applied biases between 0 and 0.6 V. However, for each applied bias there is a significant transient decay in photocurrent immediately after activation of the light and photocurrent gradually decays to significantly lower values. For applied biases of 0.0 and 0.2 V there is not a distinguishable H_2 gas signal compared to the baseline gas signal of the mass spectrometer. At applied biases of 0.4 and 0.5 V there is a slight bump in the H_2 gas signal compared to the baseline gas signal so the W:$BiVO_4$/CoPi-$CuBi_2O_4$/CdS/TiO_2/RuO_x tandem device is performing overall photoelectrochemical water splitting at those biases. At an applied bias of 0.6 V there is a dramatic increase in the H_2 gas signal, likely because the $CuBi_2O_4$/CdS/TiO_2/RuO_x photocathode is driven to an electrochemical potential that is more negative than 0.0 V vs. RHE when the applied bias is greater than 0.5 V. This is consistent with the two-electrode LSV results shown in Figure 4. These mass spectrometer results for applied biases of 0.4 and 0.5 V are the first experimental demonstration of H_2 production from a tandem device consisting of a $BiVO_4$-based photoanode and $CuBi_2O_4$-based photocathode. Recently, other researchers have reported $BiVO_4$-$CuBi_2O_4$ based tandems but hydrogen production was never confirmed.[180-182] Since the $CuBi_2O_4$ photocathodes were not protected it is possible that these tandem devices were performing water oxidation at the $BiVO_4$ photoanode and $CuBi_2O_4$ photo-corrosion at the photocathode rather than overall water splitting.

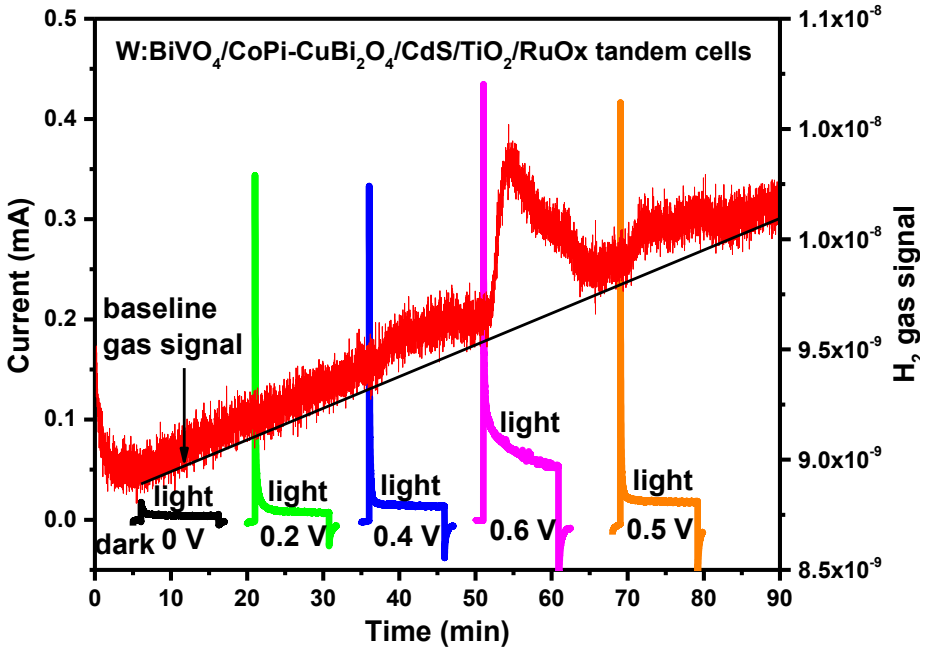

Figure 6.5. Simultaneous current and H_2 gas signal vs. time measurements for a W:$BiVO_4$/CoPi and $CuBi_2O_4$/CdS/TiO_2/RuO_x tandem cell measured in two-electrode configuration with various applied biases as labeled (0, 0.2, 0.4, 0.6, and 0.5 V). The measurements were performed in custom designed electrochemical cell with an inlet for purging with Ar gas and an outlet that was fed directly to a mass spectrometer. The electrolyte

was 0.3 M K_2SO_4 and 0.2 M phosphate buffer (pH 6.8) electrolyte. The W:$BiVO_4$/CoPi photoanode was the working electrode (WE) and the $CuBi_2O_4$/CdS/TiO_2/RuO_x photocathode was the counter electrode (CE). Simulated AM1.5 solar illumination (100 mW cm^{-2}) was activated as indicated in the figure.

In theory, the W:$BiVO_4$-$CuBi_2O_4$/CdS/TiO_2/RuO_x tandem device should be able to photoelectrochemically produce O_2 and H_2 at an applied bias at 0 V. The conduction band of $CuBi_2O_4$ estimated to be at -0.3 V vs. RHE and the valence band of $BiVO_4$ is at ~2.7 V vs. RHE so energy bands in the tandem device are wider than electrochemical potentials for proton reduction and water oxidation at 0.0 and 1.23 V vs. RHE, respectively.[26, 165] Additionally, the tandem device produced relatively low, but continuous photocurrent at an applied bias of 0 V. To gain a better understanding of the relationship between the photocurrent and the production of H_2 and O_2, we also performed differential electrochemical mass spectrometry (DEMS) measurements on the individual photoelectrodes in three-electrode configuration. These measurements allow a more sensitive detection of the evolved gases than the mass spectrometry measurements in **Figure 6.5**. The DEMS LSV scans for a $CuBi_2O_4$/CdS/TiO_2/RuO_x photocathode under illumination (light) and in the dark are shown in **Figure 6.6a** and **b**, respectively. Under illumination (**Figure 6.6a**), the $CuBi_2O_4$/CdS/TiO_2/RuO_x photocathode shows a minor photocurrent onset around ~0.9 V vs. RHE followed by a major photocurrent onset (red line) and H_2 gas signal (black line) both at ~0.3 V vs. RHE. **Figure 6.6b** shows the "photocurrent onset" at potentials negative of +0.9 V vs RHE is just the dark current. The minor photocurrent onset around ~0.9 V vs. RHE may be due to the reduction of a minute amount of dissolved oxygen, which could not be completely purged from the cell with Ar flow. Numerous electrocatalysts have shown an onset for the oxygen reduction reaction at 0.9-1.0 V vs. RHE.[185] Additionally, hydrogen electrosorption and electrochemical reduction of surface oxides (e.g. ruthenium oxide) can occur at various potentials more positive than 0.0 V vs. RHE.[186] These factors could also contribute to the photocurrent onset potential of 0.72 V vs. RHE for the $CuBi_2O_4$/CdS/TiO_2/RuO_x photocathode shown in **Figure 6.2c**, especially since that measurement was done in a larger cell that was exposed to air making it even more difficult to completely purge with Ar bubbling. The more important result shown in **Figure 6.6a** is the simultaneous onset in photocurrent and H_2 gas signal at ~0.3 V vs. RHE because that confirms that the $CuBi_2O_4$/CdS/TiO_2/RuO_x photocathode can produce H_2 photoelectrochemically at potentials more positive than the electrochemical potential for proton reduction. However, the onset of ~0.3 V vs. RHE is much worse than is expected considering that the conduction band of $CuBi_2O_4$ is approximately -0.3 V vs. RHE and the flat-band potential is 1.12-1.26 V vs. RHE based on previous reports in the literature and our Mott-Schottky analysis (see **Figure S C7** in the Supporting Information).[38, 165] The onset of H_2 gas signal at ~0.3 V vs. RHE rather than 1.12-1.26 V vs. RHE suggests that the photovoltage generated by the $CuBi_2O_4$/CdS/TiO_2/RuO_x is much smaller than the bandgap of the $CuBi_2O_4$ (1.5-1.8 eV). When the $CuBi_2O_4$/CdS/TiO_2/RuOx photocathode was tested at a constant potential of 0.0 V vs RHE for 1 h, it maintained a H_2 DEMS signal and a current of 0.13 nA and −200 μA, respectively as shown in **Figure S C8**. We also performed DEMS LSV measurements on $CuBi_2O_4$/Pt and $CuBi_2O_4$/RuO_x

photocathodes under illumination as shown in **Figure S C9** and **C10** in the Supporting Information. In these measurements the $CuBi_2O_4$/Pt and $CuBi_2O_4$/RuO_x photocathodes both showed signals for photocurrent but no H_2 gas signal was observed by DEMS at any electrochemical potential between 1.0 and 0.0 V vs. RHE, indicating that most of the photocurrent produced by these unprotected $CuBi_2O_4$ photocathodes is from photo-corrosion rather than proton reduction.

Figure 6.6c shows the DEMS measurements of W:$BiVO_4$/CoPi photoanode under illumination. The current density onset is around ~0.5 V vs. RHE while the onset for O_2 gas signal is delayed to around 0.7 V vs RHE. Similar to DEMS results for the $CuBi_2O_4$/CdS/TiO_2/RuO_x photocathode the DEMS results for the W:$BiVO_4$/Co-Pi photoanode show that the onset in photocurrent and O_2 gas signal is worse than expected. The valence band for $BiVO_4$ is estimated to be at 2.7 V vs. RHE and the Fermi level for our W:$BiVO_4$ photoanodes is 0.366 V vs. RHE based on our Mott-Schottky analysis (see **Figure S C7** in the Supporting Information) so the photovoltage provided by the W:$BiVO_4$/Co-Pi photoanodes is likely smaller than the bandgap of $BiVO_4$ (2.4 eV). Indeed, a recently developed potential-sensing electrochemical AFM technique has been used to measure the photovoltage of a $BiVO_4$/Co-Pi photoanode at ~1.05 V.[187] The difference of 0.2 V between photocurrent onset and O_2 gas signal onset that we observe is due to the delayed detection from the PEC to the mass spectrometer. Overall, the three-electrode DEMS measurement shown in **Figure 6.6a** and **6.6c** are in agreement with the two-electrode mass spectrometer results shown in **Figure 6.4**. The H_2 gas signal onset is 0.3 V vs. RHE and the O_2 gas signal onset is 0.7 V vs. RHE so there is no potential at which both gases are produced simultaneously. Moreover, the difference between the onset potentials is 0.4 V, which is the same value in applied bias at which H_2 production is first observed in **Figure 6.5**. In the dark (**Figure 6.6d**) the current and O_2 gas signal are essentially flat.

The mass spectrometry and DEMS results provide strong evidence that the internal photovoltages or quasi-Fermi level splitting of the W:$BiVO_4$ photoanode and $CuBi_2O_4$/CdS/TiO_2/RuO_x photocathode are the major limitations in the performance of the tandem device for overall water splitting. The internal photovoltage of photoelectrodes is difficult to measure using conventional photoelectrochemical apparatus.[187, 188] In an effort to quantify the photovoltage of the materials we performed photoluminescence (PL) measurements on W:$BiVO_4$, $CuBi_2O_4$, and $CuBi_2O_4$/CdS/TiO_2 photoelectrodes. PL has been demonstrated as a method for quantifying the internal photovoltage of the layers in thin film solar cells.[189] We used a PL system that can successfully detect the photovoltage of thin film materials with losses up to 0.9 V (compared to the bandgap of the materials). See **Figure S C9** in the Supporting Information as a reference. However, we could not detect a PL signal from the W:$BiVO_4$, $CuBi_2O_4$, and $CuBi_2O_4$/CdS/TiO_2 photoelectrodes even with 409 nm light excitation at a power density of 1000 suns. This suggests that the photovoltages losses in the photocathodes are at least 0.9 V. For $CuBi_2O_4$/CdS/TiO_2 photoelectrodes this would result in a photovoltage less than 0.6-0.9 V. This value is consistent with our finding

that an applied bias is required to produce H_2 from our W:$BiVO_4$/CoPi-$CuBi_2O_4$/CdS/TiO_2/RuO_x tandem device. Therefore, future work on $CuBi_2O_4$ as a photocathode material for a tandem water splitting device should focus on ways of protecting it from photocorrosion while also quantifying the photovoltage and if possible, improving it to a value that is closer to the bandgap.

In summary, we determined that this configuration with $CuBi_2O_4$ protected by a CdS/TiO_2 heterojunction overlayer and RuO_x added as a co-catalyst was ultimately required to perform overall water splitting. Unprotected $CuBi_2O_4$ did not produce a detectable amount of H_2 at any electrochemical potential. Since the electrochemical potential for the reduction of copper (Cu^{2+} + 2 e^- → Cu) is more positive than the potential for proton reduction, most of photocurrent likely went towards photo-corrosion of $CuBi_2O_4$ rather than proton reduction when bare $CuBi_2O_4$ was exposed to aqueous electrolyte even with Pt or RuO_x added as a co-catalyst. In contrast the $CuBi_2O_4$/CdS/TiO_2/RuO_x photocathode simultaneously produced photocurrent and a measurable amount of H_2 at potentials more positive than 0.0 V vs. RHE so it indeed performed hydrogen production photoelectrochemically.

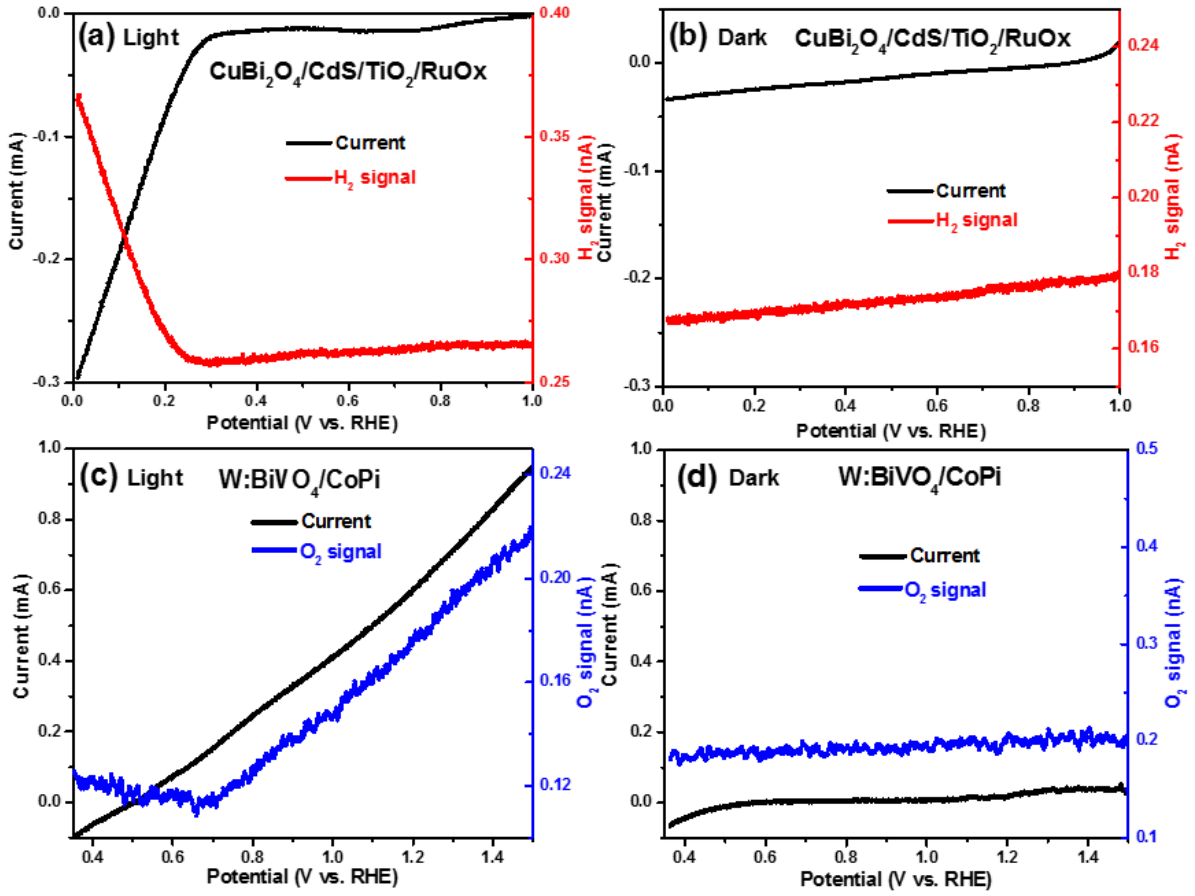

Figure 6.6. DEMS LSV scans for a $CuBi_2O_4$/CdS/TiO_2/RuO_x photocathode (a) under illumination (light) and (b) in the dark, showing measured current (red) and H_2 gas signal (black). DEMS LSV scans for a W:$BiVO_4$/CoPi photoanode

(c) under illumination (light) and (d) in the dark (d), showing measured current (blue) and O_2 gas signal (black). Measurements were done in 0.3 M K_2SO_4 and 0.2 M phosphate buffer (pH 6.8) under back illumination with a scan rate of 5 mV/s. The DEMS cell was continuously purged with Ar during the measurement.

6.3 Conclusions

In this chapter, we present a W:$BiVO_4$-$CuBi_2O_4$ photoanode/photocathode tandem photoelectrochemical cell for overall solar water splitting. Through a series of systematic investigations of the photoelectrochemical properties of this tandem device, we have clearly shown that there are several limitations in W:$BiVO_4$-$CuBi_2O_4$ tandem cell for overall water splitting. Firstly, the reflectance of W:$BiVO_4$ photoanode top absorber between 510 and 600 nm is an important factor that should be considered in the design of a tandem device. Meanwhile, the instability of the bare $CuBi_2O_4$ is another problem for this tandem device, since it does not produce a detectable amount of H_2 even when Pt or RuO_x as co-catalysts because the most of photocurrent go towards photo-corrosion of itself rather than proton reduction. This can be solved by coating a CdS/TiO_2 heterojunction protecting layer and adding RuO_x on top of $CuBi_2O_4$. However, CdS/TiO_2 heterojunction layer significantly decreases the photocurrent onset potential of $CuBi_2O_4$ from ~1.1 V to ~0.7 V vs. As a consequence, the reduced photocurrent onset potential of $CuBi_2O_4$ photocathode lead to a requirement for an applied bias for W:$BiVO_4$-$CuBi_2O_4$ tandem device. Nevertheless, this work is the first experimental demonstration of hydrogen production from a $BiVO_4$-$CuBi_2O_4$ based tandem device and the first identification of these crucial limitations in this tandem cell. These results illustrate that the limitations must be overcome for efficiently drive overall water splitting with this or other oxide-based photoelectrode materials in the future.

Chapter 7. Conclusions and outlook

7.1 Conclusions

The work conducted in this thesis aimed at developing high performance Cu-based multinary photoelectrodes for solar-driven water splitting. More specifically, this thesis mainly addressed the limitation in charge carrier transport at the interface between $CuBi_2O_4$ and n-type fluorine doped tin oxide (FTO), evaluated a novel multinary β-$Cu_2V_2O_7$ photoanode for solar water photo-oxidation, and constructed a tandem photoelectrochemical cell consisting of a W:$BiVO_4$ photoanode top absorber and a $CuBi_2O_4$ photocathode bottom absorber for overall solar water splitting. The method introduced in this work opens up possibilities in developing high performance solar water splitting devices that are based on earth-abundant, environmentally friendly Cu-based oxide semiconductors.

As has been well stated in chapter 1, the motivation for the research carried out in this thesis was described. The attractive characteristics of PEC water splitting are depicted. The fundamentals of PEC water splitting, including PEC cell basics, semiconductor physics, and requirements for photoelectrode materials are summarized in Chapter 2. Meanwhile, the constraints of P-type $CuBi_2O_4$ photocathode and n-type $BiVO_4$ photoanode for solar water splitting were presented in this part. Therefore this thesis introduced new approach to address the main limitations for $CuBi_2O_4$ and developed new lower band gap $Cu_2V_2O_7$ photoanode for solar water splitting. As discussed in details in the following chapters.

In chapter 4, we addressed the limitations of charge carrier transport at the interface between $CuBi_2O_4$ and n-type fluorine doped tin oxide (FTO) by inserting a very thin and transparent p-type Cu doped NiO (Cu:NiO) back contact layer. Due to the favourable band positions of back contact layer, the addition of Cu doped NiO improves the photoelectrochemical performance of FTO/Cu:NiO/$CuBi_2O_4$ photocathodes by reducing the barrier height at the $CuBi_2O_4$-substrate interface, while simultaneously driving selective extraction of photogenerated holes (blocking of electrons). As a result, the photocurrent density has been increased from 2.25 mA/cm^2 for FTO/$CuBi_2O_4$ photocathodes to 2.83 mA/cm^2 for FTO/Cu:NiO/$CuBi_2O_4$ photocathodes at 0.6 V versus RHE under backside illumination with H_2O_2 as an electron scavenger, which is a 24% enhancement in photocurrent density. That is the highest absolute value for a $CuBi_2O_4$ based photocathode up to date. Meanwhile, these results illustrate the importance of suitable band alignment and suggest a potential improvement strategy for other oxide-based photocathode materials.

Chapter 5 plays an important role in understanding the photoelectrochemical performance of Cu-based multinary photoelectrode (β-$Cu_2V_2O_7$) synthesized by a facile spray pyrolysis method and involves the techniques of catalyst modification. Monoclinic copper vanadate (n-type $Cu_2V_2O_7$) is a new lower band gap metal oxide-based

semiconductor photoanode material for solar water photo-oxidation. We have identified critical optoelectronic and photoelectrochemical properties of $Cu_2V_2O_7$ photoanodes, including bandgap, absorption coefficient, band positions, carrier mobility, carrier lifetime, carrier diffusion length, flat band potential, chemical composition, chemical stability, and O_2 evolution faradaic efficiency. The photoelectrochemical performance of $Cu_2V_2O_7$ photoanodes was found to be strongly limited by very poor charge carrier separation efficiency, since time-resolved microwave conductivity (TRMC) measurements revealed that the charge carrier mobility ($\sim 3.5 \times 10^{-3}$ cm^2 V^{-1} s^{-1}) and diffusion length ($\sim$28 nm) of $Cu_2V_2O_7$ photoanodes were very low and short. In addition, cobalt phosphate (Co-Pi) was used as a water oxidation co-catalyst to overcome the slow water oxidation kinetics responsible for the low performance of $Cu_2V_2O_7$.

In chapter 6, we assessed a tandem photoelectrochemical cell consisting of a W:$BiVO_4$ photoanode top absorber and a $CuBi_2O_4$ photocathode bottom absorber for overall solar water splitting. We show that the bare $CuBi_2O_4$ photocathode does not produce a detectable amount of H_2 because the photocurrent can go towards photo-corrosion of $CuBi_2O_4$ rather than H^+ reduction even when Pt or RuO_x is added as a co-catalyst. In contrast the $CuBi_2O_4$/CdS/TiO_2/RuO_x photocathode produced both photocurrent and a measurable amount of H_2 at potentials more positive than 0.0 V vs. RHE so it indeed performed hydrogen production photoelectrochemically.

In summary, nanostructured $CuBi_2O_4$ and β-$Cu_2V_2O_7$ have successfully been prepared and found to reduce the bandgap than $BiVO_4$. This thesis demonstrates an explicit way of investigating Cu-based multinary photoelectrodes and applying modification techniques to enhance their PEC performance.

7.2 Outlook

Although the high efficient and relatively stable PEC device based on Cu-based photoelectrodes were realized, there is still a long way before achieving solar-to-hydrogen efficiencies necessary for commercial application. Nevertheless, the study presented in this thesis provided an effective method to decrease the barrier height between substrates and $CuBi_2O_4$ photocathode, developed a new multinary $Cu_2V_2O_7$ photoanode for solar water oxidation. However, there are still several remaining problems to be addressed for these two different photoelectrodes.

(1) Development of new protection layers for $CuBi_2O_4$ photocathodes, since we already know that bare $CuBi_2O_4$ photocathodes suffered photo-corrosion when illuminated in aqueous electrolyte. Chapter 6 demonstrates that the CdS/TiO_2/RuOx layers can improve the stability of $CuBi_2O_4$ photocathodes for hydrogen production. However, the CdS/TiO_2 heterojunction significantly decreases the photocurrent onset potential of $CuBi_2O_4$ from ~1.1 V to ~

0.6 V vs RHE, which causing a loss in photovoltage. This is a crucial limitation in for protected $CuBi_2O_4$ photocathodes, which must be overcome for efficiently water splitting.

(2) Optimization of thin film CuO-V_2O_5 based photoelectrodes. It is known that by stoichiometric variation of the Cu to V ratio in the $Cu_xV_yO_z$ system a number of temperature dependent stoichiometric phases and polytypes can exist. Chapter 5 only evaluates an n-type $Cu_2V_2O_7$ as a photoanode material for solar water oxidation. TRMC measurements show that poor charge carrier transport are the main reason for the fast recombination in $Cu_2V_2O_7$. Considering the charge separation efficiency is still low for nanostructured $Cu_2V_2O_7$ even with CoPi as co-catalyst. To improve the photoconversion efficiency further, different OER catalysts, protection layers, and interfacial layers can be used for CuO-V_2O_5 based photoelectrodes.[169] Similar strategies can also be used in the development of other CuO-V_2O_5 based metal oxide materials for PEC water splitting.

(3) Another Cu-based photoelectrode, p-type $Cu_2V_5O_{10}$, is also a very promising photocathode material for water splitting due to its suitable bandgap of 1.8–2.0 eV and its exceptionally positive photocurrent onset potential near +1 V vs. RHE. However, there are very few reports on this material as a photocathode material for water splitting so far. Therefore, future work can also be focused on investigating $Cu_2V_5O_{10}$ for photoelectrochemical water splitting.

Appendix A: Supplemental Information for Cu:NiO as a hole-selective back contact to improve the photoelectrochemical performance of $CuBi_2O_4$ thin film photocathode

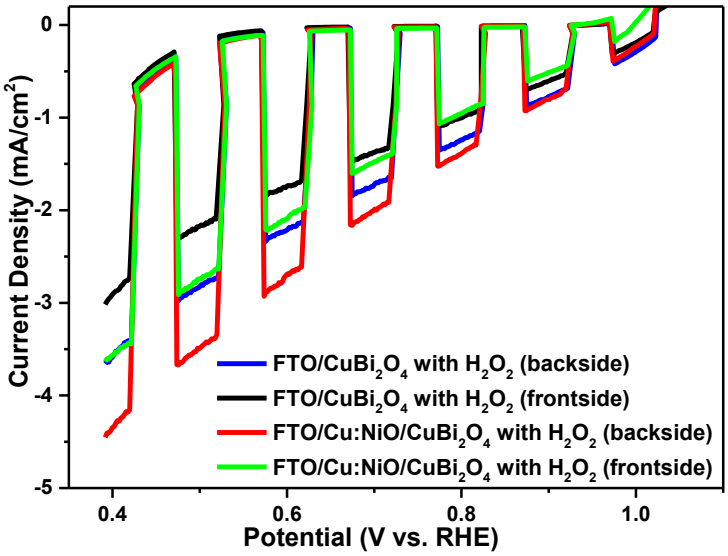

Figure S A1. LSV scans for $CuBi_2O_4$ films on FTO and FTO/Cu:NiO (7 nm) at a thicknesses of 260 nm measured in 0.3 M K_2SO_4 and 0.2 M phosphate buffer (pH 6.65) with H_2O_2 added as an electron scavenger under back and front illumination.

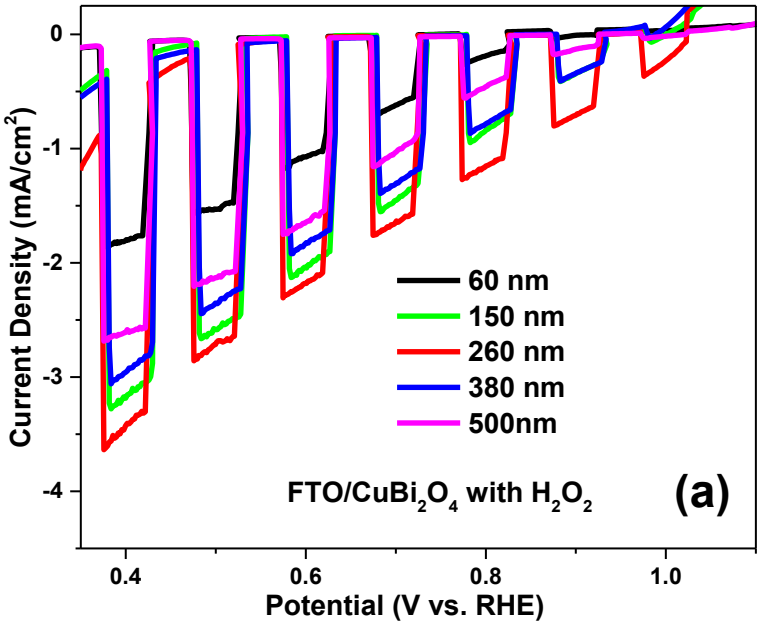

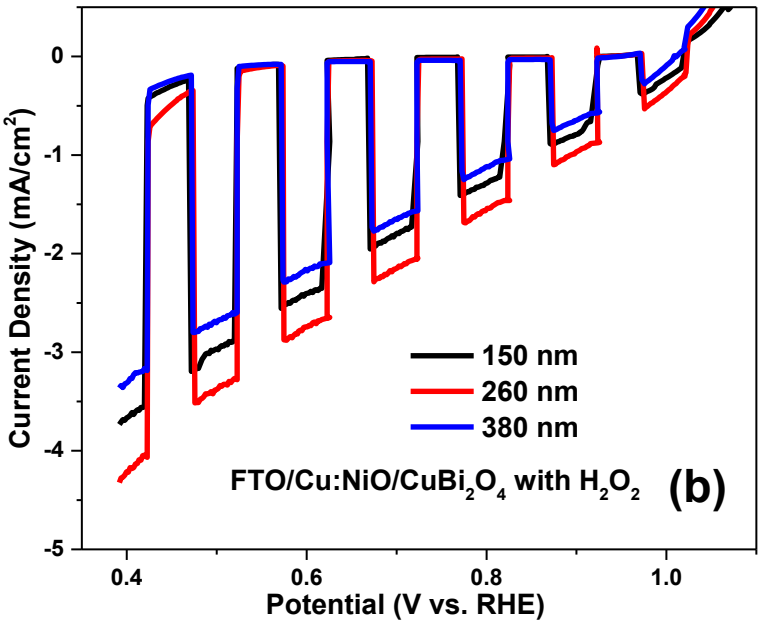

Figure S A2. (a) LSV scans for FTO/$CuBi_2O_4$ and (b) FTO/Cu:NiO (7 nm) /$CuBi_2O_4$ films at different film thicknesses measured in 0.3 M K_2SO_4 and 0.2 M phosphate buffer (pH 6.65) with H_2O_2 added as an electron scavenger under backside illumination.

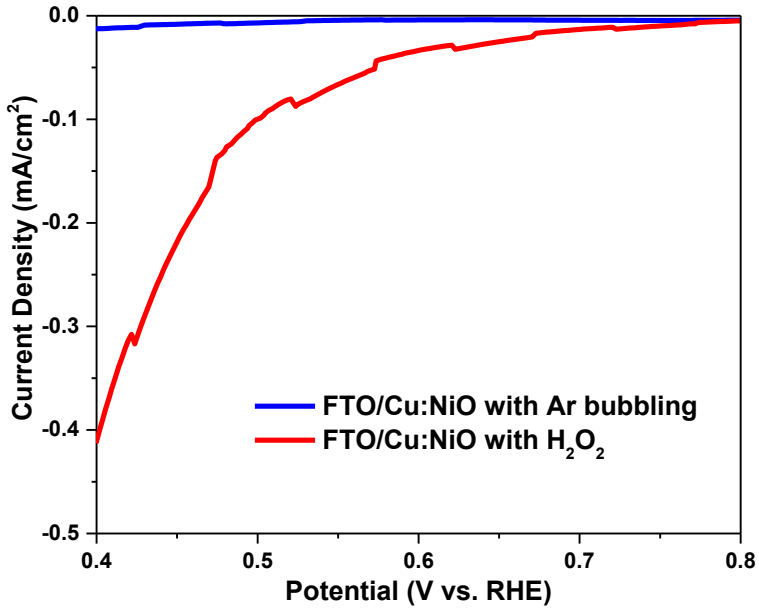

Figure S A3. LSV scans for Cu:NiO at a thicknesses of 34 nm measured in 0.3 M K_2SO_4 and 0.2 M phosphate buffer (pH 6.65) with Ar bubbling and with H_2O_2 under backside illumination.

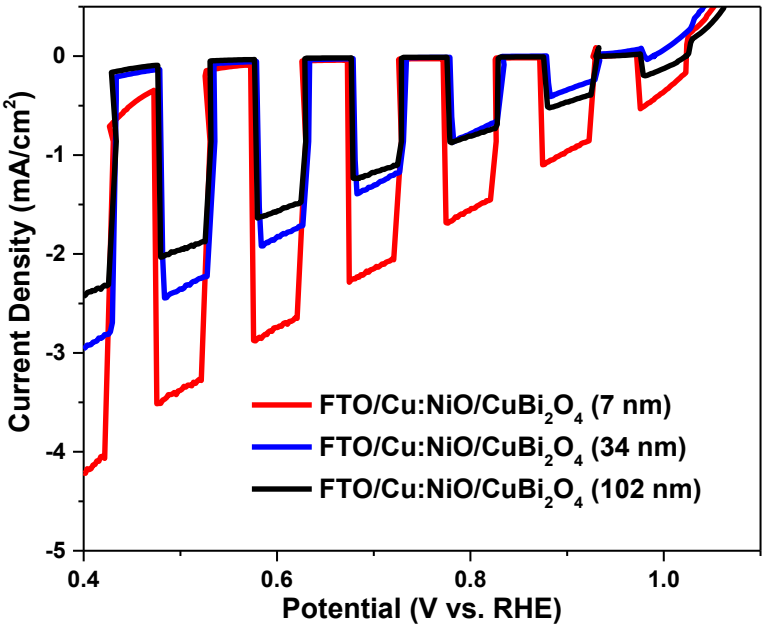

Figure S A4. LSV scans for $CuBi_2O_4$ films (~260 nm) based on different film thicknesses of Cu:NiO (7, 34, and 102 nm) measured in 0.3 M K_2SO_4 and 0.2 M phosphate buffer (pH 6.65) with H_2O_2 under backside illumination.

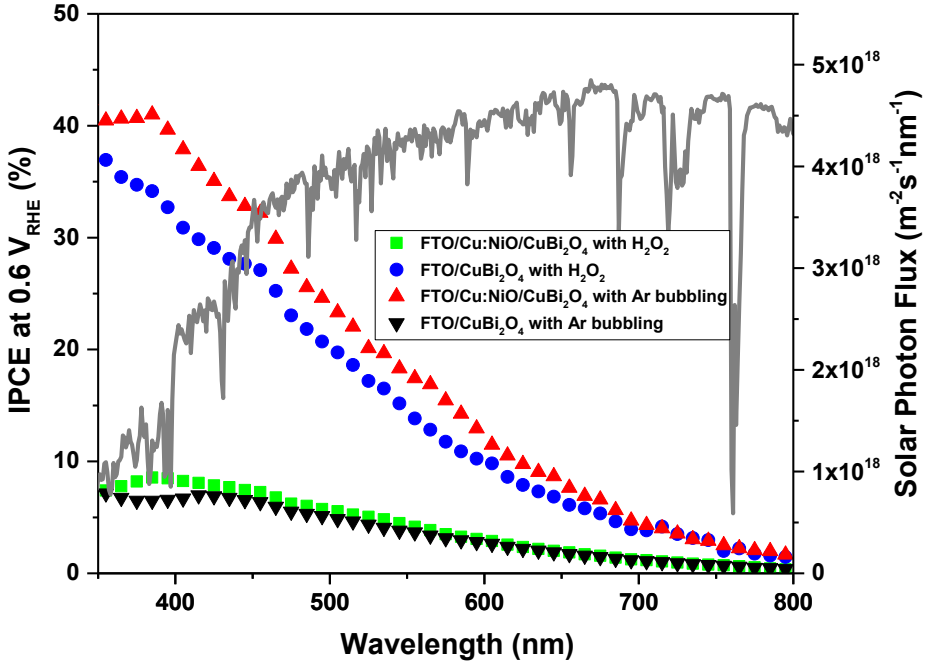

Figure S A5. IPCE spectra of $CuBi_2O_4$ on FTO (blue dot line), $CuBi_2O_4$ on Cu:NiO (red and green dot line). The measurements were performed in 0.3 M K_2SO_4 and 0.2 M phosphate buffer (pH 6.65) with H_2O_2 under backside illumination.

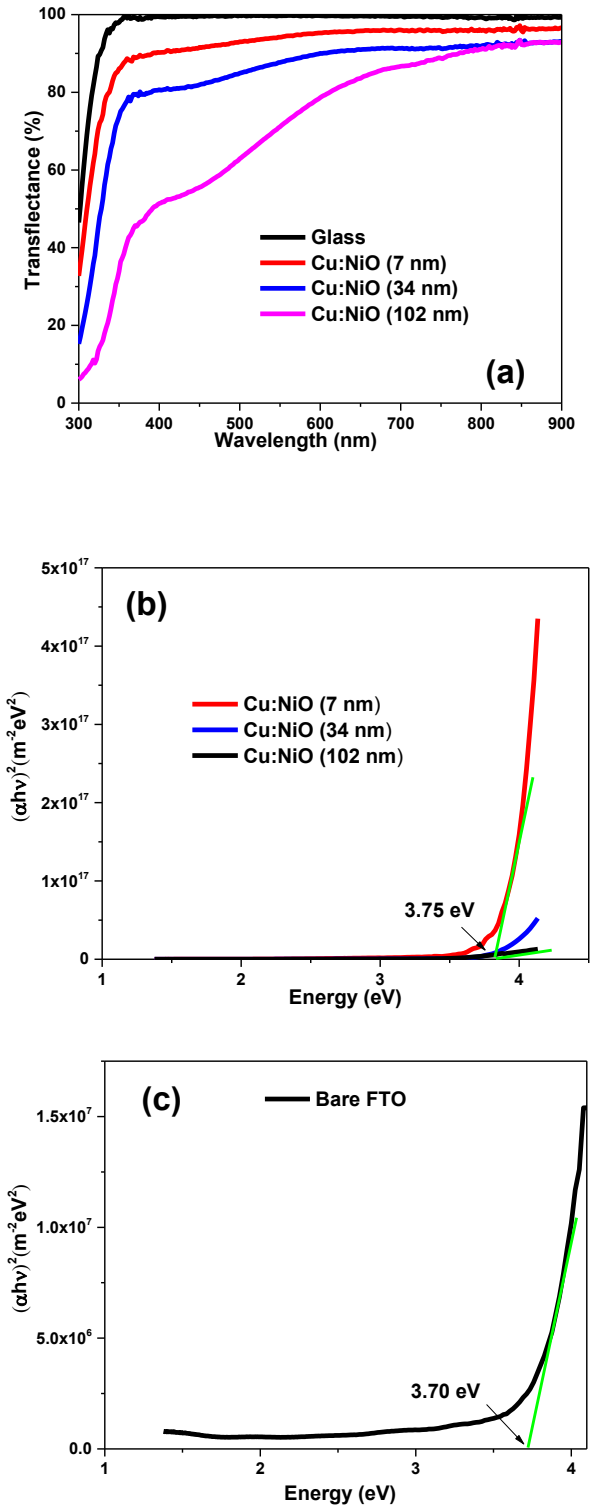

Figure S A6. (a) Transflectance spectra and (b) direct bandgap Tauc plots for Cu:NiO thin films with different thicknesses (7, 34, and 102 nm) deposited on glass substrates and (c) direct band gap Tauc plot of FTO substrate.

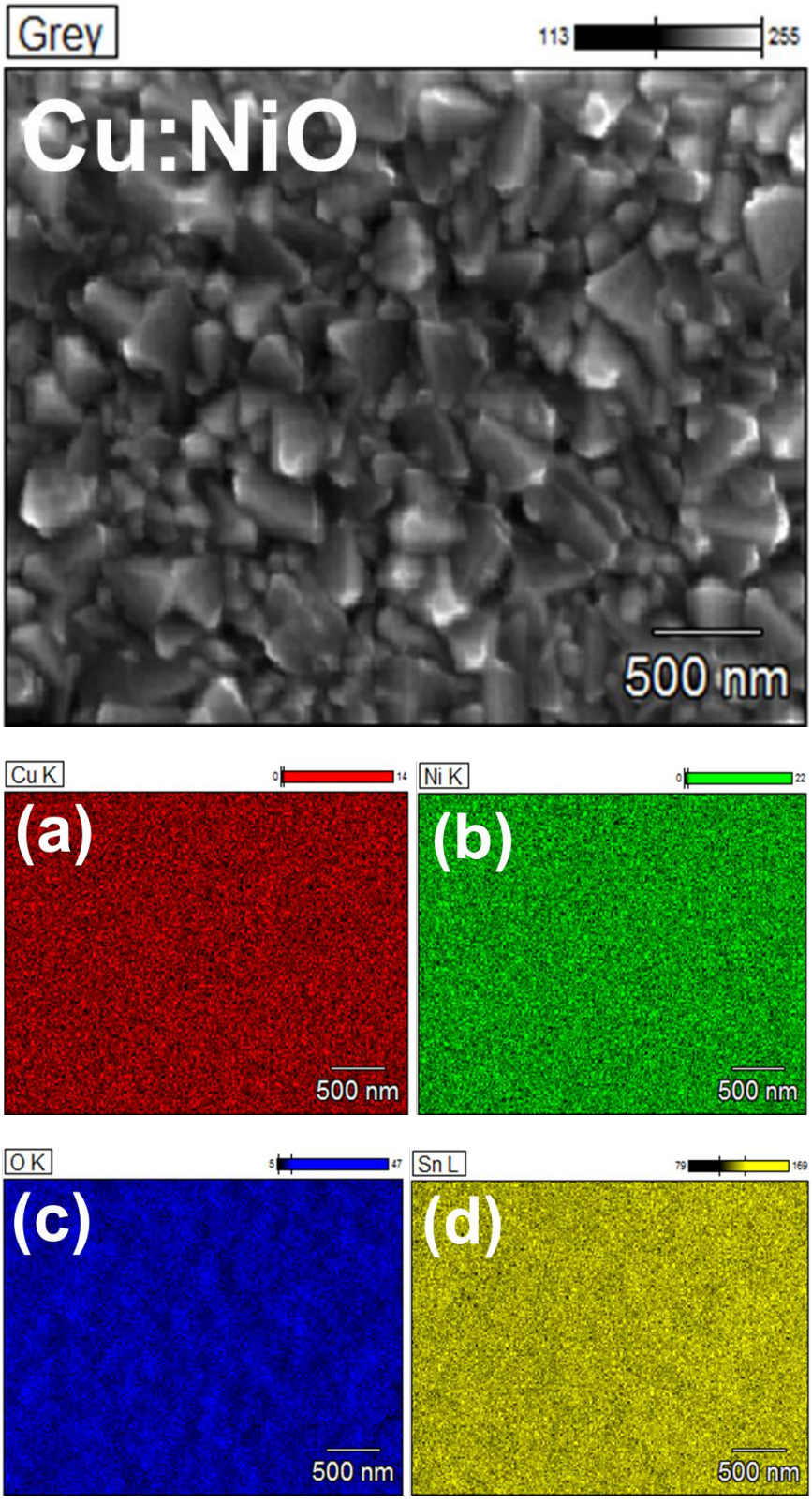

Figure S A7. Top-view SEM image of 7 nm Cu:NiO thin film deposited on FTO and corresponding EDX elemental mapping of (b) Cu (c) Bi, (d) O, and (e) Sn.

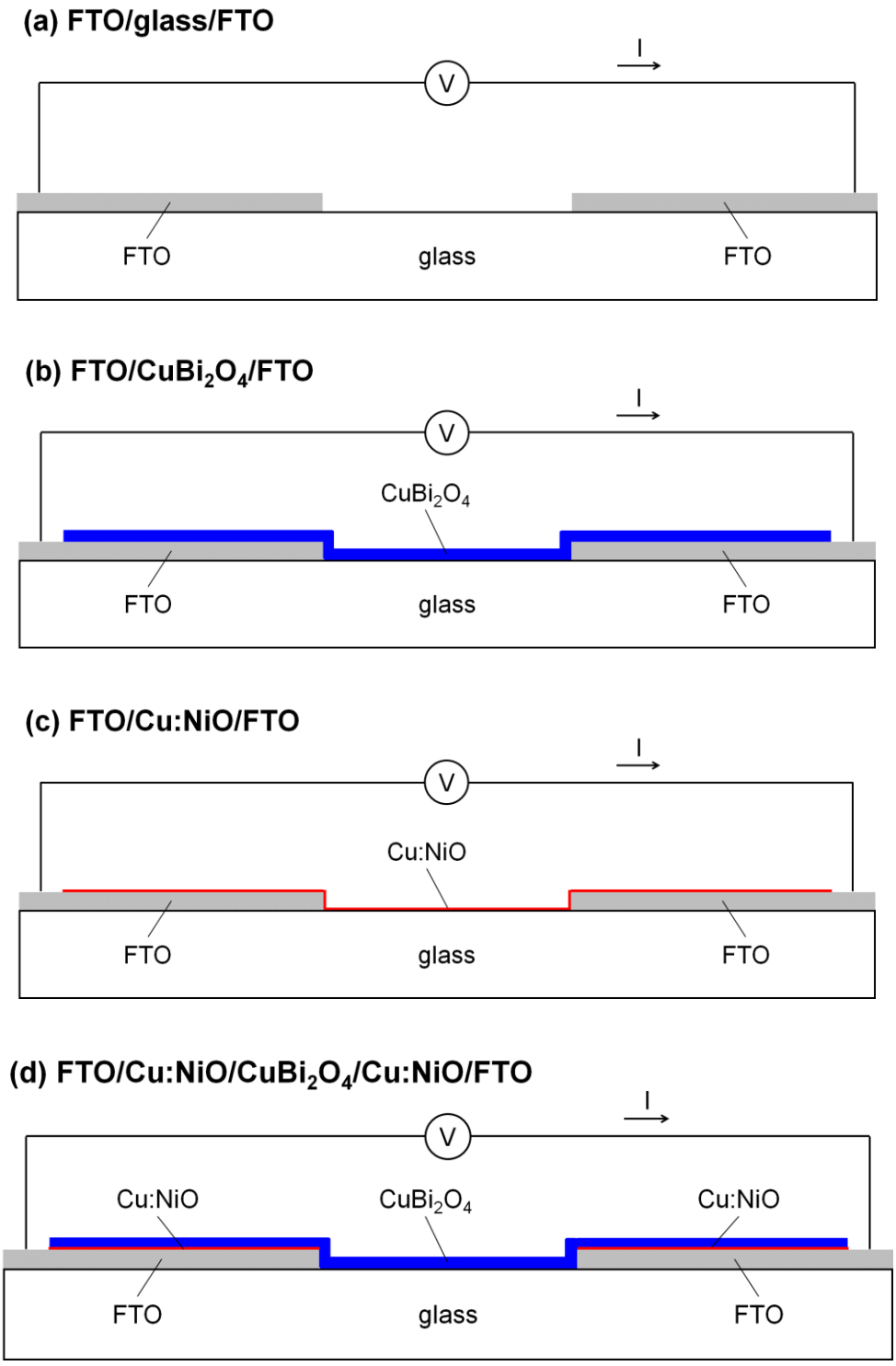

Figure S A8. Schematics of the (a) FTO/glass/FTO, (b) FTO/$CuBi_2O_4$/FTO, (c) FTO/Cu:NiO/FTO, and (d) FTO/Cu:NiO/$CuBi_2O_4$/Cu:NiO/FTO samples used for solid-state I-V measurements. The $CuBi_2O_4$ and Cu:NiO thicknesses were 260 and 7 nm, respectively.

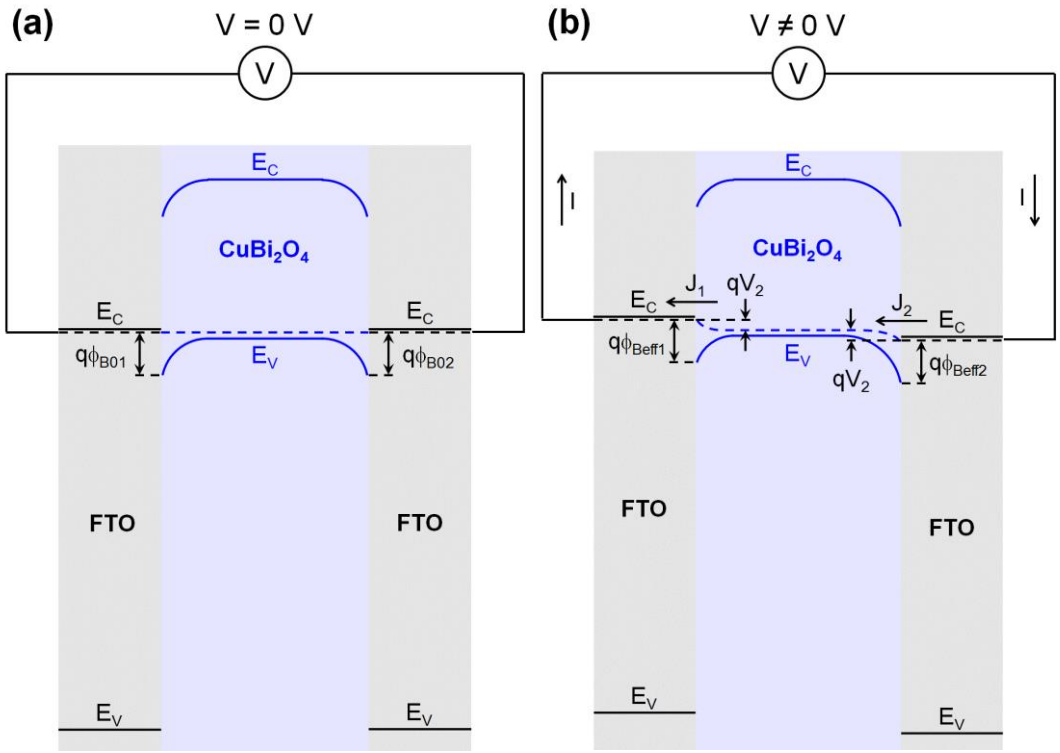

Figure S A9. Schematic illustrating the band bending of back-to-back Schottky barriers (FTO/$CuBi_2O_4$/FTO sample) at (a) V = 0 V and (b) V ≠ 0 V.

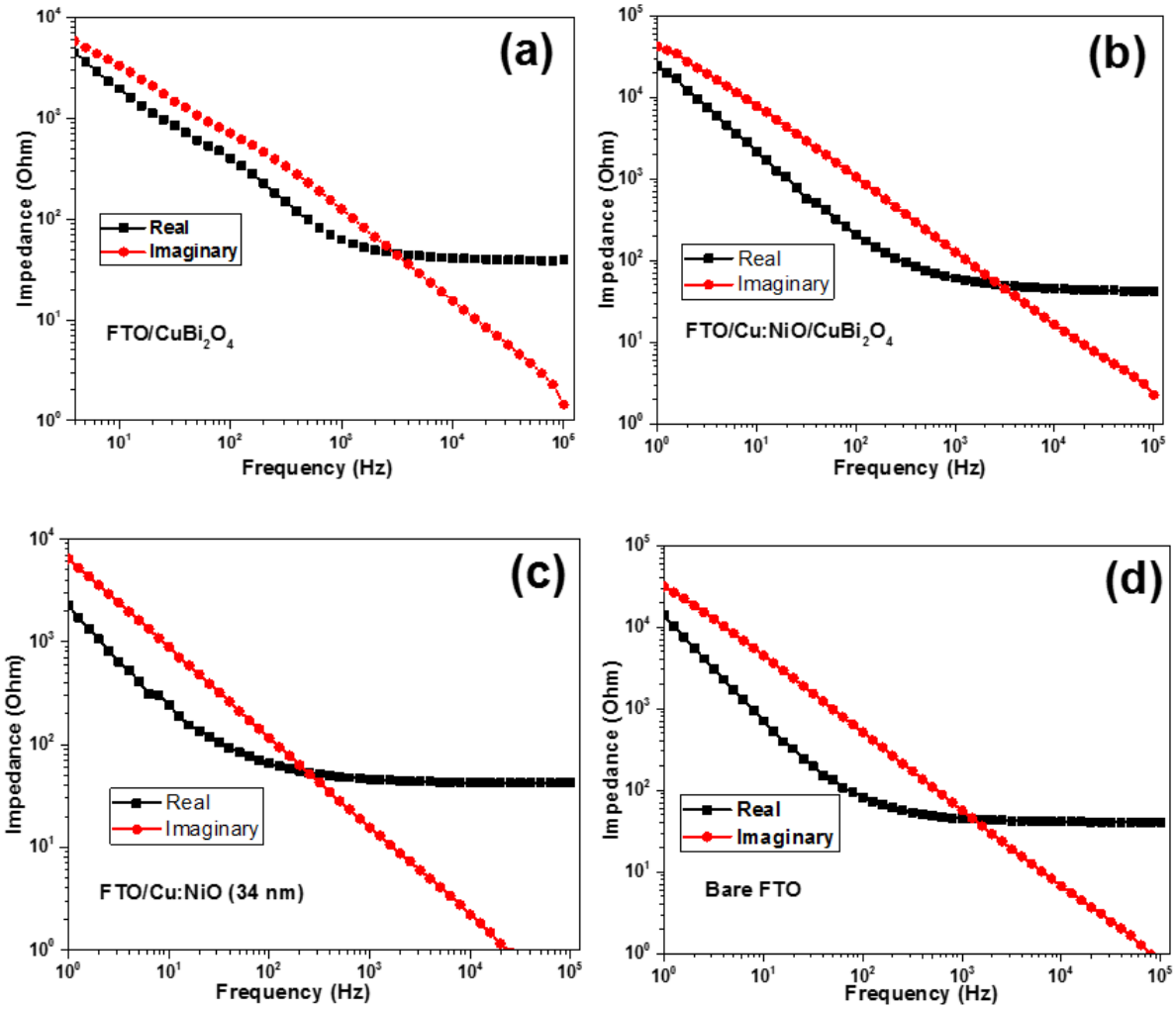

Figure S A9. Electrochemical impedance spectroscopy (EIS) at 1.00 V vs. RHE for (a) $CuBi_2O_4$ deposited on FTO, (b) $CuBi_2O_4$ (260 nm) deposited on Cu:NiO (7 nm) on FTO, (c) Cu:NiO (34 nm) deposited on FTO, and (d) bare a FTO substrate. The measurements were performed in 0.3 M K_2SO_4 and 0.2 M phosphate buffer (pH 6.65). Note that above 1 kHz, the real part of the impedance is constant, whereas the imaginary part has a slope of -1. This implies that the system behaves as a resistance in series with a pure capacitance, which is a prerequisite for Mott-Schottky analysis.

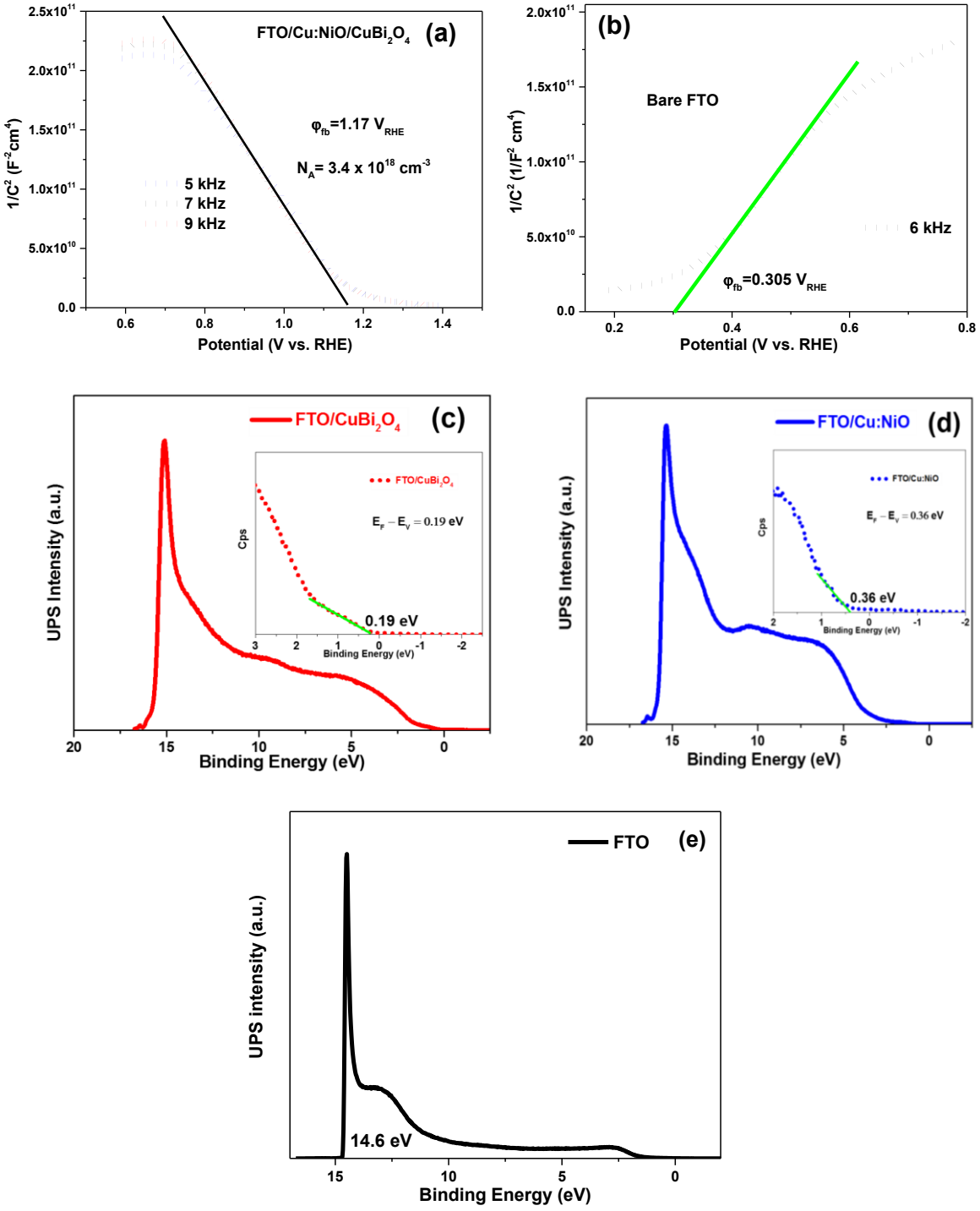

Figure S A10. Mott−Schottky plots obtained for $CuBi_2O_4$ films and bare FTO. (a) Mott−Schottky of $CuBi_2O_4$ films deposited on 5 nm Cu:NiO film (b) Mott−Schottky of bare FTO. UPS cutoff spectra measured without bias for (c) $CuBi_2O_4$ and (d) Cu:NiO thickness of 34 nm deposited on FTO substrates and UPS cutoff spectra measured with a 2 V bias for a bare FTO substrate. Mott−Schottky measurements were performed in 0.3 M K_2SO_4 and 0.2 M phosphate buffer (pH 6.65) at 5 kHz, 7 kHz, and 9 kHz.

Table SA1. Summarizing Energy Levels

Material	Band Gap, E_g (eV)	Flat Band Potential, φ_{fb} (eV / V vs. RHE)	Work Function, WF (eV / V vs. RHE)	Average, E_F (φ_{fb} & WF) (eV / V vs. RHE)	n-type N_A p-type N_D(cm^{-3})	p-type $\lvert E_V - E_F \rvert$ (eV)	Valence Band Offset $\lvert E_V - E_F \rvert$
FTO	3.7	4.81 / 0.31	4.61 / 0.11	4.71 / 0.21	1×10^{21}		
Cu:NiO	3.75	5.21 / 0.71	5.11 / 0.61	5.16 / 0.66	4.6×10^{18}	< 0.077	0.36
$CuBi_2O_4$	1.6	5.62 / 1.12	5.79 / 1.29	5.71 / 1.21	3.2×10^{18}	< 0.077	0.19

Appendix B: Supplemental Information for evaluation of β-$Cu_2V_2O_7$ as a photoanode material for photoelectrochemical water oxidation

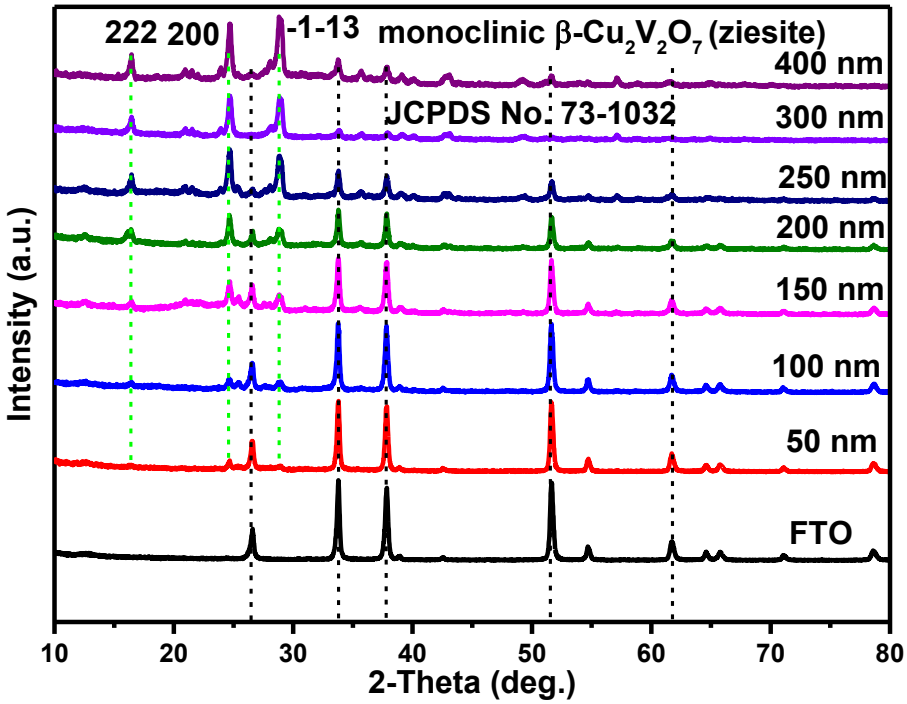

Figure S B1. X-ray diffractograms of annealed (500 °C in air for 2 hours) $Cu_2V_2O_7$ films with various thicknesses.

Figure S B2. Photograph of a $Cu_2V_2O_7$ thin film deposited on an FTO-coated glass substrate.

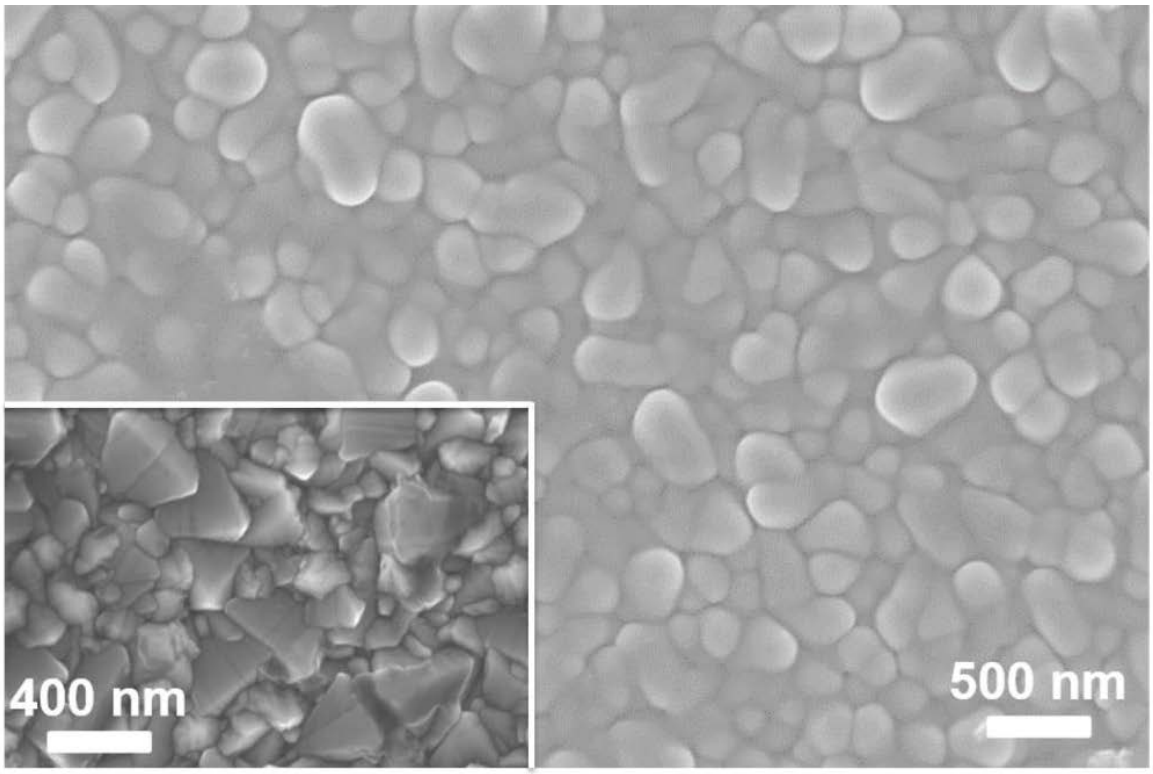

Figure S B3. Scanning electron micrograph (SEM) of $Cu_2V_2O_7$ thin film deposited on FTO at 300°C. The inset (left corner) shows the SEM of the FTO substrate for comparison.

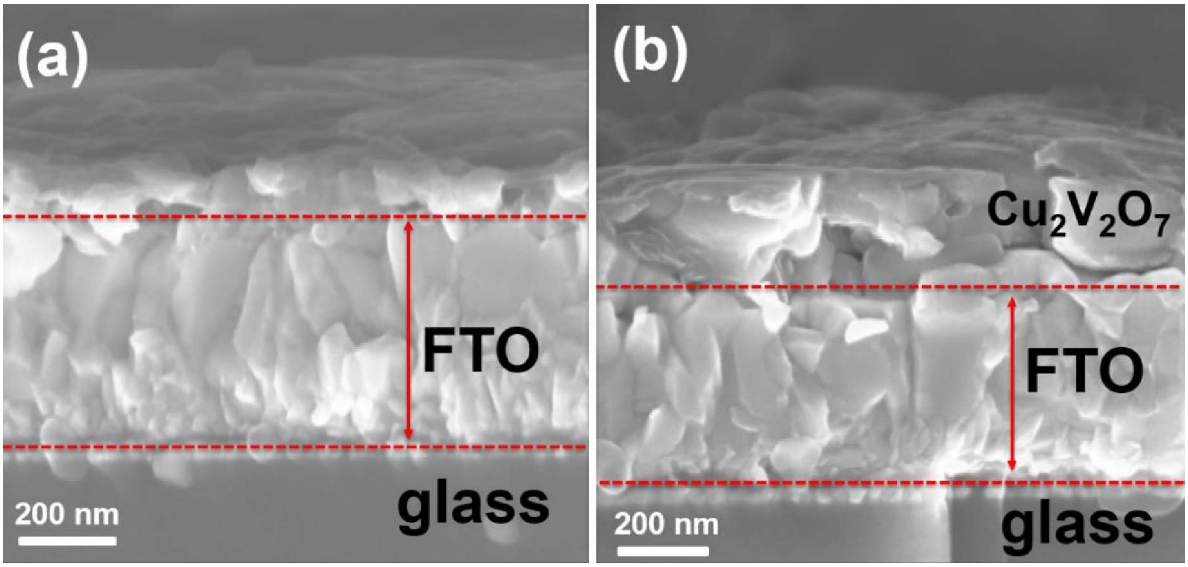

Figure S B4. Cross-section SEM images of annealed samples sprayed with (a) 100 mL and (b) 300 mL precursor.

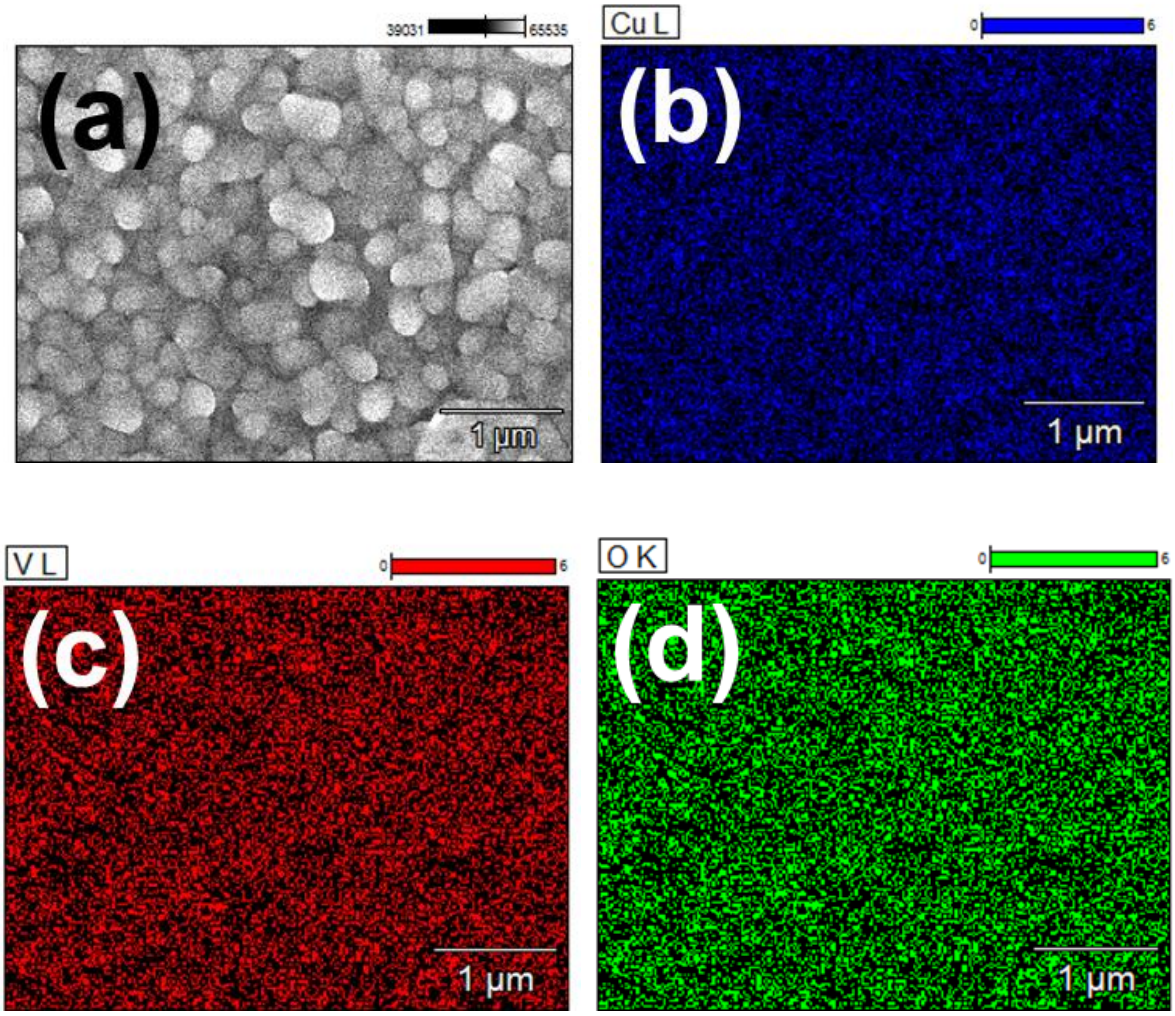

Figure S B5. Top-view SEM image of 200 nm $Cu_2V_2O_7$ deposited on FTO and corresponding EDX elemental mapping of (b) Cu (c) V, (d) O.

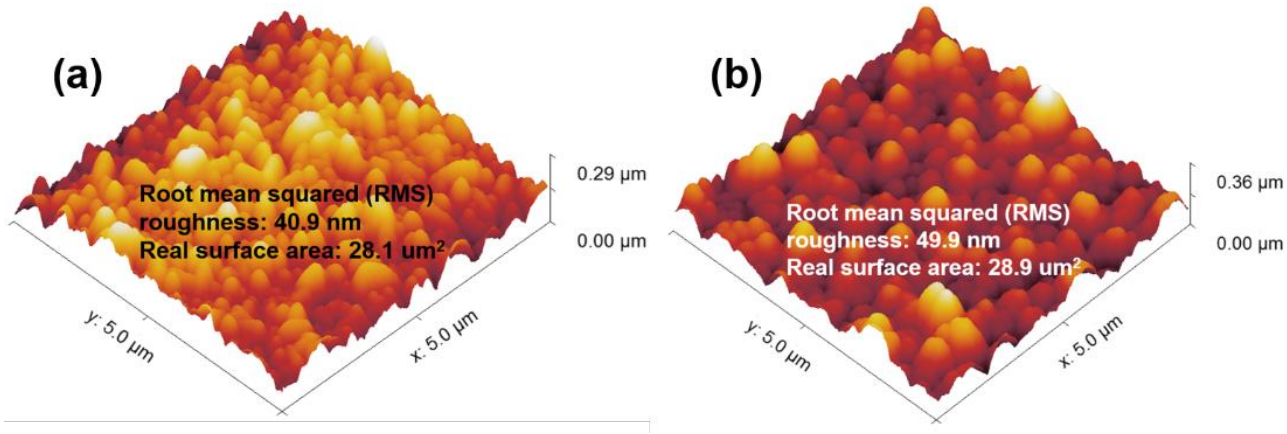

Figure S B6. AFM images of (a) a bare FTO substrate (for comparison) and (b) a ~200 nm $Cu_2V_2O_7$ film.

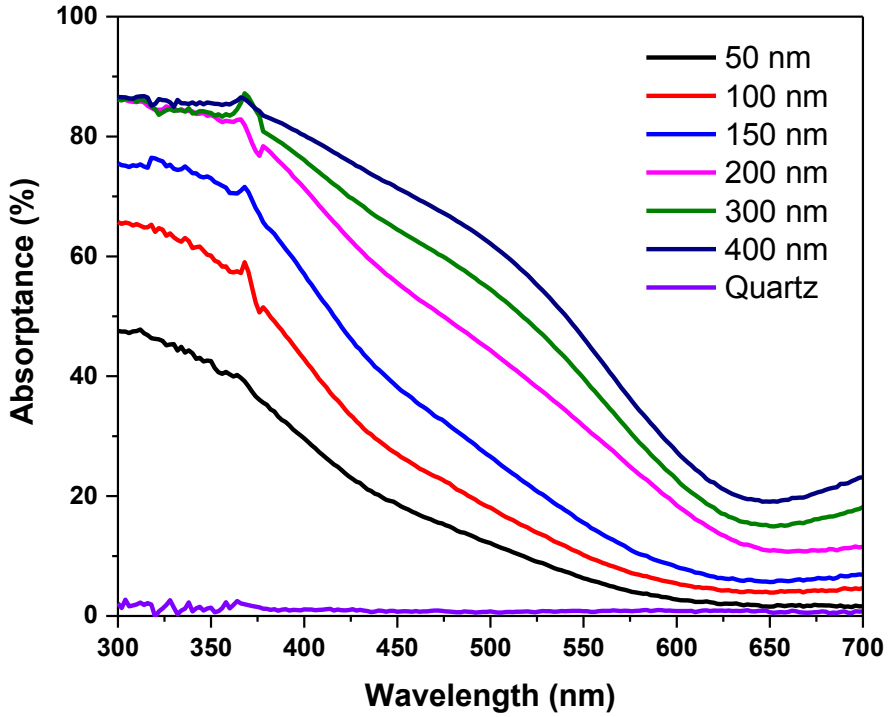

Figure S B7. Absorption spectra of annealed $Cu_2V_2O_7$ with various thicknesses.

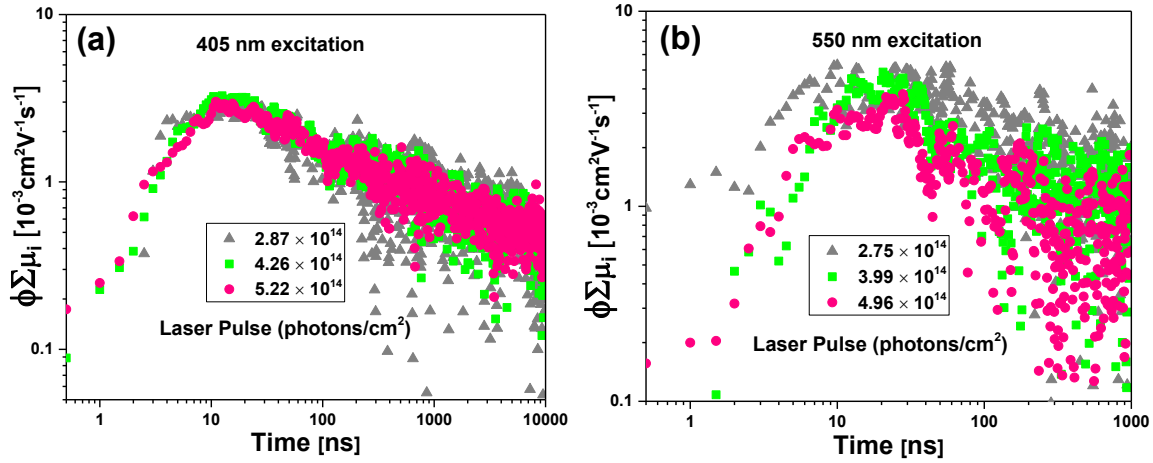

Figure S B8. TRMC signal under various incident laser pulse intensities for a $Cu_2V_2O_7$ film synthesized by spray pyrolysis on a quartz substrate under (a) 405 nm wavelength and (b) 550 nm wavelength excitation.

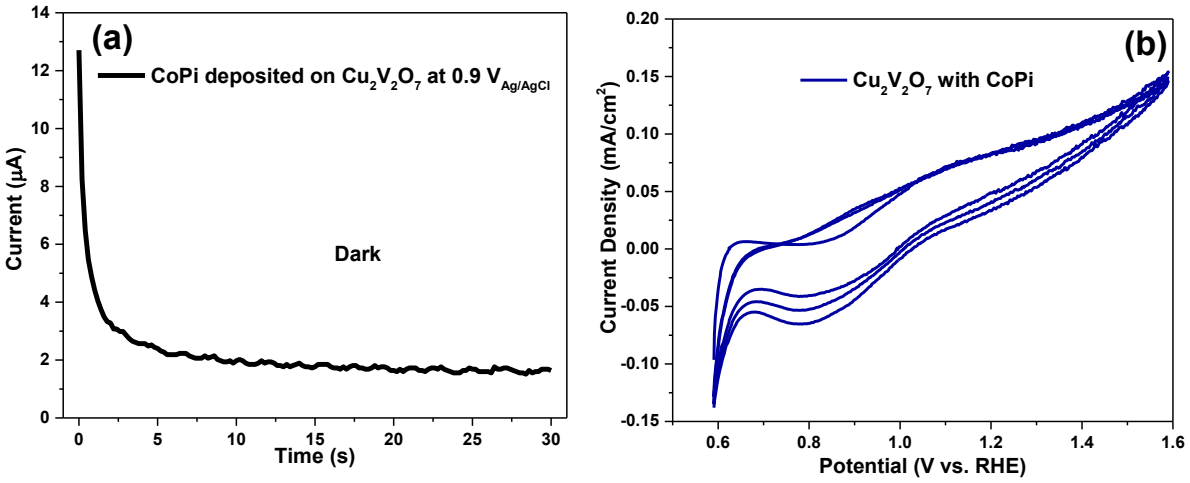

Figure S B9. (a) Current vs. time during electrodeposition Co-P_i catalyst onto $Cu_2V_2O_7$ film at a potential of 0.9 V vs. Ag/AgCl (b) Cyclic voltammograms on a 200 nm $Cu_2V_2O_7$ film modified with a CoP_i catalyst in 0.3 M K_2SO_4 and 0.2 M phosphate buffer (pH 6.8). The scan rate was 20 mV s^{-1}.

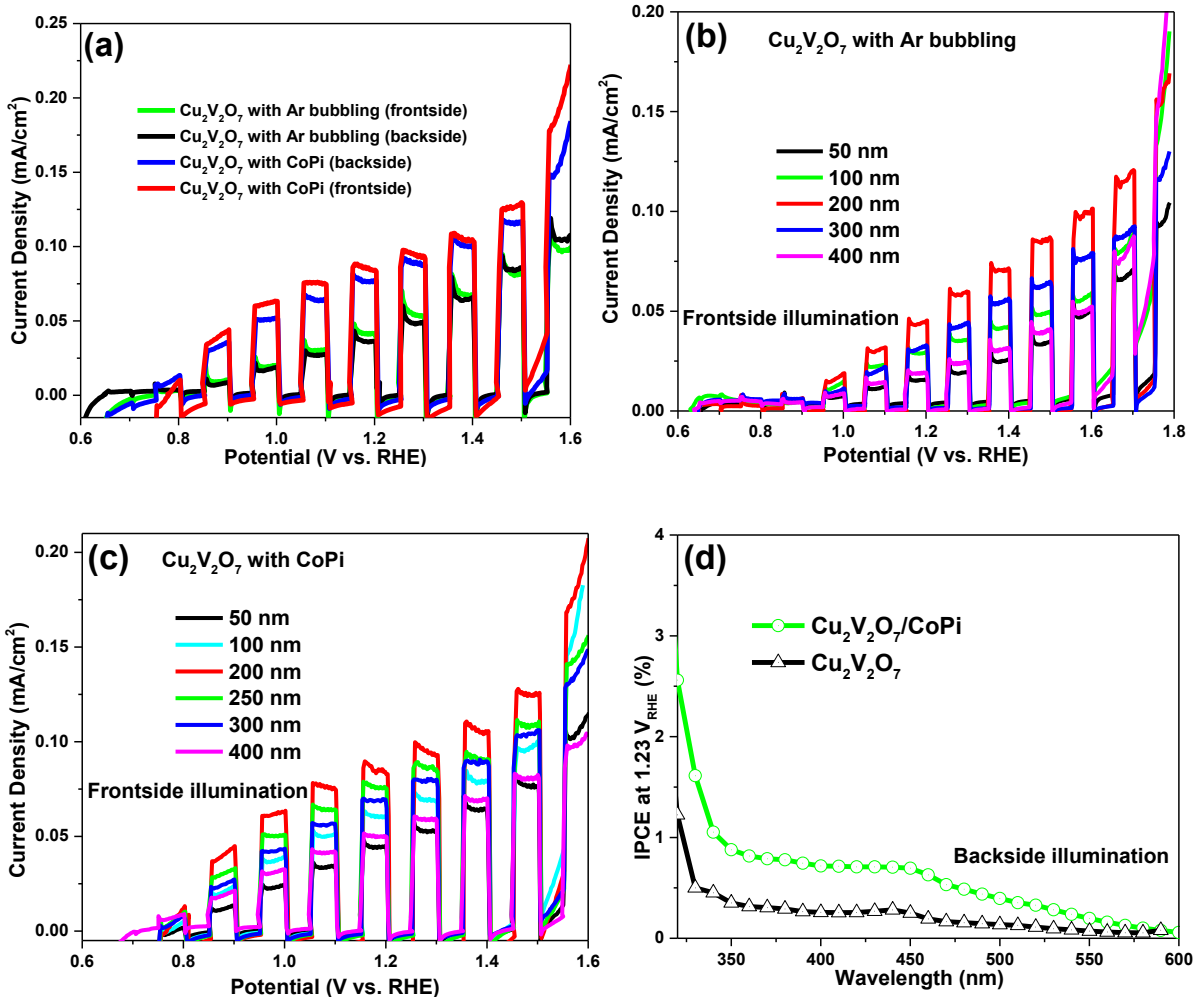

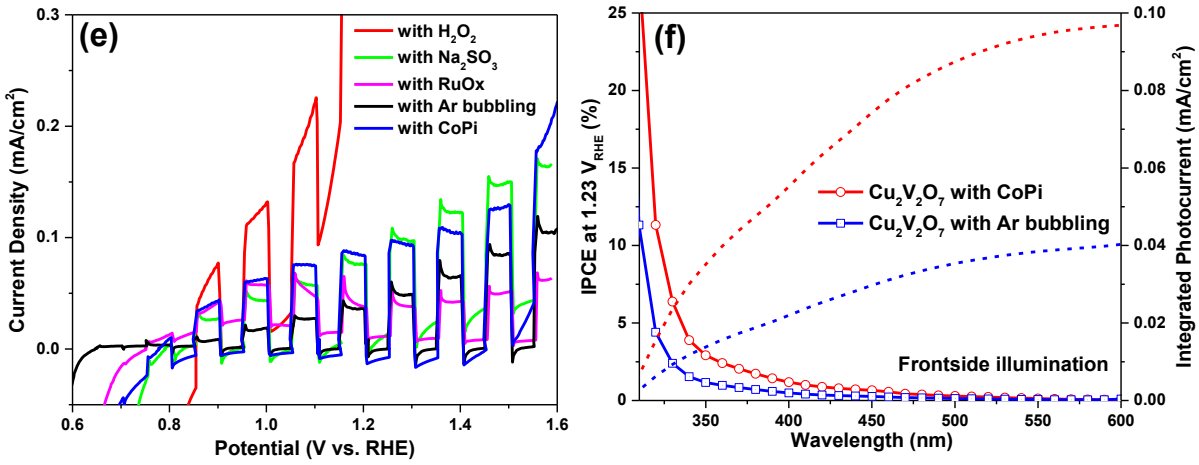

Figure S B10. (a) Chopped LSV scans for $Cu_2V_2O_7$ films with a thickness of 200 nm measured with Ar bubbling and with CoPi catalyst under backside and frontide illumination. (b) Chopped LSV scans for $Cu_2V_2O_7$ films at different film thicknesses (from 50 nm to 400 nm) measured with Ar bubbling. (c) Chopped LSV scans for $Cu_2V_2O_7$ films at different film thicknesses (from 50 nm to 400 nm) measured with with CoPi catalyst. (d) IPCE spectra of $Cu_2V_2O_7$ with Ar bubbling (black dot line) and with CoPi catalyst (green dot line) measured at a potential of 1.23 V vs. RHE under backside illumination. (e) Choped LSV scans for $Cu_2V_2O_7$ films at a thicknesses of 200 nm measured with H_2O_2, Na_2SO_3 hole scavenger, RuOx catalyst, Ar bubbling and CoPi catalyst under backside and frontide illumination. (f) IPCE spectra of $Cu_2V_2O_7$ measured with Ar bubbling (green solid line), and CoPi catalyst (red solid line), corresponding integrated photocurrents are represented by the dotted lines.

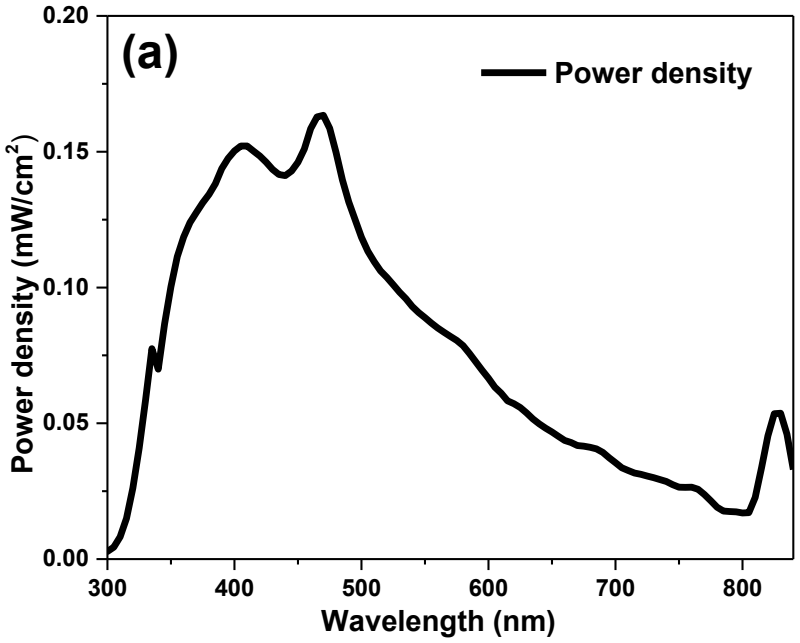

Figure S B11. Power spectra for IPCE measurements.

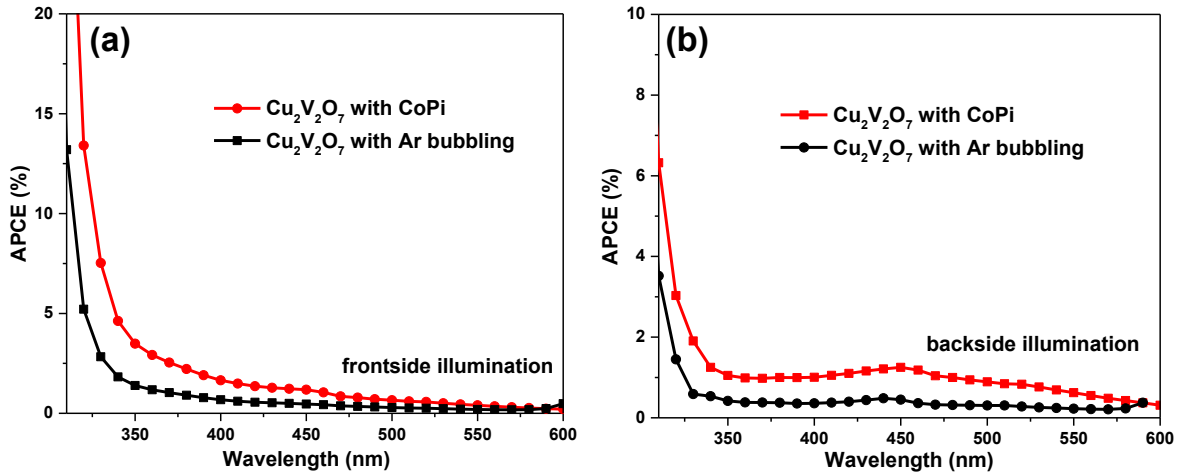

Figure S B12. APCE measurements for $Cu_2V_2O_7$ photoanodes conducted in 0.3 M K_2SO_4 and 0.2 M phosphate buffer (pH 6.8) with CoP_i catalyst and with Ar bubbling as indicated in the figure legend. Measurements were conducted under (a) frontside and (b) backside illumination as indicated.

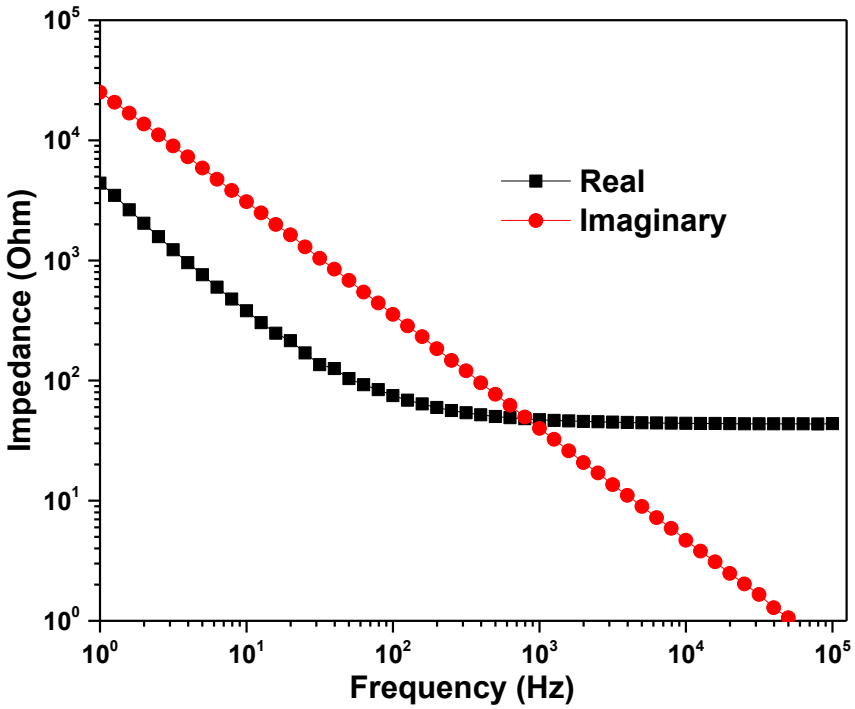

Figure S B13. Electrochemical impedance spectroscopy (EIS) at 0.65V vs. RHE for a 200 nm $Cu_2V_2O_7$ photoanode. The measurements were performed in 0.3 M K_2SO_4 and 0.2 M phosphate buffer (pH 6.8).

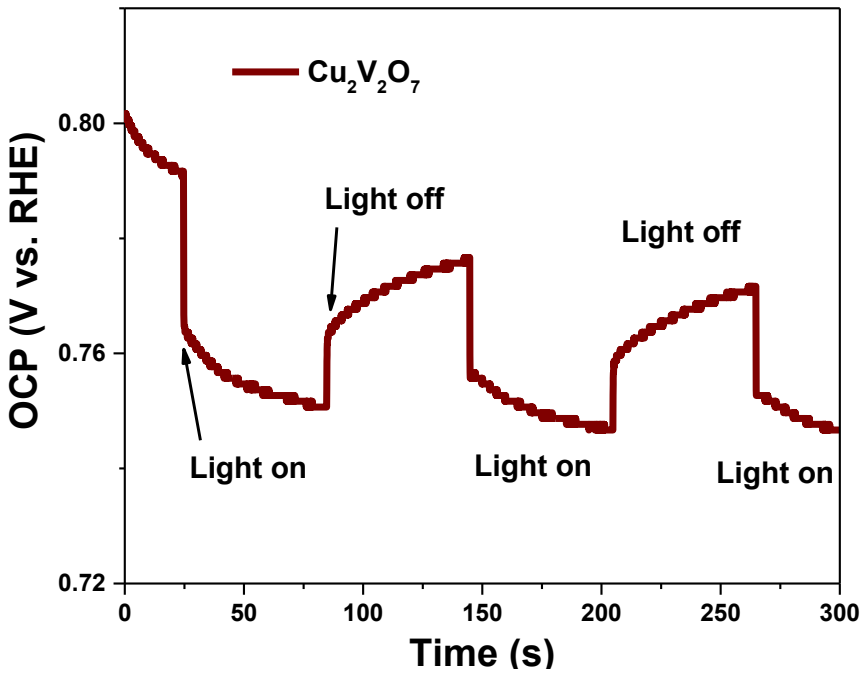

Figure S B14. Open-circuit potential (OCP) measurements in the dark and light for a $Cu_2V_2O_7$ photoanode in 0.3 M K_2SO_4 and 0.2 M phosphate buffer (pH 6.8) with Ar bubbling. The illumination was from the frontside.

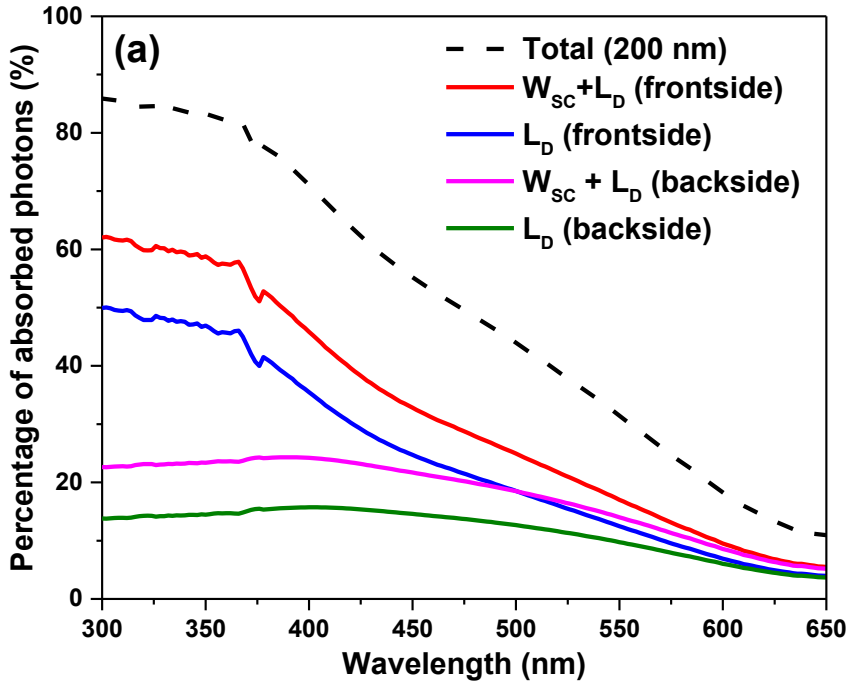

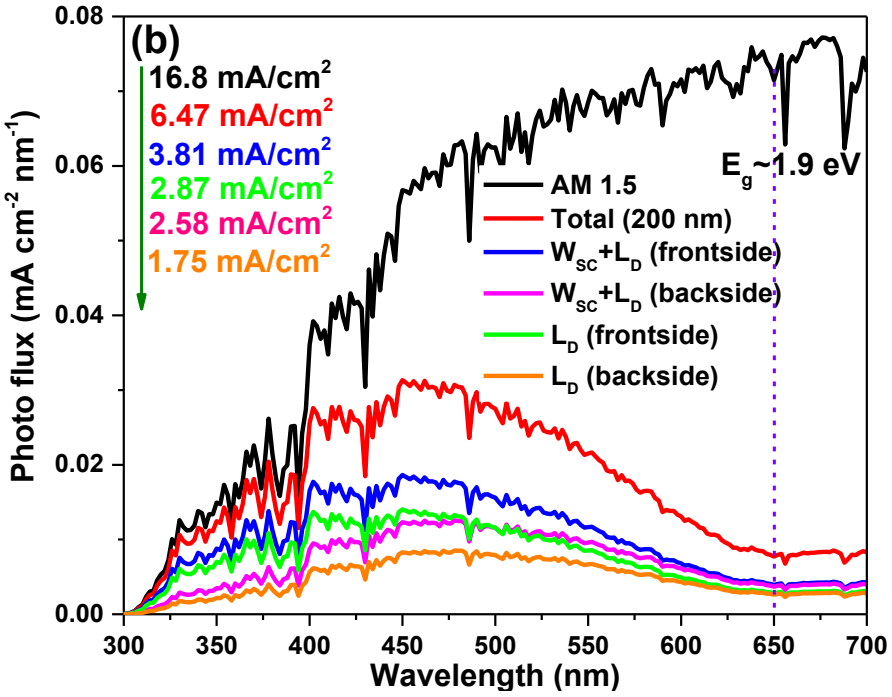

Figure S B15. (a) Absorption for a 200 nm $Cu_2V_2O_7$ photoanode based on the Gärtner model. (b) Parts of the AM1.5 spectrum absorbed by a 200 nm $Cu_2V_2O_7$ film calculated from the Gärtner model.

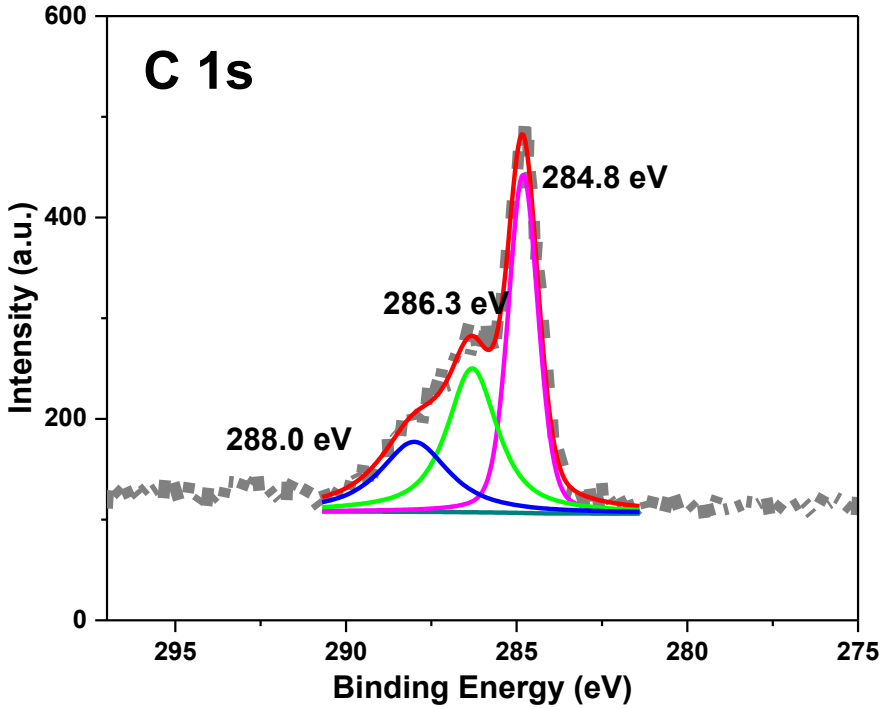

Figure S B16. XPS spectra (C 1s) of a 200 nm $Cu_2V_2O_7$ photoanode deposited on FTO. XPS measurement was carried out at the sample surface with further plasma cleaning.

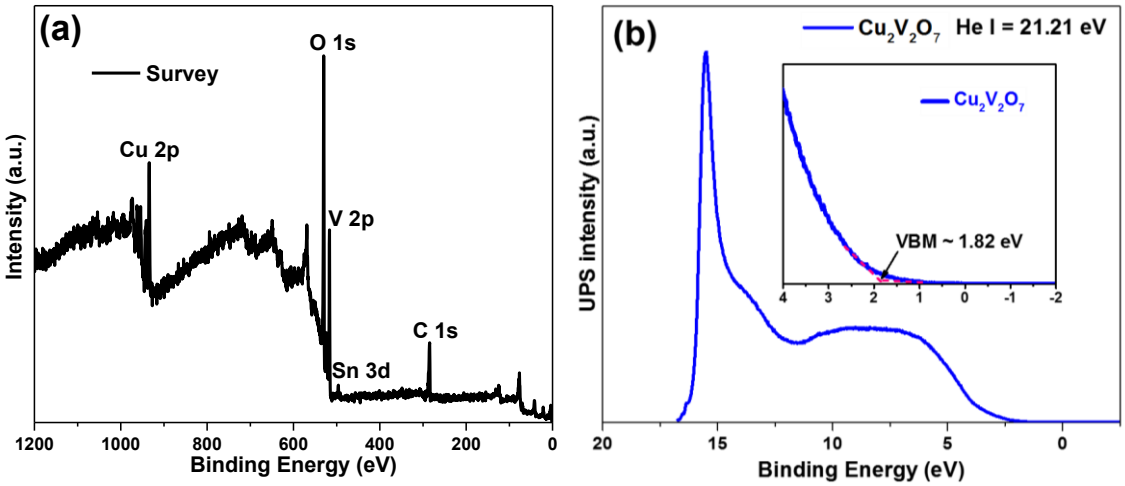

Figure S B17. XPS spectra of a 200 nm $Cu_2V_2O_7$ photoanode deposited on FTO (a) survey spectra and (b) UPS cutoff spectra measured without bias for $Cu_2V_2O_7$ thin film. XPS measurement was carried out at the sample surface with further plasma cleaning.

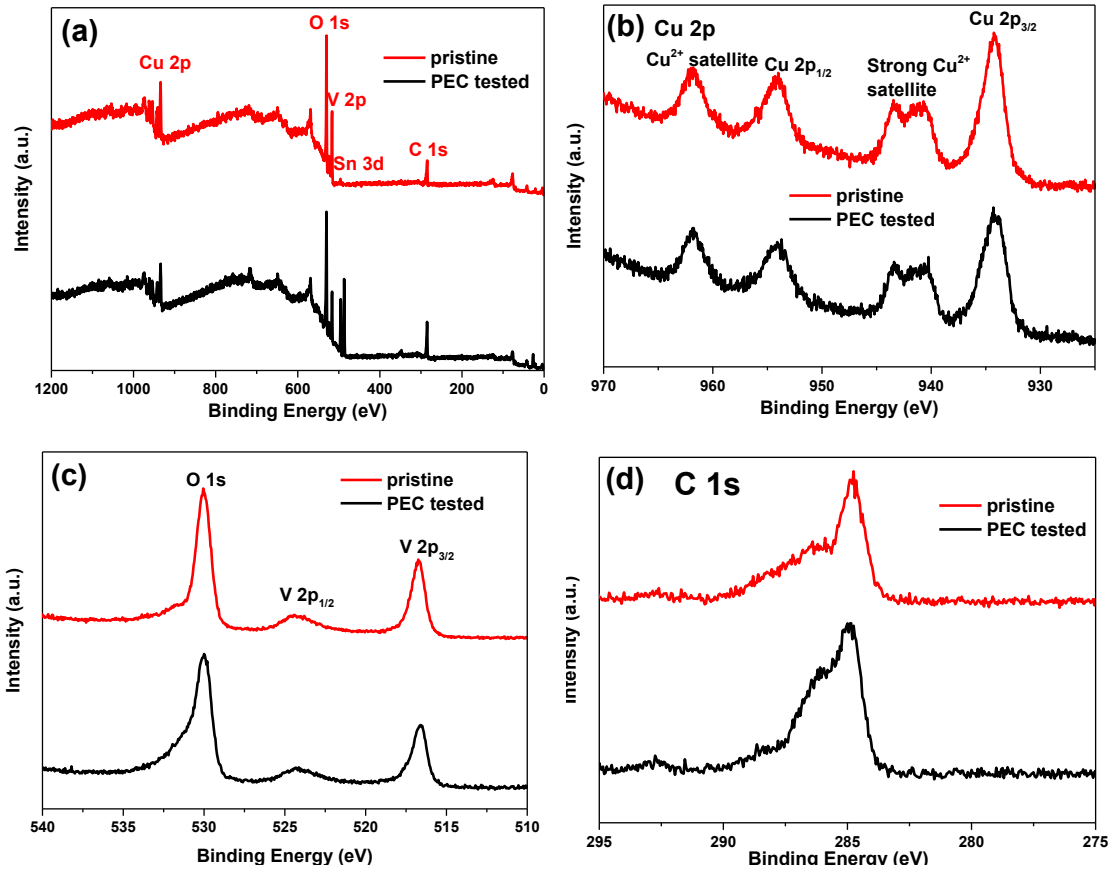

Figure S B18. XPS spectra of a 200 nm $Cu_2V_2O_7$ photoanode before (for comparison) and after PEC test (a) survey spectra, (b) Cu 2p, (c) O 1s and V 2p and (d) C 1s.

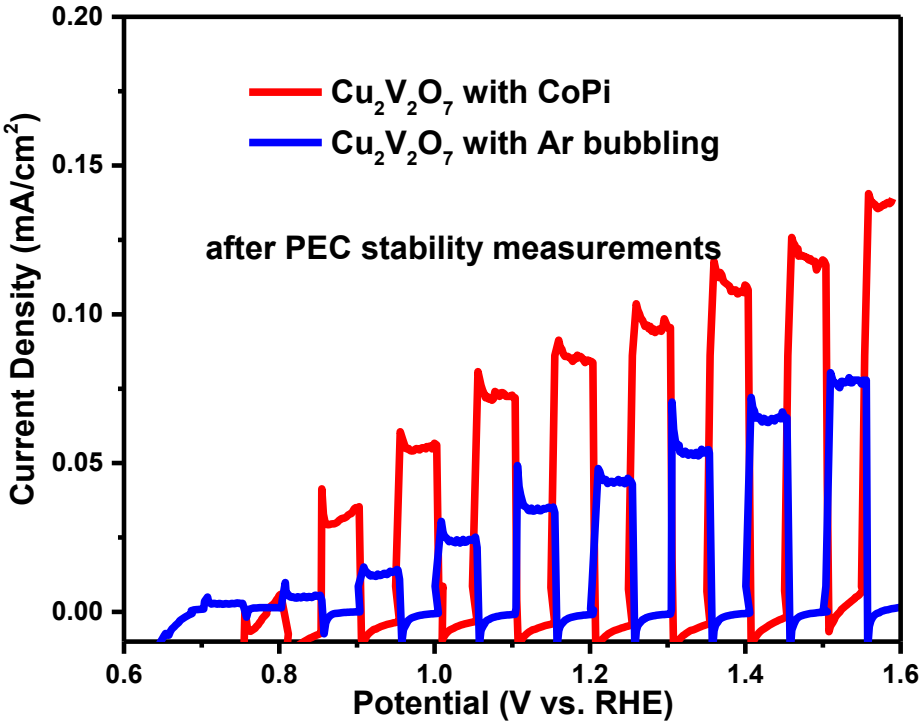

Figure S B19. Choped LSV scans for $Cu_2V_2O_7$ films at a thicknesses of 200 nm measured with Ar bubbling and with CoPi catalyst under frontside illumination after PEC stability measurements. Measurements were performed in 0.3 M K_2SO_4 and 0.2 M phosphate buffer (pH 6.8).

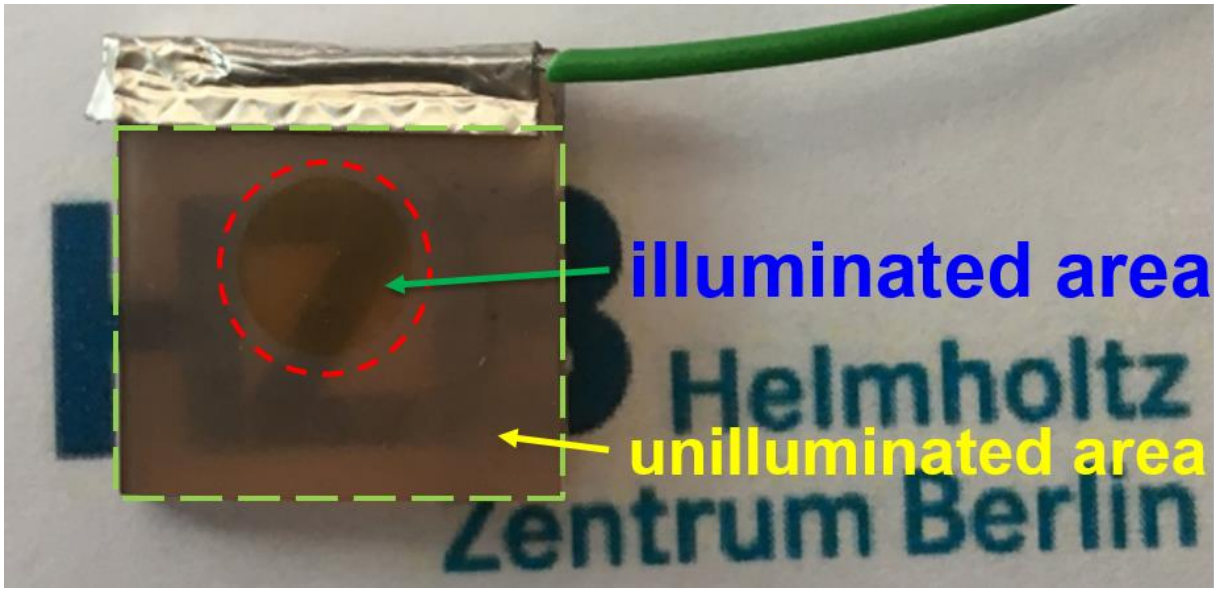

Figure S B20. Photograph of a $Cu_2V_2O_7$ thin film deposited on an FTO-coated glass substrate after PEC stability measurements.

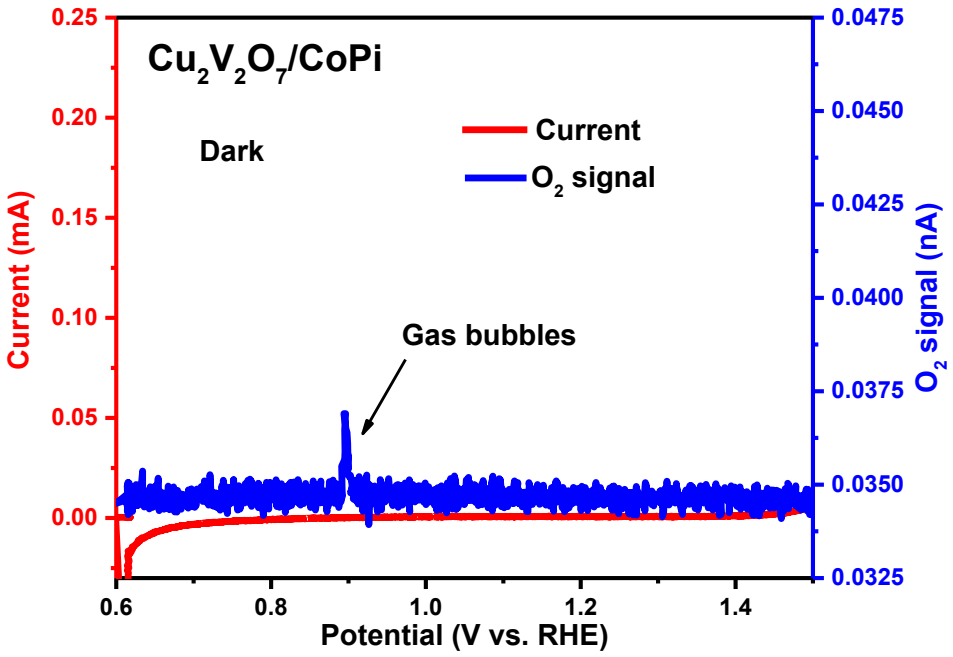

Figure S B21. DEMS LSV scans for a 200 nm $Cu_2V_2O_7$ photoanode without illumination, showing current (red) and O_2 signal (blue). Measurements were done in 0.3 M K_2SO_4 and 0.2 M phosphate buffer (pH 6.8) under back illumination with a scan rate of 2 mV/s.

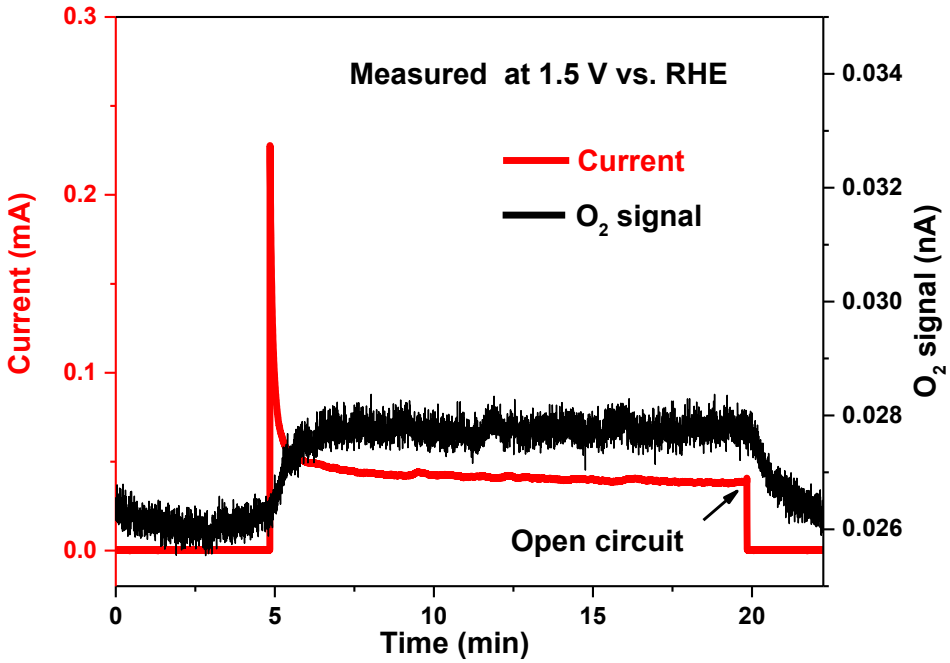

Figure S B22. DEMS constant potential measurements for a $Cu_2V_2O_7$ photoanode at 1.5 V vs. RHE, showing current (red) and O_2 signal (black). Measurements were done in 0.3 M K_2SO_4 and 0.2 M phosphate buffer (pH 6.8) under back illumination.

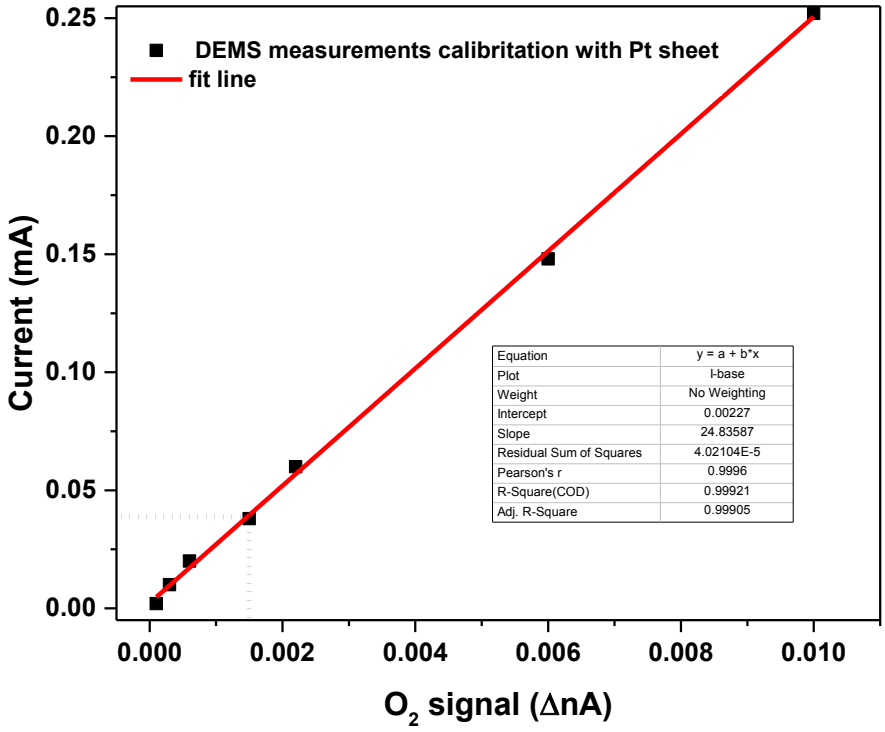

Figure S B23. Correlation between the O_2 signal and current. Measurements were done using a Pt sheet as the working electrode in 0.3 M K_2SO_4 and 0.2 M phosphate buffer (pH 6.8) under back illumination (to match the temperature of the photocathode measurements).

Appendix C: Supplemental Information for assessment of a W:$BiVO_4$–$CuBi_2O_4$ tandem photoelectrochemical cell for overall solar water splitting

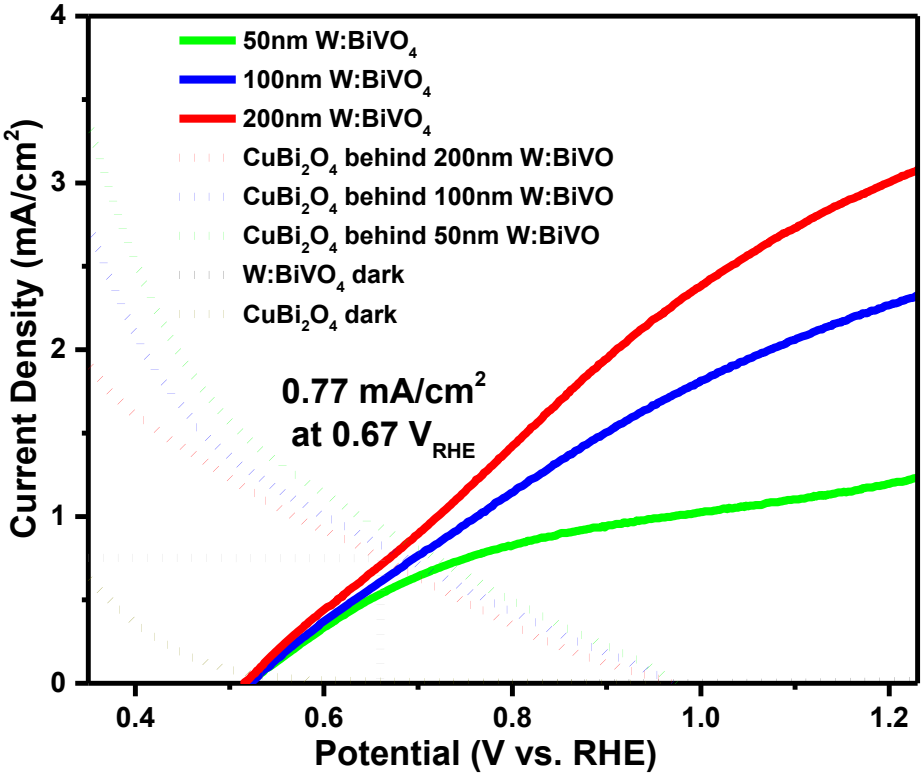

Figure S C1. LSV scans for W:$BiVO_4$ photoanodes with thicknesses of 50 nm (green solid line), 100 nm (blue solid line),, and 200 nm (red solid line), and a $CuBi_2O_4$ photocathode behind W:$BiVO_4$ photoanodes with thicknesses of 50 nm (green dotted line), 100 nm (blue dotted line), and 200 nm (red dotted line) filtering the incident AM1.5 illumination. Measurements were performed in three-electrode configuration in 0.3 M K_2SO_4 and 0.2 M phosphate buffer electrolyte (pH 6.8) as the base electrolyte with H_2O_2 added as a hole and electron scavenger. Positive current density values are used for anodic current from W:$BiVO_4$ and cathodic current from $CuBi_2O_4$.

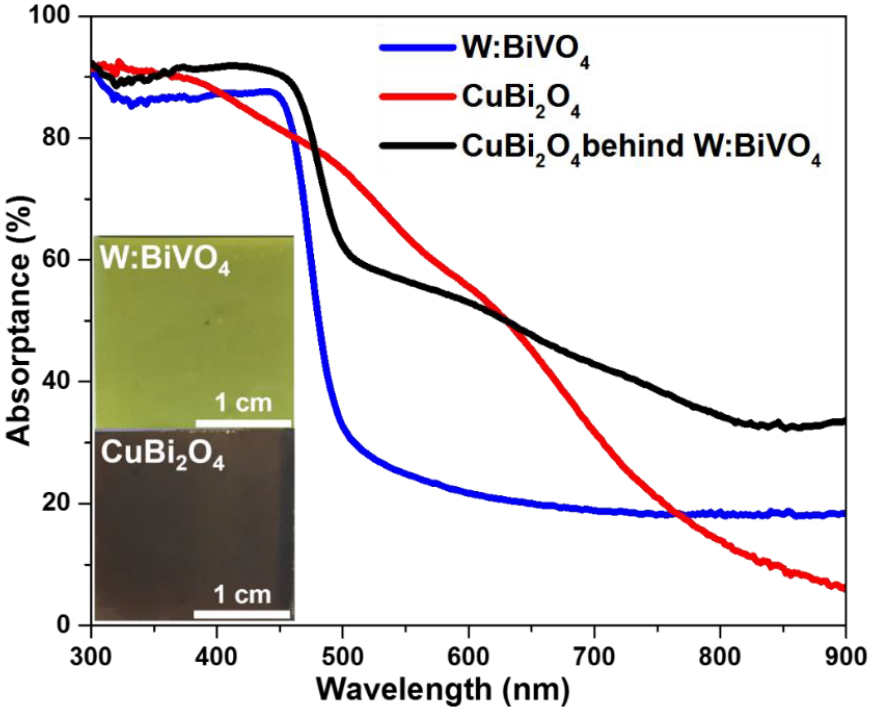

Figure S C2. UV-vis absorptiance spectra for W:$BiVO_4$ film (kblue line), $CuBi_2O_4$ film (red line), and a $CuBi_2O_4$ behind a W:$BiVO_4$ film (black line) on FTO substrates. The absorptance spectra were derived from transflectance (transmittance + reflectance) measurements. The film thickness of the $CuBi_2O_4$ and W:$BiVO_4$ photoelectrodes were 260 nm and 200 nm, respectively.

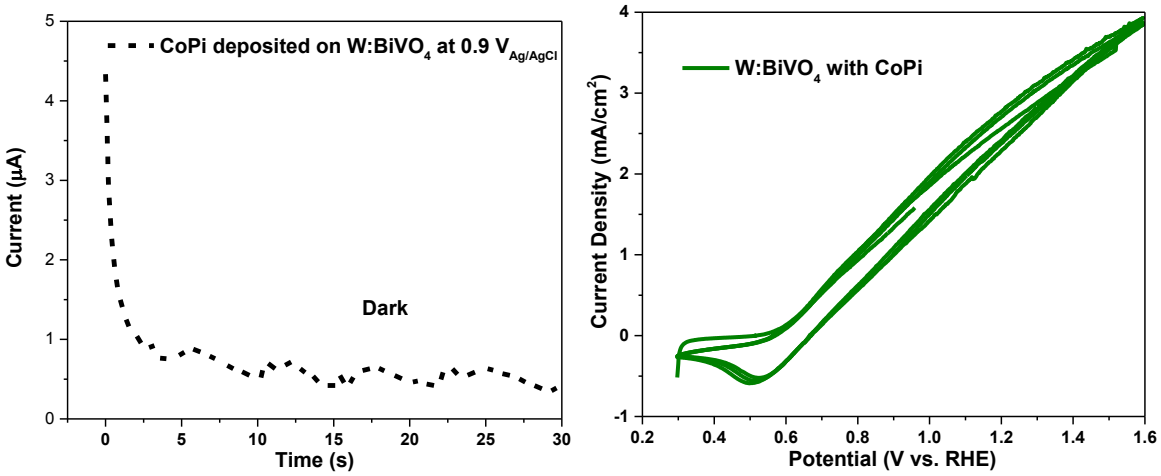

Figure S C3. (a) Electrodeposition Co-Pi catalyst onto W:$BiVO_4$ film in an electrochemical cell using a three-electrode configuration. (b) Cyclic voltammograms on a 200 nm W:$BiVO_4$ film measured with CoPi (for activation) in 0.3 M K_2SO_4 and 0.2 M phosphate buffer (pH 6.8). The scan rate was 20 mV s^{-1} for the measurements.

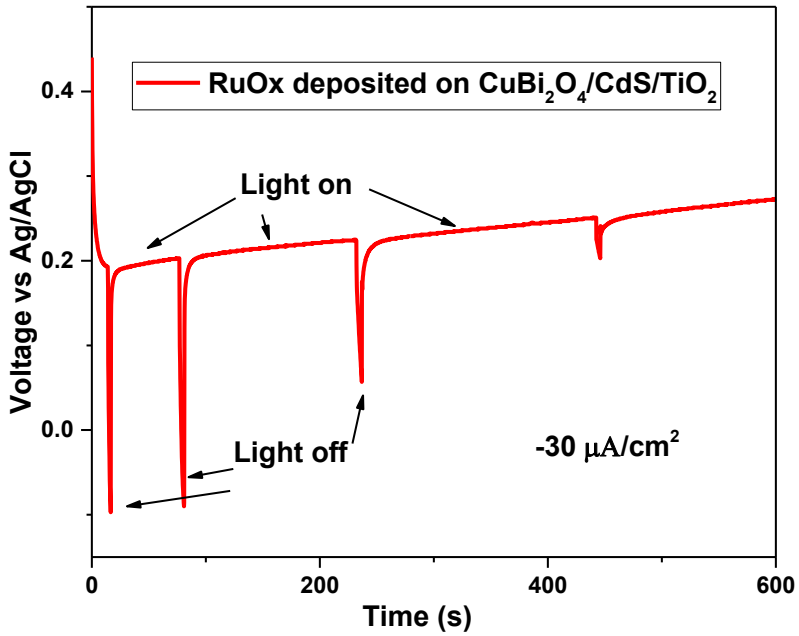

Figure S C4. Electrodeposition RuOx catalyst onto $CuBi_2O_4/CdS/TiO_2$ film in an electrochemical cell using a three-electrode configuration.

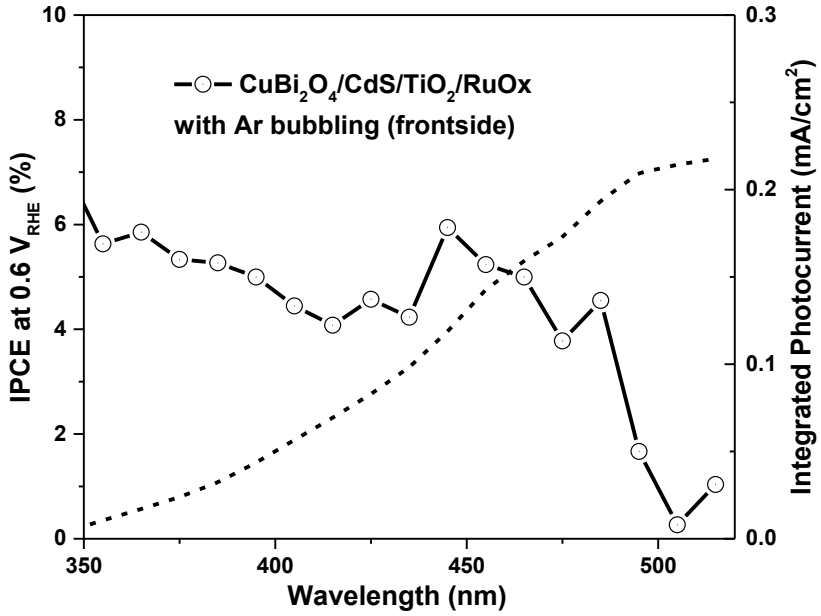

Figure S C5. IPCE spectra of protected $CuBi_2O_4$. The measurements were performed at 0.6 V versus RHE in 0.3 M K_2SO_4 and 0.2 M phosphate buffer electrolyte (pH 6.8) with Ar bubbling under back illumination.

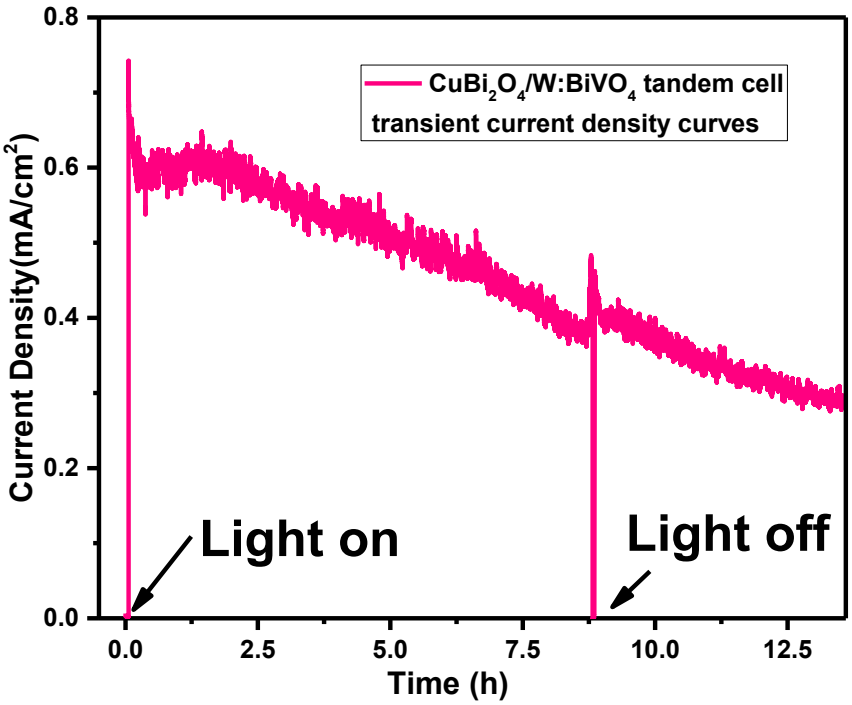

Figure S C6. Two-electrode $CuBi_2O_4$/W:$BiVO_4$ tandem cell long term transient current density curves. Simulated solar illumination (100 mW cm^{-2}) was activated after 60 s in the dark. The measurements were performed in 0.3 M K_2SO_4 and 0.2 M phosphate buffer (pH 6.8) electrolyte with H_2O_2 as scavenger.

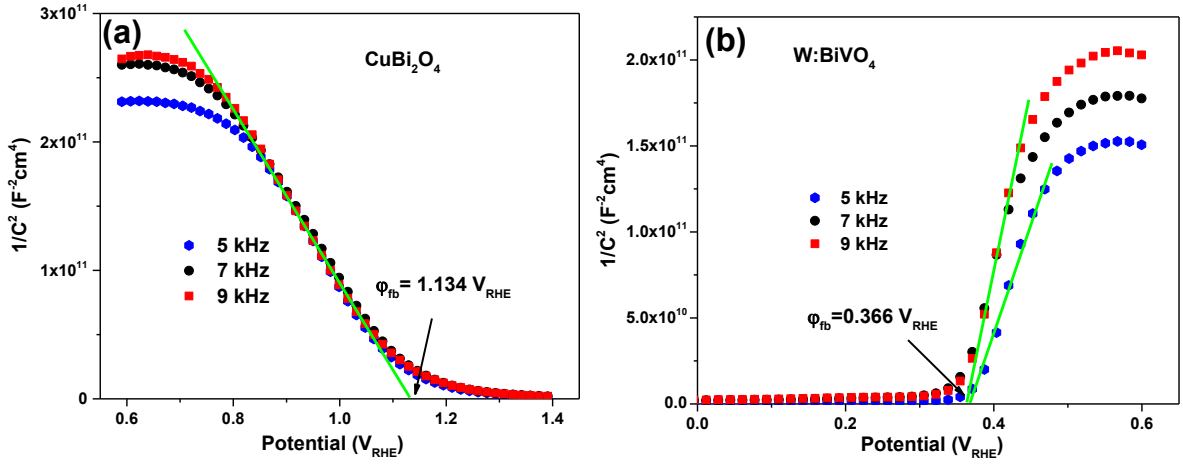

Figure S C7. Mott–Schottky plots for (a) $CuBi_2O_4$ films and (b) W:$BiVO_4$ film. Mott–Schottky measurements were performed in 0.3 M K_2SO_4 and 0.2 M phosphate buffer (pH 6.8) at 5 kHz, 7 kHz, and 9 kHz. Note that the system behaves as a simple RC series circuit for all three frequencies (Figure S4); the Mott-Schottky conditions are thus fulfilled and the changes in capacitance can be assigned to changes in the width of the space charge layer as a function of the applied potential.

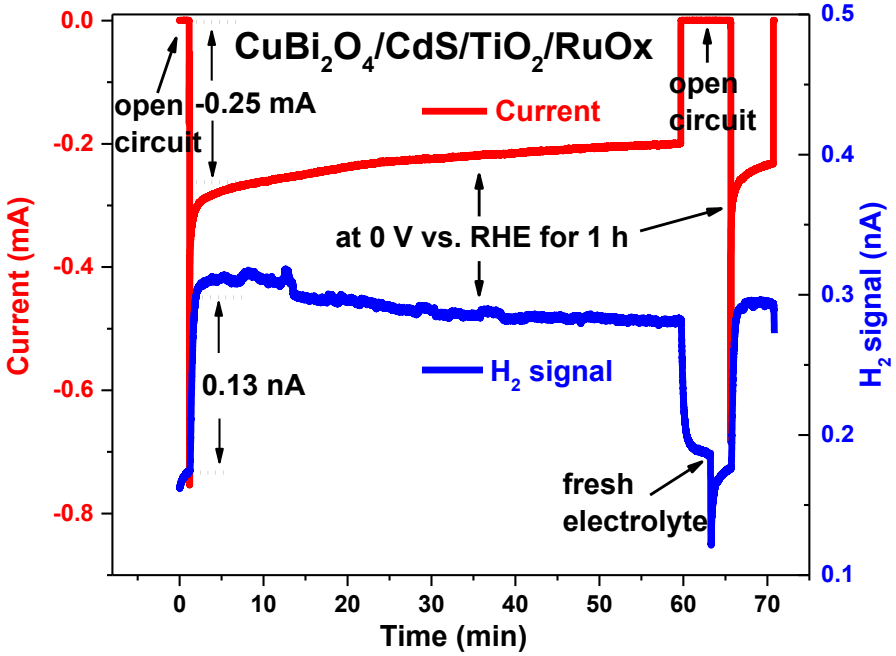

Figure S C8. DEMS constant potential measurements for a $CuBi_2O_4$/CdS/TiO_2/RuOx photocathode at 0.0 V vs. RHE, showing current (red) and H_2 signal (blue). Measurements were done in 0.3 M K_2SO_4 and 0.2 M phosphate buffer (pH 6.8) under back illumination.

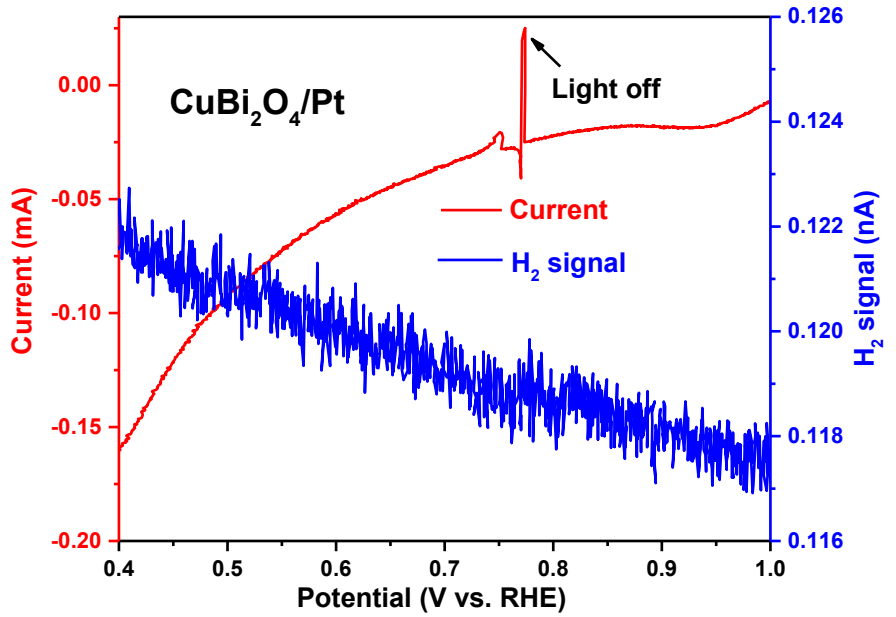

Figure S C9. DEMS LSV scans for $CuBi_2O_4$/Pt photocathode, showing current (red) and H_2 signal (blue) under back illumination. Measurements were done in 0.3 M K_2SO_4 and 0.2 M phosphate buffer (pH 6.8) under back illumination with a scan rate of 3.5 mV/s.

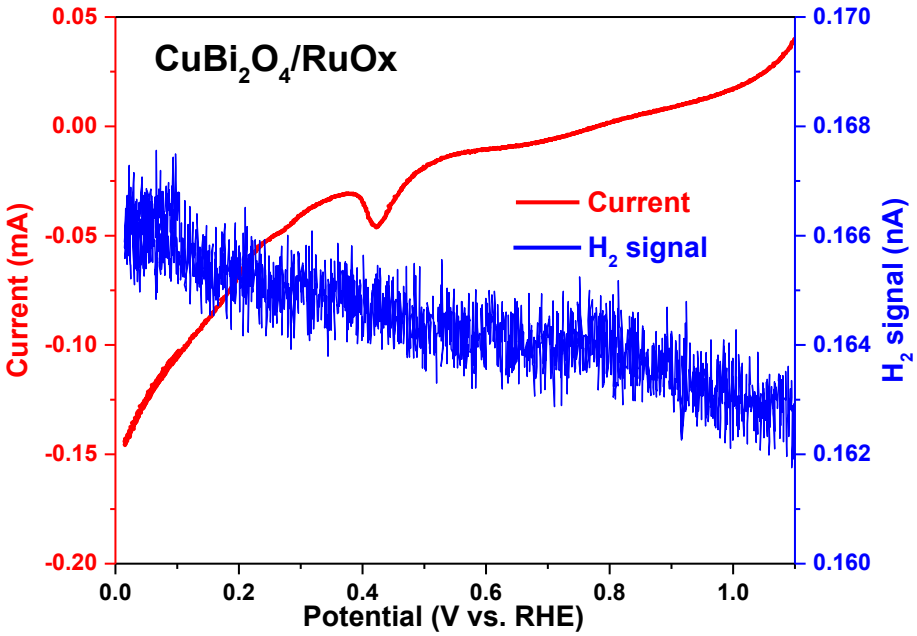

Figure S C10. DEMS LSV scans for $CuBi_2O_4$/RuOx photocathode, showing current (red) and H_2 signal (blue) under back illumination. Measurements were done in 0.3 M K_2SO_4 and 0.2 M phosphate buffer (pH 6.8) under back illumination with a scan rate of 3.5 mV/s.

List of publications

1. A. Song, P. Plate, A. Chemseddine, F. Wang, F. F. Abdi, M. Wollgarten, R. van de Krol and S. P. Berglund, *Journal of Materials Chemistry A*, 2019, **7**, 9183-9194.

2. A. Song, A. Chemseddine, I. Y. Ahmet, P. Bogdanoff, D. Friedrich, F. F. Abdi, S. P. Berglund and R. van de Krol, Evaluation of Copper Vanadate ($Cu_2V_2O_7$) as a Photoanode Material for Photoelectrochemical Water Oxidation, **prepared**.

3. A. Song, et al. Assessment of a W:$BiVO_4$−$CuBi_2O_4$ tandem photoelectrochemical cell for overall solar water splitting, **prepared**.

4. A. Song, et al. Evaluation of $Cu_5V_2O_{10}$ as a Photocathode Material for Photoelectrochemical Water Splitting, **in preparation**.

5. R. Gottesman, **A. Song,** R. van de Krol, A. Chemseddine. High-quality Stable $CuBi_2O_4$ Photoelectrodes by Combining Pulsed Laser Deposition and Rapid Thermal Processing, **prepared**.

6. Hirst, J., **Song, A.**, Berglund, S. P., Eichberger, R. et al. Defects study in $CuBi_2O_4$ by photo induced absorption spectroscopy, **in preparation**.

Acknowledgements

I would like to express my sincere gratitude to people who have helped me on the way towards this dissertation.

First of all, I give my deepest gratitude to my supervisors Prof. Roel van de Krol and Dr. Sean P. Berglund for their excellent advice and guidance. Thanks Prof. Roel van de Krol for giving me this opportunity to pursue my PhD in solar fuels group, and providing all the facilities and professional guidance. The group has a great and stimulating academic atmosphere that encourages innovations.

Special thanks to Sean for helping me drafting my research plan, reading and commenting my manuscripts, presentations and thesis. His constructive suggestions and valuable comments, based on deep scientific knowledge and high exigence standard, were always very helpful and appreciated.

I am also grateful to Dr. Karim, for his fruitful discussions and enthusiasm. I wish to extend my gratitude to all of the members in solar fuels lab including Fatwa, Karsten, Dennis, Ronen, Peter, Yimeng, Fuxian and Fanxing for their countless help in experiment and life. Thanks Moritz Gerstner for his kind help with the translation of the abstract. I gratefully acknowledge the China Scholarship Council program (File No. 201607040078) for providing me financial support.

Last but not least, I would like to thank my wife Fangfang Huo for her great understanding, patience and support during my PhD studies. Thanks Fangfang also for bringing our little angel, Yihe, to my life. Yihe, your smile makes every day full of love in our family. A lot of thanks to my parents in law and my parents for their great and unconditional support and love throughout the tough times.

Bibliography

[1] D. o. E. a. S. Affairs, *Technical report,United Nations (UN)*, 2017.

[2] B. S. R. o. W. E. 2018 and https://www.bp.com/en/global/corporate/news-and-insights/press releases/bp-statistical-review-of-world-energy-2018.html, 2018.

[3] P. K. T. Ralph., 2019.

[4] I. Dincer, *Renewable and Sustainable Energy Reviews*, 2000, **4**, 157-175.

[5] O. Ellabban, H. Abu-Rub and F. Blaabjerg, *Renewable and Sustainable Energy Reviews*, 2014, **39**, 748-764.

[6] E. D. Dr Fatih Birol, IEA, 2018.

[7] N. Kannan and D. Vakeesan, *Renewable and Sustainable Energy Reviews*, 2016, **62**, 1092-1105.

[8] V. Balzani, A. Credi and M. Venturi, *ChemSusChem*, 2008, **1**, 26-58.

[9] P. M. Yinghao Chu, *Global Energy Network Institute (GENI)*, 2011.

[10] G. R. Timilsina, L. Kurdgelashvili and P. A. Narbel, *Renewable and Sustainable Energy Reviews*, 2012, **16**, 449-465.

[11] F. Barbir, *Solar Energy*, 2005, **78**, 661-669.

[12] A. Fujishima and K. Honda, *Nature*, 1972, **238**, 37-38.

[13] R. Van de Krol and M. Grätzel, *Photoelectrochemical hydrogen production*, Springer, 2012.

[14] S. Hu, N. S. Lewis, J. W. Ager, J. Yang, J. R. McKone and N. C. Strandwitz, *The Journal of Physical Chemistry C*, 2015, **119**, 24201-24228.

[15] T. Bak, J. Nowotny, M. Rekas and C. C. Sorrell, *International Journal of Hydrogen Energy*, 2002, **27**, 991-1022.

[16] M. G. Walter, E. L. Warren, J. R. McKone, S. W. Boettcher, Q. Mi, E. A. Santori and N. S. Lewis, *Chemical Reviews*, 2010, **110**, 6446-6473.

[17] M. F. Weber and M. J. Dignam, *Journal of The Electrochemical Society*, 1984, **131**, 1258-1265.

[18] E. L. Miller, B. Marsen, D. Paluselli and R. Rocheleau, *Electrochemical and Solid-State Letters*, 2005, **8**, A247-A249.

[19] E. L. Miller, D. Paluselli, B. Marsen and R. E. Rocheleau, *Solar Energy Materials and Solar Cells*, 2005, **88**, 131-144.

[20] L. M. Peter and K. G. Upul Wijayantha, *ChemPhysChem*, 2014, **15**, 1983-1995.

[21] S. Hoang, S. Guo, N. T. Hahn, A. J. Bard and C. B. Mullins, *Nano Letters*, 2012, **12**, 26-32.

[22] K. Sivula and R. van de Krol, *Nature Reviews Materials*, 2016, **1**, 15010.

[23] Y. He, T. Hamann and D. Wang, *Chemical Society Reviews*, 2019, **48**, 2182-2215.

[24] Y. He, J. E. Thorne, C. H. Wu, P. Ma, C. Du, Q. Dong, J. Guo and D. Wang, *Chem*, 2016, **1**, 640-655.

[25] J. Augustynski, R. Solarska, H. Hagemann and C. Santato, 2006.

[26] S. P. Berglund, D. W. Flaherty, N. T. Hahn, A. J. Bard and C. B. Mullins, *The Journal of Physical Chemistry C*, 2011, **115**, 3794-3802.

[27] Y. Kuang, Q. Jia, G. Ma, T. Hisatomi, T. Minegishi, H. Nishiyama, M. Nakabayashi, N. Shibata, T. Yamada, A. Kudo and K. Domen, *Nature Energy*, 2016, **2**, 16191.

[28] D. K. Lee and K.-S. Choi, *Nature Energy*, 2018, **3**, 53.

[29] R. F. Bunshah, *Handbook of deposition technologies for films and coatings: science, technology, and applications*, William Andrew, 1994.

[30] F. F. Abdi and S. P. Berglund, *Journal of Physics D: Applied Physics*, 2017, **50**, 193002.

[31] Y. J. Jang and J. S. Lee, *ChemSusChem*, 2019.

[32] D. K. Lee, D. Lee, M. A. Lumley and K.-S. Choi, *Chemical Society Reviews*, 2019.

[33] Z. Wang, C. Li and K. Domen, *Chemical Society Reviews*, 2019.

[34] B. Y. Alfaifi, H. Ullah, S. Alfaifi, A. A. Tahir and T. K. Mallick, *Veruscr. Funct. Nanomater*, 2018, **2**, 1-26.

[35] Y. He, T. Hamann and D. Wang, *Chemical Society Reviews*, 2019.

[36] W. Septina, R. R. Prabhakar, R. Wick, T. Moehl and S. D. Tilley, *Chemistry of Materials*, 2017, **29**, 1735-1743.

[37] W. Niu, T. Moehl, W. Cui, R. Wick-Joliat, L. Zhu and S. D. Tilley, *Advanced Energy Materials*, 2018, **8**, 1702323.

[38] S. P. Berglund, F. F. Abdi, P. Bogdanoff, A. Chemseddine, D. Friedrich and R. van de Krol, *Chemistry of Materials*, 2016, **28**, 4231-4242.

[39] M. S. Prévot, N. Guijarro and K. Sivula, *ChemSusChem*, 2015, **8**, 1359-1367.

[40] K. Skorupska, P. A. Maggard, R. Eichberger, K. Schwarzburg, P. Shahbazi, B. Zoellner and B. A. Parkinson, *ACS Combinatorial Science*, 2015, **17**, 742-751.

[41] U. A. Joshi, A. M. Palasyuk and P. A. Maggard, *The Journal of Physical Chemistry C*, 2011, **115**, 13534-13539.

[42] M. Harb, D. Masih and K. Takanabe, *Physical Chemistry Chemical Physics*, 2014, **16**, 18198-18204.

[43] U. A. Joshi, A. Palasyuk, D. Arney and P. A. Maggard, *The Journal of Physical Chemistry Letters*, 2010, **1**, 2719-2726.

[44] P. P. Sahoo, B. Zoellner and P. A. Maggard, *Journal of Materials Chemistry A*, 2015, **3**, 4501-4509.

[45] J. Azevedo, S. D. Tilley, M. Schreier, M. Stefik, C. Sousa, J. P. Araújo, A. Mendes, M. Grätzel and M. T. Mayer, *Nano Energy*, 2016, **24**, 10-16.

[46] S. Ida, K. Yamada, T. Matsunaga, H. Hagiwara, Y. Matsumoto and T. Ishihara, *Journal of the American Chemical Society*, 2010, **132**, 17343-17345.

[47] Q. Yu, X. Meng, T. Wang, P. Li, L. Liu, K. Chang, G. Liu and J. Ye, *Chemical Communications*, 2015, **51**, 3630-3633.

[48] G. S. Pawar and A. A. Tahir, *Scientific Reports*, 2018, **8**, 3501.

[49] L. Pan, J. H. Kim, M. T. Mayer, M.-K. Son, A. Ummadisingu, J. S. Lee, A. Hagfeldt, J. Luo and M. Grätzel, *Nature Catalysis*, 2018, **1**, 412.

[50] A. Paracchino, V. Laporte, K. Sivula, M. Grätzel and E. Thimsen, *Nature Materials*, 2011, **10**, 456.

[51] F. Wang, W. Septina, A. Chemseddine, F. F. Abdi, D. Friedrich, P. Bogdanoff, R. van de Krol, S. D. Tilley and S. P. Berglund, *Journal of the American Chemical Society*, 2017, **139**, 15094-15103.

[52] U. Kang, S. K. Choi, D. J. Ham, S. M. Ji, W. Choi, D. S. Han, A. Abdel-Wahab and H. Park, *Energy & Environmental Science*, 2015, **8**, 2638-2643.

[53] C. G. Read, Y. Park and K.-S. Choi, *The journal of physical chemistry letters*, 2012, **3**, 1872-1876.

[54] Y. Oh, W. Yang, J. Kim, S. Jeong and J. Moon, *ACS Applied Materials & Interfaces*, 2017, **9**, 14078-14087.

[55] M. S. Prévot, X. A. Jeanbourquin, W. S. Bourée, F. Abdi, D. Friedrich, R. Van De Krol, N. s. Guijarro, F. Le Formal and K. Sivula, *Chemistry of Materials*, 2017, **29**, 4952-4962.

[56] Y. J. Jang, Y. B. Park, H. E. Kim, Y. H. Choi, S. H. Choi and J. S. Lee, *Chemistry of Materials*, 2016, **28**, 6054-6061.

[57] F. F. Abdi, A. Chemseddine, S. P. Berglund and R. van de Krol, *The Journal of Physical Chemistry C*, 2017, **121**, 153-160.

[58] M. Kölbach, I. J. Pereira, K. Harbauer, P. Plate, K. Höflich, S. P. Berglund, D. Friedrich, R. van de Krol and F. F. Abdi, *Chemistry of Materials*, 2018, **30**, 8322-8331.

[59] D. H. Taffa, R. Dillert, A. C. Ulpe, K. C. L. Bauerfeind, T. Bredow, D. W. Bahnemann and M. Wark, *Photoelectrochemical and theoretical investigations of spinel type ferrites for water splitting: a mini-review*, SPIE, 2016.

[60] Y. Gao, O. Zandi and T. W. Hamann, *Journal of Materials Chemistry A*, 2016, **4**, 2826-2830.

[61] S. K. Biswas and J.-O. Baeg, *International Journal of Hydrogen Energy*, 2013, **38**, 14451-14457.

[62] Y.-G. Lin, Y.-K. Hsu, Y.-C. Lin and Y.-C. Chen, *Electrochimica Acta*, 2016, **213**, 898-903.

[63] W. Guo, W. D. Chemelewski, O. Mabayoje, P. Xiao, Y. Zhang and C. B. Mullins, *The Journal of Physical Chemistry C*, 2015, **119**, 27220-27227.

[64] C.-M. Jiang, M. Farmand, C. H. Wu, Y.-S. Liu, J. Guo, W. S. Drisdell, J. K. Cooper and I. D. Sharp, *Chemistry of Materials*, 2017, **29**, 3334-3345.

[65] Q. Yan, G. Li, P. F. Newhouse, J. Yu, K. A. Persson, J. M. Gregoire and J. B. Neaton, *Advanced Energy Materials*, 2015, **5**, 1401840.

[66] E. S. Kim, N. Nishimura, G. Magesh, J. Y. Kim, J.-W. Jang, H. Jun, J. Kubota, K. Domen and J. S. Lee, *Journal of the American Chemical Society*, 2013, **135**, 5375-5383.

[67] W. D. Chemelewski, N. T. Hahn and C. B. Mullins, *The Journal of Physical Chemistry C*, 2012, **116**, 5255-5261.

[68] W. J. Jo, J.-W. Jang, K.-j. Kong, H. J. Kang, J. Y. Kim, H. Jun, K. P. S. Parmar and J. S. Lee, *Angewandte Chemie International Edition*, 2012, **51**, 3147-3151.

[69] S. U. M. Khan, M. Al-Shahry and W. B. Ingler, *Science*, 2002, **297**, 2243.

[70] A. Kudo, K. Omori and H. Kato, *Journal of the American Chemical Society*, 1999, **121**, 11459-11467.

[71] F. F. Abdi, N. Firet and R. van de Krol, *ChemCatChem*, 2013, **5**, 490-496.

[72] F. F. Abdi, L. Han, A. H. M. Smets, M. Zeman, B. Dam and R. van de Krol, *Nature Communications*, 2013, **4**, 2195.

[73] S. Wang, P. Chen, Y. Bai, J.-H. Yun, G. Liu and L. Wang, *Advanced Materials*, 2018, **30**, 1800486.

[74] F. F. Abdi and R. van de Krol, *The Journal of Physical Chemistry C*, 2012, **116**, 9398-9404.

[75] J. Su, L. Guo, N. Bao and C. A. Grimes, *Nano Letters*, 2011, **11**, 1928-1933.

[76] A. J. E. Rettie, H. C. Lee, L. G. Marshall, J.-F. Lin, C. Capan, J. Lindemuth, J. S. McCloy, J. Zhou, A. J. Bard and C. B. Mullins, *Journal of the American Chemical Society*, 2013, **135**, 11389-11396.

[77] K. J. McDonald and K.-S. Choi, *Energy & Environmental Science*, 2012, **5**, 8553-8557.

[78] Y. Kuang, Q. Jia, H. Nishiyama, T. Yamada, A. Kudo and K. Domen, *Advanced Energy Materials*, 2016, **6**, 1501645.

[79] S. Xiao, C. Hu, H. Lin, X. Meng, Y. Bai, T. Zhang, Y. Yang, Y. Qu, K. Yan and J. Xu, *Journal of Materials Chemistry A*, 2017, **5**, 19091-19097.

[80] Y. Pihosh, I. Turkevych, K. Mawatari, J. Uemura, Y. Kazoe, S. Kosar, K. Makita, T. Sugaya, T. Matsui, D. Fujita, M. Tosa, M. Kondo and T. Kitamori, *Scientific Reports*, 2015, **5**, 11141.

[81] J. H. Kim, J.-W. Jang, Y. H. Jo, F. F. Abdi, Y. H. Lee, R. van de Krol and J. S. Lee, *Nature Communications*, 2016, **7**, 13380.

[82] J. H. Kim, Y. Jo, J. H. Kim, J. W. Jang, H. J. Kang, Y. H. Lee, D. S. Kim, Y. Jun and J. S. Lee, *ACS Nano*, 2015, **9**, 11820-11829.

[83] Y.-S. Chen, J. S. Manser and P. V. Kamat, *Journal of the American Chemical Society*, 2015, **137**, 974-981.

[84] P. Chakthranont, T. R. Hellstern, J. M. McEnaney and T. F. Jaramillo, *Advanced Energy Materials*, 2017, **7**, 1701515.

[85] N. Kornienko, N. A. Gibson, H. Zhang, S. W. Eaton, Y. Yu, S. Aloni, S. R. Leone and P. Yang, *ACS Nano*, 2016, **10**, 5525-5535.

[86] F. F. Abdi, L. Han, A. H. Smets, M. Zeman, B. Dam and R. van de Krol, *Nat Commun*, 2013, **4**, 2195.

[87] Y. Pihosh, I. Turkevych, K. Mawatari, J. Uemura, Y. Kazoe, S. Kosar, K. Makita, T. Sugaya, T. Matsui and D. Fujita, *Scientific reports*, 2015, **5**, 11141.

[88] X. Shi, H. Jeong, S. J. Oh, M. Ma, K. Zhang, J. Kwon, I. T. Choi, I. Y. Choi, H. K. Kim and J. K. Kim, *Nature communications*, 2016, **7**, 11943.

[89] A. J. Nozik, in *Photoelectrochemical Water Splitting: Materials, Processes and Architectures*, The Royal Society of Chemistry, 2013, DOI: 10.1039/9781849737739-00359, pp. 359-388.

[90] L. M. Peter and K. Upul Wijayantha, *ChemPhysChem*, 2014, **15**, 1983-1995.

[91] F. Wang, W. Septina, A. Chemseddine, F. F. Abdi, D. Friedrich, P. Bogdanoff, R. van de Krol, S. D. Tilley and S. P. Berglund, *J Am Chem Soc*, 2017, **139**, 15094-15103.

[92] A. A. Bunaciu, E. G. UdriŞTioiu and H. Y. Aboul-Enein, *Critical Reviews in Analytical Chemistry*, 2015, **45**, 289-299.

[93] T. Kikuchi, *Rigaku J*, 1990, **7**, 27-35.

[94] G. Binnig, C. F. Quate and C. Gerber, *Physical Review Letters*, 1986, **56**, 930-933.

[95] Y. Ma, S. R. Pendlebury, A. Reynal, F. Le Formal and J. R. Durrant, *Chemical Science*, 2014, **5**, 2964-2973.

[96] F. F. Abdi, T. J. Savenije, M. M. May, B. Dam and R. van de Krol, *The Journal of Physical Chemistry Letters*, 2013, **4**, 2752-2757.

[97] M. Ziwritsch, S. n. Müller, H. Hempel, T. Unold, F. F. Abdi, R. van de Krol, D. Friedrich and R. Eichberger, *ACS Energy Letters*, 2016, **1**, 888-894.

[98] T. J. Savenije, A. J. Ferguson, N. Kopidakis and G. Rumbles, *The Journal of Physical Chemistry C*, 2013, **117**, 24085-24103.

[99] J. E. Kroeze, T. J. Savenije, M. J. W. Vermeulen and J. M. Warman, *The Journal of Physical Chemistry B*, 2003, **107**, 7696-7705.

[100] D. Cao, N. Nasori, Z. Wang, Y. Mi, L. Wen, Y. Yang, S. Qu, Z. Wang and Y. Lei, *Journal of Materials Chemistry A*, 2016, **4**, 8995-9001.

[101] M. K. Hossain, G. F. Samu, K. Gandha, S. Santhanagopalan, J. P. Liu, C. Janáky and K. Rajeshwar, *The Journal of Physical Chemistry C*, 2017, **121**, 8252-8261.

[102] A. Elaziouti, N. Laouedj and A. Bekka, *Environ Sci Pollut Res Int*, 2016, **23**, 15862-15876.

[103] R. Patil, S. Kelkar, R. Naphade and S. Ogale, *J. Mater. Chem. A*, 2014, **2**, 3661-3668.

[104] T. Arai, Y. Konishi, Y. Iwasaki, H. Sugihara and K. Sayama, *Journal of Combinatorial Chemistry*, 2007, **9**, 574-581.

[105] J. R. Bolton, S. J. Strickler and J. S. Connolly, *Nature*, 1985, **316**, 495.

[106] L. C. Seitz, Z. Chen, A. J. Forman, B. A. Pinaud, J. D. Benck and T. F. Jaramillo, *ChemSusChem*, 2014, **7**, 1372-1385.

[107] G. Sharma, Z. Zhao, P. Sarker, B. A. Nail, J. Wang, M. N. Huda and F. E. Osterloh, *Journal of Materials Chemistry A*, 2016, **4**, 2936-2942.

[108] H. S. Park, C. Y. Lee and E. Reisner, *Phys Chem Chem Phys*, 2014, **16**, 22462-22465.

[109] N. T. Hahn, V. C. Holmberg, B. A. Korgel and C. B. Mullins, *The Journal of Physical Chemistry C*, 2012, **116**, 6459-6466.

[110] F. Wang, A. Chemseddine, F. F. Abdi, R. van de Krol and S. P. Berglund, *Journal of Materials Chemistry A*, 2017, **5**, 12838-12847.

[111] M. S. Prévot, X. A. Jeanbourquin, W. S. Bourée, F. Abdi, D. Friedrich, R. van de Krol, N. Guijarro, F. Le Formal and K. Sivula, *Chemistry of Materials*, 2017, **29**, 4952-4962.

[112] M. S. Prévot and K. Sivula, *The Journal of Physical Chemistry C*, 2013, **117**, 17879-17893.

[113] A. Paracchino, J. C. Brauer, J.-E. Moser, E. Thimsen and M. Graetzel, *The Journal of Physical Chemistry C*, 2012, **116**, 7341-7350.

[114] Y. Nakato, S. Tonomura and H. Tsubomura, *Berichte der Bunsengesellschaft für physikalische Chemie*, 1976, **80**, 1289-1293.

[115] D. Kang, J. C. Hill, Y. Park and K.-S. Choi, *Chemistry of Materials*, 2016, **28**, 4331-4340.

[116] M. G. Helander, M. T. Greiner, Z. B. Wang, W. M. Tang and Z. H. Lu, *Journal of Vacuum Science & Technology A: Vacuum, Surfaces, and Films*, 2011, **29**, 011019.

[117] D. Cahen, G. Hodes, M. Grätzel, J. F. Guillemoles and I. Riess, *The Journal of Physical Chemistry B*, 2000, **104**, 2053-2059.

[118] T. Minami, T. Miyata and T. Yamamoto, *Surface and Coatings Technology*, 1998, **108-109**, 583-587.

[119] M. A. E.H. Rhoderick, M.Sc., Ph.D., C.Eng., F.Inst. P., F.I.E.E., *IEE REVIEW*, 1982, **. 129, Pt. I, No. 1**, 0143-7100/.

[120] S. M. Sze and K. K. Ng, *Physics Of Semiconductor Devices* A JOHN WILEY & SONS, JNC., PUBLICATION, 2007.

[121] P. Chatchai, Y. Murakami, S. y. Kishioka, A. Y. Nosaka and Y. Nosaka, *Electrochemical and Solid-State Letters*, 2008, **11**, H160.

[122] M.-K. Son, L. Steier, M. Schreier, M. T. Mayer, J. Luo and M. Grätzel, *Energy & Environmental Science*, 2017, **10**, 912-918.

[123] Y. Liang, T. Tsubota, L. P. A. Mooij and R. van de Krol, *The Journal of Physical Chemistry C*, 2011, **115**, 17594-17598.

[124] I. M. Chan, T.-Y. Hsu and F. C. Hong, *Applied Physics Letters*, 2002, **81**, 1899-1901.

[125] M. T. Greiner, M. G. Helander, Z.-B. Wang, W.-M. Tang and Z.-H. Lu, *The Journal of Physical Chemistry C*, 2010, **114**, 19777-19781.

[126] K. X. Steirer, J. P. Chesin, N. E. Widjonarko, J. J. Berry, A. Miedaner, D. S. Ginley and D. C. Olson, *Organic Electronics*, 2010, **11**, 1414-1418.

[127] E. H. Rhoderick, *IEE Proceedings I - Solid-State and Electron Devices*, 1982, **129**, 1.

[128] S. Sze, *Physics of semiconductor devices*, 2007, **3**.

[129] X.-L. Tang, H.-W. Zhang, H. Su and Z.-Y. Zhong, *Physica E: Low-dimensional Systems and Nanostructures*, 2006, **31**, 103-106.

[130] T. Nagano, M. Tsutsui, R. Nouchi, N. Kawasaki, Y. Ohta, Y. Kubozono, N. Takahashi and A. Fujiwara, *The Journal of Physical Chemistry C*, 2007, **111**, 7211-7217.

[131] R. Nouchi, *Journal of Applied Physics*, 2014, **116**, 184505.

[132] H. Peelaers, E. Kioupakis and C. G. Van de Walle, *Applied Physics Letters*, 2012, **100**, 011914.

[133] T. J. Coutts, D. L. Young and X. Li, *MRS Bulletin*, 2011, **25**, 58-65.

[134] S. C. Dixon, D. O. Scanlon, C. J. Carmalt and I. P. Parkin, *Journal of Materials Chemistry C*, 2016, **4**, 6946-6961.

[135] G. A. Sawatzky and J. W. Allen, *Physical Review Letters*, 1984, **53**, 2339-2342.

[136] S. P. Berglund, S. Hoang, R. L. Minter, R. R. Fullon and C. B. Mullins, *The Journal of Physical Chemistry C*, 2013, **117**, 25248-25258.

[137] A. E. Rakhshani, *Solid-State Electronics*, 1986, **29**, 7-17.

[138] L. Wei, C. Shifu, Z. Sujuan, Z. Wei, Z. Huaye and Y. Xiaoling, *Journal of Nanoparticle Research*, 2009, **12**, 1355-1366.

[139] J. Zhang and Y. Jiang, *Journal of Materials Science: Materials in Electronics*, 2015, **26**, 4308-4312.

[140] M. A. B. a. D. S. Ginley, *Journal of the Electrochemical Society*, 1978, **125**, 228-232.

[141] M. S. Prévot, Y. Li, N. Guijarro and K. Sivula, *Journal of Materials Chemistry A*, 2016, **4**, 3018-3026.

[142] M. D. Irwin, D. B. Buchholz, A. W. Hains, R. P. H. Chang and T. J. Marks, *Proceedings of the National Academy of Sciences*, 2008, **105**, 2783-2787.

[143] S.-H. Han, D.-Y. Lee, S.-J. Lee, C.-Y. Cho, M.-K. Kwon, S. P. Lee, D. Y. Noh, D.-J. Kim, Y. C. Kim and S.-J. Park, *Applied Physics Letters*, 2009, **94**, 231123.

[144] K.-C. Wang, P.-S. Shen, M.-H. Li, S. Chen, M.-W. Lin, P. Chen and T.-F. Guo, *ACS Applied Materials & Interfaces*, 2014, **6**, 11851-11858.

[145] C.-M. Jiang, G. Segev, L. H. Hess, G. Liu, G. Zaborski, F. M. Toma, J. K. Cooper and I. D. Sharp, *ACS Applied Materials & Interfaces*, 2018, **10**, 10627-10633.

[146] L. Zhou, Q. Yan, A. Shinde, D. Guevarra, P. F. Newhouse, N. Becerra-Stasiewicz, S. M. Chatman, J. A. Haber, J. B. Neaton and J. M. Gregoire, *Advanced Energy Materials*, 2015, **5**, 1500968.

[147] J. M. Hughes and R. W. Birnie, *American Mineralogist*, 1980, **65**, 1146-1149.

[148] C. Gadiyar, M. Strach, P. Schouwink, A. Loiudice and R. Buonsanti, *Chemical Science*, 2018, **9**, 5658-5665.

[149] A. Hassan, T. Iqbal, M. B. Tahir and S. Afsheen, *International Journal of Energy Research*, 2018, **43**, 9-28.

[150] M.-w. Kim, B. Joshi, H. Yoon, T. Y. Ohm, K. Kim, S. S. Al-Deyab and S. S. Yoon, *Journal of Alloys and Compounds*, 2017, **708**, 444-450.

[151] M. A. Lumley and K.-S. Choi, *Chemistry of Materials*, 2017, **29**, 9472-9479.

[152] M. K. Hossain, P. Sotelo, H. P. Sarker, M. T. Galante, A. Kormányos, C. Longo, R. T. Macaluso, M. N. Huda, C. Janáky and K. Rajeshwar, *ACS Applied Energy Materials*, 2019, **2**, 2837-2847.

[153] F. A. Benko and F. P. Koffyberg, *Canadian Journal of Physics*, 1992, **70**, 99-103.

[154] J. A. Seabold and N. R. Neale, *Chemistry of Materials*, 2015, **27**, 1005-1013.

[155] B. V. Slobodin and R. F. Samigullina, *Inorganic Materials*, 2010, **46**, 196-200.

[156] M. Schindler and F. C. Hawthorne, *Journal of Solid State Chemistry*, 1999, **146**, 271-276.

[157] P. N. Cherepansky, S. V. Krivovichev, S. K. Filatov, T. Armbruster and O. Y. Pankratova, *The Canadian Mineralogist*, 2005, **43**, 671-677.

[158] M. Yashima and R. O. Suzuki, *Physical Review B*, 2009, **79**.

[159] P. Newhouse, D. Boyd, A. Shinde, D. Guevarra, L. Zhou, E. Soedarmadji, G. Li, J. B. Neaton and J. M. Gregoire, *Journal of Materials Chemistry A*, 2016, **4**, 7483-7494.

[160] S. Shuang, L. Girardi, G. A. Rizzi, A. Sartorel, C. Marega, Z. Zhang and G. Granozzi, *Nanomaterials*, 2018, **8**, 544.

[161] D. de Waal and C. Hutter, *Materials Research Bulletin*, 1994, **29**, 843-849.

[162] J. Wiktor, I. Reshetnyak, M. Strach, M. Scarongella, R. Buonsanti and A. Pasquarello, *J Phys Chem Lett*, 2018, **9**, 5698-5703.

[163] M. Zhang, Y. Ma, D. Friedrich, R. van de Krol, L. H. Wong and F. F. Abdi, *Journal of Materials Chemistry A*, 2018, **6**, 548-555.

[164] D. K. Zhong, S. Choi and D. R. Gamelin, *Journal of the American Chemical Society*, 2011, **133**, 18370-18377.

[165] A. Song, P. Plate, A. Chemseddine, F. Wang, F. F. Abdi, M. Wollgarten, R. van de Krol and S. P. Berglund, *Journal of Materials Chemistry A*, 2019, **7**, 9183-9194.

[166] Z. H. Gan, G. Q. Yu, B. K. Tay, C. M. Tan, Z. W. Zhao and Y. Q. Fu, *Journal of Physics D: Applied Physics*, 2003, **37**, 81-85.

[167] J. Ghijsen, L. H. Tjeng, J. van Elp, H. Eskes, J. Westerink, G. A. Sawatzky and M. T. Czyzyk, *Physical Review B*, 1988, **38**, 11322-11330.

[168] Y. Liu, Y. Guo, L. T. Schelhas, M. Li and J. W. Ager, *The Journal of Physical Chemistry C*, 2016, **120**, 23449-23457.

[169] D. K. Lee, D. Lee, M. A. Lumley and K.-S. Choi, *Chemical Society Reviews*, 2019, **48**, 2126-2157.

[170] C. Li, T. Hisatomi, O. Watanabe, M. Nakabayashi, N. Shibata, K. Domen and J.-J. Delaunay, *Energy & Environmental Science*, 2015, **8**, 1493-1500.

[171] Y. J. Jang and J. S. Lee, *ChemSusChem*, 2019, **12**, 1835-1845.

[172] B. Alfaifi, H. Ullah, S. Alfaifi, A. Tahir and T. Mallick, *Photoelectrochemical solar water splitting: From basic principles to advanced devices*, 2018.

[173] P. Bornoz, F. F. Abdi, S. D. Tilley, B. Dam, R. van de Krol, M. Graetzel and K. Sivula, *The Journal of Physical Chemistry C*, 2014, **118**, 16959-16966.

[174] L. Pan, J. H. Kim, M. T. Mayer, M.-K. Son, A. Ummadisingu, J. S. Lee, A. Hagfeldt, J. Luo and M. Grätzel, *Nature Catalysis*, 2018, **1**, 412-420.

[175] C.-Y. Lin, Y.-H. Lai, D. Mersch and E. Reisner, *Chemical Science*, 2012, **3**, 3482-3487.

[176] H. Kim, S. Bae, D. Jeon and J. Ryu, *Green Chemistry*, 2018, **20**, 3732-3742.

[177] Y. Liu, B. R. Wygant, O. Mabayoje, J. Lin, K. Kawashima, J.-H. Kim, W. Li, J. Li and C. B. Mullins, *ACS applied materials & interfaces*, 2018, **10**, 12639-12650.

[178] S. P. Berglund, A. J. E. Rettie, S. Hoang and C. B. Mullins, *Physical Chemistry Chemical Physics*, 2012, **14**, 7065-7075.

[179] C. Du, J. Yang, J. Yang, Y. Zhao, R. Chen and B. Shan, *International Journal of Hydrogen Energy*, 2018, **43**, 22807-22814.

[180] J. Li, M. Griep, Y. Choi and D. Chu, *Chemical Communications*, 2018, **54**, 3331-3334.

[181] Y.-H. Lai, K.-C. Lin, C.-Y. Yen and B.-J. Jiang, *Faraday Discussions*, 2019, DOI: 10.1039/C8FD00183A.

[182] J. H. Kim, A. Adishev, J. Kim, Y. S. Kim, S. Cho and J. S. Lee, *ACS Applied Energy Materials*, 2018, **1**, 6694-6699.

[183] S. D. Tilley, M. Schreier, J. Azevedo, M. Stefik and M. Graetzel, *Advanced Functional Materials*, 2014, **24**, 303-311.

[184] F. Le Formal, K. Sivula and M. Grätzel, *The Journal of Physical Chemistry C*, 2012, **116**, 26707-26720.

[185] M. Shao, Q. Chang, J.-P. Dodelet and R. Chenitz, *Chemical Reviews*, 2016, **116**, 3594-3657.

[186] H. A.-K. S. Hadzi-Jordanov, M. Vukoviff, ~ and B. E. Conway, *J. Electrochem. Soc.*, 1978, **125**, 1471-1480.

[187] M. R. Nellist, J. Qiu, F. A. L. Laskowski, F. M. Toma and S. W. Boettcher, *ACS Energy Letters*, 2018, **3**, 2286-2291.

[188] J. E. Thorne, S. Li, C. Du, G. Qin and D. Wang, *The Journal of Physical Chemistry Letters*, 2015, **6**, 4083-4088.

[189] D. Abou-Ras, T. Kirchartz and U. Rau, *Advanced characterization techniques for thin film solar cells*, John Wiley & Sons, 2016.